A Fused Silica Cherenkov Detector for the Parity-Violating P2 Experiment at MESA

Kathrin IMAI

born in Mainz

A thesis submitted in fulfillment of the requirements
for the degree of
Doktor der Naturwissenschaften

Faculty 08: Physics, Mathematics and Computer Science

Johannes Gutenberg University Mainz

June 13, 2021

Dean of the faculty	: Prof. Dr. M. Hanke-Bourgeois
Date of the oral examination	: 10/27/2022

Contents

Chapter 1

Motivation and Aims of the P2 Experiment

Fundamental physics is a method for gaining a deeper understanding of the world. Just as it is crucial for every child to explore its environment in a playful way without any immediate purpose, it is of utmost importance for us to strive for more knowledge of what fundamental particles the world consists of and how it is held together "in its innermost core".

The Standard Model attempts to explain the ultimate building blocks of reality and how they interact. It sums up our current fundamental knowledge of particle physics. Although called a model, it is rather an elaborate mathematical theory formulated in terms of Lagrangians. It is based on the symmetry group $SU(3)_C \times SU(2)_L \times U(1)_Y$, in which the first term describes the strong force, and the second and third terms describe the weak and the electromagnetic force. These interactions occur between quarks and leptons via the exchange of force carrier particles, the gauge bosons. The strong interaction is mediated by the eight gluons. The electroweak force is the unified description of the weak and the electromagnetic forces, and its gauge bosons are the W^+, W^- and the Z^0 and the photon.

Within the Standard Model, both quarks and leptons exist in 6 variants called "flavours" which can be grouped into three pairs called generations. The "up" and the "down" quark, which have the lowest mass and are the most stable are shown in the left most column of figure 1.1. The heavier quarks, the charm, strange as well as top and bottom quarks are less stable and quickly decay into up and down. The leptons are also subdivided into three generations of doublets, the stable electron and its neutrino, the muon and muon neutrino, and the tau and tau neutrino. All gauge bosons have spin quantum number 1. The Higgs boson with spin 0 does therefore not qualify as a gauge boson. Figure 1.1 lists quarks, leptons and gauge bosons with their intrinsic properties mass, electric charge, and
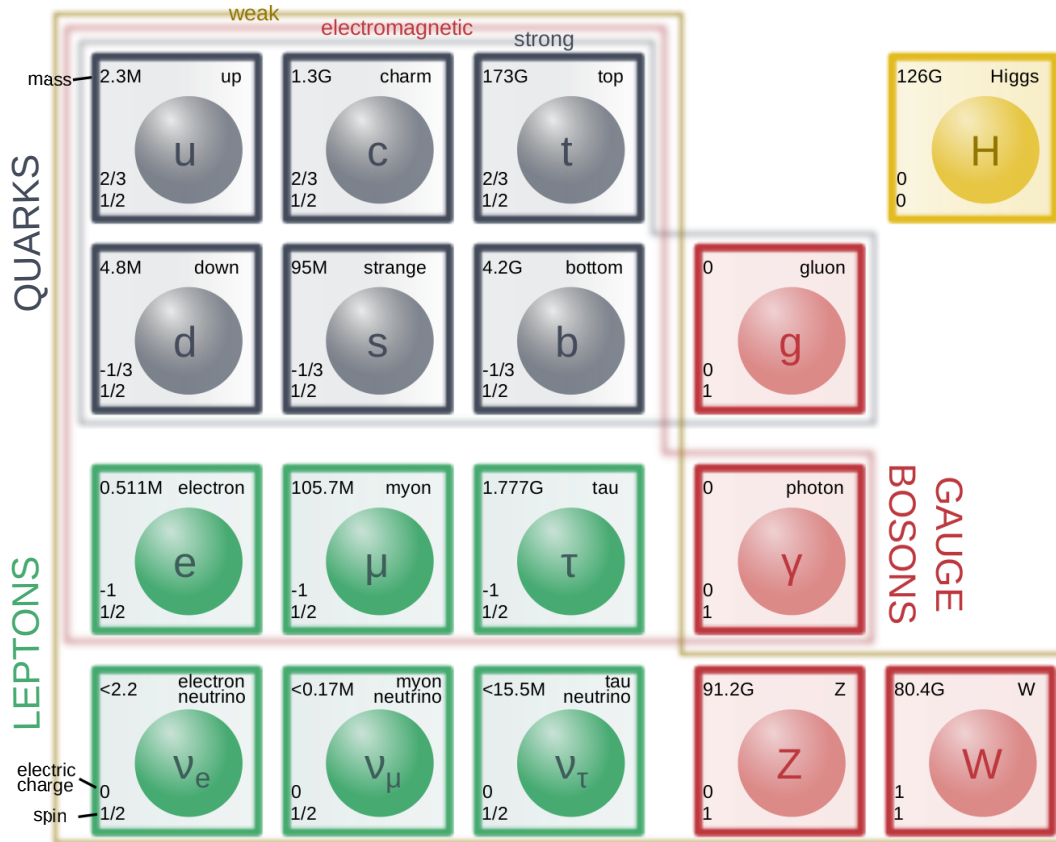
FIGURE 1.1: Particles in the Standard Model with their classification and intrinsic properties. Masses are shown in eV.

spin. Each of these particles has an antiparticle with opposite value of electric charge, colour charge, and flavour, but the same mass and spin.

The Standard Model describes the world in a very concise and comprehensive way and has repeatedly proven to be one of the most successful theories in science. It has predicted the existence and masses of the Higgs boson, as well as those of the Z and W bosons, the gluon, and top, and charm quark very accurately before there was experimental evidence of these particles.

However, we know that the theory is incomplete. Its most apparent shortcoming is perhaps the complete lack of a description of gravity, the most frequently observed fundamental force in our daily life. Moreover, the vast matter-antimatter asymmetry in our universe cannot be explained to date. The recent measurement of neutrino oscillations has proven that neutrinos have a non-zero mass, but in the Standard Model they appear as massless particles. These are some examples that demonstrate the necessity of Standard Model extensions, and numerous theories have in the past been elaborated on.

The most central task of experimental particle physics today is to provide measurement data to corroborate or falsify these models. Scientists at CERN use high

energy collisions in order to potentially create and detect new particles. The experimental determination of Standard Model observables at very high precision is complementary to these high energy experiments: Small deviations of experimental data and theoretical predictions can provide an indication of the existence of the same unknown particles, as higher-order physical processes lead to radiative corrections in the observable.

One such observable whose measurement may be sensitive to "new physics" is the electroweak mixing angle Θ_W, often referred to as the Weinberg angle. It is the central parameter of the electroweak theory. A theoretical introduction of the electroweak interaction and the weak mixing angle within the Standard Model is given in chapter 2 of this thesis.

The future P2 Experiment is going to access the electroweak mixing angle via the determination of the weak charge of the proton at the future *Mainz Energy recovering Superconducting Accelerator* (MESA). The weak mixing angle has been measured before, and section 2.2 contains an overview of past and future experiments while at the same time motivating why P2 is necessary and important. The experimental approach used in the P2 Experiment and the specific parts and setup are described in chapter 3.

The main task of this thesis is the development of an electron detector for the P2 Experiment. This required suitability considerations as well as preparatory material studies, which are presented in chapter 4. The prototypes emerging from the design choices based on these studies have been tested at the MAMI electron beam. After an introduction of the operating principle of Cherenkov detectors, which are found to be suitable for the P2 Experiment, the implementation, analysis, and results of these prototype tests are presented in chapter 5.

As the P2 detector is going to be exposed to a substantial amount of radiation the proposed Cherenkov medium has been tested for its radiation hardness as described in chapter 6.

In order to examine the feasibility of the measurement of the weak charge of the proton with the P2 Experimental setup and specifically with the quartz Cherenkov detector as designed within this thesis, a GEANT4 simulation of the physics processes of the signal and background particles was performed and validated by means of the data taken during the detector prototype tests. This simulation is the subject of chapter 7. It can quantify the signal yield of the detector to all relevant particles that occur during the data taking and is thus crucial for the determination of the achievable precision of the experiment, which is discussed in chapter 8.

Chapter 2

Theory of the Weak Mixing Angle

A complete coverage of the electroweak theory is beyond the scope of this thesis and is treated in depth in numerous textbooks, e.g. in [1, 2]. The main goal of this chapter is to provide a definition of the weak mixing angle and to enlighten the experimental method that is utilized in order to measure this quantity in the P2 Experiment.

2.1 Electroweak Interaction and the Weak Mixing Angle

The three fundamental forces described in the Standard Model are the strong, the electromagnetic, and the weak force. Particles typically decay by the strong interaction in $\tau_s \sim 10^{-23}$ s and by electromagnetic interaction in $\tau_{em} \sim 10^{-16}$ s, whereas weak processes can take up to $\tau_w = 2.2 \times 10^{-6}$ s for the $\mu^- \to e^- \overline{\nu}_e \nu_\mu$ muon decay [1].

The weak force is mediated by two types of gauge bosons, the charged W-boson and the neutral Z-boson, which couple to weak hypercharges carried by all leptons and quarks. While particles that interact via a Z-boson stay the same, conservation laws require that the electric charge of the particle changes during the emission of a W-boson. Charged leptons convert into neutrinos of the same lepton generation and vice versa, and quarks convert from up-like to down-like and vice versa. Weak charges and form factors can be defined in analogy with the electromagnetic charges and form factors.

Compared to the other fundamental forces, the weak interaction is unique in a few regards:

- All leptons and quarks are subject to weak interactions.

- The weak force is mediated by massive gauge bosons.

- Weak interactions violate parity.

- Particles change flavour in specific weak interaction processes, namely the so-called charged current interactions.

2.1.1   Electroweak Unification

The weak interactions by themselves are not based on a symmetry that can be observed in nature. Expressing the weak interactions in terms of a symmetry principle inevitably leads to a combined explanation of the electromagnetic interaction with the weak interaction. The unification of these two forces —which are phenomenologically of a very different nature— was performed in the 1960s by Sheldon Lee Glashow [3], Steven Weinberg [4] and Abdus Salam [5] with the intention to construct a re-normalizable and gauge-invariant theory in analogy with the previously developed *quantum electrodynamics* (QED).

The symmetry group under which the electroweak Lagrangian remains invariant is the

$$SU(2)_L \times U(1)_Y \tag{2.1}$$

group.

$SU(2)_L$ describes weak isospin transformations, and has the form

$$SU(2)_L = e^{ig\vec{T}\cdot\vec{f}(x)} \tag{2.2}$$

where $\vec{T}$ are the three generators of the transformations and $\vec{f}(x)$ corresponds to rotations in isospin space.

$U(1)_Y$ describes weak hypercharge transformations of the form

$$U(1)_Y = e^{ig'YP(x)} \tag{2.3}$$

with one generator Y and a phase transformation $P(x)$.

The invariance of the field Lagrangians under 2.1 implies the existence of one gauge field for each generator. The gauge field associated with $U(1)_Y$ is usually called B whereas the fields corresponding to the $SU(2)_L$ generators are called W_1, W_2, and W_3. The subscript L indicates the coupling to exclusively left-handed fermions,

which leads to the parity-violating nature of weak interactions. The symbols g and g' in equations 2.2 and 2.3 denote the coupling strengths of the respective interactions.

W_1, W_2, W_3, and B are not the experimentally observable exchange particles of the electroweak interaction, but they form a complete basis in the space of electroweak gauge fields. Consequently the measurable eigenstates of the mass operator, W^+, W^-, Z and A can be redefined in terms of these gauge fields W_1, W_2, W_3, and B.

According to experimental observations the charged W-bosons couple exclusively to left-handed fermions. Their fields can be written as linear combinations of W_1 and W_2:

$$\begin{pmatrix} W^+ \\ W^- \end{pmatrix} = \begin{pmatrix} \frac{1}{\sqrt{2}} & -\frac{i}{\sqrt{2}} \\ \frac{1}{\sqrt{2}} & \frac{i}{\sqrt{2}} \end{pmatrix} \begin{pmatrix} W_1 \\ W_2 \end{pmatrix} \tag{2.4}$$

Z-bosons and photons on the other hand couple to both right-handed and left-handed fermions and therefore have to be described as a *mixing* of the fields W_3 and B:

$$\begin{pmatrix} Z \\ A \end{pmatrix} = \begin{pmatrix} \cos\Theta_W & -\sin\Theta_W \\ \sin\Theta_W & \cos\Theta_W \end{pmatrix} \begin{pmatrix} W_3 \\ B \end{pmatrix} \tag{2.5}$$

The angle Θ_W is called the electroweak mixing angle or Weinberg angle. It is directly related to the coupling constants g and g' via

$$\frac{g'}{g} = \tan\Theta_W \tag{2.6}$$

or, written in terms of the electromagnetic coupling $e = gg'/\sqrt{g^2 + g'^2}$:

$$\frac{e}{g} = \sin^2\Theta_W \tag{2.7}$$

and can therefore be interpreted as the ratio of the strengths of the electromagnetic and the weak forces. It relates to the W- and Z-boson masses by

$$\sin^2\Theta_W = 1 - \frac{M_W^2}{M_Z^2} \tag{2.8}$$
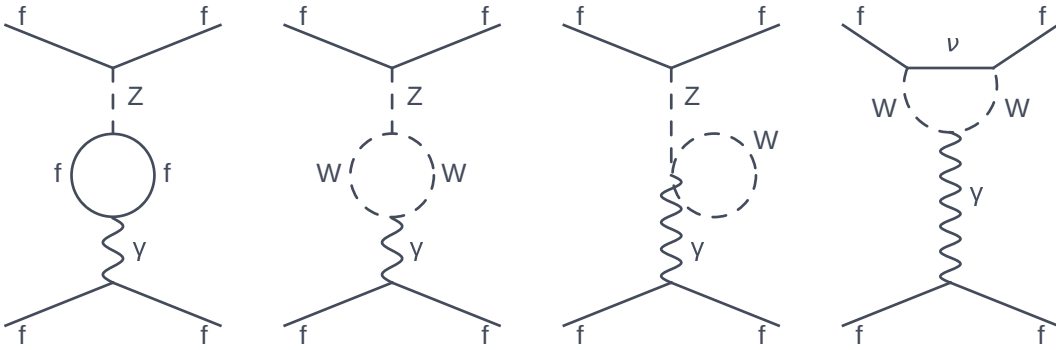
FIGURE 2.1: Radiative corrections which lead to the Q^2 dependence of the weak mixing angle $\sin^2 \Theta_W$ represented as Feynman diagrams.

The weak mixing angle is a central parameter of the Standard Model and can be determined from many different physical processes involving small momentum transfers of the order of $\mathcal{O}(1\,\mathrm{MeV})$ in atomic parity violation experiments up to values as high as the mass of the Z-boson $m_Z = 91.1876(21)\,\mathrm{GeV}$ [6] in scattering experiments. Its value at the Z-pole is

$$\sin^2 \Theta_W(\mu = m_Z) = \left\langle \hat{s}_Z^2 \right\rangle = 0.23125(16) \tag{2.9}$$

2.1.2 Scale Dependence of the Weak Mixing Angle

While the weak mixing angle as defined in 2.6, 2.7, and 2.8 is clearly a constant, the incorporation of kinematic-dependent radiative corrections due to higher order physical processes as shown in the Feynman diagrams in figure 2.1 leads to a dependence on the value of the momentum transfer $\mu = \sqrt{|Q^2|}$. This so-called *running* of the weak mixing angle is depicted in figure 2.2 [7], which shows measurements of the weak mixing angle along with the standard model prediction.

The two most precise ones have been made at electron-positron colliders at high energies $E = m_Z c^2$. These measurements fix the curve at the so-called Z-pole while calculations of the influence of the incorporated radiative corrections determine the running, so that the scale dependent value of the weak mixing angle can be written as

$$\sin^2 \Theta_W(\mu) = \kappa(\mu) \cdot \sin^2 \Theta_W(m_Z) \tag{2.10}$$

where known physics processes are incorporated in $\kappa(\mu)$. High precision measurements of the weak mixing angle are regarded as a probe for physics beyond the Standard Model because the existence of the latter would lead to deviations from the predicted curve. The running of the weak mixing angle clarifies the necessity of
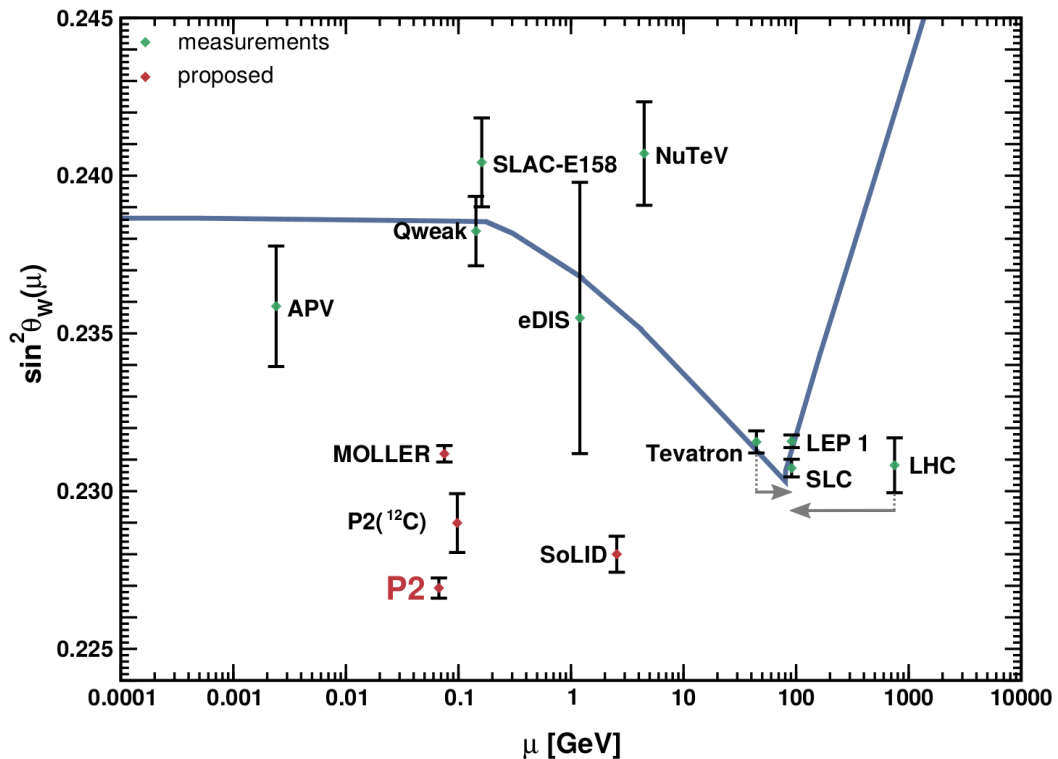
FIGURE 2.2: Standard Model prediction of the running of the weak mixing angle $\sin^2 \Theta_W(\mu)$ with the momentum transfer $\mu = \sqrt{|Q^2|}$ along with past and future measurements [7]. The position of the proposed experiments along the y-axis is chosen arbitrarily. Tevatron and LHC are Z-pole experiments but the markers have been shifted horizontally for sake of clarity. The Qweak result was added according to the collaboration's recent publication [8].

several measurements at different momentum transfers. Additionally it is crucial to measure the weak charges of different particles and nuclei, because each weak charge would be subject to individual shifts if physics beyond the standard model existed, e.g. in the form of a dark photon [9]. Details on the sensitivity of the weak charges of the electron, the proton, and ^{12}C and ^{133}Cs nuclei to new physics effects can be found in [10] and are refered to once more in section 2.2.4 of this chapter.

2.2 Complementarity of Various Measurements of $\sin^2 \Theta_W$

The weak mixing angle has been measured numerous times using various physical processes. Gaining an overview of the previous and planned experiments is important for understanding the motivation for a further measurement at the MESA

accelerator in Mainz. There is a clear discrepancy between the theoretically pre-
dicted running of the electroweak mixing angle and the measurement data shown
in figure 2.2. The most precise measurements at the Z-pole differ by more than
three standard deviations from each other. Data extracted from atomic parity vio-
lation and neutron scattering show large deviations as well. Various attempts have
been made to explain this anomaly, but there is an obvious need for more high
precision determinations. While measurements at $Q^2 = M_Z$ have little sensitivity
to verifying the existence of a dark photon, experiments run at low momentum
transfers $Q^2 \ll M_Z$ are a promising means in the search for new physics involving
such scenarios.

2.2.1 Collider Experiments at the Z-pole

Towards the end of the 20th century large electron-positron colliders reaching
center-of-mass energies above $91\,\mathrm{GeV}$ became available for experiments and al-
lowed on-shell productions of the Z-boson. One of those machines was the *Large
Electron Positron collider* (LEP) at CERN in Geneva, Switzerland; another was
the *Stanford Linear Collider* (SLC) at the *Stanford Linear Accelerator Center*
(SLAC) in California, USA. At both of these facilities a high precision measure-
ment of the weak mixing angle was performed at center-of-mass energies near the
Z^0-resonance. The SLC used longitudinally polarized electrons to collide with
unpolarized positrons.

The parity-violating nature of the weak interaction results in a left-right asymme-
try in the Z-boson production:

$$A_{LR} = \frac{1}{P_e} \frac{\sigma_L - \sigma_R}{\sigma_L + \sigma_R} \tag{2.11}$$

The electron polarization P_e was as high as 75%, measured to a precision of $\frac{\delta P_e}{P_e} \approx$
0.5%. The result of data collected between 1992 and 1998 has been published
in [11]

$$\sin^2 \Theta_W = 0.23097 \pm 0.00027 \tag{2.12}$$

At LEP high luminosities were reached to create Z-bosons which in turn decay
to fermions: $e^+ e^- \to Z \to b\bar{b}$. Both electrons and positrons were unpolarised.
An effective polarisation along the beam axis of the created gauge bosons results
from the difference between left- and right-handed coupling of the Z^0-boson to
fermions. Due to the parity-violating nature of the weak interaction one can
measure a forward-backward asymmetry when the Z-bosons decay to fermions:
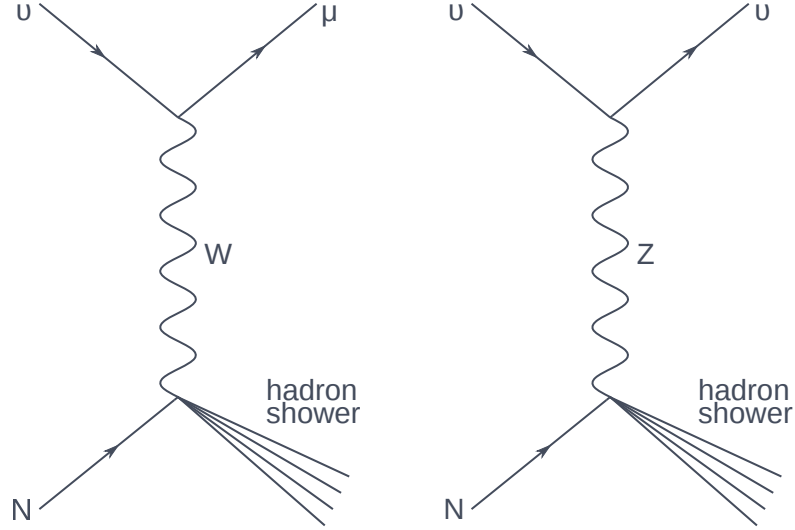
FIGURE 2.3: Feynman diagrams of scattering processes which were used in the NuTeV-experiment to access the weak mixing angle. The left diagram shows the charged current interaction mediated by a W-boson, the right one shows the neutral current interaction via a Z-boson.

$$A_{FB}(b\bar{b}) = \frac{N_F - N_B}{N_F + N_B} \tag{2.13}$$

N_F is the number of fermions emitted in beam direction and N_B is the number of fermions emitted in backward direction.

The value of the weak mixing angle from this measurement is [12]

$$\sin^2 \Theta_W = 0.23193 \pm 0.00029 \tag{2.14}$$

The results from SLC and LEP differ by 3.2 standard deviations. The expectation value $\langle \hat{s}_Z^2 \rangle$ determined from all measurements at the Z-pole is

$$\left\langle \hat{s}_Z^2 \right\rangle = 0.23125 \pm 0.00016 \tag{2.15}$$

2.2.2 Neutrino-Nucleon Deep Inelastic Scattering

The NuTeV experiment at Fermilab measured the cross sections of the neutrino and anti-neutrino deep-inelastic scattering from atomic nuclei in an $18\,\mathrm{m}$ long steel target at $\mu = 5\,\mathrm{GeV}$. The underlying processes mediated by weak neutral currents and by weak charged currents between the neutrinos and target nuclei are depicted in the Feynman diagrams of figure 2.3.

The electroweak mixing angle is extracted using the relation [13]

$$\frac{\sigma_{nc}^{\nu} - \sigma_{nc}^{\bar{\nu}}}{\sigma_{cc}^{\nu} - \sigma_{cc}^{\bar{\nu}}} = \rho^2(\frac{1}{2} - \sin^2\Theta_W) \tag{2.16}$$

where σ_{nc}^{ν} and $\sigma_{nc}^{\bar{\nu}}$ are the neutral current cross sections, and σ_{cc}^{ν} and $\sigma_{cc}^{\bar{\nu}}$ are the charged current cross sections for neutrinos and anti-neutrinos. The distinction between the processes was made based on event duration, as charged current interactions —since a muon is produced— take longer than neutral current interactions.

The result was propagated to the Z-pole assuming standard model scaling behaviour, giving a value of [14]

$$\sin^2\Theta_W(m_Z) = 0.2277 \pm 0.0013_{\text{stat}} \pm 0.0009_{\text{syst}} \tag{2.17}$$

which lies above the standard model prediction by three standard deviations. Attempts to explain this discrepancy include unaccounted for QCD modeling effects [13] as well as physics beyond the standard model [15].

2.2.3 Atomic Parity Violation

The lowest energy determination of $\sin^2\Theta_W$ was done at $\mu = 2.4\,\text{MeV}$ by measuring the weak charge of the ^{133}Cs nucleus. The caesium atom is particularly suitable, because its electronic structure is well known, which is required for a high precision determination of the weak mixing angle.

Figure 2.4 shows a simplified atomic energy level diagram of the states in caesium atoms that are relevant for the determination of the weak mixing angle. A transition between two atomic states with the same parity is forbidden by selection rules and suppressed by a factor of 10^{-22} with respect to allowed dipole transitions. However, the weak neutral current interaction mixes a small amount of P states into the $6S$ and $7S$ states. The transition amplitude A_{PNC}[1] between the $6S$ and $7S$ levels in caesium can therefore be used to quantify the weak interaction, but is too small to measure directly. Therefore the so-called *Stark interference* method was utilized. The application of an electric field E additionally mixes S and P states, and the resulting Stark-induced transition amplitude A_E is typically 10^5 times larger than A_{PNC}. The transition rates are then [16]

$$R = |A_E + A_{PNC}|^2 = (A_E)^2 \pm 2A_E A_{PNC} + (A_{PNC})^2 \tag{2.18}$$

where the second term can be accessed experimentally by changing parity. The excitation $6S \rightarrow 7S$ was performed with a dye laser tuned to $540\,\text{nm}$ and the

---

[1]PNC stands for Parity Non-Conservation
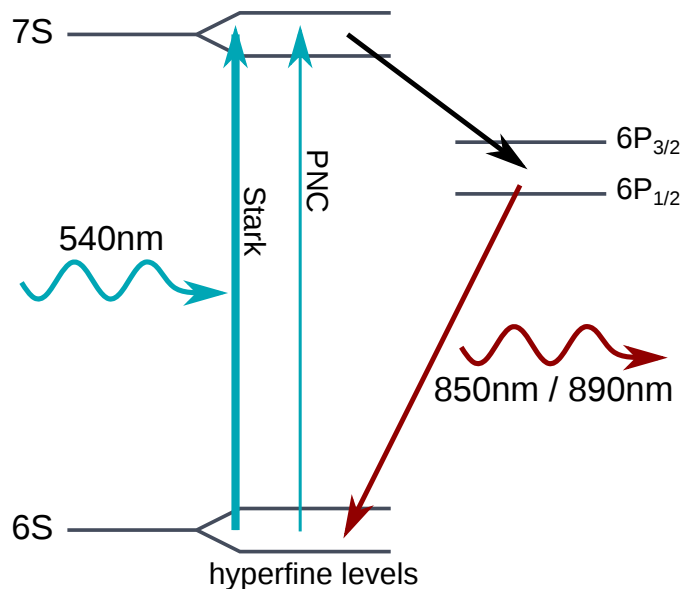
FIGURE 2.4: Electron transitions used in the measurement of the weak mixing angle using atomic parity violation in ^{133}Cs atoms.

transition rate for $6P \rightarrow 6S$ was determined by detecting $850\,\mathrm{nm}$ and $890\,\mathrm{nm}$ light.

This determination of the weak mixing angle is particularly sensitive to another beyond Standard Model extension predicting the existence of additional Z-bosons, because of the almost vanishing Q^2. Additionally it is a more suitable probe for a different set of model-independent lepton-quark coupling constants than high energy measurements. [17]

The result [10]

$$\sin^2 \Theta_W(m_Z) = 0.2283 \pm 0.002 \tag{2.19}$$

lies 1.5σ off the SM value.

2.2.4 Parity-Violating Electron Scattering (PVES) Experiments

The method that P2 in Mainz is going to use in order to measure the electroweak mixing angle is *Parity-Violating Electron Scattering* (PVES). The general principle and theory behind PVES will be covered in chapter 2.3. This section gives an overview of some complementary past and planned experiments using this technique to determine the weak mixing angle. In these experiments, the weak charges of various target materials like protons (liquid hydrogen), electrons (shell electrons, e.g. in a hydrogen target), or nuclei (e.g. carbon in a graphite target) are determined by scattering electrons off them.
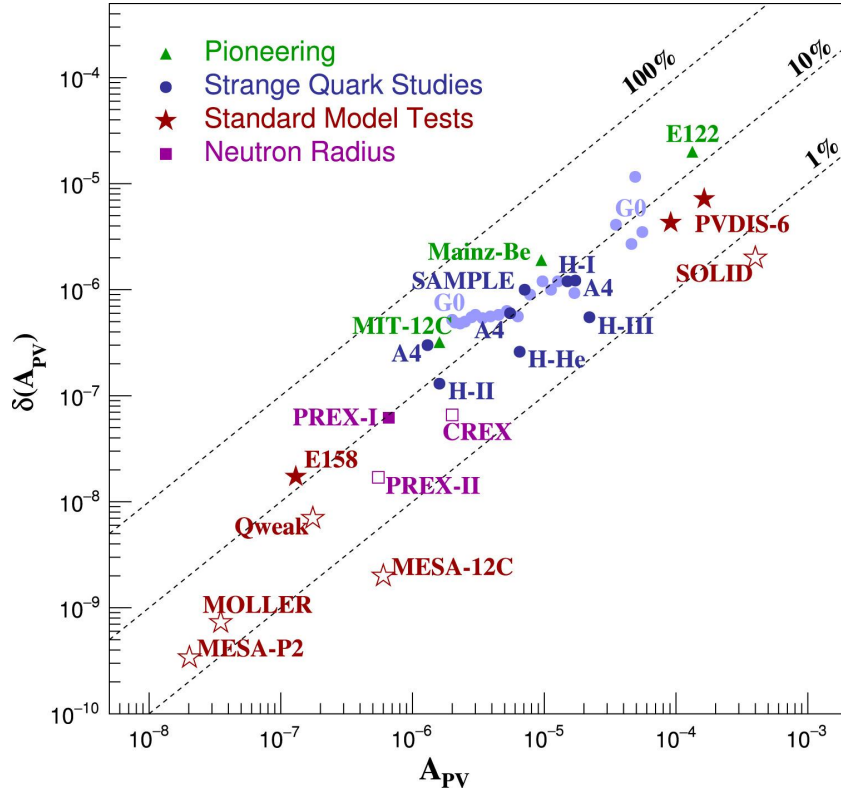
FIGURE 2.5: Overview of past (solid symbols) and future (outlined symbols) PVES experiments. The picture is taken from [18]. The vertical lines indicate the relative error $\delta(A_{PV})/A_{PV}$ in the asymmetry. P2 and MESA-12C at MESA in Mainz are going to be two of the most precise measurements making them extremely challenging.

Figure 2.5 is an overview of past and future PVES experiments and shows the parity-violating asymmetry A_{PV} on the horizontal axis and the error δA_{PV} of past (solid symbols) and future (outlined symbols) PVES experiments on the y-axis. The diagonal lines indicate three fixed relative error values $\delta(A_{PV})/A_{PV}$. More elaborate recent and future experiments like SOLID, MOLLER and P2 are located further to the bottom or right. They are challenging and require state of the art technical expertise and equipment. Having hosted the A4 experiment at the Mainzer Mikrotron MAMI the Institut für Kernphysik of the Johannes Gutenberg-University in Mainz is well experienced in the field of PVES.

At tree level both the weak charge of the proton and the electron have a value of approximately

$$Q_W^P = -Q_W^e = 1 - 4\sin^2\Theta_W = 0.075 \tag{2.20}$$

Standard model electroweak radiative corrections considering one-loop processes lead to the expected values

$Q_W^P = 0.0716$ $Q_W^e = -0.0499$

├─○─┤ ±0.0029   Experiment   ├─○─┤ ±0.0051

SUSY

E_6 Z'

RPV SUSY

Leptoquarks
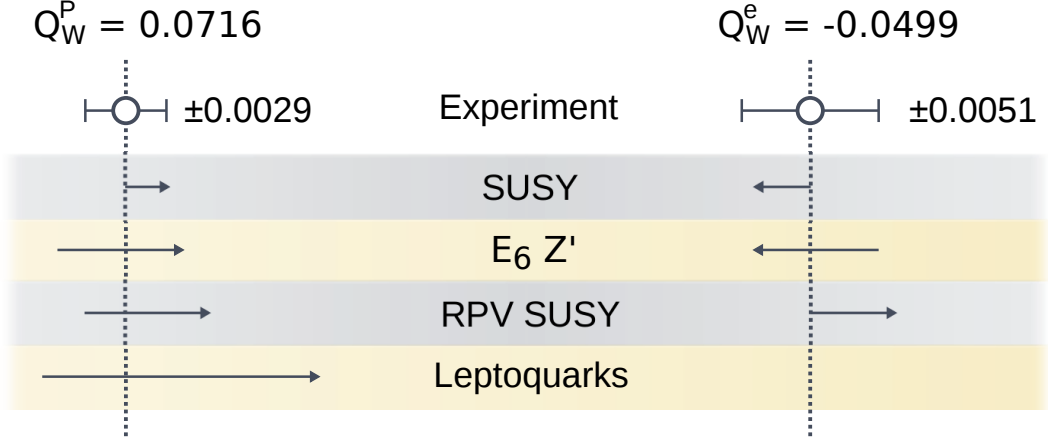
FIGURE 2.6: Deviations of the weak charges of the proton (Q_W^P) and the electron (Q_W^e) from the standard model expectation value caused by hypothetical new physics scenarios. The dashed line is the standard model expectation. The error bars show the anticipated experimental uncertainty [19]. The arrows indicate how a certain beyond standard model physics hypothesis would affect the weak charges.

$$Q_W^P = 0.071 \qquad \text{and}$$
$$Q_W^e = -0.045 \tag{2.21}$$

shown in figure 2.6. The error bars represent the presently achievable experimental precision. Some examples of standard model extensions are the existence of Z'-bosons that emerge from a new $U(1)'$-symmetry, which is proposed in *Grand Unified Theory* (GUT) models, supersymmetry (SUSY), and leptoquark theories. The graphic shows that these new physics scenarios —if true— would shift the weak charges of electron and proton by different degrees. While both measurements have a similar sensitivity to R-parity-violating SUSY loops, they are anti-correlated concerning SUSY and Z'-bosons. The weak charge of the electron is not shifted by the existence of leptoquarks at all, but the weak charge of the proton is sensitive to it. In conclusion the measurements of both weak charges are highly complementary.

The weak charge of a nucleus in general is —again at tree level— related to the numbers of protons Z and neutrons N it contains by

$$Q_W(Z, N) = Z(1 - 4\sin^2\Theta_W) - N \tag{2.22}$$

2.2.4.1   The Weak Charge of the Electron

The SLAC E158 experiment and the future MOLLER experiment both access the
weak mixing angle via the weak charge of the electron by measuring the parity
violation in electron-electron (Møller) scattering. One advantage of using this
purely leptonic process are the small hadronic corrections one has to account for.
It is therefore possible to determine $\sin^2 \Theta_W$ with a very high precision.

The squared momentum transfer of $Q^2 = 0.026 \, \text{GeV}/c^2$ [20] in the SLAC E158
experiment was chosen right below the value where screening effects in figure 2.2
start playing a role. 45 GeV electrons from a longitudinally polarised beam were
directed onto a fixed liquid hydrogen target. The beam helicity was reversed
with a frequency of 120 Hz, and electrons scattered into angles between 4.4 mrad
and 7.5 mrad and energies between 13 GeV and 24 GeV served as signal. With a
measured asymmetry of only $A_{PV} = (-131 \pm 14_{\text{stat}} \pm 10_{\text{sys}})$ppb [10] care had to
be taken to eliminate possible false asymmetries like helicity correlated changes
in the beam properties. The last measurement run was taken in 2003, and the
extracted value for the weak charge of the electron from SLAC E158 data is

$$Q_W^e = -0.0369 \pm 0.0052 \tag{2.23}$$

in the static limit (E and $Q^2 \rightarrow 0$) and the corresponding value for the weak
mixing angle is

$$\sin^2 \Theta_W(m_Z) = 0.2329 \pm 0.0013 \tag{2.24}$$

This is so far the most precise determination of the weak mixing angle at low Q^2
and was the first experiment to deliver proof of its scale dependence.

The MOLLER collaboration is planning a measurement of the weak charge of the
electron with a relative uncertainty $\Delta Q_W^e / Q_W^e = 2.4\%$ which reduces the relative
uncertainty by a factor of five compared to SLAC E158.

2.2.4.2   The Weak Charge of the ^{12}C-Nucleus

Aside from measuring the weak charge of the proton the P2 collaboration is plan-
ning a measurement of the weak charge of the carbon-12 nucleus. According to
equation 2.22 the weak charge of the ^{12}C-nucleus is $Q_W^{^{12}\text{C}} = -24 \sin^2 \Theta_W$ when
radiative corrections are neglected. Aside from being complementary to electron-
electron and electron-proton scattering experiments a measurement of $\sin^2 \Theta_W$ via
$Q_W^{^{12}\text{C}}$ has several advantages.

- A major contribution to the uncertainty of the weak charge of the proton
  as measured in the P2 experiment will be the statistical error. Achieving

the desired precision will require $10\,000\,\mathrm{h}$ of data taking. As scattering cross sections are quadratic in the atomic number Z, heavier nuclei as target material allow to reach the same statistics in much shorter time.

- The absence of spin and isospin allows a much simpler analysis of the measurement data. The electric form factor dependence in particular cancels out completely and the weak mixing angle will depend purely on the measurable asymmetry A_{PV}, the momentum transfer Q^2 and well-known constants.

- The first order (tree-level) term of the interaction of electrons with the ^{12}C-nucleus is very large, so that corrections are relatively small.

- The installation and maintenance of a ^{12}C target e.g. in the form of several layers of graphite is much simpler in comparison with a liquid hydrogen target.

The results of a measurement of the parity-violating asymmetry in elastic scattering of polarised electrons from ^{12}C at the MIT-Bates Linear Accelerator Center was published in 1990 [21]. They determined a value of the parity-violating coupling constant at $\mu = 150\,\mathrm{MeV}$ of $\tilde{\gamma} = 0.136 \pm 0.032 \pm 0.009$. The weak coupling constant is related to the weak mixing angle by $\tilde{\gamma} = \frac{2}{3}\sin^2\Theta_W$, which leads to the result

$$\sin^2\Theta_W = 0.204 \pm 0.048 \pm 0.014 \tag{2.25}$$

In [21] the authors state that this is consistent with the SM, and that in future experiments a higher precision can be reached by increasing the data rate. First investigations into the feasibility of a ^{12}C measurement at the future P2 facility have been performed and published in [22].

2.2.4.3 The Weak Charge of the Proton

The P2 experiment is going to access the weak mixing angle via a measurement of the weak charge of the proton Q_W^P at a low momentum transfer.

A similar measurement of Q_W^P has previously been done by the Qweak collaboration at the Thomas Jefferson National Accelerator Facility in Newport News, Virginia, USA. Data taking was finished in 2012 and results have been published in 2018 [8] and in 2020 [23]. A highly simplified schematic of the experimental design is depicted in figure 2.7.

Longitudinally polarised electrons were directed onto a $35\,\mathrm{cm}$ long liquid hydrogen target and the elastically scattered electrons originating from processes with the
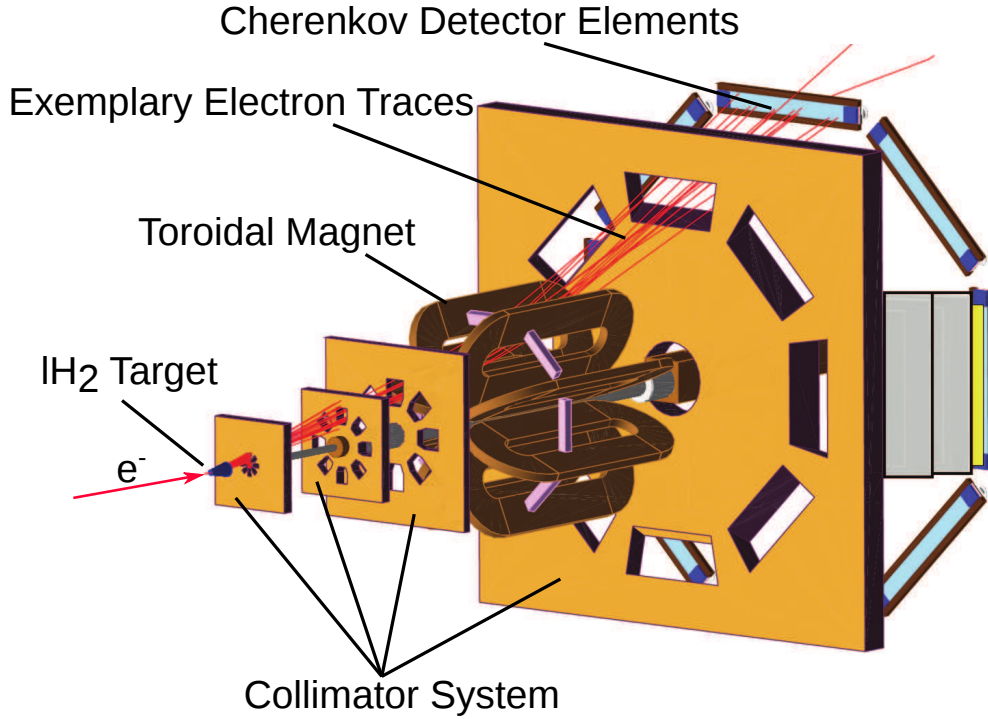
FIGURE 2.7: Schematic of the Qweak experiment showing the liquid hydrogen target, the 8 coils of the toroid spectrometer, the collimator system, and the 8 fused silica Cherenkov detector elements. Picture taken from [24].

desired momentum transfer Q^2 were detected in 8 quartz Cherenkov detectors. The average Q^2 in the experiment was $0.0248\,\mathrm{GeV/c^2}$. Background like inelastically scattered electrons or electrons outside of the desired Q^2-region were deflected away from the detectors in the field of a toroidal magnet or absorbed by an array of collimators.

The helicity of the electron beam of the *Continuous Electron Beam Accelerator Facility* (CEBAF) with beam energy $E = 1.165\,\mathrm{GeV}$ was changed with a frequency of $960\,\mathrm{Hz}$. The measured quantity was the parity-violating asymmetry, which was determined from the signals in the Cherenkov detectors during the different helicity windows as described in section 2.3.

The measured asymmetry in the Qweak experiment was

$$A_{ep} = (-226.5 \pm 7.3_{\mathrm{stat}} \pm 5.8_{\mathrm{syst}})\mathrm{ppb} \qquad (2.26)$$

The total uncertainty achieved was $9.3\,\mathrm{ppb}$. The value for the weak charge of the proton derived from this asymmetry is [8]

$$Q_W^P = 0.0719 \pm 0.0045 \qquad (2.27)$$

which is in very good agreement with the standard model prediction.

Qweak was the first high precision measurement of the weak charge of the proton and can be seen as a trailblazer experiment for P2.

2.3 Parity-Violating Asymmetry in Electron-Proton Scattering

The previous paragraphs put the planned P2 experiment in historic context by giving an overview of experiments which are considered complementary, pioneering, or similar in their approach. Section 2.2.4 listed experiments which —like P2— measure the weak charge of particles using PVES. The principles of this method will be explained in the following section.

2.3.1 Elastic Electron-Nucleon Scattering

In parity-violating electron scattering the cross section and asymmetry depend on the momentum transfer, usually given as the negative square of the intermediary particle's four-momentum $q = (\omega, \vec{q})$:

$$Q^2 = -q^2 = 4EE' \sin^2(\Theta_L/2) \tag{2.28}$$

E is the electron's initial energy, E' its final energy, and Θ_L is the laboratory scattering angle. At the energies considered here, the rest mass m_e can be neglected.

Energy and momentum conservation for elastic e-p scattering require that

$$Q^2 = 2m_p(E - E') \tag{2.29}$$

The relation of the laboratory scattering angle and the negative four-momentum transfer is graphically shown in figure 2.8.

The electromagnetic differential cross section of the electron-proton scattering process is given by the Rosenbluth formula in terms of electric and magnetic Sachs form factors $G_e^{N\gamma}$ and $G_m^{N\gamma}$ of the nucleon:

$$\frac{d\sigma_{ep}}{d\Omega_L} = \left(\frac{d\sigma_{Mott}}{d\Omega_L}\right) \cdot \left[\frac{\left(G_e^{N\gamma}\right)^2 + \tau \left(G_m^{N\gamma}\right)^2}{1 + \tau} + 2\tau \left(G_m^{N\gamma} \tan\left(\frac{\Theta_L}{2}\right)\right)^2\right] \tag{2.30}$$

where
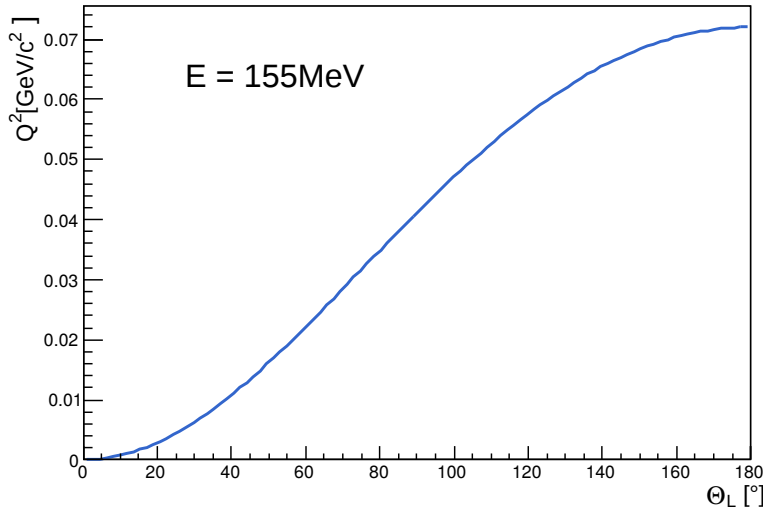
FIGURE 2.8: Negative four-momentum transfer Q^2 as a function of the scattering angle Θ_L for the initial electron energy $E = 155\,\text{MeV}$

$$\left(\frac{d\sigma_{Mott}}{d\Omega_L}\right) = \frac{(2\alpha_{em}\hbar c)^2 \cdot [1 - \beta^2 \sin^2(\Theta_L/2)] \cdot (E')^3}{(\vec{q})^4 \cdot E \cdot c^4} \tag{2.31}$$

is the Mott cross section for spinless targets.

The scattering kinematics was treated in great detail in Dominik Becker's PhD thesis [25] with regard to optimizing the P2 Experiment's specifications in order to achieve the best possible precision for a measurement of the weak charge of the proton.

2.3.2 Parity-Violating Electron-Proton Scattering

Parity transformation is the reflection at the point of origin. For a three-dimensional space one has:

$$P : \begin{pmatrix} x \\ y \\ z \end{pmatrix} \mapsto \begin{pmatrix} -x \\ -y \\ -z \end{pmatrix} \tag{2.32}$$

Vectors such as the position of a particle in space or its momentum change sign under parity transformation. Scalars and axial vectors such as the angular momentum $\vec{L} = \vec{r} \times \vec{p}$ in the following example remain invariant:

$$P(\vec{L}) = (-\vec{r}) \times (-\vec{p}) = \vec{L} \tag{2.33}$$

(a) Electromagnetic interaction via the exchange of a virtual photon, which couples to the electric charge of the interacting particles

(b) Weak interaction via the exchange of a Z-boson, which couples to the weak charges of the interacting particles
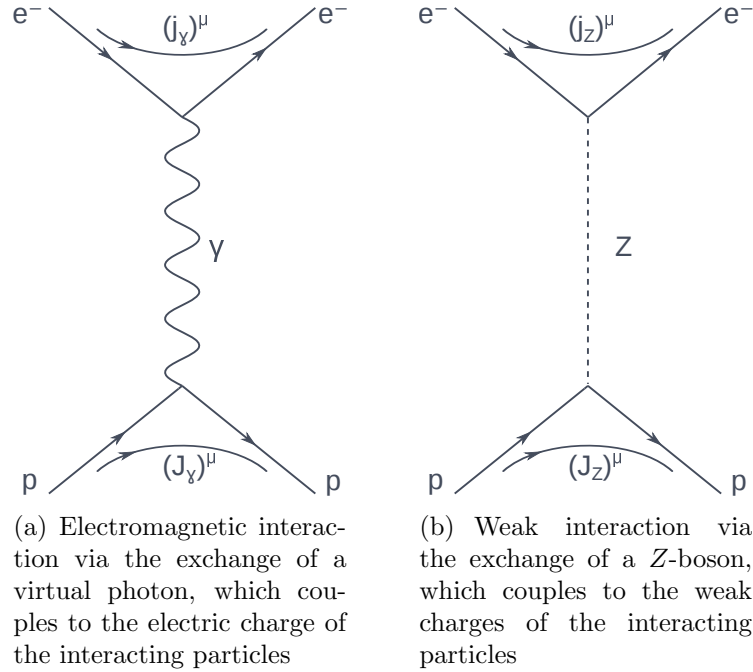
FIGURE 2.9: Leading order Feynman diagrams of e-p-scattering

All physics phenomena in our macroscopic world are parity conserving, meaning that they can take place the exact same way in a parity transformed system. Of the four fundamental interactions we only observe gravity and electromagnetism in our every day life, and both are symmetric under parity transformation, as is the strong nuclear interaction. Solely the weak interaction is parity-violating.

The P2 Experiment is going to scatter longitudinally polarised electrons from an unpolarised proton target and aims to quantify the weak interaction in this process. At leading order proton and electron interact electromagnetically via the exchange of a virtual photon and weakly via the exchange of a Z-boson. The respective Feynman diagrams are shown in figure 2.9.

Because of the large mass of the exchange particle the weak interaction contribution to the electron-proton scattering cross section at small momentum transfer ($Q^2 \approx 0.2\,\mathrm{GeV}^2/\mathrm{c}^2$) is suppressed to a degree that makes it impossible to determine it directly. The experimental approach exploits the fact that QED is parity conserving and that the weak contribution can be accessed by measuring the parity-violating asymmetry:

$$A_{PV} := \frac{\sigma_L - \sigma_R}{\sigma_L + \sigma_R} \tag{2.34}$$

where $\sigma_{L/R}$ denotes the cross section for left- and right-handed electrons.

The matrix elements $\mathcal{M}_\gamma$ and $\mathcal{M}_Z$ are associated with the respective Feynman diagrams in figure 2.9, and the cross sections of the elastic electron-proton scattering can be calculated according to the Feynman rules from the squared sum of these transition matrix elements:

$$\begin{aligned}
\sigma_R &= C|\mathcal{M}_\gamma + \mathcal{M}_{Z,R}|^2 = C\left(|\mathcal{M}_\gamma|^2 + 2\operatorname{Re}(\mathcal{M}_\gamma \mathcal{M}_{Z,R}^*) + |\mathcal{M}_{Z,R}|^2\right) \\
\sigma_L &= C|\mathcal{M}_\gamma + \mathcal{M}_{Z,L}|^2 = C\left(|\mathcal{M}_\gamma|^2 + 2\operatorname{Re}(\mathcal{M}_\gamma \mathcal{M}_{Z,L}^*) + |\mathcal{M}_{Z,L}|^2\right)
\end{aligned} \tag{2.35}$$

if radiative corrections are neglected.

Inserting these relations in 2.34 the factor C, which contains phase space and state densities equal for both helicities, cancels out, resulting in

$$A_{PV} = \frac{2\operatorname{Re}(\mathcal{M}_\gamma \mathcal{M}_{Z,R}^*) + |\mathcal{M}_{Z,R}|^2 - 2\operatorname{Re}(\mathcal{M}_\gamma \mathcal{M}_{Z,L}^*) - |\mathcal{M}_{Z,L}|^2}{2|\mathcal{M}_\gamma|^2 + 2\operatorname{Re}(\mathcal{M}_\gamma \mathcal{M}_{Z,R}^*) + |\mathcal{M}_{Z,R}|^2 + 2\operatorname{Re}(\mathcal{M}_\gamma \mathcal{M}_{Z,L}^*) + |\mathcal{M}_{Z,L}|^2} \tag{2.36}$$

The transition amplitudes can be expressed in terms of the transition currents j^μ of the electron and J^μ of the proton:

$$\begin{aligned}
\mathcal{M}_\gamma &= (j_\gamma)_\mu \frac{1}{Q^2}(J_\gamma)^\mu \\
\mathcal{M}_Z &= (j_Z)_\mu \frac{1}{Q^2 + m_Z^2}(J_Z)^\mu
\end{aligned} \tag{2.37}$$

The electromagnetic and weak neutral currents of the structureless electron are composed of the initial and final spinor states u_i and u_f and the coupling expressed in terms of the Dirac matrices:

$$\begin{aligned}
(j_\gamma)_\mu &= -\bar{u}_f \gamma_\mu u_i \\
(j_Z)_\mu &= -\bar{u}_f (g^V \gamma^\mu + g^A \gamma^\mu \gamma^5) u_i
\end{aligned} \tag{2.38}$$

while the respective currents for the proton include the Dirac and Pauli form factors $F_1(Q^2)$ and $F_2(Q^2)$ as well as the axial form factor $G_A^Z(Q^2)$ to account for its inner structure consisting of quarks, gluons, and a sea of quark-antiquark pairs:

$$(J_\gamma)_\mu = \bar{U}_f \left(\gamma^\mu F_1^\gamma(Q^2) + i \frac{\sigma^{\mu\nu} q_\nu}{2M} F_2^\gamma(Q^2) \right) U_i$$
$$(J_Z)_\mu = \bar{U}_f \left(\gamma^\mu F_1^Z(Q^2) + i \frac{\sigma^{\mu\nu} q_\nu}{2M} F_2^Z(Q^2) + \gamma^\mu \gamma^5 G_A^Z(Q^2) \right) U_i$$

(2.39)

The parity-violating asymmetry as expressed in equation 2.36 is vastly dominated[2] by $|\mathcal{M}_\gamma|$ and is often approximated by

$$A_{PV} \approx \frac{\mathrm{Re}(\mathcal{M}_\gamma [\mathcal{M}_{Z,R} - \mathcal{M}_{Z,L}]^*)}{|\mathcal{M}_\gamma|^2}$$

(2.40)

The parity-violating part of the Lagrangian, which describes contact interactions, has the form [6]

$$\mathcal{L} = -\frac{G_F}{\sqrt{2}} \sum_{f=u,d,s} \left(C_{1q_f} \bar{e}\gamma^\mu \gamma_5 e \bar{q}_f \gamma_\mu q_f + C_{2q_f} \bar{e}\gamma^\mu e \bar{q}_f \gamma_\mu \gamma_5 q_f \right)$$

(2.41)

The fields $\bar{e}$ and e are the annihilation and creation operators of the electron, and $\bar{q}$ and q those of the quarks. The sum is over the quark flavours "up", "down", and "strange". Heavier quarks are neglected. γ^5 is the product of the four Dirac matrices γ^μ. The terms, which contain γ_5 change sign under parity transformation. Hence, the sum contains the products $\mathcal{V}(e) \cdot \mathcal{A}(q)$ and $\mathcal{V}(q) \cdot \mathcal{A}(e)$ of the axial and vector contributions to the scattering process. The weak couplings for these quarks are given by

$$\begin{aligned} C_{1q} &\equiv -g_e^A g_q^V \\ C_{2q} &\equiv \ \ g_e^V g_q^A = (1 - 4\sin^2 \Theta_W) g_q^A \end{aligned}$$

(2.42)

and their values are listed in table 2.1.

---

[2]For $Q^2 \ll m_Z^2 c^2$ the mixed term $\mathrm{Re}(\mathcal{M}_\gamma \mathcal{M}_Z^*)$ is smaller by six orders of magnitude and $|\mathcal{M}_Z|^2$ is another six orders of magnitude smaller.

q	C_{1q}	C_{2q}
u	$-\frac{1}{2} + \frac{4}{3}\sin^2\Theta_W$	$-\frac{1}{2} + 2\sin^2\Theta_W$
d	$\frac{1}{2} - \frac{2}{3}\sin^2\Theta_W$	$\frac{1}{2} - 2\sin^2\Theta_W$
s	$\frac{1}{2} - \frac{2}{3}\sin^2\Theta_W$	$\frac{1}{2} - 2\sin^2\Theta_W$

TABLE 2.1: Effective couplings at tree level.

The asymmetry can be expressed as a term proportional to the weak charge of the proton and a term F^P containing form factor information due to the hadronic structure of the proton [26]:

$$A_{PV} = \frac{-G_F Q^2}{4\pi\alpha\sqrt{2}} \left[Q_W^P - F^P(Q^2) \right] \tag{2.43}$$

F^P can be decomposed into three form factor contributions:

$$F^P(Q^2) = F^{em}(Q^2) + F^a(Q^2) + F^s(Q^2) \tag{2.44}$$

where

$$F^{em}(Q^2) = \frac{\epsilon G_e^{p\gamma} G_e^{n\gamma} + \tau G_m^{p\gamma} G_m^{n\gamma}}{\epsilon (G_e^{p\gamma})^2 + \tau (G_m^{p\gamma})^2} \tag{2.45}$$

contains the proton's and neutron's electromagnetic form factor,

$$F^a(Q^2) = \frac{(1 - 4\sin^2\Theta_W)\sqrt{1-\epsilon^2}\sqrt{\tau(1-\tau)}G_m^{p\gamma} G_a^{pZ}}{\epsilon (G_e^{p\gamma})^2 + \tau (G_m^{p\gamma})^2} \tag{2.46}$$

is proportional to the axial form factor of the proton, and

$$F^s(Q^2) = \frac{\epsilon G_e^{p\gamma} G_e^s + \tau G_m^{p\gamma} + \epsilon G_e^{p\gamma} G_e^{ud} + \tau G_m^{p\gamma} G_m^{ud}}{\epsilon (G_e^{p\gamma})^2 + \tau (G_m^{p\gamma})^2} \tag{2.47}$$

is given by the strangeness vector form factors.

The term

$$\epsilon = \frac{1}{1 + 2(1 + \tau)\tan^2 \frac{\theta_L}{2}} \tag{2.48}$$

contains the laboratory scattering angle θ_L and the kinematically relevant quantity $\tau = Q^2/4m_p^2$ with the proton mass m_p.
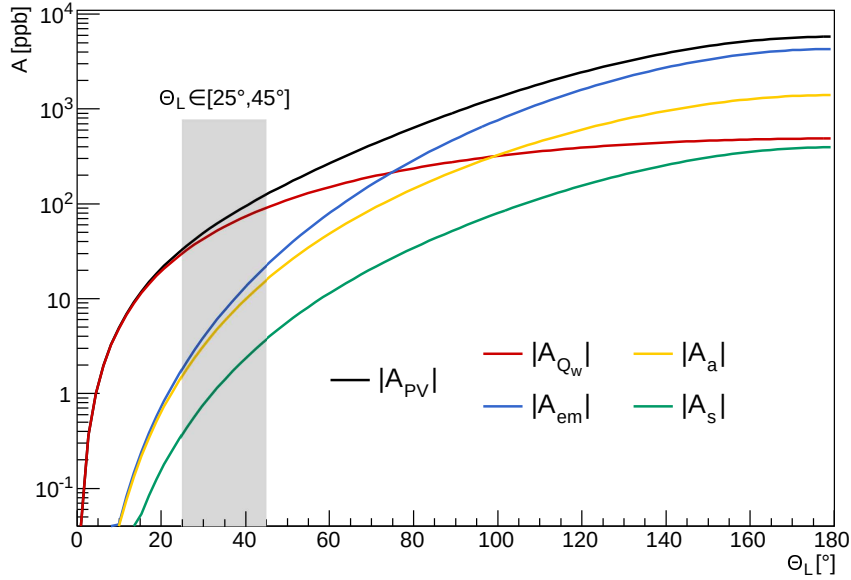
FIGURE 2.10: Form factor contributions to the total asymmetry. At small scattering angles the hadronic structure may be neglected and the asymmetry is dominated by the term proportional to the weak charge of the proton. The form factor parametrisation, which was used to generate this plot, is taken from [27].

Figure 2.10 shows the absolute contributions of Q_W^P, $F^{em}(Q^2)$, $F^a(Q^2)$, and $F^s(Q^2)$ to the total asymmetry A_{PV} as a function of the scattering angle Θ_L. At low Q^2 for a scattering angle range $\Theta_L \in [25°, 45°]$ the nucleon's form factors are small and the asymmetry A_{PV} is dominated by the term proportional to the weak charge of the proton, which is [28]

$$Q_W^P = 1 - 4\sin^2\Theta_W \tag{2.49}$$

at tree level, where higher order corrections are neglected. The weak mixing angle can thus be accessed by examining the scattering cross sections or the rates of particles scattered into a specific laboratory angle range in PVES from protons.

However, in order to precisely determine the weak charge of the proton during the P2 experiment the consideration of electroweak corrections is required. Aside from the ones already incorporated in figure 2.2 two boson exchange effects have been subject to extensive theoretical studies. Corrections which result from higher order effects represented by loops in Feynman diagrams as well as missing higher order QCD corrections and the resulting theoretical uncertainties are addressed in [19]. The effect of γZ-exchange in particular is addressed in [29].

The next chapter will go into detail regarding the realisation of parity-violating electron-proton scattering within the course of the P2 experiment.

Chapter 3

The P2 Experiment at MESA

Particle physics experiments often have to be integrated into already existing facilities which means that they have to adapt to the infrastructure offered. In contrast the P2 Experiment and the Mainz Energy-recovering Superconducting Accelerator (MESA) have been envisioned and planned as two aspects of the same project. They are funded within the Cluster of Excellence in Mainz called PRISMA ("Precision Physics, Fundamental Interactions and Structure of Matter") and the Collaborative Research Center 1044 (SFB 1044). Parity experiments work closely with their accelerators, as they have high demands, e.g. on beam specifications, polarimetry, and synchronised helicity flips. P2 additionally requires challenging beam stability and exceptionally high beam currents/luminosity at relatively low energies. These demands can be considered already in the planning phase of the accelerator and the experiments.

The subject of this chapter is the description of the experiment and its components. The first section is dedicated to explaining the experimental approach and to introducing the aims of the measurement, which put constraints and demands on the experiment's hardware components. In the following sections an overview of the P2 experimental setup is given before going into the details of each component, focusing on those unique demands of P2 and how they can be met.

3.1 Experimental Access to the Weak Mixing Angle

P2 is a parity-violating electron scattering experiment. As such it aims to compare the outcome of a scattering experiment to that of the parity transformed experiment. During the P2 data-taking longitudinally polarised electrons are going to be scattered from a proton target. Parity transformation changes the sign of all
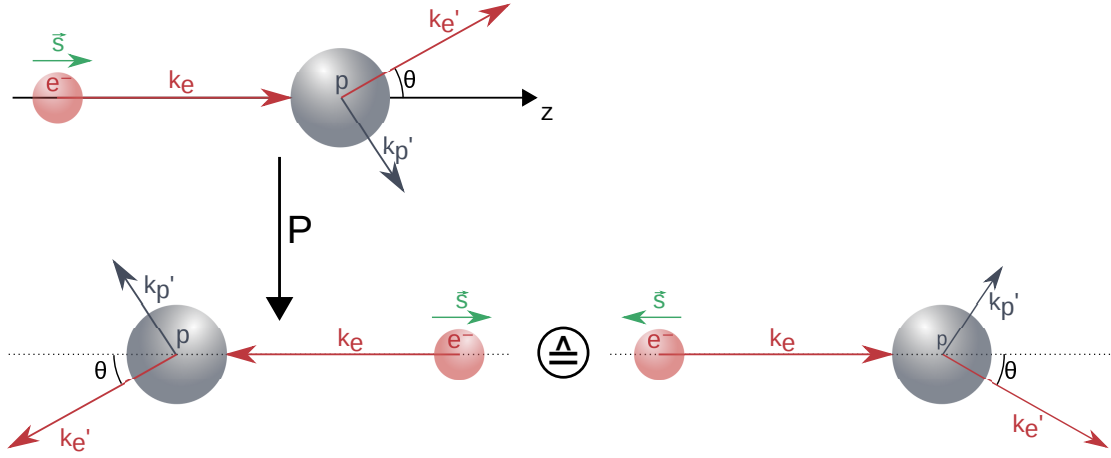
FIGURE 3.1: Electron-proton scattering process before and after parity transformation. The electron initially has a 4 momentum of k_e and after the scattering process a 4-momentum of k'_e. The reference frame in this schematic is one, in which the proton initially rests and the electron moves along the z-axis. The process is then symmetric with respect to both the x- and y-axis. The proton's 4-momentum after the scattering is k'_p. The electron's spin is parallel to its momentum before the parity transformation (upper picture) and antiparallel after the transformation (lower pictures)

location and momentum vectors involved. Due to cylindrical symmetry of the P2 apparatus this transformation is equivalent to a rotation of the whole experiment including the accelerator by 180° about the vertical axis. Being an axial vector, the electron's spin remains unaltered as depicted on the left-hand side of figure 3.1. Therefore, if we assume isotropy of space, we can rotate the parity-transformed experiment by 180° and see that the only difference to the original setup lies in the spin orientation of the electrons, which is inverted. Parity transformation in the P2 Experiment can thus be achieved via inversion of the electron beam's polarisation. The scattering rates of this process for electron helicities +1 and -1 are going to be compared and the parity-violating asymmetry determined according to equation 2.34.

The measurement principle is depicted in figure 3.2. After being scattered in a long liquid hydrogen target the electrons traverse the field of a solenoid magnet and a system of collimators. Both serve to filter signal electrons scattered into a certain laboratory scattering angle $\Theta_L \in [\Theta_L^{min}, \Theta_L^{max}]$ from undesired background. The beam helicity is reversed frequently. The helicity change leads to a change in the raw signal $S_{raw}^{\pm}$ in the detector, which is due to the parity-violating nature of the weak interaction and helicity correlated changes in the beam parameters. The resulting measured asymmetry

$$A_{raw} = \frac{S_{raw}^L - S_{raw}^R}{S_{raw}^L + S_{raw}^R} = P \cdot A_{PV} + A_{false} \qquad (3.1)$$
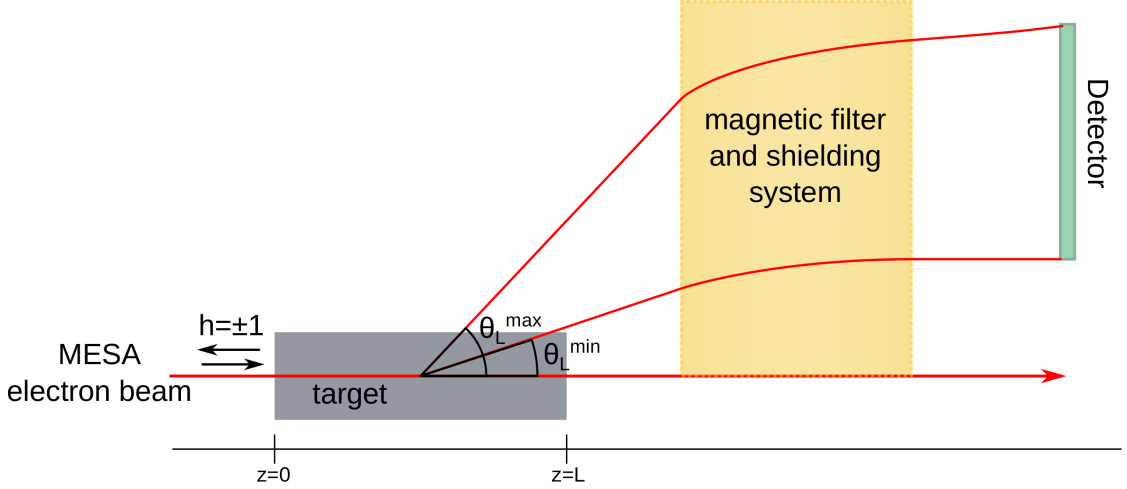
FIGURE 3.2: Simplified depiction of the P2 approach to measuring the parity-violating electron scattering from a liquid hydrogen target. The beam helicity is flipped periodically and the electrons, which have been elastically scattered from the target into angles corresponding to the desired Q^2 range, are detected.

is thus a sum of the parity-violating asymmetry A_{PV} in the electron-proton scattering weighted with the degree of beam polarisation and the so-called false asymmetries A_{false}. In equation 2.34 left- and right-handed cross sections were used in the definition of the parity-violating asymmetry. The translation of detector signals into cross sections requires the precise knowledge of the luminosity

$$\mathcal{L} = \Phi \cdot \rho \cdot L \tag{3.2}$$

from accurate measurements of the beam electron flux Φ, the target density ρ and the target length L. In an ideal setting these factors cancel out when calculating the asymmetry according to equation 3.1, which is one of the incentives to perform asymmetry measurements. It must be noted however that in reality at least the electron flux and target density can exhibit helicity correlated changes, which beaks this assumption. If these effects are small, we can absorb them into the term A_{false} and treat them as a disturbance.

The thesis [25] describes the process and results of optimising the experiment's kinematics and minimising uncertainties of the form factors involved in the scattering process with regard to achieving the maximum precision in $\sin^2 \Theta_W$. Figure 3.3 shows the uncertainty $\Delta \sin^2 \Theta_W$ of the measurement of the weak mixing angle in the P2 Experiment with respect to the mean scattering angle $\bar{\Theta}_L$ of the detected signal electrons measured for an angular acceptance of the detector of $\delta \Theta_L = 20°$ and an electron beam energy $E = 155\,\mathrm{MeV}$. The coloured curves in the plot are the contributions to the total uncertainty (black curve) resulting from false asymmetries, the statistical uncertainty, error bars of the form factors, and the
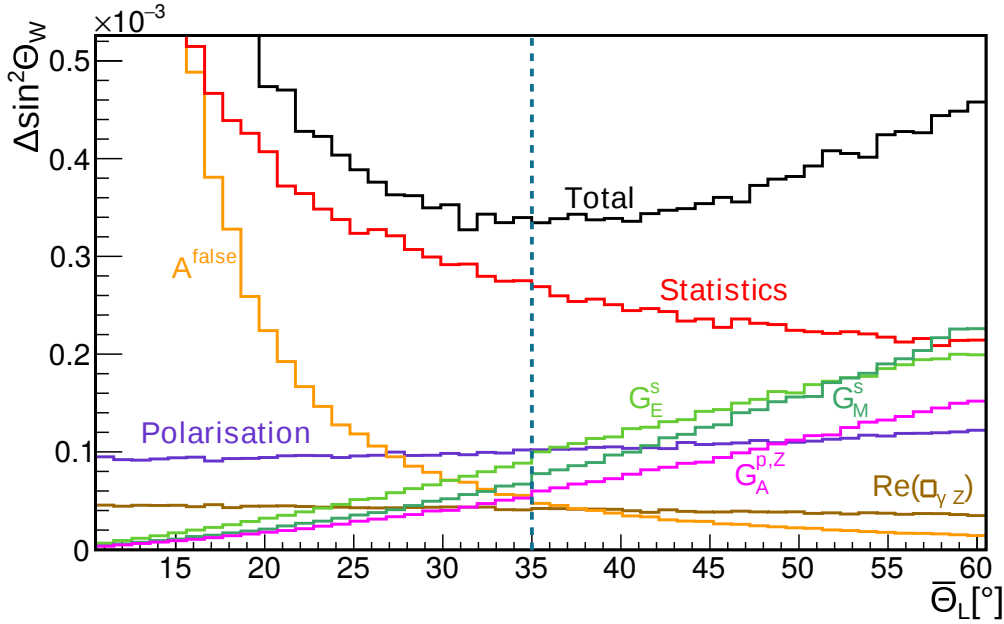
FIGURE 3.3: Uncertainty $\Delta \sin^2 \Theta_W$ of the measurement of the weak mixing angle in the P2 Experiment with respect to the mean scattering angle $\bar{\Theta}_L$ of the detected signal electrons. The dashed line marks the mean scattering angle at which P2 will measure [25]. The form factor contributions used herein require a form factor measurement within the scope of the P2 Experiment.

uncertainty of the contributions of a higher order physics process, in which both a photon and a Z-boson are exchanged.

P2 will use a mean laboratory scattering angle of 35°. The total uncertainty is

$$\Delta \sin^2 \Theta_W = 3.3 \times 10^{-4} \tag{3.3}$$

which corresponds to a relative uncertainty of

$$\frac{\Delta \sin^2 \Theta_W}{\sin^2 \Theta_W} = 0.14\% \tag{3.4}$$

So the aim is to detect electrons that are scattered into an azimuth range $\theta_L \in [\theta_L^{min}, \theta_L^{max}] = [25°, 45°]$. The expected parity-violating asymmetry at these scattering angles is 30 ppb to 40 ppb and thereby smaller than any asymmetry measured in PVES experiments to date. In order to keep the error in A_{PV} small the false asymmetries in equation 3.1 have to be eliminated as much as possible and the inevitable remainder has to be measured precisely. Aside from these systematic uncertainties, the statistical uncertainties have to be minimised as well. Assuming Poisson distribution the statistical uncertainty ΔA_{raw} of a measurement of A_{raw}

$$\Delta A_{\mathrm{raw}} = \frac{1}{\sqrt{N}} \tag{3.5}$$

is equal to the inverse square root of the total number of signal events registered. In order to achieve the collaboration's declared goal for a high precision determination of the weak mixing angle, the statistical uncertainty may not exceed $\mathcal{O}(10^{-9})$. According to equation 3.5 this implies that $N \approx 10^{18}$ exploitable events are needed for the analysis of the measurement. This is tantamount to the necessity of high scattering rates over a long data-taking period, which puts challenging demands on all hardware components.

3.2 The MESA Accelerator

The measurement of the weak charge of the proton requires precise control of the electron beam properties and is more demanding on the accelerator than other experiments run in Mainz. The *Mainz Energy recovering Superconducting Accelerator* (MESA) is customised to meet these requirements. Furthermore the P2 data acquisition has to be synchronised with the electron beam's helicity flip. MESA is therefore considered an integral part of the experiment. It will deliver a polarised electron beam of 155 MeV with alternating helicity to the experiment.

3.2.1 Overview

Figure 3.4 shows the ground floor of the new MESA hall along with the accelerator's components and the locations of the proposed experiments, P2, MAGIX, and the *Beam Dump Experiment* (BDX). The acronyms in this drawing are listed along with short explanations in table 3.1. MESA is designed to run as a superconducting recirculating continuous wave accelerator.

MESA is going to be operated in two modes. The internal beam mode serves experiments which are installed directly in the circulations of the microtron. The MAGIX experiment's pseudo-internal gas target with its relatively small density will leave the beam almost unaltered. The beam energy can therefore be recovered in the accelerator's cavities. For external beam mode experiments like P2 on the other hand the beam is extracted and after passing the experiment, the electrons are stopped in a heavily shielded beam dump. The specifications of the external beam mode are tuned for the P2 Experiment. These parameters are listed in table 3.2 along with the values for the internal beam mode. The two beam currents for the internal beam mode refer to operation with two different photocathode types [30].
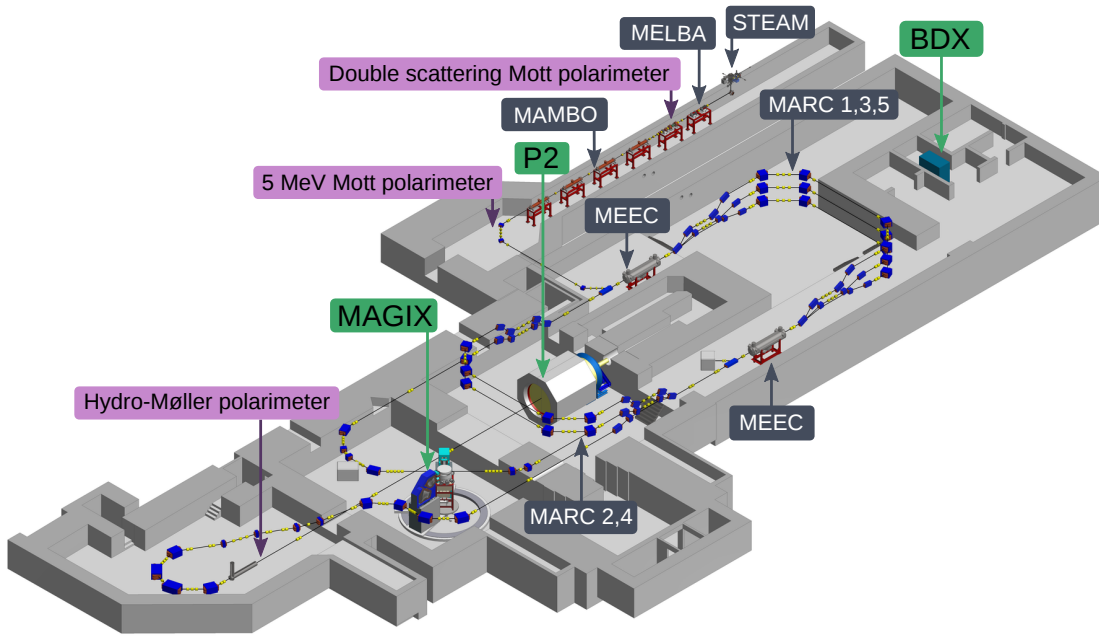
FIGURE 3.4: Simplified computer aided design (CAD) of MESA with the three experiment sites and dedicated spaces for polarimetry (Mott and Møller). The new accelerator is partly going to be placed in the existing hall structure of former experiments run at MAMI. Image courtesy of Kurt Aulenbacher.

Abbreviation	Meaning	Explanation
STEAM	Small Thermalized Electron source At Mainz	Photoelectron source
MELBA	MESA Low Energy Beam Apparatus	Spin manipulation system
MAMBO	Milliampere booster	5 MeV electron injector
MEEC	MESA Elbe-enhanced cryomodule	25 MeV linear accelerator
MARC	MESA Arc	Recirculation
BDX	Beam Dump Experiment	Search for dark matter
MAGIX	MESA Gas Internal Target Experiment	Search for dark photon

TABLE 3.1: Acronyms used in figure 3.4

Operation mode	External target	Internal target
Beam energy [MeV]	155	105
Mean current [μA]	150	1000/10000
Experiments	P2/BDX	MAGIX

TABLE 3.2: Specifications of the MESA electron beam for internal beam mode and external beam mode respectively according to [31].
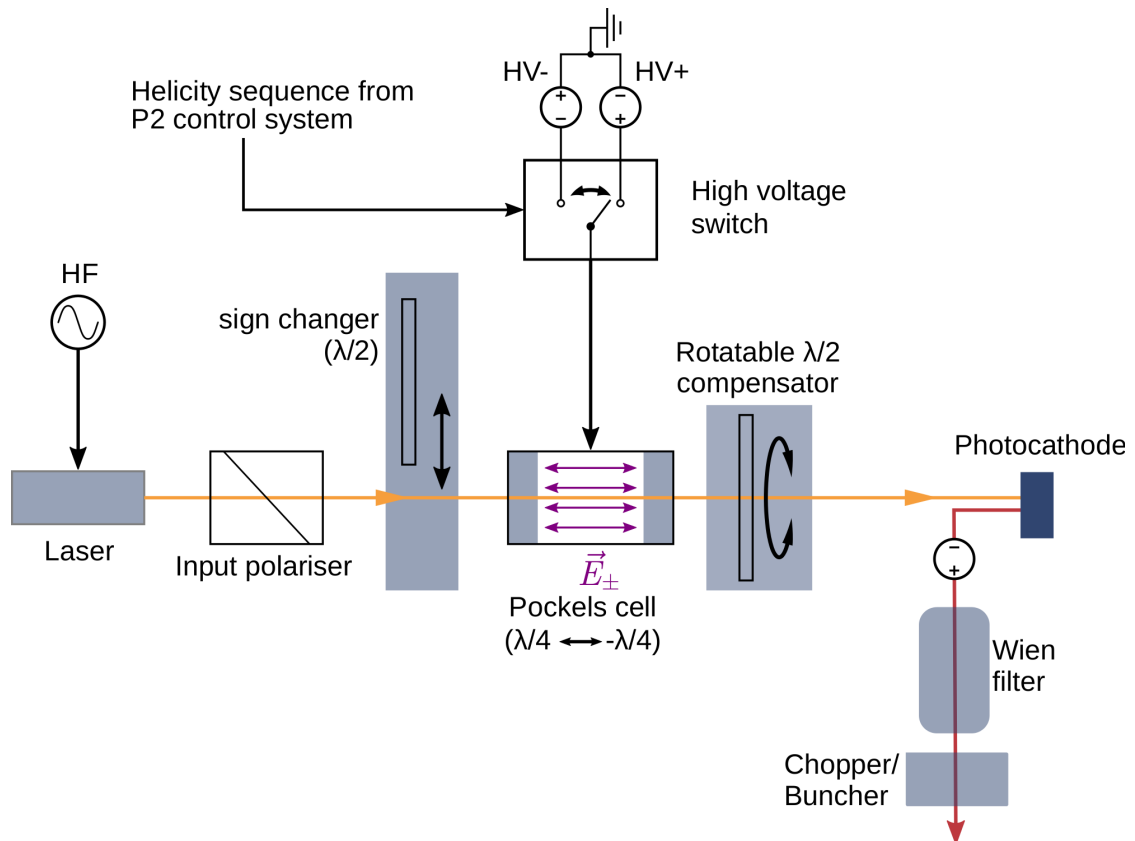
FIGURE 3.5: Polarised electron source for the MESA accelerator. The drawing is adapted from [32].

3.2.2 The Polarised Electron Beam

Achieving the desired precision in the P2 Experiment within $10\,000\,\mathrm{h}$ requires a beam polarisation of 85%. Figure 3.5 shows a scheme of the polarised electron source STEAM, whose design is adapted from the one installed at MAMI. The helicity switch is realised by reversing the circular polarisation of a laser beam, which is used to induce the emission of photoelectrons from a GaAs cathode. The high beam intensity produced for P2 will reduce the life time of the photocathode. Regeneration and renewal of the material will therefore be scheduled in the run time plan of P2.

The next stage of the accelerator, called the *MESA Low-energy Beam Apparatus* (MELBA), manipulates the beam to achieve a precise spin direction longitudinal to the beam. The *MilliAMpere BOoster* (MAMBO) accelerates the electrons from $100\,\mathrm{keV}$ to $5\,\mathrm{MeV}$. In three circulations the beam is then accelerated to $155\,\mathrm{MeV}$ before being extracted via a magnetic chicane. A more than $10\,\mathrm{m}$ long straight beam line in front of the P2 Experiment provides space for beam stabilisation and diagnostics.

For the P2 Experiment knowledge of the beam polarisation to a relative accuracy of better than $\Delta P/P = 0.5\%$ is foreseen. Effective polarimetry is thus a key issue. MESA will use a chain of three polarimeters: a Møller polarimeter directly in front of the P2 Experiment and two Mott polarimeters. The Mott polarimeters measure transverse spin polarisation and are going to be placed right downstream of the source and behind the injector respectively. They can not be operated during the run time of P2. The Møller polarimeter has online capability and will measure the longitudinal polarisation needed in the P2 Experiment at full beam energy of 155 MeV and current of 150 μA.

Helicity changes at the MESA source can slightly alter the beam position, angle, energy, and intensity at the location of the experiment leading to false asymmetries. At MESA these helicity-correlated beam fluctuations will be measured precisely and continuously corrected for. For the P2 Experiment a false asymmetry of no more then 0.1 ppb after 10.000 hours of data-taking is acceptable. The development of a beam stabilisation apparatus which meets this criterion is described in [33].

3.3   The P2 Apparatus

Figure 3.6 is a rendered *Computer Aided Design* (CAD) of the P2 Experiment as it is going to be installed in the experimental hall. The electrons, of energy $E_{\text{beam}} = 155$ MeV and helicity alternating between $+1$ and -1, are going to enter the scattering chamber, traverse the liquid hydrogen target and undergo a variety of interaction processes. The elastic scattering from protons (hydrogen nuclei) into laboratory angles between $\Theta_{\text{L}}^{\text{min}} = 25°$ and $\Theta_{\text{L}}^{\text{max}} = 45°$ are of interest for the determination of the weak mixing angle Θ_W. An elaborate magnetic field and lead shielding system is going to spatially separate the electrons stemming from these processes from undesired background. The quartz Cherenkov detector's dimensions and placement is optimised with respect to signal-to-background ratio.

3.3.1   The Liquid Hydrogen Target

The necessary scattering rates for a precision measurement of the small asymmetries occurring in P2 can only be realised by employing a high power target, which is implemented by using a 60 cm long target cell filled with liquid hydrogen[1]. Beam currents of 150 μA lead to energy depositions of 3.1 kW in the target. An elaborate cryogenics and monitoring system is going to be necessary in order to compensate for this heat load and to minimise density reduction and fluctuations,

---

[1]proton density in liquid hydrogen: $\rho = 42.67 \times 10^{21}$ cm^{-3}
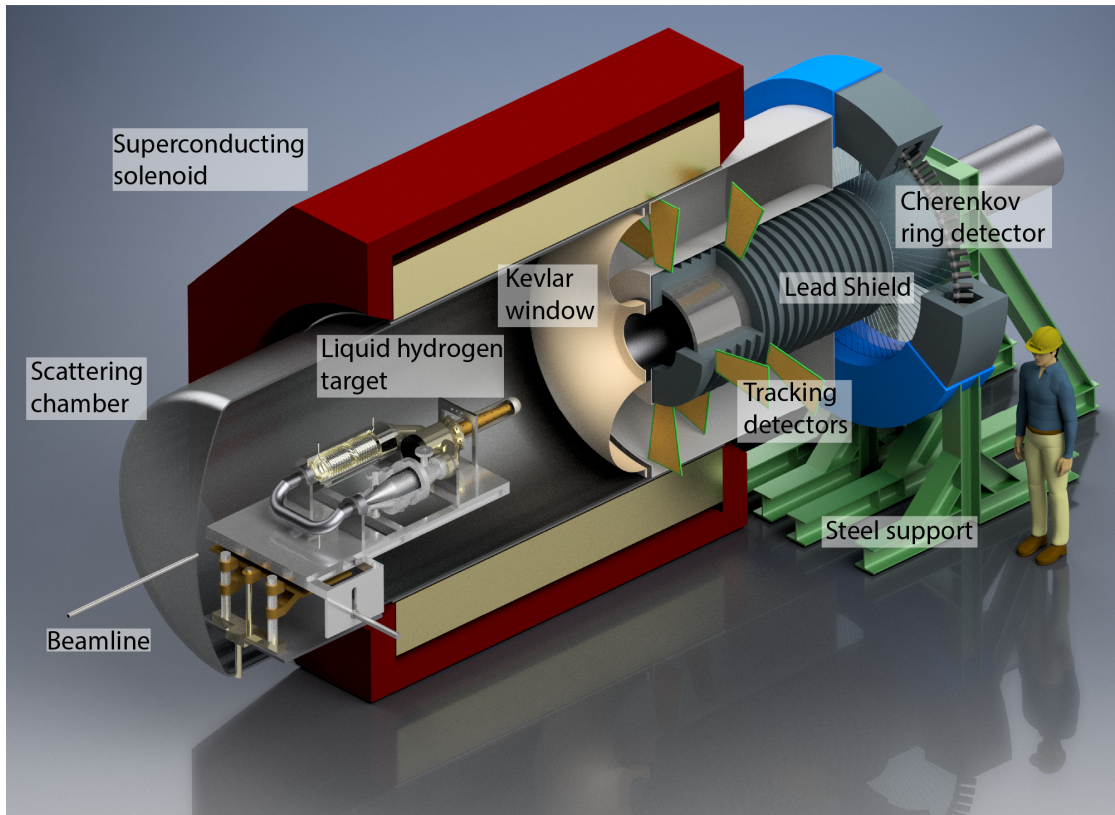
FIGURE 3.6: P2 experimental setup [34]. Note: The target's cryogenic system
might be placed further away from the beam line as shown in figure 3.8.

which would lead to systematic errors in the measured asymmetry. In order for P2
to meet its precision goal the liquid hydrogen density reduction may not exceed
2 % and the density fluctuations over the time period of electron beam helicity
reversal may not exceed 10 ppm [34]. Furthermore the target's geometry has to
allow for the exploitation of the full azimuth angle.

The concept and design is based on the target which was used in the G0-Experiment
[35] but will —with 60 cm— be twice as long. It is reengineered by S. Covrig and
his group. A conceptual drawing of the cryogenic system is shown in figure 3.7.
The heat exchanger liquefies the hydrogen and compensates for the heat load de-
posited in the target cell by the electron beam. It is based on the double coil
counterflow design, in which liquid helium is pumped through a copper pipe coil
around the lH_2-flow. Because the cooler is not able to react to fast changes in the
electron beam current such as beam trips, a high power heater is installed in the
lH_2-circuit to counterbalance fluctuations in the heat load. A centrifugal pump is
used to move the lH_2 through the cryogenic loop. The operation of a high perfor-
mance pump in cryogenic environment is challenging due to thermal contractions.
The anticipated mass flow generated by the pump will be less than 2 kg/s with
0.1 bar of pressure at the pump head. The target cell itself is cylindrical with a
dome-shaped end cap. One of the design constraints is the minimisation of target
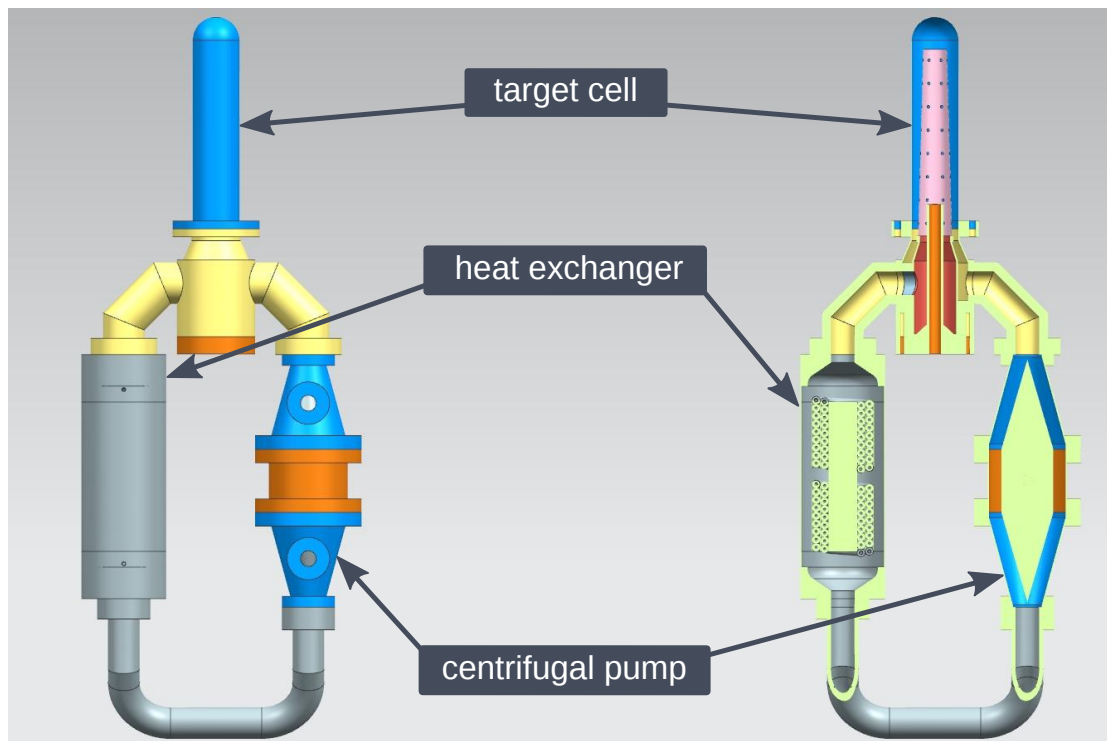
FIGURE 3.7: Design of the liquid hydrogen circuit including the target cell, heat exchanger, and centrifugal pump. The actual arrangement of the target's components will differ (see figure 3.8). Picture provided courtesy of S. Covrig.

cell wall material to reduce scattering on the wrong target material. Two thin aluminium vacuum windows will confine the liquid hydrogen. A total thickness of $\leq 0.25\,\text{mm}$ is pursued for this material.

The target cell will be placed onto a translation/rotation stage to allow for precise alignment in the beam as shown in figure 3.8. Furthermore a motion mechanism will enable the experimentalists to move the target in and out and to remotely switch between the liquid hydrogen target and solid targets, like e.g. a graphite target. Pump and heat exchanger will be located further away from the beam and outside of the bore of the solenoid magnet. Connection to the target cell will be realised via a flexible pipe system.

3.3.2   The Solenoid Spectrometer

The high luminosity in the P2 Experiment entails high particle flux. The hit rates onto the detector are going to be much too high to differentiate between them, because the signal pulses from the photomultipliers overlap so much that merely a continuous current can be recorded. The measurement will have to take place in an integrating mode, meaning that instead of counting single events the signal currents during defined time intervals are going to be measured. This method does

FIGURE 3.8: Placement of the target in the vacuum chamber of the P2 Experiment. The heat exchanger and pump will be placed outside of the magnet's bore and connected via flexible pipes with the target cell. Picture taken from [34].
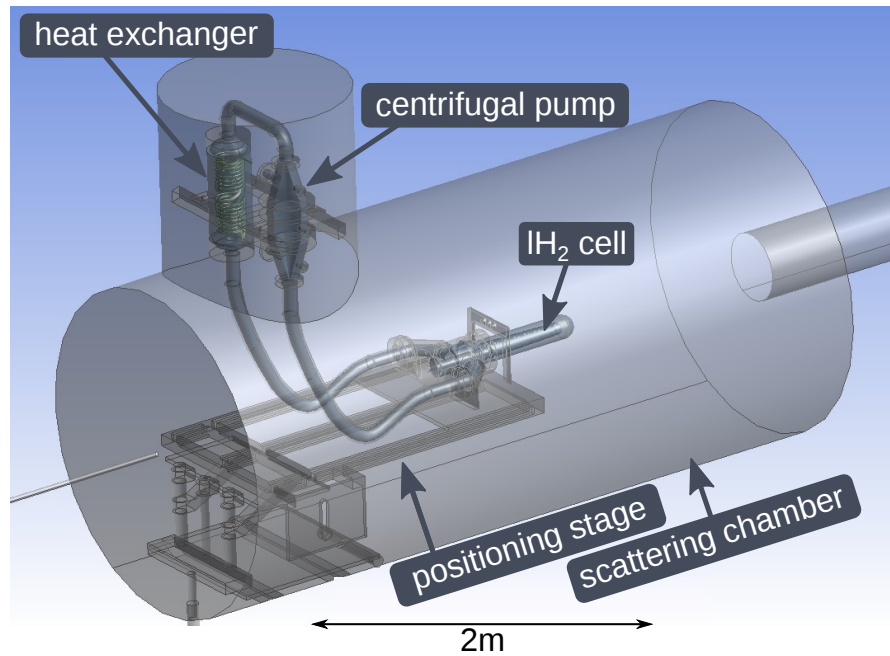
not allow for an analytic separation of signal and background, which means that the apparatus will have to be optimised with regard to minimising the background flux onto the detector.

A superconducting solenoid magnet will be installed to spatially separate signal from background. It will serve to focus desired signal particles from elastic electron-proton scattering events onto the detector ring, while large fraction of the undesired background is effectively filtered out by the magnetic field and shielding arrangement.

Figure 3.9 shows the magnet with its dimensions along with the shielding system. The solenoid's operating field strength will be $0.6\,\mathrm{T}$. The target cell will be placed inside the bore of this magnet. A major background source will be electrons from elastic electron-electron (Møller) scattering in the target. As these electrons have low energies and are concentrated to forward angles, they curl closely around the beam axis in the presence of such a strong magnetic field.

A second large contribution are photons produced by Bremsstrahlung in the target cell. The expected rate of photons is about four orders of magnitude higher than the electron rate from the signal-giving process. For lack of electric charge these particles cannot be deflected using a magnetic field. For this reason, the Cherenkov detectors have to be be shielded from direct view from the target by a heavy lead barrel with steel core. The trajectories of the signal electrons stemming from elastic e-p-scattering in the target are bent in the magnetic field and focussed
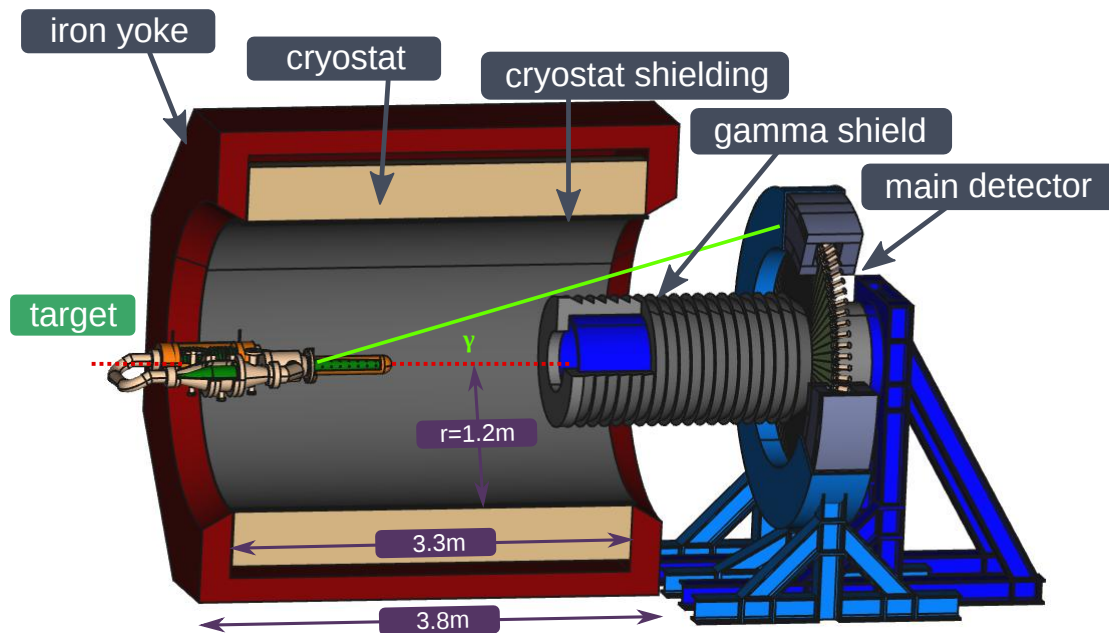
FIGURE 3.9: Solenoid spectrometer with shielding and support. The target will be placed inside the magnet's bore. The spectrometer will focus the desired signal electrons onto the main detector while spatially separating large parts of the background.

onto the detector elements, while photons are stopped. The photomultipliers and electronics will be additionally shielded against radiation damage. In order to protect the cryostat from heat load stemming from ionising radiation out of the target cell, a 5 mm thick layer of lead is foreseen on the inside of the cryostat.

A PMT shield serves to protect the photomultipliers from radiation damage. A 20 cm long part of the fused silica bars is also covered by this lead shield. This area of the quartz bars is intended as light guide for the Cherenkov light so that the delicate PMTs and electronics may be positioned further away from the area of most radiation and shielded effectively.

3.3.3 Q^2 Determination

The extraction of the weak charge of the proton from an integrating measurement of the parity-violating asymmetry requires the knowledge of kinematic properties of the scattering process which the detected signal electrons underwent. In particular, the four-momentum transfer distribution of the elastic electron-proton scattering in the target has to be determined. For this purpose a tracking detector array is going to be installed. It will reconstruct the trajectories of individual

FIGURE 3.10: Projection of the P2 experimental setup and the signal electron trajectories onto the x-z-plane. The tracking detector planes are indicated schematically.

electrons during dedicated tracking runs at lower beam currents. In this operating mode coincidences of tracking detector signals and single elect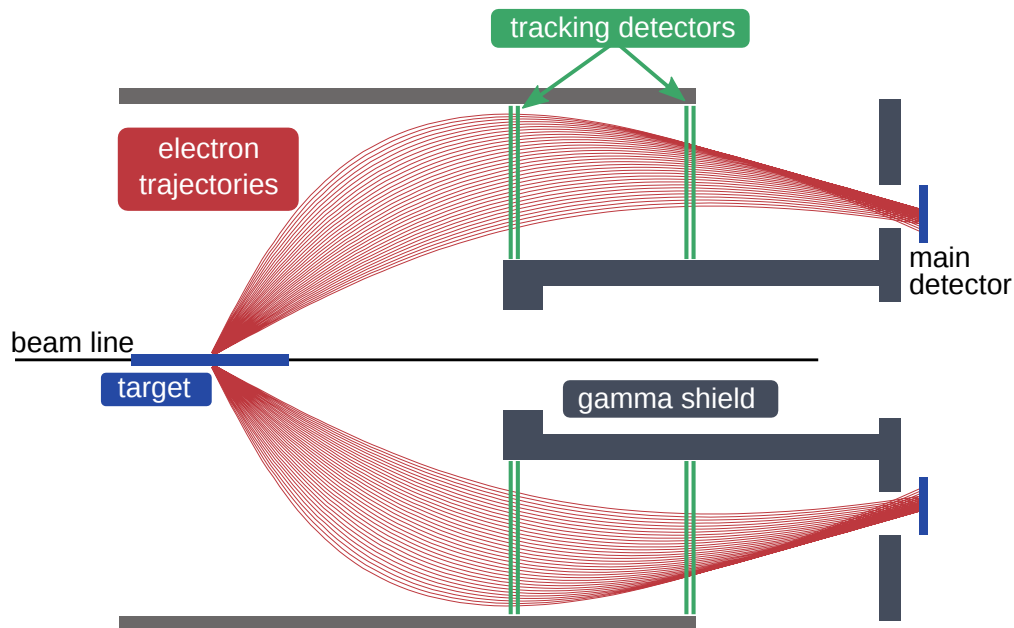ron events in the main detector are going to be used to find the relation between signal strength in the Cherenkov detector and Q^2-values. This implies that the tracker acceptance area covers at least the particles which are mapped on one quartz detector element. The tracking detectors are going to be placed inside the solenoid's bore, where the particles' trajectories are bent depending on their momentum. Figure 3.10 shows signal electron trajectories simulated with GEANT4 [25] and the planned position of the tracking detectors. Two pairs of thin detector planes are foreseen. The long drift distance between these pairs allows for precise curvature measurement of the electron tracks and thus a good momentum resolution. As shown in figure 3.11 four such arrangements are planned, each covering 15° of the azimuth angle.

The tracking detectors will stay in place during the P2 data-taking time at nominal beam current of $150\,\mu\text{A}$ to render the possibility to study background particles and rate-, position-, and momentum-dependent systematic effects. They will therefore have to remain in place during the whole operation time of the P2 Experiment and endure significant amounts of radiation and heat load deposited onto them. Their position inside the background separator's magnetic field exposes them to high rates of Bremsstrahlung photons from the target. At the position of the first tracker plane these are expected to outnumber the signal electron rates by three orders of magnitude. Along with the precision requirements this calls for very fast, radiation hard, and thin detectors. The technology employed for the P2 tracking detectors is based on the high-voltage monolithic active pixel sensors (HV-MAPS)
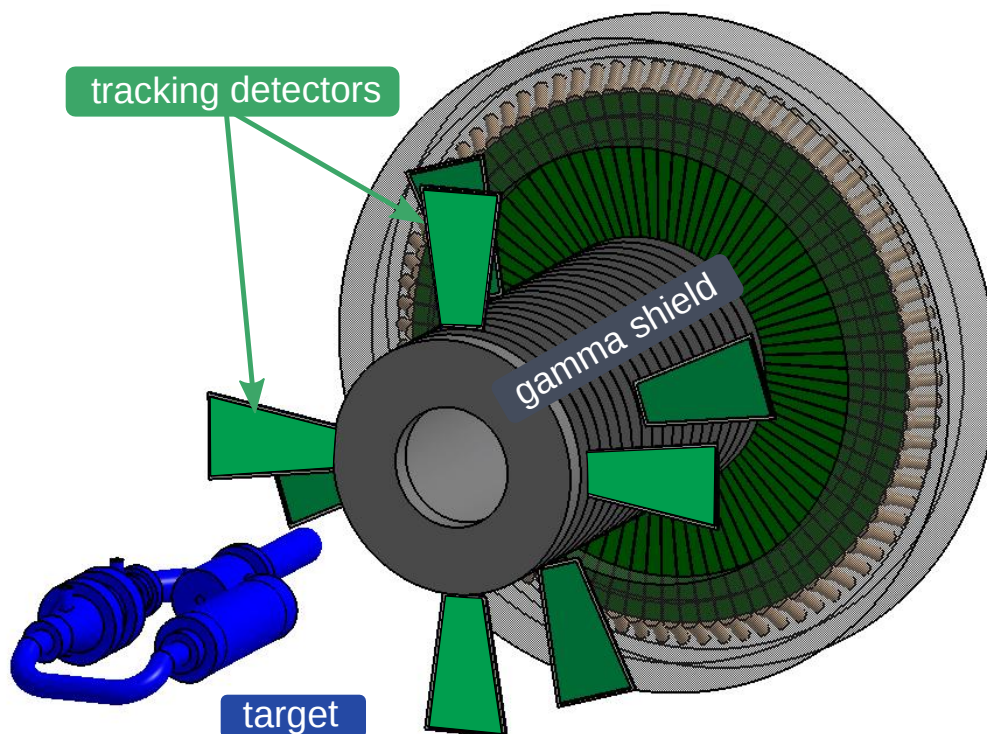
FIGURE 3.11: One tracking detector arrangement per quadrant will be in-
stalled, each covering at least the particles which are mapped onto one
Cherenkov detector element.

used in the Mu3e experiment [36]. These complete system-on-chip sensors are
no more than $50\,\mu$m thick while providing extremely high detection efficiencies
(99%) and a time resolution better than $15\,$ns. The HV-MAPS have proven to
be heat resistant. Only small amounts of additional noise have been recorded at
temperatures of $90\,°$C. However the elements have to be actively cooled. Gaseous
helium is a suitable cooling agent due to its long radiation length and fluidity.

3.3.4 The P2 Integrating Detector Ring

The high particle rates, radiation dose, and precision goals place substantial de-
mands on the P2 detector. While the actual design process and construction
details are covered in chapter 4, the reasons for the principal design choices will
be outlined here beforehand. They are made based on boundary conditions that
arise from the P2 experimental method (summarised in table 3.3) and are herein
roughly grouped into four consecutive decision steps.

Challenge	Solution	Method
High statistics required	high e^- detection efficiency	Cherenkov detector
	gap-free azimuth coverage	Ring geometry and wedged elements
High photon background	Suppression of photon signal	Cherenkov detector
Radiation exposure	Radiation hard material	Fused silica
		PMTs for light readout
Tracking and high statistics measurement	Operability in two modes	Switchable PMT amplification
High helicity switching frequency	Fast detectors	Cherenkov
Integrating measurement	Excess noise $< 1\%$	$n_{PE} > 50$

TABLE 3.3: Overview of requirements for the P2 electron detector and methods used to meet these requirements.

P2 is a high statistics experiment. All components of the P2 apparatus are designed to allow for a high signal event rate in order to achieve the necessary statistics within a feasible data-taking time. The design luminosity of the P2 experiment of $\mathcal{L} = 2.38 \times 10^{39}\,\mathrm{cm}^{-2}\,\mathrm{s}^{-1}$ result in a sufficiently high signal electron flux onto the detector plane. In order to detect the $N \approx 10^{18}$ elastically scattered electron events necessary to achieve the envisioned precision of $\sin^2 \Theta_W$ within $10\,000\,\mathrm{h}$, the detectors have to provide good detection efficiency.

The electron hit rates onto the whole detector ring during data-taking are going to be as high as $1.57 \times 10^{11}\,\mathrm{s}^{-1}$ [25]. Photonic background yet exceeds this rate by one order of magnitude even after shielding. One boundary condition for all materials used in the main detector is therefore extreme radiation hardness. In addition, it is desirable to use a detector type which intrinsically suppresses photon signals. To meet both these criteria, the P2 detector is based on the Cherenkov effect, which occurs only if high energy charged particles pass through the Cherenkov medium. The detection efficiency for electrons with energies above the Cherenkov threshold is close to 100%. Photons can only contribute to the signal if they convert to charged particles inside the detector and are therefore suppressed.

Cherenkov radiation is mainly emitted in the ultraviolet part of the spectrum. To avoid signal attenuation in the medium itself, a material permeable to UV is advised. For the P2 detector highly pure fused silica bars were chosen as a
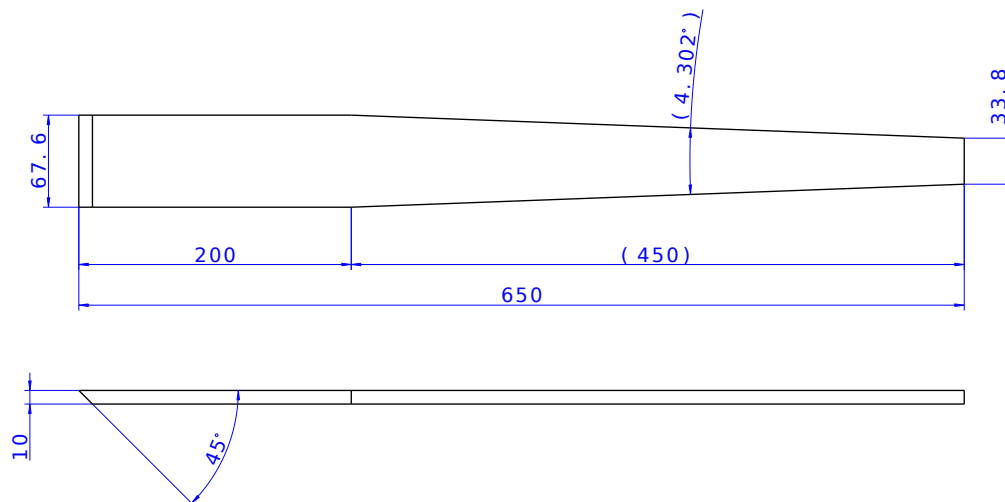
FIGURE 3.12: Technical drawing of a fused silica bar used as Cherenkov medium in P2. Dimensions in units of mm.

Cherenkov medium. They have proven to endure the radiation the detector will be exposed to, and they are transparent down to wavelengths of 200 nm.

A quartz Cherenkov bar exhibits no afterglow effect like a scintillating material. This is important because even though the electron event rates occurring in the P2 Experiment will not be resolved, the detector needs to be fast enough for the signals to not overlap from one helicity window to the next.

The P2 detector has to cover as much of the azimuth angle as possible. Any gaps between detector elements leading to undetected particles have to be compensated by extending the data-taking time. Therefore a disk-shaped geometry as shown in figure 3.13 was chosen. The ring consists of 72 radially arranged autonomous detector modules. The wedged geometry of the individual fused silica bars is depicted in the technical drawing 3.12. Each module is 650 mm long and can be subdivided into a 450 mm long tapered detection area and a 200 mm long straight section, which is going to be shielded by lead. This part of the quartz bar serves as light guide for the Cherenkov photons to the PMTs. It features a 45° optical outlet to allow the photons to transit from the quartz material into air at that end of the bar. Gaps between the bars are limited to only the thickness of wrapping material and support. This way, a fraction of the ring as high as 86% can be covered.

The Cherenkov light generated in the quartz bars is in large part contained inside the bars and directed towards the PMT by total internal reflection. For containment of the small percentage of light which exits the bar, the bars are encased in highly reflective aluminium, which —along with a thin carbon construction or small amounts of aluminium U-profiles— also serves as support for the quartz bars.

A photomultiplier is attached to each fused silica bar for Cherenkov light readout. PMTs are more radiation resistant than semiconductor light sensors, but the main reason to use them is that they may be operated in different modes. The measurement of the mean four-momentum transfer in the parity-violating electron-proton scattering process requires tracking runs at low beam current. During these runs, single events in the quartz bars have to be recorded. The PMT photocathode current has to be amplified by a factor of order $\mathcal{O}(10^6)$. During the P2 data-taking on the other hand, the electron rates are so high that if the same amplification was applied the PMT's anode would decay too quickly. A suitable PMT base with switchable amplification was designed and tested in [37].

In chapter 5.1 it will be shown that at least 50 photoelectrons per event are needed in order to reach an accuracy close to counting statistics with an integrating measurement. Suitable detector geometries and materials as well as particularly sensitive photomultipliers have been chosen for tests at the MAMI beam.

The electric signal from the PMTs gets passed onto the data acquisition system, which is described in the following section.

3.3.5   Data Acquisition

The electron hit rates onto the Cherenkov detector are in the order of $10^{11}\,\text{Hz}$ and cannot be resolved into individual signal pulses. The asymmetry is therefore going to be measured in current (or "integrating") mode. This means that instead of counting single events the currents from the PMT bases are integrated over specific time periods and evaluated by the P2 *Data Acquisition System* (DAQ). The P2 electronics is based on the low-noise electronics of the Qweak DAQ system, which is also used with little modification in the MOLLER experiment. During the P2 integrating mode measurement, the PMT bases are going to be operated to deliver an amplification factor of ≈ 1000. The electron incidence rate onto a quartz radiator of $\approx 1\,\text{GHz}$ and a photoelectron yield of about 75 per electron event then lead to a steady current from each PMT's anode of approximately $I_A^\pm(t)=12\,\mu\text{A}$. During the course of the experiment these currents are subject to variations due to beam and target condition drifts and decay of PMT sensitivity. Furthermore they generally depend on the beam helicity due to the parity-violating nature of the scattering process and the helicity-correlated beam changes. The anode current can be expressed as:

$$I_A^\pm(t) = I_S^\pm(t) + \sum_B I_B^\pm(t) + I_D(t) \tag{3.6}$$
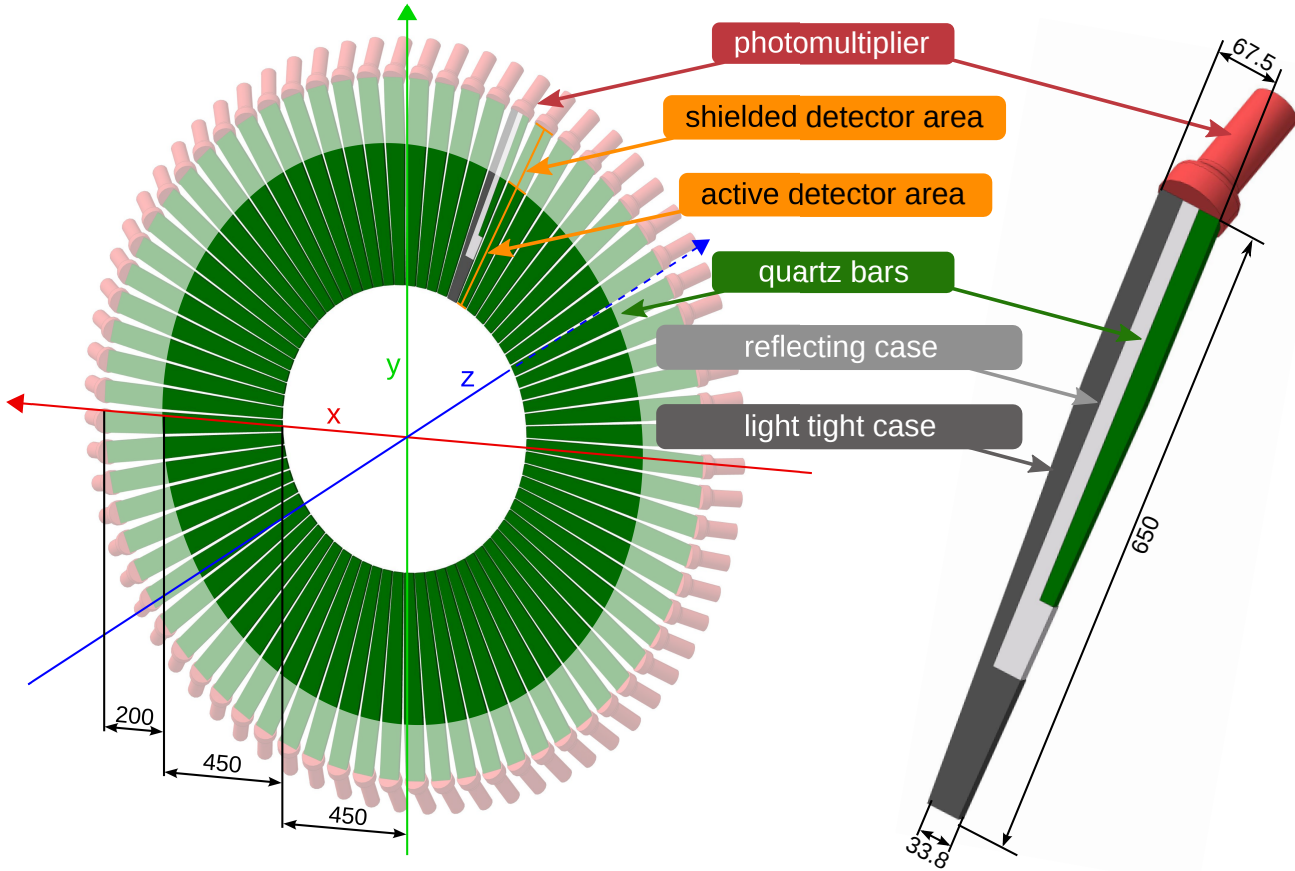
FIGURE 3.13: Geometry of the P2 Cherenkov detector ring. 72 autonomous detector modules will cover a ring shaped area. The inner part of the detector bars at $R = [450\,\text{mm}, 900\,\text{mm}]$ will be tapered to avoid gaps and overlap. Dimensions in units of mm.

where $I_S^{\pm}(t)$ is the signal current stemming from elastically scattered electrons and the secondary particles they produce. $I_B^{\pm}(t)$ is the contribution from various background particles, and $I_D(t)$ is the PMT's dark current.

This current is first converted into a voltage signal

$$V_A^{\pm}(t) = g^{\pm}(t) \cdot I_A^{\pm}(t) + V_0^{\pm}(t) \tag{3.7}$$

by a transimpedance amplifier with gain factor $g^{\pm}(t)$. $V_0^{\pm}(t)$ is the sum of a potential amplifier offset and the voltage signal stemming from dark current.

Beam and target related drifts lead to a time dependence of the voltage signal, which manifests itself in the asymmetry:

$$A_{\text{raw}} = \frac{V^{+}(t_+) - V^{-}(t_-)}{V^{+}(t_+) + V^{-}(t_-)} \tag{3.8}$$

Time dependence due to relatively slow drifts can be countered by performing fast helicity flips of about $1\,\mathrm{kHz}$ to $2\,\mathrm{kHz}$. The pseudo-random succession of helicity sequences "+- -+" and "-++-" helps eliminate linear as well as quadratic changes in target and beam parameters. The voltage signal from the pre-amplifier is digitised by an *Analogue-Digital Converter* (ADC). In order to resolve the helicity reversal signal, the ADC's bit resolution and the sampling rate are optimised with respect to a $1\,\mathrm{kHz}$ spin-flip frequency. P2 is going to use an 18-bit resolution ADC with a sampling speed of $15\,\mathrm{MSps}$.

The data acquisition has to be well synchronised with the beam's helicity switch. Electronic coupling of the helicity signal with any electronic parts like the preamplifier has to be suppressed, e.g. by avoiding ground loops.

When changing the helicity of the MESA electron beam, small influences on the beam energy, position and angle are unavoidable. A chain of beam monitors is going to be installed to measure the influence of these beam changes on the Cherenkov detector signal. These correlations make it possible to account for fast beam changes by normalising the Cherenkov detector output to the beam monitors' signal. This requires compatibility of the readout electronics of the integrating detector and the beam monitors. For the readout of the P2 ADCs, so-called *Field-Programmable Gate Arrays* (FPGAs) are going to be used in order to ensure this compatibility.

Chapter 4

Development of the P2 Integrating Detector

This chapter is going to address the design choices and the process of developing prototypes of a single module of the P2 main detector. A common choice for the detection of relativistic charged particles relies on the Cherenkov effect. The first section is therefore going to elucidate the generation and nature of Cherenkov radiation. It will explain how to use the Cherenkov effect for the detection of electrons in the P2 Experiment and what is needed for the realisation of such a device. The subsequent sections are going to cover preparatory material studies and geometry considerations for the individual parts of a Cherenkov detector for the P2 Experiment.

4.1 Cherenkov Detectors

When a charged particle travels through a dielectric medium, it will interact with the molecules of the medium and excite them, causing local, non-isotropic electrical polarisation. When the molecules return to their ground states, photons are emitted. In general, this light will quickly be destroyed by destructive interference. If, however, the original particle moves at a faster speed than the phase velocity of light in that said medium, constructive interference of the produced light takes place. This phenomenon is often explained as an optical analogue to the supersonic boom that propagates from objects such as aircraft that move through air faster than sound. This comparison can provide a pictorial understanding and — together with the Huygens-Fresnel principle— be used to derive several properties of Cherenkov radiation.
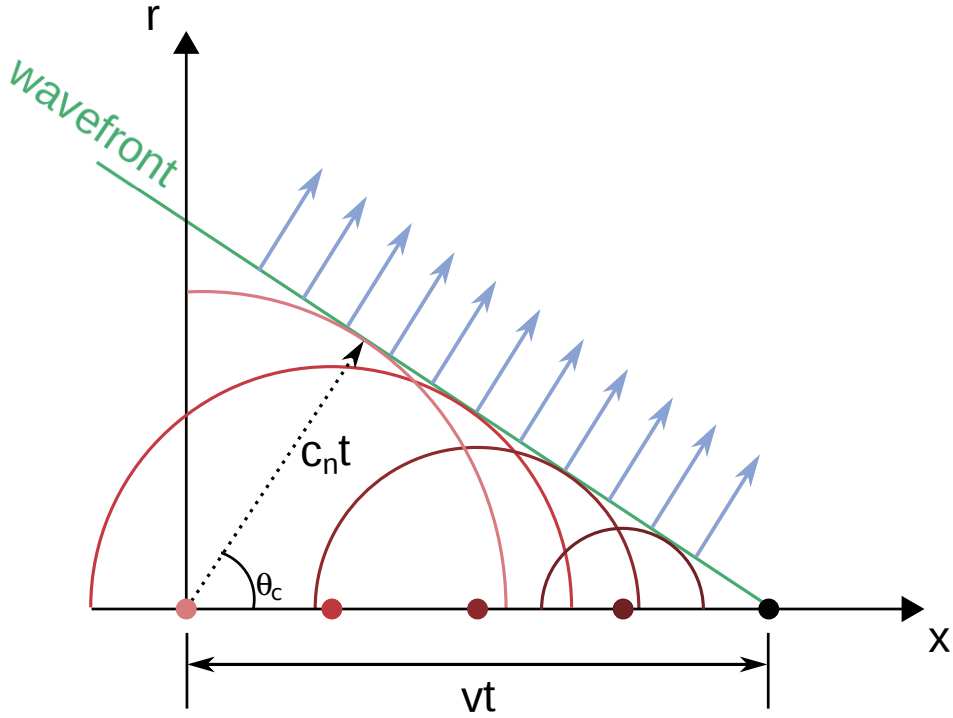
FIGURE 4.1: Graphical clarification of the relation between Cherenkov angle and phase velocity of light c_n in the Cherenkov medium.

The Cherenkov light is emitted on the surface of a cone aligned in the direction of the charged particle's propagation as shown in figure 4.1. The opening angle of this cone can be derived from this drawing in a geometrical approach.

$$\begin{aligned}\cos\Theta_C &= \frac{c_n(\lambda)t}{vt} \\ &= \frac{c}{n(\lambda)v} = \frac{1}{\beta \cdot n(\lambda)}\end{aligned} \qquad (4.1)$$

Figure 4.2 illustrates the principle of a general Cherenkov detector. The Cherenkov medium consists of an optically dense material, which is transparent to Cherenkov light. The Cherenkov cone and light propagation inside the medium are indicated in yellow. A reflective wrapping material helps constrain the light inside the detector, while the whole detector is shielded against ambient light by a light-tight housing. The Cherenkov light is transformed into electric signals by a photosensor. Cherenkov detectors using this principle exist in many different geometries and sizes and can be made of various materials.

FIGURE 4.2: Principle of a general Cherenkov detector with a Cherenkov medium wrapped in a reflective material. The Cherenkov cone and light propagati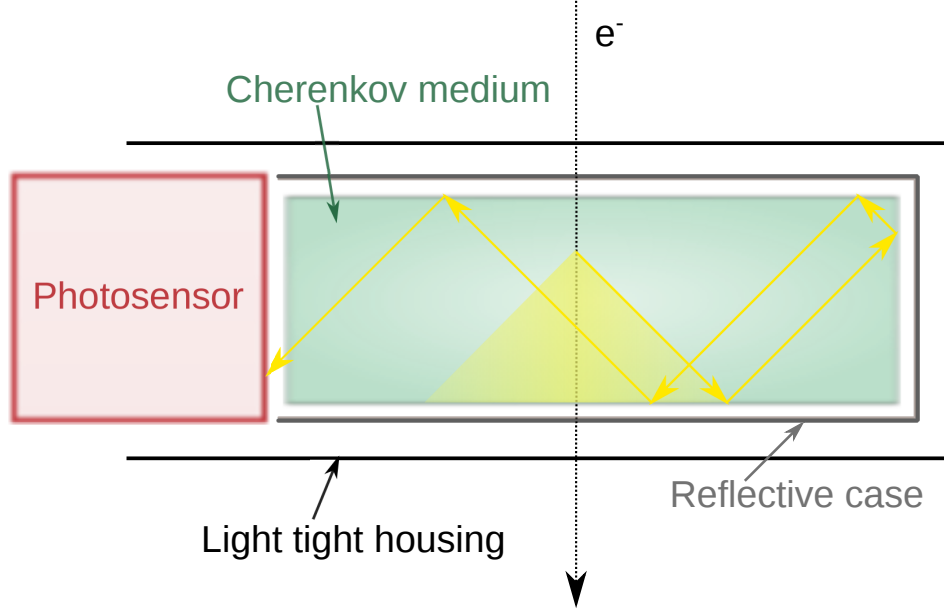on in the medium are schematically illustrated in yellow. A photosensor transforms the Cherenkov light into an electric signal. The whole detector is shielded against ambient light by a light tight housing.

4.2 Preparatory Studies

When designing a particle detector, the signal yield to particles traversing the radiator is of central interest. The number N_{Ch} of Cherenkov photons provoked per path length dx and wavelength range $d\lambda$ by a particle with charge z travelling through a material with refractive index n is given by the Frank-Tamm formula [38]:

$$\frac{d^2 N_{\text{Ch}}}{d\lambda dx} = \frac{2\pi z^2 \alpha}{\lambda^2}\left(1 - \frac{1}{\beta^2 n^2(\lambda)}\right) = \frac{2\pi\alpha z^2}{\lambda^2}\cdot\sin^2(\Theta_{\text{Ch}}) \qquad (4.2)$$

where α is the fine structure constant, $n(\lambda)$ is the wavelength dependent refractive index of the Cherenkov medium, z is the primary particle's charge, and β is the particle's velocity relative to the speed of light. Under the approximation that the Cherenkov angle is wavelength-independent, the total number of photons generated per dx is determined by integrating equation 4.2 over the wavelength range $[\lambda_{\text{min}}, \lambda_{\text{max}}]$:

$$\frac{dN_{\text{Ch}}}{dx} = \int_{\lambda_{\text{min}}}^{\lambda_{\text{max}}} \frac{d^2 N_{\text{Ch}}}{d\lambda dx}d\lambda = 2\pi\alpha z^2 \cdot \sin^2(\Theta_{\text{Ch}})\left(\frac{1}{\lambda_{\text{min}}} - \frac{1}{\lambda_{\text{max}}}\right) \qquad (4.3)$$

The use of an optically dense material leads to a larger Cherenkov angle Θ_{Ch} and better Cherenkov light yield.

The photons then propagate through the medium until they reach the photosensor. They are subject to transmission losses inside the medium as well as to reflection losses at optical boundaries of the detector. The resulting signal can be quantified by

$$\frac{d^2 S}{d\lambda dx} = \underbrace{\frac{d^2 N_{\mathrm{Ch}}}{d\lambda dx}}_{\mathrm{I}} \cdot \underbrace{e^{-k(\lambda)s(x)}}_{\mathrm{II}} \cdot \underbrace{R_{\mathrm{Q}}(\lambda)^{n_{\mathrm{RQ}}(x)}}_{\mathrm{III}} \cdot \underbrace{R_{\mathrm{W}}(\lambda)^{n_{\mathrm{RW}}(x)}}_{\mathrm{IV}} \cdot \underbrace{QE(\lambda)}_{\mathrm{V}} \tag{4.4}$$

where

  I is the number of produced Cherenkov photons from equation 4.2,

 II is the transmission loss while the photons travel a distance s in the medium. This distance depends on the origin of the Cherenkov light x. $k(\lambda)$ is the attenuation coefficient.

III is the reflection loss at the optical surfaces between Cherenkov medium and surrounding material. These depend on the reflectivity $R_{\mathrm{Q}}(\lambda)$ and the number of reflections $n_{\mathrm{RQ}}(x)$ the light undergoes.

IV is the reflection loss on the wrapping material, again depending on the reflectivity and the number of reflections.

 V is the spectral sensitivity of the light sensor.

All factors in this expression depend on the wavelength λ. As Cherenkov light is to a large part in the UV region, the losses in the UV region are to be minimised by choosing UV suitable material: The Cherenkov medium has to be transmissive down to very low wavelengths; Wrapping material has to be highly reflective for UV; The light sensor has to exhibit outstanding efficiency to UV light.

As reflection and transmission losses can never be reduced to zero, the geometry of the detector is to be chosen with regard to minimising the path length s of the Cherenkov light as well as the number of reflections n_{RQ} and n_{RW}.

4.2.1   Fused Silica as Cherenkov Medium

As described and motivated in section 3.3.4, the most important traits of the P2 main detector are a good signal-to-background ratio, radiation hardness and little

Sellmeier Coefficients	
$b_1 = 4.73115591 \cdot 10^{-1}$	$c_1 = 1.29957170 \cdot 10^{-2}$
$b_2 = 6.31038719 \cdot 10^{-1}$	$c_2 = 4.12809220 \cdot 10^{-3}$
$b_3 = 9.06404498 \cdot 10^{-1}$	$c_3 = 9.87685322 \cdot 10^{1}$

Source: Heraeus datasheet 2011

$b_1 = 6.961663 \cdot 10^{-1}$	$c_1 = 4.679148 \cdot 10^{-3}$
$b_2 = 4.079426 \cdot 10^{-1}$	$c_2 = 1.351206 \cdot 10^{-2}$
$b_3 = 8.974794 \cdot 10^{-1}$	$c_3 = 9.793400 \cdot 10^{1}$

Source: I. H. Malitson 1965 [39]

TABLE 4.1: Empirically determined sets of Sellmeier coefficients describing the dispersion of light in fused silica. The two sets lead to the plots shown in 4.3. c_1, c_2, and c_3 are in μm^2.

to no afterglow. These demands limit the choice of Cherenkov media drastically. Fused silica[1] is a well-established material for use in Cherenkov detectors. With its high optical density ($n \approx 1.45$), it provides a good Cherenkov light yield.

The refractive index n of fused silica of types Heraeus Suprasil and Spectrosil as a function of the wavelength λ is given by the dispersion formula

$$n^2 - 1 = \frac{b_1 \lambda^2}{\lambda^2 - c_1} + \frac{b_2 \lambda^2}{\lambda^2 - c_2} + \frac{b_3 \lambda^2}{\lambda^2 - c_3} \tag{4.5}$$

with the empirically determined Sellmeier coefficients from the datasheet provided by the manufacturer for Spectrosil 2000, which are listed in table 4.1. The table also contains an alternative set of Sellmeier coefficients for fused silica published by I. H. Malitson [39]. As illustrated in figure 4.3, the refractive indices calculated with the respective sets of coefficients do not differ significantly.

---

[1]Silicon dioxide can be manufactured as a crystalline as well as an amorphous material. The structure which is formed depends solely on the conditions during the process of solidification from the melt. Amorphous materials are bound into topologically disordered networks. In the case of SiO_2 this network consists of SiO_4^{4-} tetrahedra, the basic unit of all silicates. Amorphous silicon dioxide is less dense than the crystalline form, as it contains more free volume. Fused silica and fused quartz are both non-crystalline amorphous materials consisting of highly pure silicon dioxide, but their manufacturing processes differ substantially. Fused quartz is produced by melting high purity, naturally occurring quartz crystals or other silicon dioxide containing minerals. Historically fused silica was produced by melting fine sand. In order to make synthetic fused silica suitable silicon-containing chemical precursors are burned in the presence of oxygen to form silicon dioxide. The material used for the P2 Cherenkov detector is distributed by its manufacturer Heraeus Conamic as "quartz glass" as well as "fused silica" or "synthetic fused silica". All these terms as well as "synthetic quartz" or, for brevity, simply "quartz" are used synonymously in this work.
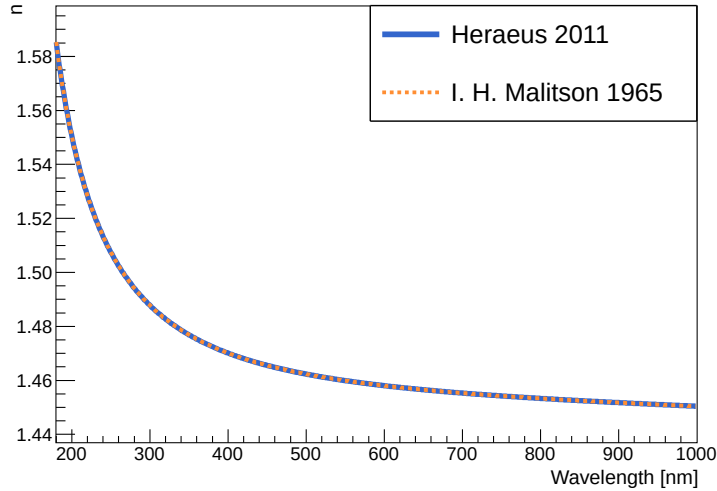
(a) Refractive index n from dispersion formula with two different sets of Sellmeier coefficients (table 4.1)
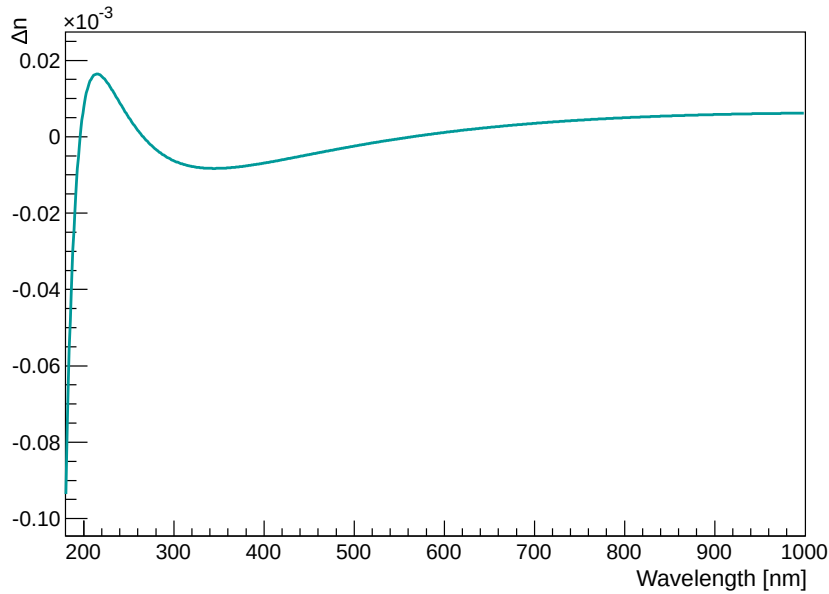
(b) Difference $\Delta n = n_{\mathrm{Heraeus}} - n_{\mathrm{Malitson}}$

FIGURE 4.3: Spectral refractive index for Heraeus Spectrosil 2000

Fused silica is exceptionally transmissive to UV light down to a wavelength of 180 nm. Furthermore, it produces no significant amounts of a delayed signal caused by scintillation effects [40].

The Cherenkov threshold is the primary particle's minimal energy needed to produce Cherenkov radiation. Its calculation for electrons near the speed of light in fused silica in Appendix C renders

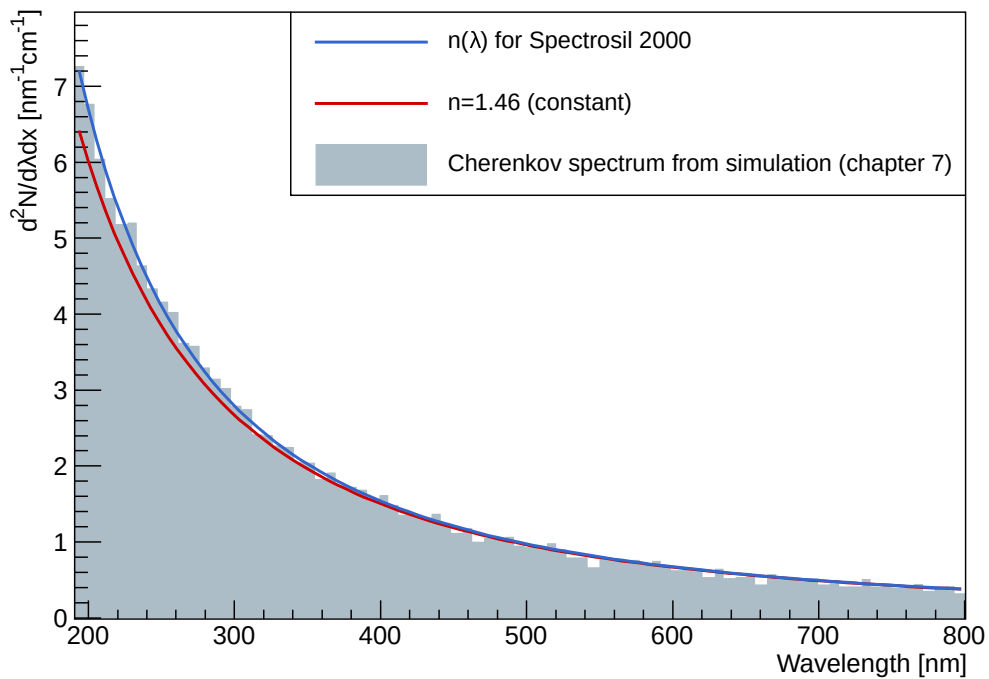$$E_S(m_i = m_e, n \approx 1.45) = 0.71\,\mathrm{MeV} \tag{4.6}$$

FIGURE 4.4: Cherenkov spectrum for a relativistic electron in Spectrosil 2000 with the dispersion $n(\lambda)$ defined by the dispersion relation 4.5 with the manufacturer's Sellmeier coefficients (4.1). The red curve shows the Cherenkov spectrum for a hypothetical material with $n = 1.46$. The histogram is the spectrum of light generated by electrons with energy $155\,\text{MeV}$ in the GEANT4 simulation described in chapter 7.

as a result.

Figure 4.4 shows the Cherenkov spectrum for an electron at nearly the speed of light in fused silica with the brand name "Spectrosil 2000" produced by Heraeus Conamic compared to the spectrum in a hypothetical material with the wavelength-independent refractive index of 1.46. As Cherenkov light is mainly generated in the UV region, the number of produced photons is highly sensitive to the short wavelength limit of the material used in the detector. This substantial fact is illustrated in figure 4.5, where the number of Cherenkov photons produced when an electron passes through $1\,\text{cm}$ of fused silica is plotted against the lower wavelength cut λ_{min}. In practice, λ_{min} is determined under consideration of the transmittance spectrum of the fused silica, the reflectance of the wrapping material, and the spectral photon detection efficiency of the light sensor. If, for example, a photosensor was used which exhibits no sensitivity to photons below a wavelength of $300\,\text{nm}$, the resulting signal would be reduced to less than 50% compared to the signal yield if the sensor was sensitive down to a wavelength of $200\,\text{nm}$.
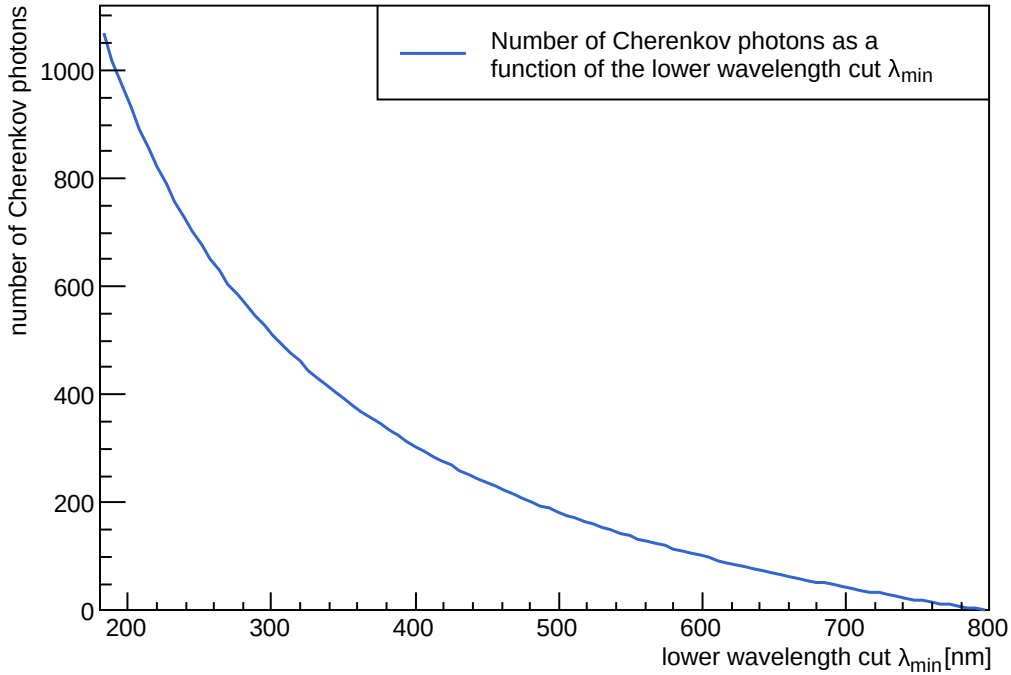
FIGURE 4.5: Number of Cherenkov photons produced by an electron passing 1 cm of fused silica as calculated in equation 4.3 plotted as a function of the lower wavelength cut λ_{min}

4.2.1.1   Optical Properties of Fused Silica

Highly pure synthetic quartz shows exceptional transmittance for UV and visible light. Light transmission spectra of material samples were measured with a Shimadzu UV-2101PC spectrophotometer with MPC-3100 large sample compartment. Figure 4.6 is a reduced scheme of the apparatus.

For a wide spectral range, the device is equipped with a tungsten halogen lamp, which is used for wavelengths from 360 nm to 800 nm, as well as a deuterium lamp for wavelengths down to 200 nm. A monochromator breaks down the spectra of the respective lamps into their constituent wavelengths and isolates a narrow spectral band (± 2.5 nm). This is done by means of a diffraction grating and a mechanical slit. The beam is then split into a reference beam and a sample beam. Calibration is performed by determining the scaling factor

$$k = \frac{S_{\text{ref}}}{S_{\text{samp}}} \tag{4.7}$$

from the sample beam signal S_{samp} and the reference beam signal S_{ref}, when there is no sample placed in the sample compartment.
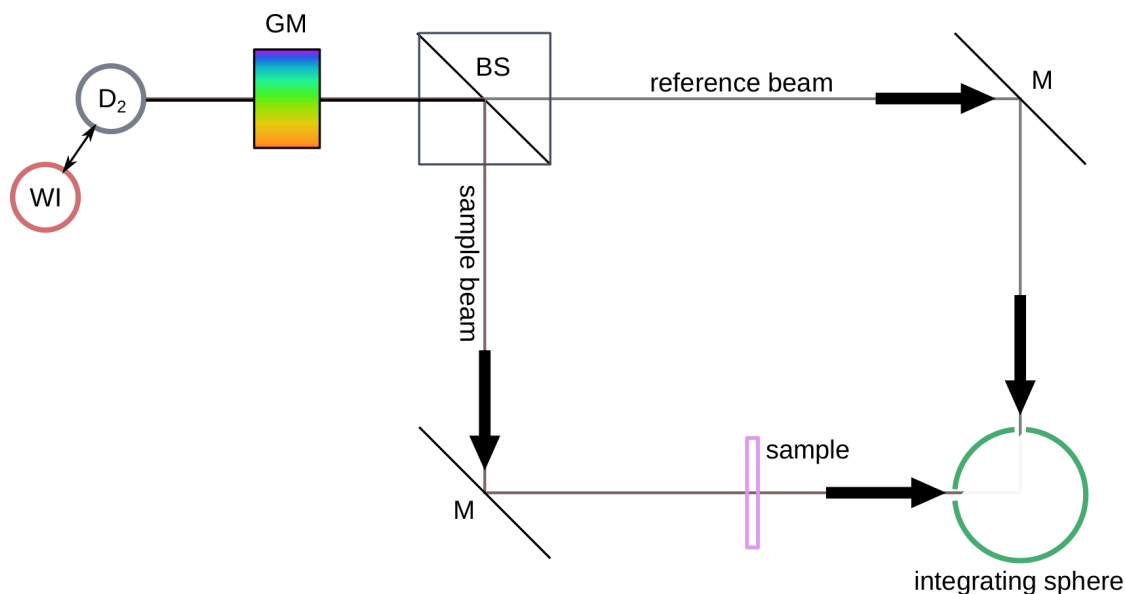
FIGURE 4.6: Reduced scheme of the Shimadzu UV-2101PC / MPC-3100 spectrophotometer arrangement. WI: tungsten halogen lamp; D_2: deuterium lamp; GM: grating monochromator, BS: beam splitter, M: mirrors, IS: integrating sphere.

During a measurement, the wavelength is decreased from $800\,\mathrm{nm}$ down to $200\,\mathrm{nm}$ in steps of $1\,\mathrm{nm}$ and reference beam and sample beam are detected alternatingly. This is realised by means of a chopping wheel, which allows only one of the beams to enter the integrating sphere at a time. The integrating sphere is coated with barium sulfate $BaSO_4$, providing a white, diffusely reflecting surface. The light from inside the integrating sphere can reach a photodetector through an opening in the integrating sphere.

The result of a spectrophotometer measurement is a relative intensity spectrum of the light beam traversing the sample with respect to the reference beam, which does not traverse a sample. These spectra were taken for two cuboid Spectrosil 2000 samples of dimensions $300\,\mathrm{mm}$ by $70\,\mathrm{mm}$ by $15\,\mathrm{mm}$, and the measurements were done for two orientations of the bar inside the spectrophotometer with the light incident at perpendicular angles to the surface. For one orientation the light beam traversed $70\,\mathrm{mm}$ inside the quartz glass bar. For the other orientation, the beam traversed $15\,\mathrm{mm}$. Figure 4.7 shows the mean of 7 measurements of the intensity of a beam traversing $15\,\mathrm{mm}$ and $70\,\mathrm{mm}$ of fused quartz, respectively. The indicated error is the standard deviation divided by the square root of the number of measurements.

The light losses are caused by both transmission losses in the quartz glass and Fresnel reflection losses at the surface between quartz and air. The overall reflection losses at both surfaces are determined in percent from the per-surface reflectivity R as given by the Fresnel formula for perpendicular light incidence via:
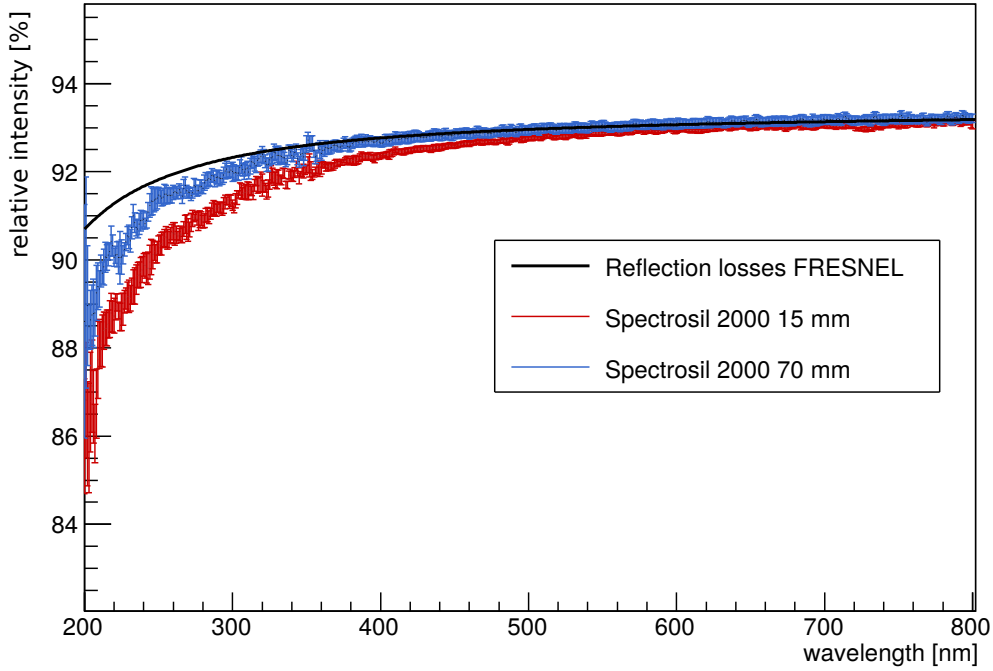
FIGURE 4.7: Relative intensity spectra of light traversing Spectrosil 2000 samples for path lengths of 15mm and 70mm. Light attenuation is caused by transmission losses and reflection losses at the surfaces. The reflection losses as calculated with the Fresnel formula are indicated by the black curve.

$$l_{\text{ref}} = (1 - R)^2 \cdot 100 = \left(1 - \left(\frac{n(\lambda) - n_a(\lambda)}{n(\lambda) - n_a(\lambda)}\right)^2\right)^2 \cdot 100 \qquad (4.8)$$

where n is the refractive index of fused silica and n_a is the refractive index of air. The Fresnel curve is also plotted in figure 4.7 to provide a reference. For the application of the material as a Cherenkov medium however, its transmittance spectrum is the relevant quantity. Therefore the pure transmission losses have to be extracted from the relative intensity spectra by eliminating the reflection losses. In order to not having to account for the Fresnel losses and systematic errors occurring at the surfaces of the quartz glass samples the transmittance T_1 per $1\,\text{cm}$ of fused silica is determined from the intensity spectra for the two quartz thicknesses.

The light intensity after passing a sample of thickness s can be expressed in terms of an attenuation coefficient A and the reflection losses f as

$$I(s) = f \cdot I_0 \cdot e^{-As} \qquad (4.9)$$

In the quotient of the measured intensities with $s = 15\,\mathrm{mm}$ and $s = 70\,\mathrm{mm}$ the reflection losses cancel out

$$\frac{I_{15}}{I_{70}} = e^{A \cdot (70\,\mathrm{mm} - 15\,\mathrm{mm})} \tag{4.10}$$

and the attenuation coefficient A can therefore be determined from the measurements as

$$A = \frac{\ln(I_{15}/I_{70})}{70\,\mathrm{mm} - 15\,\mathrm{mm}} \tag{4.11}$$

The purely internal transmittance per $10\,\mathrm{mm}$ fused silica can hereby be extracted as

$$T(10\,\mathrm{mm}) = e^{-A \cdot 10\,\mathrm{mm}} \tag{4.12}$$

The transmission of $10\,\mathrm{mm}$ Spectrosil 2000 is plotted in figure 4.8 together with the respective data from the manufacturer's datasheet. The spectrophotometer measurement was able to confirm an outstanding transmittance above 99% per $1\,\mathrm{cm}$ of material even in the deep UV region down to $200\,\mathrm{nm}$, although we have to note that our data is systematically below the manufacturer's specifications. The statistic error in our measurement is quite large due to the small light intensity, especially in the wavelength region $\lambda \in [200\,\mathrm{nm}, 360\,\mathrm{nm}]$ of the deuterium lamp. One source of the discrepancy might be a different degree of surface quality of the large plane-parallel surfaces and the narrow ones.

In the starting phase of the detector design, two fused silica variants were considered: Spectrosil 2000 and Suprasil 2A, both by Heraeus Conamic.

The manufacturer specifies the transmittance of Spectrosil 2000 only down to a wavelength of $190\,\mathrm{nm}$, while transmission data for Suprasil is available down to $120\,\mathrm{nm}$. Both spectra are congruent in the decisive spectral range of $\lambda \in [180\,\mathrm{nm}, 800\,\mathrm{nm}]$. They merely differ in the infrared region (see figure 4.9), which is irrelevant for a Cherenkov detector. A decision as to which material grade to use for the P2 detector cannot be made purely based on transmittance data. Both, Spectrosil 2000 and Suprasil 2A quartz glass bars were therefore tested at the MAMI electron beam, which is covered in section 5.5.2. Both material grades have undergone radiation hardness tests described in chapter 6, which revealed a substantial difference in radiation-induced material degradation and lead to a decision in favour of Spectrosil 2000.
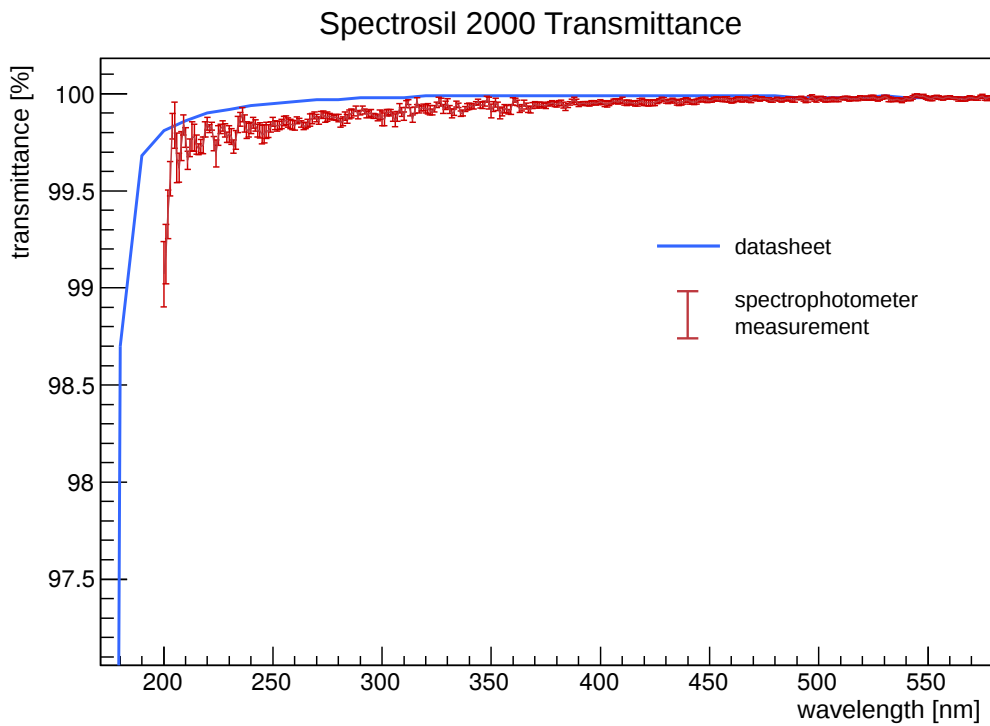
FIGURE 4.8: Transmission spectrum of 10 mm Heraeus Conamic Spectrosil 2000
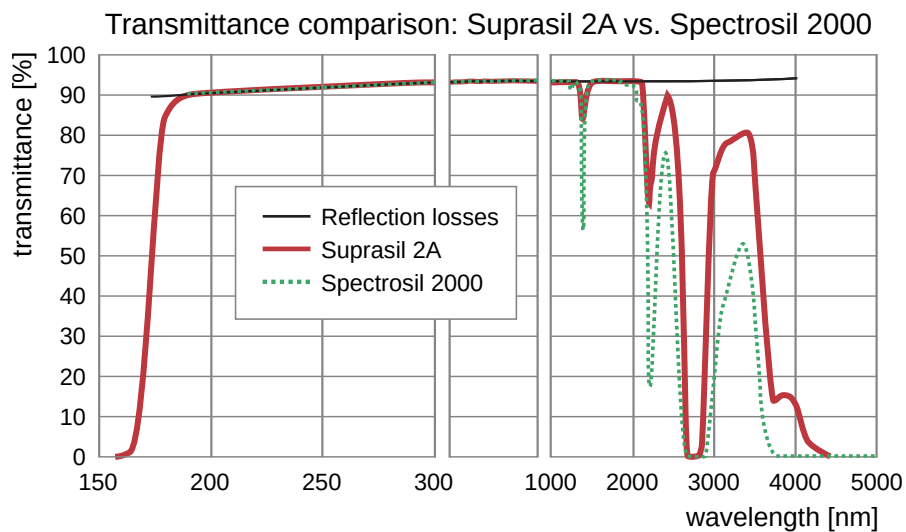from datasheet and measurement with Shimadzu spectrophotometer.

FIGURE 4.9: Transmission spectra of Heraeus Conamic Spectrosil 2000 and
Suprasil 2A as provided by the manufacturer.

4.2.2 Solid Angle Coverage

The choice of detector geometry is determined by two major concerns: First, the optimal placement in the laboratory in order to collect the signal particles and avoid background. Second, functionality in terms of best signal yield and background particle suppression. The area, which the Cherenkov detector has to cover, has been determined by Dominik Becker [25] with the help of a GEANT4 simulation, which was also used to design and optimise the shielding against background, the geometric configuration of the target, and the magnetic field. Figure 4.10 shows the structure of this simulation consisting of the liquid hydrogen target, the solenoid magnet, and the bremsstrahlung photon shield. As a first step the interaction of beam electrons with the target was simulated using GEANT4 intrinsic methods for Møller and Bhabha scattering, bremsstrahlung, (multiple) Compton scattering, electron-positron pair production, and annihilation. For the elastic electron-proton scattering processes, a special event generator was developed. The P2 collaboration intends to use a solenoid magnet similar to the one used in the FOPI experiment [41] for the separation of signal and background particles and the focussing of the signal electrons onto the sensitive detector area. The implementation of the magnetic field map of the FOPI magnet[2] allows for the simulation of particle tracks. Particles from secondary physics processes in the shielding and other components were tracked as well. All particles which pass a sensitive area are detected along with their physical state. This simulation is referred to again in chapter 8, where the achievable precision of the P2 Experiment is derived from the particle rates and the Cherenkov detector response simulation. Figure 4.11 shows the resulting particle rate distribution at the location of the detector plane.

The electrons directly originating from an elastic electron-proton scattering process in the target are shown in two different shades of purple distinguishing between those scattered in the laboratory angle range of interest $\Theta_L \in [25°, 45°]$ and those outside this range. Secondary particles produced when these elastically scattered particles interact with the experimental hardware also carry asymmetry information. The dashed lines indicate the optimal placement and length of the detector. The signal electrons are focussed onto this ring shaped area with inner radius 450 mm and outer radius 900 mm. The drastic decrease of photonic background at $r = 450$ mm is due to the photon shield. The Møller electron background is constrained closer to the beam line.

The area to cover by the electron-sensitive part of the detector is therefore a ring with inner radius 450 mm and outer radius 900 mm. As the light read-out and other delicate electronics have to be placed behind shielding and further away from the beamline, an additional length of 200 mm has to be bridged by a light guide.
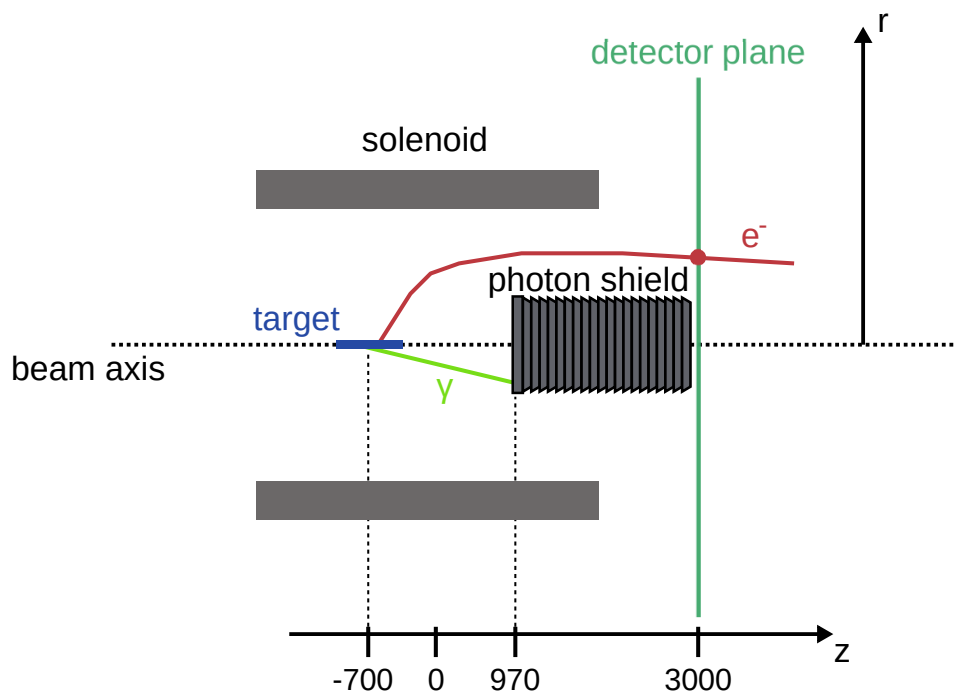
[2]Provided by the FOPI group at GSI

FIGURE 4.10: Draft of the geometric configuration used in the GEANT4 particle tracing simulation. Particles from processes in the target as well as secondary particles are detected and recorded along with their location, momentum, and energy when passing through the detector plane at $z = 3000\,\text{mm}$.

A range of different solutions for this light guide was considered, but detector prototype tests (5.5.5) showed that the best light yield is achieved by using fused silica – the same material as the active Cherenkov medium – as light guide.

4.2.3 Detector Element Geometry

The detector ring resulting from the considerations discussed in the previous section will be segmented into individual detector modules. The light read-out is going to take place at the end of the quartz glass bar facing away from the beam line. The width of each element is determined by the dimensions of the light sensors used and the practicability of processing the fused quartz into the specific shape. The P2 Experiment is going to use photomultiplier tubes with a diameter of three inches. The photocathodes of those devices are usually photo-sensitive over a diameter of approximately 65 mm. The following three subsections are going to address the geometry of the individual detector ring elements.
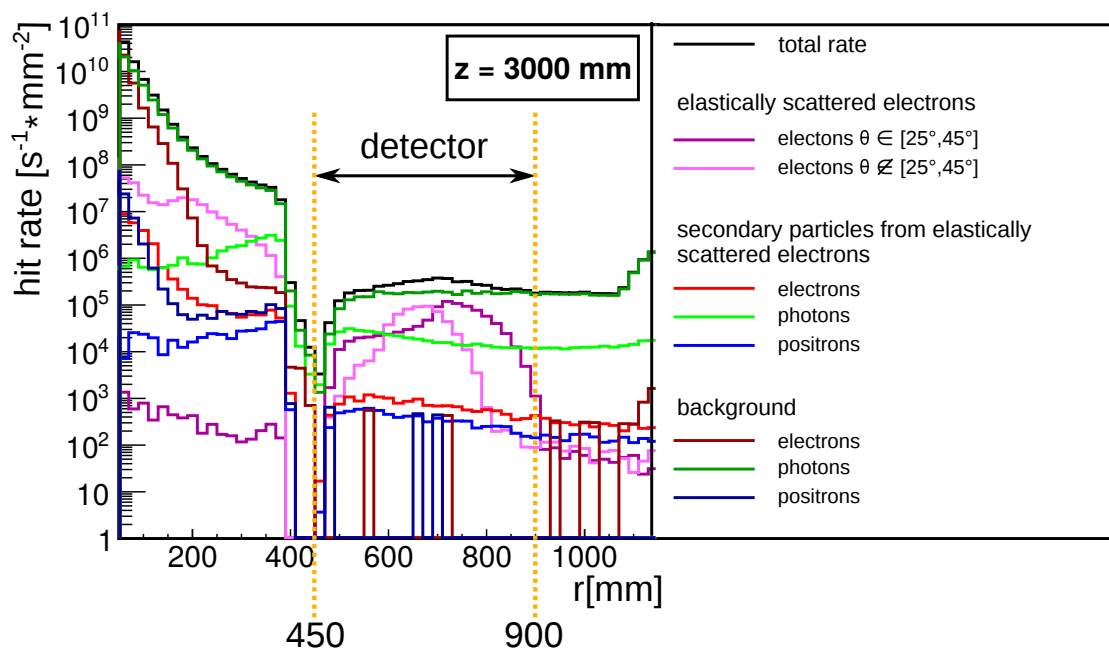
FIGURE 4.11: Particle rate distribution in the detector plane (see figure 4.10) from GEANT4 simulation. Positrons, protons, and neutrons are not included for better clarity. A plot including these particles can be found in [25]. The region to cover by the sensitive area of the Cherenkov detector elements is indicated by the orange dashed lines.

4.2.3.1 Tapered Bars for Optimal Ring Coverage

The first designs of the Cherenkov detector modules used cuboid quartz bars, but as the planning of the experiment proceeded, it became clear, that gaps and overlaps of the bars had to be avoided or minimised. The pictures in table 4.2 show two different solutions with cuboid bars accepting gaps and overlap respectively and in the third column the final design with tapered quartz bars. Values for the relative coverage of the ring, gaps and overlapping surface are listed below the pictures.

By using tapered quartz glass pieces gaps can be limited to 13.9% while totally avoiding overlap. The tapered quartzes are much harder to cut and polish and therefore almost twice as expensive as the cuboid variants, but the advantages outweigh, because lost signal due to gaps has to be compensated by elongation of the data taking time. Double detection of particles in the case of overlapping detector modules on the other hand causes additional complication to the data analysis.
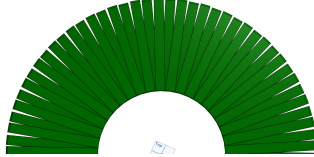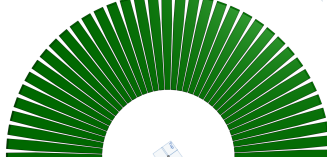
Case A	Case B	Case C
Geometry: Cuboid	Cuboid	Tapered
No of bars: 39	82	72
Coverage [%]: 62.2	100	86.1
Overlap [%]: 0	47.1	0

TABLE 4.2: Three different detector module geometry and arrangement solutions. In Case A and B cuboid quartz bars are used. As a result large gaps or overlapping areas have to be put up with. In Case C the bars are partly tapered leading to a reduction of the gaps while overlap is totally avoided.

4.2.3.2   Internal Reflections to Guide the Light to the PMT

The Cherenkov angle and critical angle of total internal reflection for fused silica are plotted in figure 4.12. For a relativistic electron the opening angle of the generated light cone is slightly larger than the angle of total internal reflection leading to a trapping of the Cherenkov light in the module. The phenomenon of total internal reflection at optical boundaries between silica and air is also used in optical fiber technology and in DIRC (Detection of internally reflected Cherenkov light) detectors [42] and is an effective way to guide the Cherenkov light towards the location of light read out. For electrons hitting the synthetic quartz surface roughly orthogonally as shown in figure 4.13 the light is contained in the quartz. While the end of the fused silica bar facing towards the beamline will be covered by a highly reflective aluminium mirror, the end facing the photosensor has an optical outlet in form of a 45° cut applied to it. As sketched in figure 4.13 the light can exit the quartz at this optical outlet.

The photograph of a fused silica bar used for one of the P2 detector prototypes in figure 4.14 shows how the beam of a laser pointer is internally reflected at the optical surface between silica and air. Of course the effect is only visible because the quartz has suboptimal surface finish and was dusty at the time of picture taking. Quartz is a brittle material and thus prone to chipping —especially at the edges— during the polishing procedure. It is thus necessary to apply a protective chamfer prior to polishing. The photograph shows that substantial amounts of light can exit the bar at the chamfers in the back. The chamfers have to be minimised to a degree that they vanish during the polishing process.

We can deduce that in order to efficiently guide the Cherenkov light towards the PMT the quartz glass bar has to have
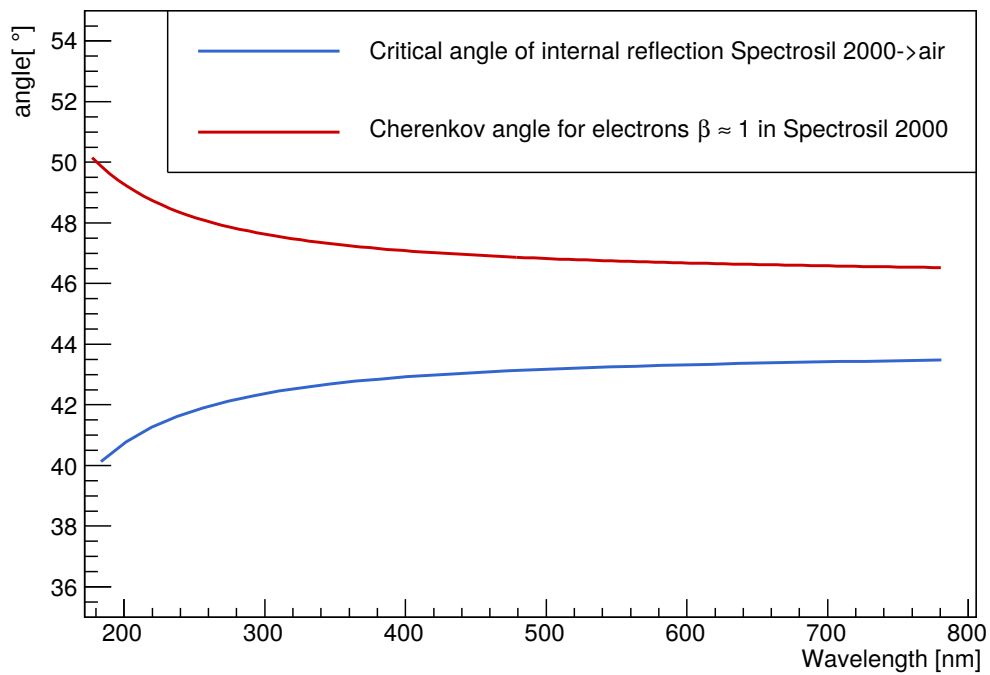
FIGURE 4.12: Cherenkov angle for relativistic electrons in fused silica and the critical angle of total internal reflection at the boundary of quartz glass and air.
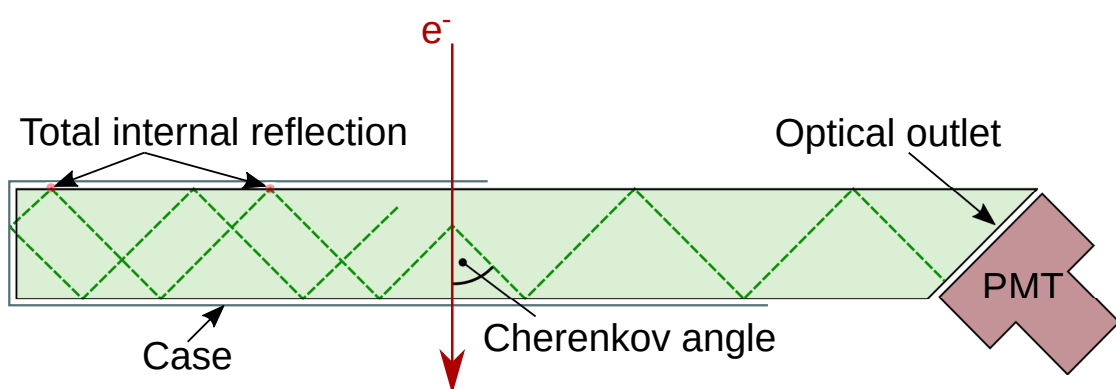
FIGURE 4.13: Internal reflection at the two plane parallel sides of the fused silica bar for an electron traversing the quartz orthogonally to those faces. One end of the quartz is covered by a highly reflective case, while the one facing the photo-sensor is open and has an optical outlet in form of a 45° cut applied.
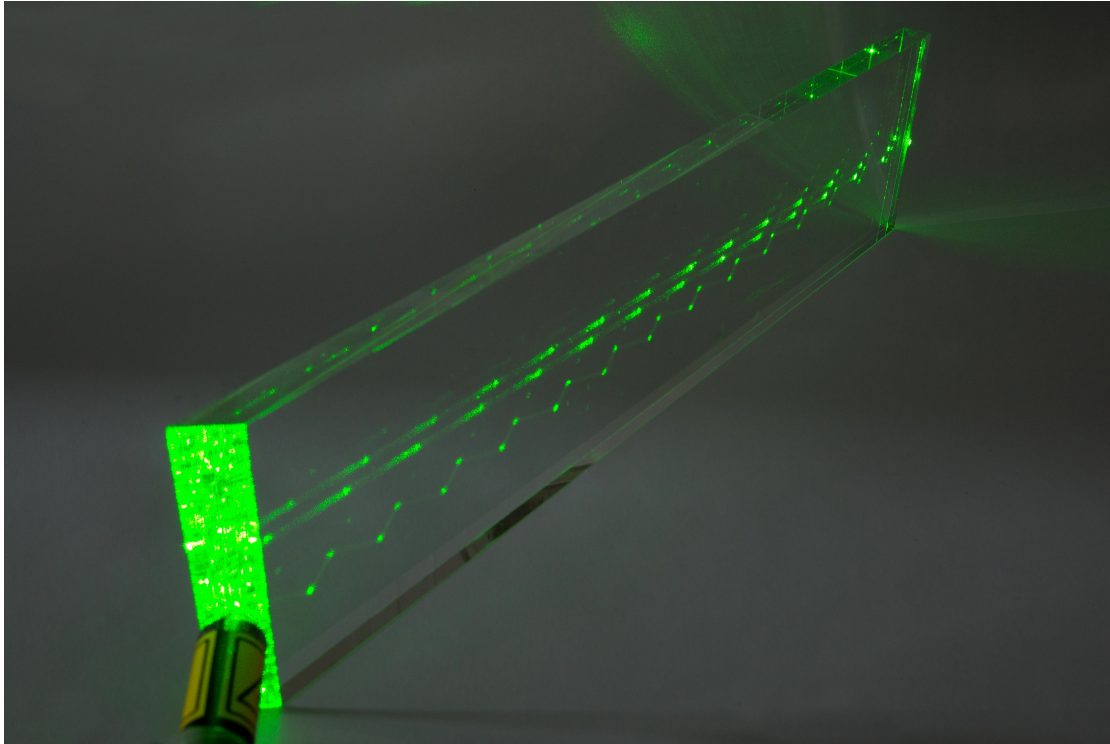
FIGURE 4.14: Laser pointer beam reflections at the optical boundary between quartz and air. Surface finish and cleanness are suboptimal so that large enough fractions of the light are scattered there making the effect of internal reflection visible. Additionally one can see that light can exit the quartz at the applied protective chamfers in the back. Camera Model: Canon EOS 5D Mark IV on a tripod, aperture value: f/18.0, exposure time: 30 s, ISO speed rating: 200, focal length: 35 mm

- plane parallel surfaces orthogonal to the incident electron momentum

- well polished surfaces

- an optical outlet where the PMT is attached

- minimal or no protective chamfers

4.2.3.3   Number of Cherenkov Detector Modules

In order to being able to record and account for beam and target fluctuations, eight luminosity monitors (LUMIs) are going to be installed upstream of the Cherenkov detector and closer to the beam line. As it is favourable to cover an integer number of quartz bars with each LUMI, the detector ring should consist of a number of elements divisible by eight. Another reason for choosing an even number of detector elements are azimuthal asymmetries, which occur as a result of inaccurate beam spin orientation. This effect cancels out when summing over the signals of two
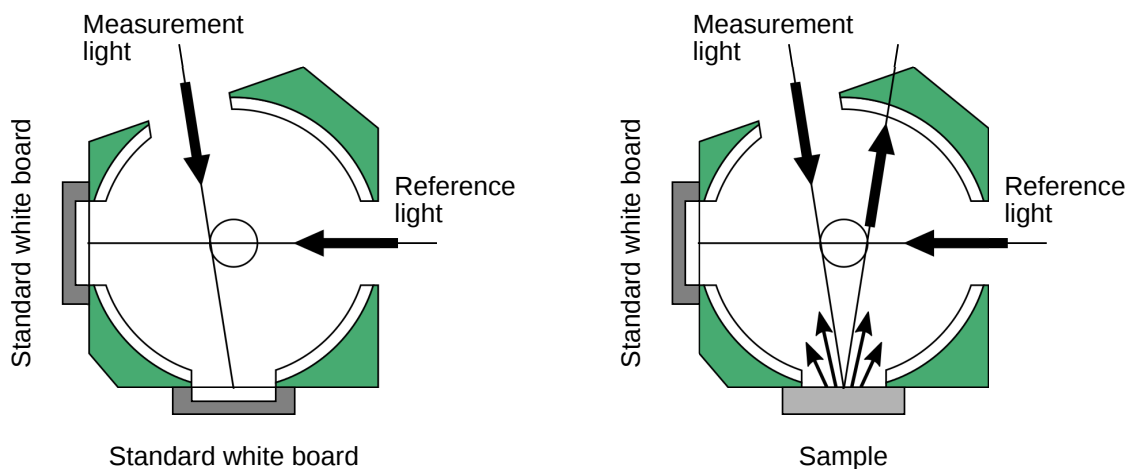
FIGURE 4.15: Spectrophotometer integrating sphere setup for reflectivity measurements

opposing detector elements. The ring therefore has to be symmetric with respect to 180° rotations about the beam axis, which can be achieved with even numbers of identical detector elements. The P2 detector ring is going to be segmented into 72 individual detector elements.

4.2.4 Reflector Materials

The fused silica bars need to be cased and protected from ambient light. Even though the containment of Cherenkov light in the detector mainly takes place by internal reflections at the surface between fused silica and air it is advisable to use a highly reflective material for the housing. This will help contain even the small amounts of light that exit the quartz for example at surface imperfections or chipped edges.

The reflectivity of several materials has been measured in the spectrophotometer. The measurement principle is very similar to the transmission measurement explained in section 4.2.1.1. Instead of placing the sample in front of the entrance window of the integrating sphere, the area of the integrating sphere —where the sample beam hits first— is replaced by the sample as shown in figure 4.15. The obtained reflectivity values are thus always relative to the reflectivity of the standard white board —in our case barium sulfate.

Two of the candidates for reflective casing were diffuse reflectors. Tyvek[3] is a nonwoven fabric of polyethylene fibers. It is known to be tear resistant and withstand high radiation doses as well as other physical and chemical stress. Millipore

---

[3]Registered trademark of DuPont de Nemours, Inc.
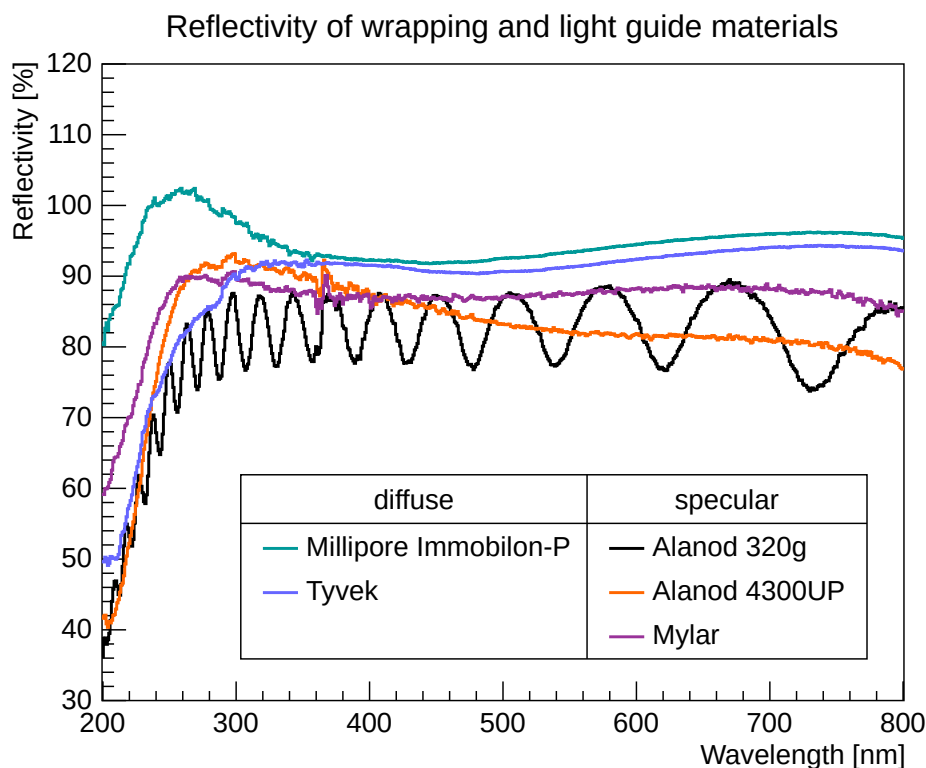
FIGURE 4.16: Reflectivity of potential wrapping materials measured in a Shimadzu spectrophotometer.

Immobilon-P is a thermoplastic fluoropolymer membrane designed for the immobilisation of aminoacids and protein samples for bio-molecular examination. It shows the best reflectivity in the UV range of all materials in the test. Its reflectivity between 230 nm and 260 nm even exceeds the reference standard of barium sulfate, which according to the manufacturer of the integrating sphere can be taken to be 100%[4].

Alanod 320g exhibits periodical variations of the reflectivity spectrum, which are attributed to interference effects due to surface coating. This property disqualifies the material from being used in the P2 detector.

Due to their very good reflectivity, especially in the ultraviolet range, Millipore Immobilon-P, Alanod 4300UP, and Mylar foil were chosen for further examination in the P2 detector prototype tests at MAMI.

---

[4]See manufacturer's instructions: https://www.shimadzu.com/an/service-support/technical-support/analysis-basics/fundamentals-uv/integratingspheres.html
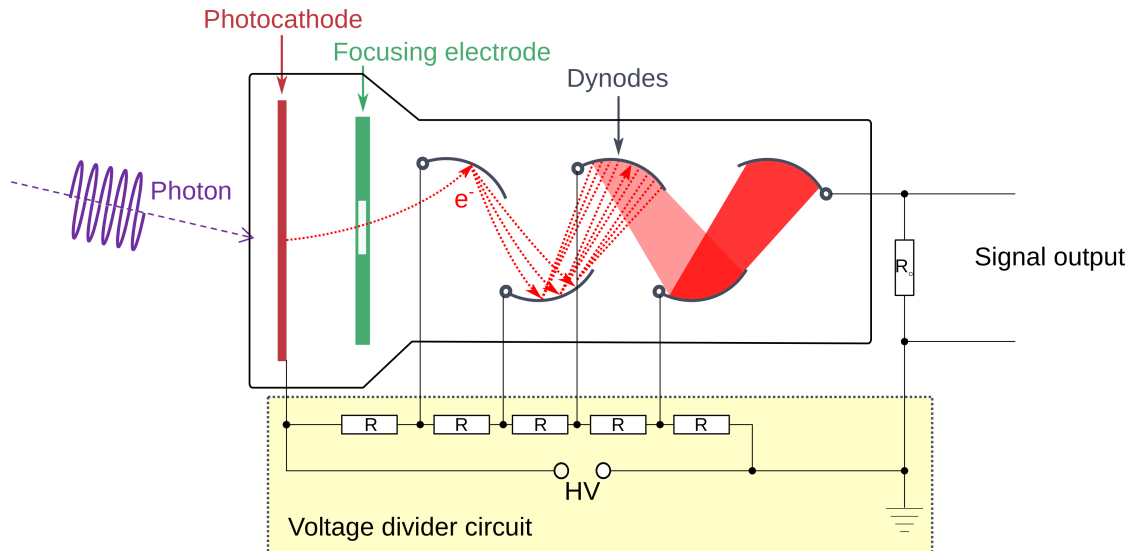
FIGURE 4.17: Scheme of a photomultiplier tube

4.2.5   Photon Detection

The light produced inside the Cherenkov medium has to be read out and converted into electric signals in order to obtain processable and analysable data. A commonly used device for this purpose is the classical vacuum photomultiplier tube (PMT). It takes advantage of the photoelectric effect to release electrons from a cathode material and of impact ionization to amplify the electric signal, when the free electrons are accelerated by a high voltage and hit the dynodes inside the evacuated tube, where additional electrons are emitted and an avalanche effect is started.

Figure 4.17 is a schematic picture of the construction of a photomultiplier tube according to [43]. Photons enter the tube through the front window and hit the photo sensitive cathode. The photocathode material is chosen in order to minimise the work function to remove electrons from it and to maximise the quantum efficiency, which is defined as the ratio between the electrons emitted from the cathode and the number of photons absorbed, for the wavelengths one wishes to detect:

$$QE(\lambda) = \frac{N_e}{N_\gamma(\lambda)} \tag{4.13}$$

Figure 4.18 shows the spectral quantum efficiencies of several PMT candidates for Cherenkov light detection in the P2 detector.
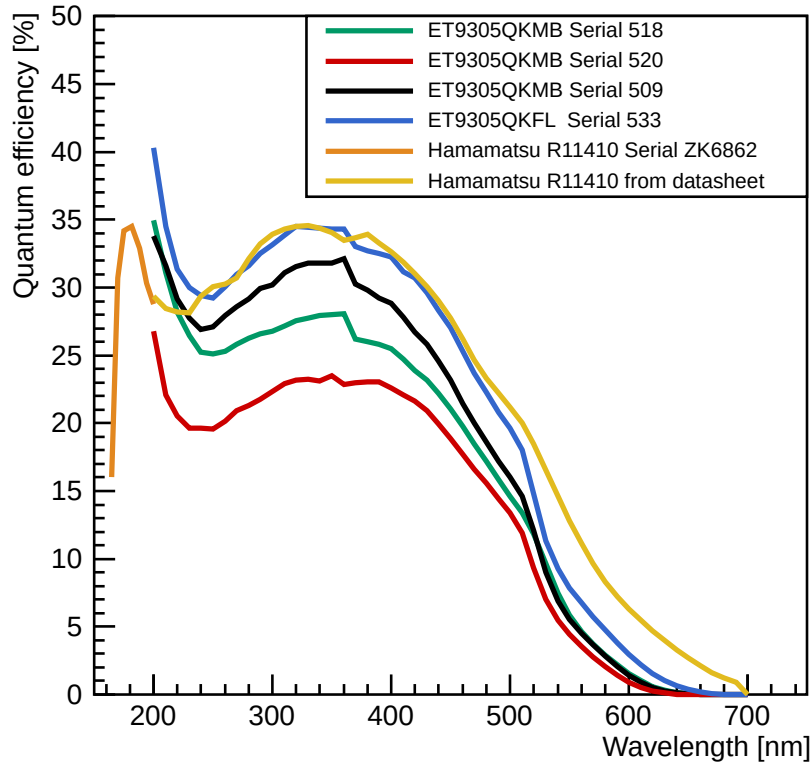
FIGURE 4.18: Quantum efficiencies (QE) of potential PMTs for the P2 main detector. These models are all designed for UV light detection.

The PMTs by Electron Tubes (ET)[5] all came with measured spectral QE data for each individual specimen in the wavelength range from 200 nm to 700 nm. For our Hamamatsu model the individual QE was specified only in the wavelength range 160 nm to 200 nm. The data above 200 nm was taken from the model's data sheet and is thus only an average value for the model. All of these models are designed for UV light detection. They have quartz glass windows for high transparency and bi-alkali photocathodes for high QE. Specimen of these PMT models have been tested at the MAMI beam in 2015.

4.3 Summary of Preparatory Studies for the Prototype Design

During the first stage of design considerations for the P2 main detector it was decided to use a Cherenkov detector. As a Cherenkov medium fused silica has many

---

[5]ET Enterprises, Ltd, Uxbridge, UK

positive traits, both concerning the Cherenkov light generation and its transmission and containment inside the material. In addition, the material is exceptionally radiation hard. The hardware of the P2 Experiment is going to be exposed to extreme levels of radiation. For the same reason, the choice of light sensors is limited to classical photomultipliers. For the detection of Cherenkov light, special UV sensitive PMTs are needed. Resulting from the preparatory material studies and considerations explained in the preceding sections of this chapter, we designed several detector prototypes and tested them at the MAMI beam for their signal response to relativistic electrons. One prototype was also tested at the A2 facility to measure its signal yield to photons, which occur as background in the P2 Experiment. These prototype tests are the subject of the following chapter.

Chapter 5

Prototype Detector Tests

After having limited the choice of materials and geometry of the P2 detector by means of preparatory material studies and considerations as described in chapter 4, a variety of detector prototypes was developed and built. These were tested in the MAMI electron beam for functionality and signal yield. The response of these prototypes to electrons hitting them at a range of impact angles and positions was analysed and compared. In the first section of this chapter the signal yield requirement for the detector to a single electron incidence is derived.

The subsequent sections describe measurements of these protoypes at the X1-facility in MAMI hall B and how the data was acquired and analysed.

The various detector prototypes were rotated and translated in the MAMI beam in order to examine their response to the exposure to electrons hitting them at different angles and at different locations. This procedure is described in section 5.4.

This method of scanning the detector response at various incidence angles and locations was employed for the comparison of the P2 detector module prototypes. These prototypes differed in geometry, materials and processing quality of the different parts. In order to find a suitable set of these parameters, single detector parts were varied and comparative measurement series were done. The results of a variety of such measurements is presented and discussed in section 5.5.

One of the prototypes was tested at the A2 real photon source to verify its supposed suppression of photonic background in the P2 Experiment. The beamtime at A2, the results and comparison with a GEANT4 simulation are subject of section 5.6.

5.1 Photoelectron Yield Requirement

In the P2 Experiment a PMT will be used to read out Cherenkov light generated in the fused silica bars. The experimental asymmetry A_{exp} will manifest itself in an asymmetry in the numbers of photoelectrons released from the PMT cathodes, which we will deduce from the anode current, which is the actually measured quantity. The asymmetry in the number of cathode electrons is:

$$A_{\text{exp}} = \frac{N_{\text{Pe}}^+ - N_{\text{Pe}}^-}{N_{\text{Pe}}^+ + N_{\text{Pe}}^-} \tag{5.1}$$

The statistical error

$$\Delta A_{\text{exp}} = \sqrt{\left(\frac{\partial A_{\text{exp}}}{\partial N_{\text{Pe}}^+} \Delta N_{\text{Pe}}^+\right)^2 + \left(\frac{\partial A_{\text{exp}}}{\partial N_{\text{Pe}}^-} \Delta N_{\text{Pe}}^-\right)^2} \tag{5.2}$$

follows from simple Gaussian error propagation. The expected number of photoelectrons is the product of the number of elastically scattered electrons N reaching the detector and the mean number $\bar{n}_{\text{Pe}}$ of photoelectrons per such event:

$$N_{\text{Pe}} = N \cdot \bar{n}_{\text{Pe}} \tag{5.3}$$

Its error is given by

$$\begin{aligned}
\Delta N_{\text{Pe}} &= \sqrt{(\bar{n}_{\text{Pe}} \cdot \Delta N)^2 + (N \cdot \Delta \bar{n}_{\text{Pe}})^2} \\
&= \sqrt{(\bar{n}_{\text{Pe}} \cdot \sqrt{N})^2 + \left(N \cdot \frac{\sigma_{\text{Pe}}}{\sqrt{N}}\right)^2} \\
&= \sqrt{N} \cdot \bar{n}_{\text{Pe}} \cdot \sqrt{1 + \left(\frac{\sigma_{\text{Pe}}}{\bar{n}_{\text{Pe}}}\right)}
\end{aligned} \tag{5.4}$$

where σ_{Pe} is the standard deviation in the photoelectron yield.

With the assumptions

$$\begin{aligned}
N^+ = N^- \quad &= N/2 \tag{5.5} \\
\bar{n}_{\text{Pe}}^+ = \bar{n}_{\text{Pe}}^- \quad &= \bar{n}_{\text{Pe}} \tag{5.6} \\
\sigma_{\text{Pe}}^+ = \sigma_{\text{Pe}}^- \quad &= \sigma_{\text{Pe}} \tag{5.7}
\end{aligned}$$

equation 5.2 becomes

$$\Delta A_{\text{exp}} = \frac{1}{\sqrt{N}} \sqrt{1 + \left(\frac{\sigma_{\text{Pe}}}{\bar{n}_{\text{Pe}}} \right)^2} \qquad (5.8)$$

The term $\sigma_{\text{Pe}}/\bar{n}_{\text{Pe}} := \alpha$ is due to additional variation in photoelectron count caused by showers inside the quartz. This so-called excess noise enlarges the asymmetry uncertainty and may become critical when the light collection and quartz geometry are suboptimal. In order to meet the P2 precision goals, we demand that α may not exceed 1%:

$$\sqrt{1 + \alpha^2} < 1.01 \qquad (5.9)$$

Compensating for this value by means of improvement of the statistical error by the same factor:

$$\sqrt{N'} = 1.01\sqrt{N} \qquad (5.10)$$

would then require an additional data taking time of 2.1%, which amounts to 210 hours in the framework of the P2 Experiment.

Assuming Poisson statistics in the photoelectron distribution the standard deviation is $\sigma_{\text{Pe}} = \sqrt{\bar{n}_{\text{Pe}}}$ and the number of photoelectrons from the PMT cathode per electron incidence onto the quartz detector needs to be equal or larger than 50 in order to meet requirement 5.9.

5.2 Implementation of the Detector Tests at the X1 Test Site

From the preparatory studies and considerations a few detector geometries as well as materials for the detector components emerged as candidates for the final detector design. In order to assess the effect of different design options it was necessary to quickly exchange individual components of the prototype setup without affecting the other parts. Therefore a modular design approach was chosen. Figure 5.1 shows a CAD drawing of the mounting solution which allowed to assemble different combinations of quartz bars, wrapping materials, light guides and PMTs.

For the measurement of the response of a detector element to incident electrons the prototype was placed in the MAMI-beam at the X1 facility. A floorplan, which gives an overview of the first stages of the accelerator, is shown in figure 5.2. The X1 testsite is situated after MAMI's third racetrack microtron (RTM3), where
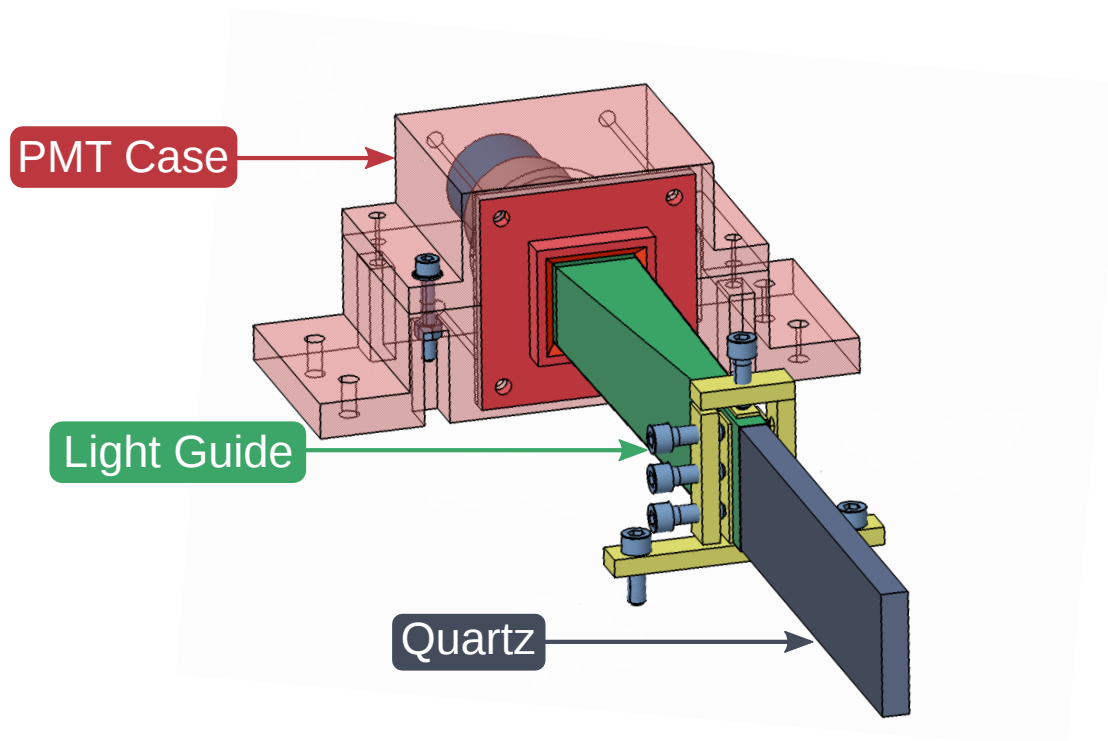
FIGURE 5.1: Prototype assembly mount. The mount allows to quickly exchange the individual detector components. An air light guide is inserted in this option.
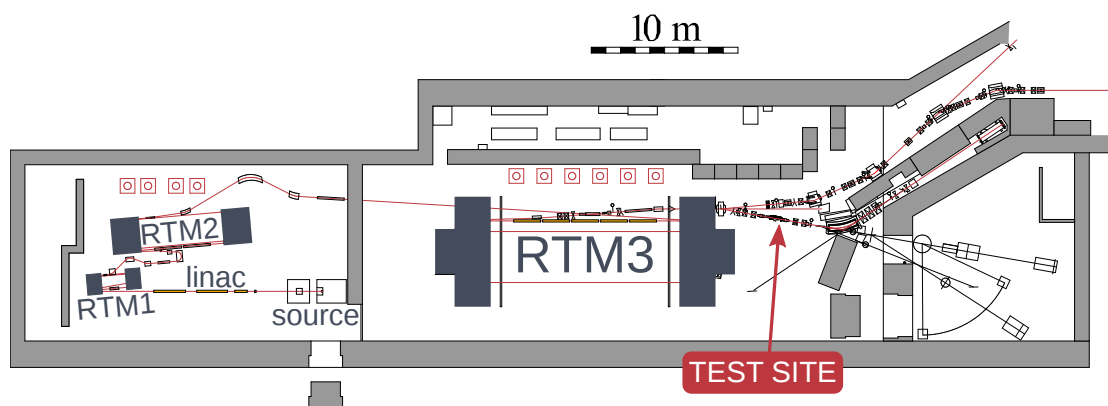
FIGURE 5.2: MAMI floorplan with prototype test setting in hall B.

the beam can reach energies up to 855 MeV. The detector prototype tests were done at this energy, eventhough the signal electrons in the P2 Experiment will fall below 150 MeV at the nominal energy of the MESA beam. As we operate in the ultrarelativistic regime for electrons, the Cherenkov light yield is in good approximation independent of the actual energy[1]. A piece of beam line was taken out and an aluminium vacuum window of 200 µm thickness was placed on the end flange of the beam pipe.

---

[1]This is illustrated in figure 7.24
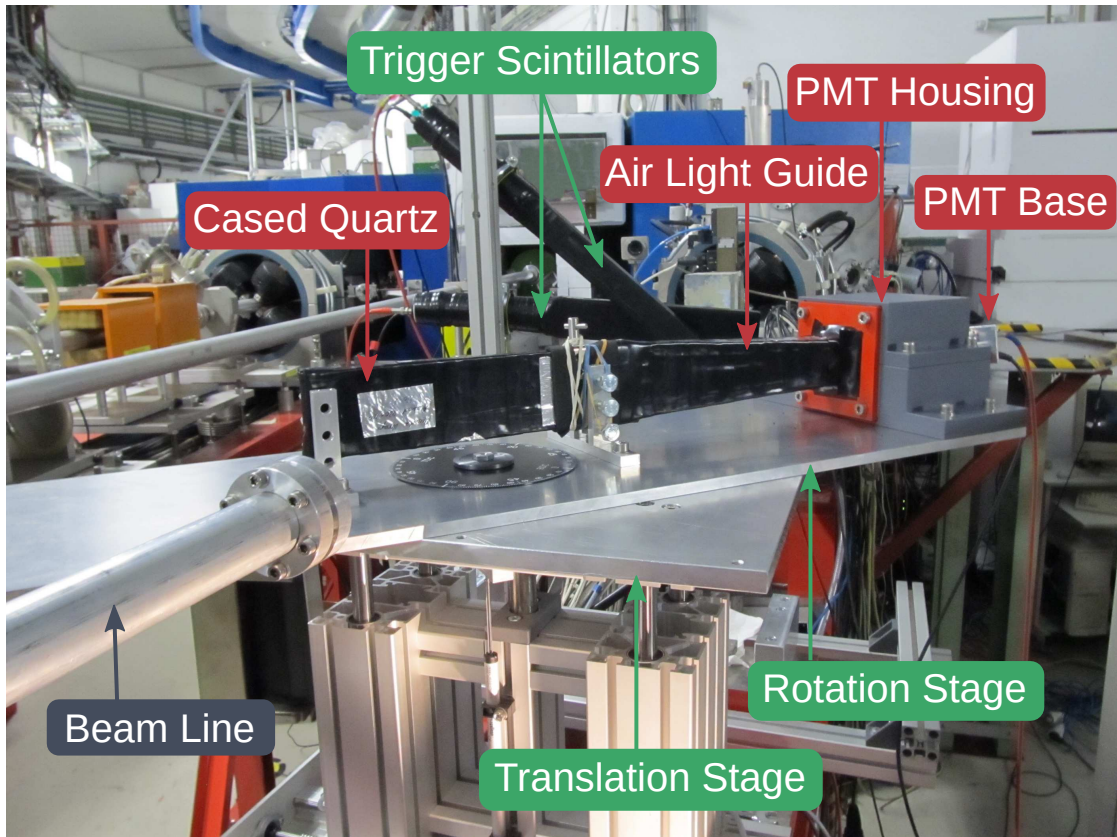
FIGURE 5.3: Photograph showing a P2 detector prototype test implementation in MAMI hall B. The detector prototype is aligned in the electron beam and mounted on a translation and rotation stage allowing the variation of the electron beam incidence angle and location onto the quartz bar. Two trigger scintillation detectors serve as gate for the quartz detector signal measurement.

The quartz Cherenkov detector was mounted onto a remote control translation and rotation stage 70 cm (45 cm in another beamtime) downstream from the vacuum window, and two scintillator detectors were placed another 80 cm down. They were aligned in a way that a beam electron passes through all three of them causing coincident signals. This allows the usage of the scintillator signals as measurement gates in order to suppress background signals from other sources. Figure 5.3 is a photograph of this setup.

A scheme of the data acquisition system is shown in 5.4. In the case of an electron passing through the quartz, Cherenkov light is generated, which ultimately causes an electric signal from the PMT. A charge-to-digital converter (CAEN[2] V965 QDC) is used to quantify this analogue signal by integrating the released charge over a specific time (gate). The output of this QDC is a number (channel) which is in good approximation linear to the charge of the PMT signal. The scintillator detectors served as triggers for the QDC. As depicted in figure 5.4 their signals are fed into a logic unit after passing a constant fraction discriminator. The QDC

---

[2]CAEN S.p.A., Via Vetraia, 11, 55049 Viareggio (LU), Italy
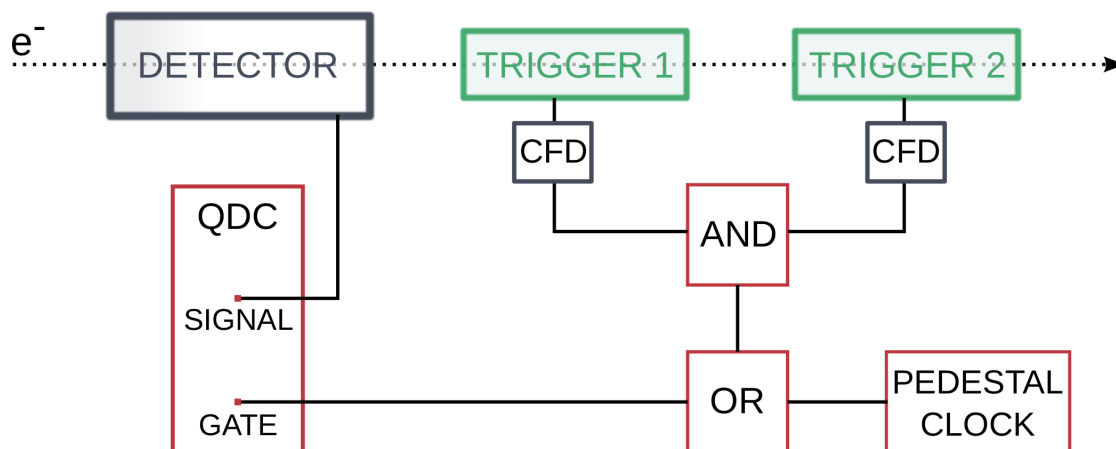
FIGURE 5.4: Scheme of the data acquisition circuit with prototype detector at the signal input of the QDC and a coincidence of two trigger scintillators or a clock as gate.
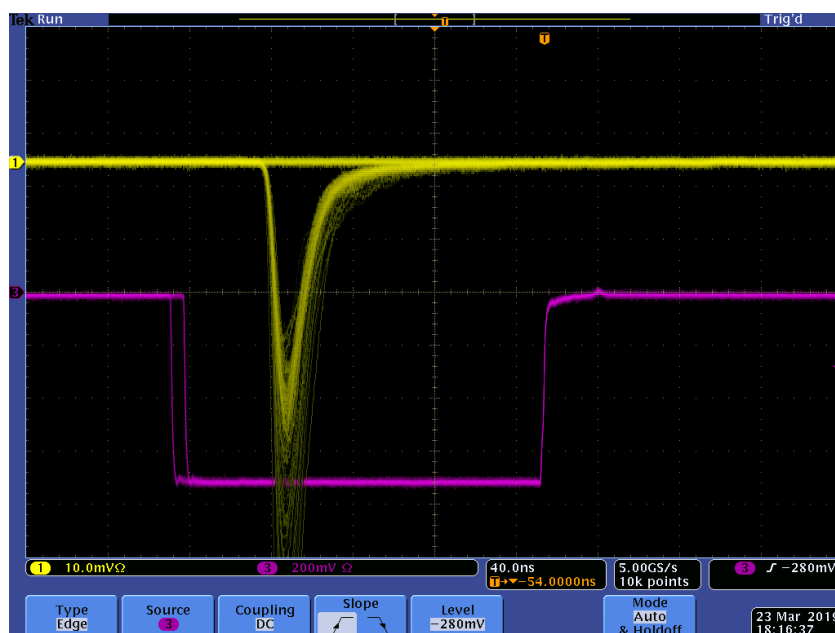
FIGURE 5.5: Oscilloscope showing timing of QDC gate and Cherenkov detector signal. The gate was provided by a coincidence of two trigger scintillators in line with the quartz detector. Timing was adjusted by means of delay cables.

gate is open if either both triggers deliver a signal or a pedestal clock does. The clock causes the gate to open at times, which are uncorrelated with the electron events, in order to record the noise level which appears as a pedestal peak in the QDC histograms. Timing was done by visualising both gate and raw signal from the Cherenkov prototype detector with an oscilloscope and synchronising them by use of delay cables. A picture of the final timing for the measurements during beamtime 03/2019 in shown in figure 5.5. For data taking the P2 Cherenkov detector prototype was then plugged into channel 00 of the CAEN V965 QDC.

During each gate the QDC channel number corresponding to the integrated charge is written into a histogram. QDC spectra were recorded over a measurement time of typically $180\,\mathrm{s}$ or $300\,\mathrm{s}$ at beam rates between $f_\mathrm{B} \in [2\,\mathrm{kHz}, 4\,\mathrm{kHz}]$ resulting into an approximate number of $n_\mathrm{m} \in [5\cdot10^5, 3\cdot10^6]$ events per measurement run. The number of QDC histogram entries is the sum of these events and the pedestal entries.

5.3 Analysis of the Detector Response to Electrons

Figure 5.6 is a typical data example from a measurements run of a P2 detector prototype test at the MAMI beam. This QDC histogram shows the number of counts in each histogram channel. The aim of analysing the histograms is to extract the expected number of photoelectrons emitted from the PMT cathode (N_Pe) as a result of an electron incidence. This is not directly possible, because even though the QDC channels are ideally in linear relation to N_Pe they are not calibrated. The electrons from the cathode are amplified by the avalanche effect at the PMT's dynodes. In the following a method to evaluate the histograms with respect to N_Pe that does not require the knowledge of amplification factors and QDC calibration will be derived.

The QDC histogram 5.6 shows two distinct peaks. The pedestal can be characterised by a Gaussian distribution. For the signal peak, a more sophisticated method is needed.

5.3.1 Extraction of the Number of PMT Cathode Electrons by Means of a Landau-Gauss Fit

The signal peak in 5.6 has a noticeable tail to higher channels. This can be explained by the presence of secondary charged particles that cause Cherenkov light in addition to the primary beam electrons. In order to characterise each measured QDC spectrum, we apply a fit function to the signal peak. It consists of a convolution $C_\mathrm{LG} = l \otimes g$ of a Gaussian g, which describes purely statistic fluctuations and a Landau distribution l to account for the tail.

In the context of this thesis all numerical data analysis was performed with programs written in C++ using the ROOT software framework developed by CERN [44].
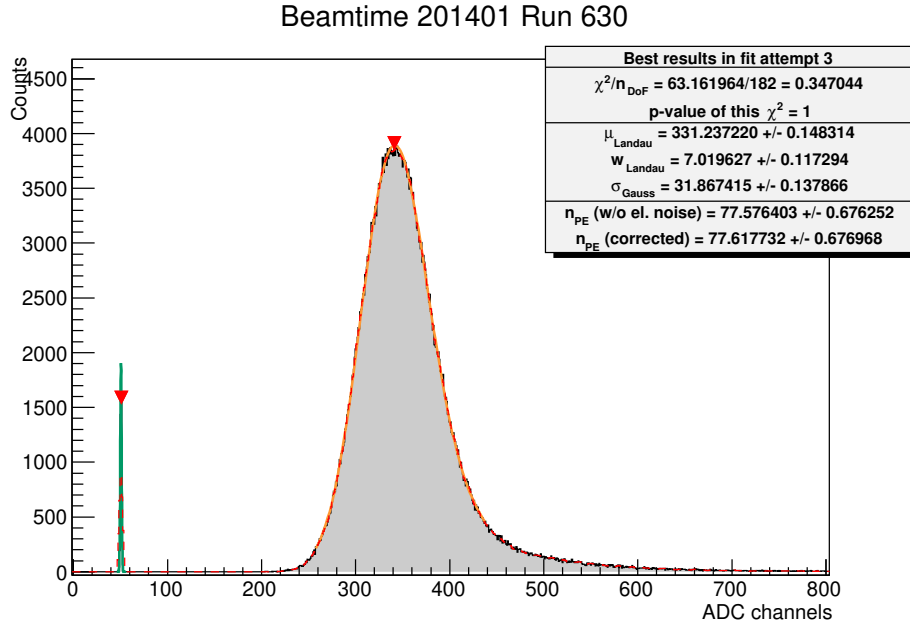
FIGURE 5.6: Example QDC histogram from MAMI beamtime 01/2014. Quartz: Suprasil 2A geometry I, 10 mm thick; Alanod wrap; PMT: ET9305QKMB serial number 518; electron incidence: 0° at horizontal center and vertical center of the amorphous quartz bar.

In its original form, the Landau density function

$$\Phi(x) = \frac{1}{2\pi i} \int_{c+i\infty}^{c-i\infty} e^{xs+s\ln s} ds \tag{5.11}$$

has its maximum value at $x_0 = -0.22278$.

The generalisation is

$$l(x) = \frac{1}{\xi}\Phi(\lambda) \tag{5.12}$$

where $\lambda = (x - \mu)/\xi$ contains the width parameter ξ and the position parameter μ. The ROOT software framework uses a numerical parametrisation from the CERNLIB library to approximate this function.

The convolution of the Landau density function and a Gaussian

$$C_{\mathrm{LG}} = l \otimes g = \int_{-\infty}^{+\infty} l(x-t)g(t)dt \tag{5.13}$$

depends on 4 parameters:

- ξ: The Landau width parameter

(a) Total integral varied

(b) Landau width parameter varied

(c) Position parameter varied

(d) Gaussian smearing varied
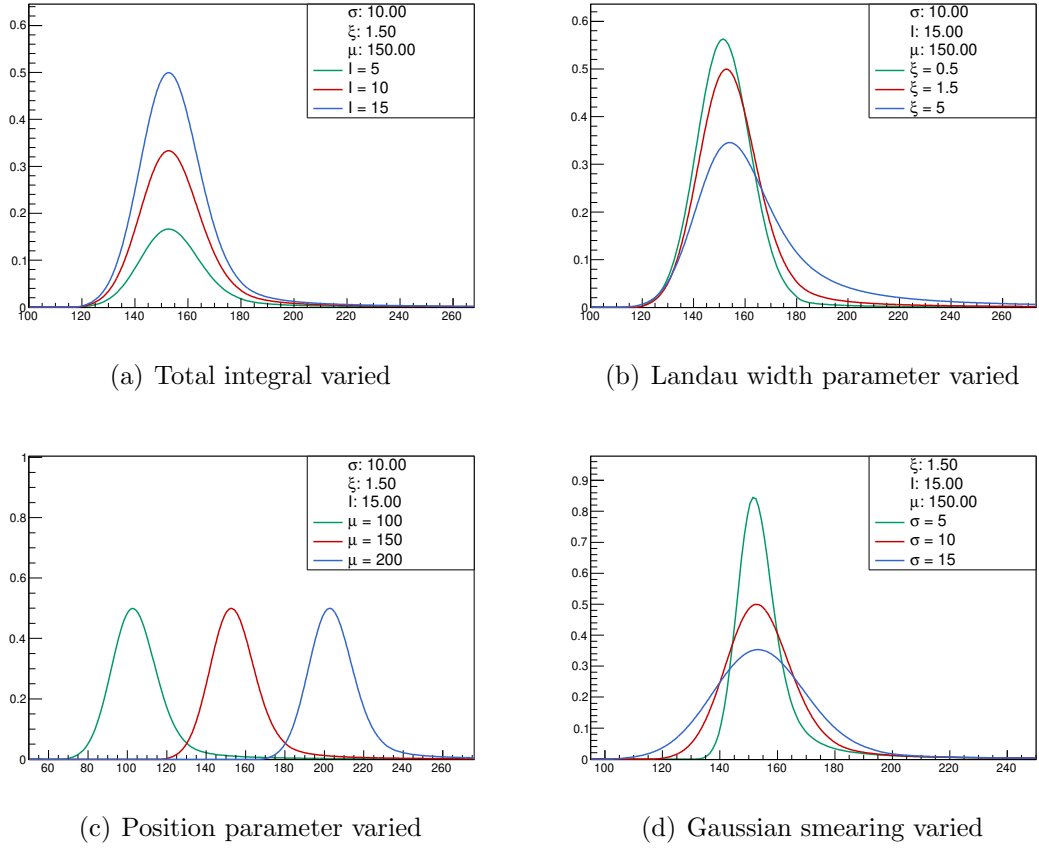
FIGURE 5.7: Effect on the Landau-Gauss distribution when individual parameters are varied

- μ: The position parameter, where the distribution reaches its most probable value

- I: The total area, which is the product of the integrals of the Gaussian and the Landau distributions, and

- σ_{G}: The Gaussian smearing.

Figure 5.7 demonstrates the effect of the variation of individual parameters separately, while all other parameters in each plot are fixed.

The aim of fitting a Landau-Gauss convolution to the measured QDC histograms is to extract the standard deviation σ_{G} of the Gaussian distribution and the most probable value of the convolution (μ). Both these values have to be corrected for electronic offsets and noise by subtracting the pedestal position and width respectively:

$$\mu_{\mathrm{true}} = \mu - \mathrm{Ped} \qquad \text{and} \qquad \sigma_{\mathrm{true}} = \sqrt{\sigma_{\mathrm{G}}^2 - \sigma_{\mathrm{Ped}}^2}$$

where Ped is the offset in the signal electronics and σ_{Ped} is the smearing of the pedestal.

The QDC output number (channel) is in good approximation linear to N_{Pe}. This results into the relation

$$\mu_{\mathrm{true}} = k \cdot N_{\mathrm{Pe}} \qquad (5.14)$$

between the pedestal corrected position parameter and N_{Pe} with the calibration constant k, which depends on the signal amplification in the PMT and the relation between QDC input charge and output channel.

Assuming Gaussian statistics σ_{true} is the manifestation of purely statistic fluctuations of the detector prototype signal. As σ_{true} is the signal width in terms of QDC channels, it is connected to the inverse square root of the number of photoelectrons via the calibration factor k:

$$\sigma_{\mathrm{true}} = k \cdot \sqrt{N_{\mathrm{Pe}}} \qquad (5.15)$$

It follows from equations 5.14 and 5.15 that

$$N_{\mathrm{Pe}} = \frac{(\mu - \mathrm{Ped})^2}{\sigma_{\mathrm{G}}^2 - \sigma_{\mathrm{Ped}}^2} = \frac{\mu_{\mathrm{true}^2}}{\sigma_{\mathrm{true}}^2} \qquad (5.16)$$

where the calibration factor k has cancelled out allowing the extraction of N_{Pe} from the QDC histograms without the knowledge of PMT amplification and QDC calibration.

5.3.2 Error Calculation

The errors of the raw fit parameters μ, σ_{G}, Ped, and σ_{Ped} are determined internally by the MINUIT fit algorithm employed by the ROOT analysis framework. Since the parameters μ and σ_{G} of the signal peak as well as the pedestal position and width result from the same fits to the histogram, their uncertainties $\sigma(\mu)$ and $\sigma(\sigma_{\mathrm{G}})$ are correlated. The same holds true for Ped and its standard deviation σ_{Ped}. Therefore the covariances $\sigma(\mu, \sigma_{\mathrm{G}})$ and $\sigma(\mathrm{Ped}, \sigma_{\mathrm{Ped}})$ have to be included into the error calculation, resulting in the covariance matrix

$$\Sigma = \begin{pmatrix} \sigma(\mu)^2 & \sigma(\mu, \sigma_{\mathrm{G}}) & 0 & 0 \\ \sigma(\mu, \sigma_{\mathrm{G}}) & \sigma(\sigma_{\mathrm{G}})^2 & 0 & 0 \\ 0 & 0 & \sigma(\mathrm{Ped})^2 & \sigma(\mathrm{Ped}, \sigma_{\mathrm{Ped}}) \\ 0 & 0 & \sigma(\mathrm{Ped}, \sigma_{\mathrm{Ped}}) & \sigma(\sigma_{\mathrm{Ped}})^2 \end{pmatrix} \qquad (5.17)$$

with the variances of the fit parameters on the diagonal and the covariances between them in parenthesis in the off-diagonal matrix elements.

The covariance matrix of the derived quantities

$$N_{\text{Pe}} = \frac{(\mu - \text{Ped})^2}{\sigma_{\text{G}}^2 - \sigma_{\text{Ped}}^2} \tag{5.18}$$

$$\mu_{\text{true}} = \mu - \text{Ped} \tag{5.19}$$

is calculated using the Jacobian matrix

$$
J = \begin{pmatrix}
\frac{\partial N_{\text{Pe}}}{\partial \mu} & \frac{\partial N_{\text{Pe}}}{\partial \sigma_{\text{G}}} & \frac{\partial N_{\text{Pe}}}{\partial \text{Ped}} & \frac{\partial N_{\text{Pe}}}{\partial \sigma_{\text{Ped}}} \\
\frac{\partial \mu_{\text{true}}}{\partial \mu} & \frac{\partial \mu_{\text{true}}}{\partial \sigma_{\text{G}}} & \frac{\partial \mu_{\text{true}}}{\partial \text{Ped}} & \frac{\partial \mu_{\text{true}}}{\partial \sigma_{\text{Ped}}}
\end{pmatrix}
$$

$$
= \begin{pmatrix}
2\frac{\mu - \text{Ped}}{\sigma_{\text{G}}^2 - \sigma_{\text{Ped}}^2} & -2\sigma_{\text{G}}\frac{(\mu - \text{Ped})^2}{(\sigma_{\text{G}}^2 - \sigma_{\text{Ped}}^2)^2} & -2\frac{\mu - \text{Ped}}{\sigma_{\text{G}}^2 - \sigma_{\text{Ped}}^2} & 2\sigma_{\text{Ped}}\frac{(\mu - \text{Ped})^2}{(\sigma_{\text{G}}^2 - \sigma_{\text{Ped}}^2)^2} \\
1 & 0 & -1 & 0
\end{pmatrix}
$$

as

$$\tilde{\Sigma} = J\Sigma J^T \tag{5.20}$$

The resulting $2{\times}2$-matrix corresponds to a skew 1σ uncertainty ellipse around each data point in the μ_{true}-N_{Pe} coordinate frame. It is later used in the QDC channel calibration procedure presented in subsection 5.3.4 to account for the errors of both N_{Pe}, μ_{true}, and their correlation in a Monte-Carlo based approach.

During the analysis process it was evident that the values of the fit parameters as determined by MINUIT strongly depend on the chosen fit range. To quantify this effect each signal distribution was fitted numerous times varying both the upper and lower fit limit. The lower fit range was varied between $l_{\text{min}} \in [\mu - 2\sigma, \mu - 1.3\sigma]$ and the upper fit rage between $l_{\text{min}} \in [\mu + 1.3\sigma, \mu + 2\sigma]$, both in steps of 0.1σ. An additional error in N_{Pe} was obtained by determination of the variance of this parameter depending on the fit range.

5.3.3 Investigation of the High Voltage Dependence

The data analysis method described in section 5.3.1 has to prove to be independent of the photomultiplier gain and amplification. In order to verify this HV scans have been run in which the high voltage supply of the photomultiplier was systematically varied.
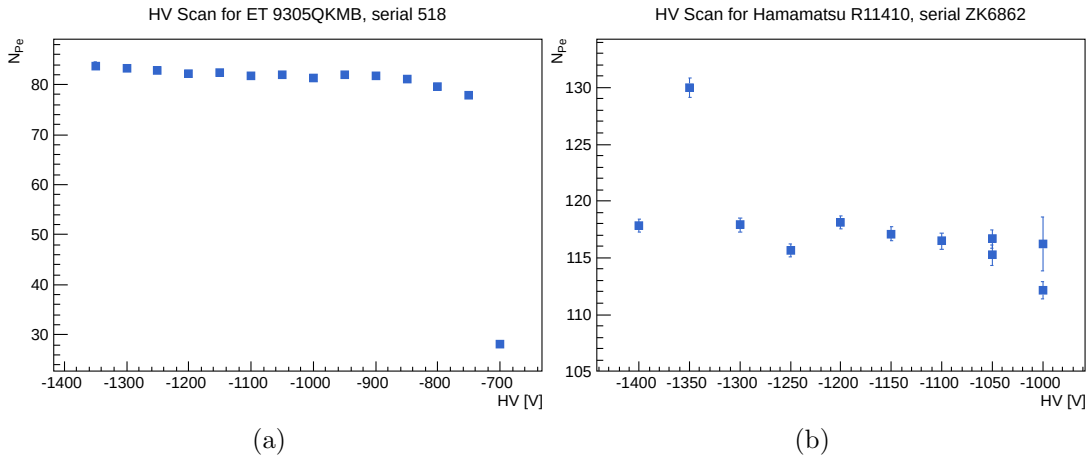
FIGURE 5.8: Number of photoelectrons N_{Pe} as determined by the statistical method explained in the previous section for various high voltages at two photomultipliers. The outlier in (a) shows that the PMT was operated below the critical high voltage supply necessary to achieve an avalanche effect.

The two plots in figure 5.8 show the results of such high voltage scans for the two photomultiplier tubes used for most beamtime runs. The corresponding graphs for all other PMTs used during the P2 prototype tests can be found in Appendix E.

The measurement series demonstrate that there is a plateau region, in which the reconstruction of the number of photoelectrons is independent of the amplification. Aside from the outlier at $-1350\,\mathrm{V}$ for the Hamamatsu PMT all data points in this region agree within well below 5%. This means that the determination of the number of photoelectrons emitted from the PMT cathode as a result of an electron event on the detector is in good approximation stable with regard to the high voltage supply. This demonstrates that the width of the signal peak in the QDC spectrum is — as assumed — dominated by the statistical uncertainty in the photoelectrons emitted from the cathode as a result of Cherenkov light incidence. Any additional noise would lead to a stronger widening of the peak and N_{Pe} as determined by equation 5.16 would increase with the high voltage supply.

For later data taking a high voltage value in the centre of this plateau region was chosen.

5.3.4 Calibration of the Charge-to-Digital Converter Channels

The number of photoelectrons N_{Pe} found by means described in 5.3.1 is prone to fluctuation depending on the choice of start values and fit range. The position of the most probable value of the distribution in the QDC spectrum on the other hand can easily be determined and is not subject to fitting failure. Assuming that
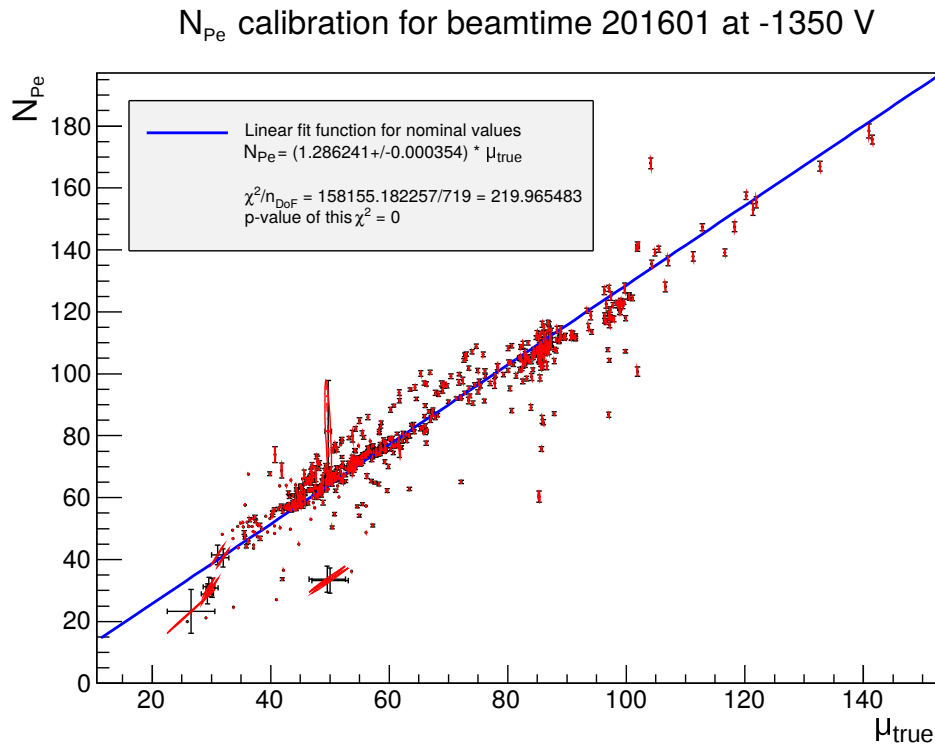
FIGURE 5.9: Linear regression of N_{Pe} and position parameter μ_{true} of runs 2 to 830 of beamtime 01/2016 as example of QDC channel calibration. Note that zero is suppressed on the x-axis.

the PMT output signal and QDC channels are linear with respect to the number of photoelectrons we can attempt to perform a calibration of the QDC channels with respect to N_{Pe}. Figure 5.9 shows the number of cathode photoelectrons obtained by the method described in 5.3.1 plotted against the peak position parameter μ for measurements taken at beamtime 01/2016 using a Hamamatsu R11410 (Serial ZK6862) with a high voltage supply of $-1350\,\mathrm{V}$. We can see that the data points follow a linear behaviour that allows the application of a linear fit of the form

$$N_{Pe} = C \cdot \mu_{true} \tag{5.21}$$

This relation can then be used to derive the number of photoelectrons for each run directly from μ_{true} thereby reducing the scatter of the extracted values.

The uncertainties of the individual data points (N_{Pe}, μ_{true}) in 5.9 are correlated as they arise from the same Landau-Gauss convolution fit to the histogram of the respective measurement run. To account for this, the error in N_{Pe} is determined using a Monte-Carlo approach. In 64 iterations the analysis program randomly generates a set of N_{Pe} and μ_{true} values of the chosen data subrange used for the QDC calibration. These values are generated within their error range as discussed

in 5.3.2. A linear fit is performed for each of these data sets and the value N_{Pe} for each measurement run is determined and stored from each of these calibrations. In order to determine the most probable N_{Pe} and its error, mean and standard deviation of these stored values are retrieved and stored as the actual analysis result.

As we have used different photomultipliers and as the data acquisition electronic components vary in noise levels, the calibration has to be performed anew for each measurement setup. The QDC calibration for each subset of measurement runs is listed in Appendix D.

5.4   Systematic Studies

During the MAMI beamtimes the different detector prototypes were moved and tilted with respect to the beam in order to determine its response to various angles and positions of electron incidence. The comparative measurements done in order to determine the optimal material and geometry for the P2 detector element have been performed as angle scans and position scans. These test series are the subject of section 5.5. Herein the method is described and one exemplary test series result is shown for horizontal and vertical position scans as well as angular scans respectively.

5.4.1   Horizontal Position Scans

Horizontal position scans were done to measure the detector prototype response in dependence of the distance of electron incidence from the location of Cherenkov light detection. They were implemented by placing the detector module prototype on a translation stage as shown in photograph 5.3 and moving the detector assembly horizontally in between measurement runs.

Figure 5.10 has a drawing of the fused silica bar with an indication of the scan line along which the impact position was varied.
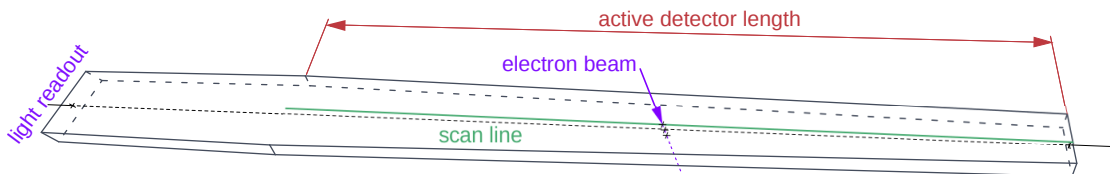

FIGURE 5.10: Horizontal position scans. The location of electron incidence onto the detector bar was varied along the indicated scan line.
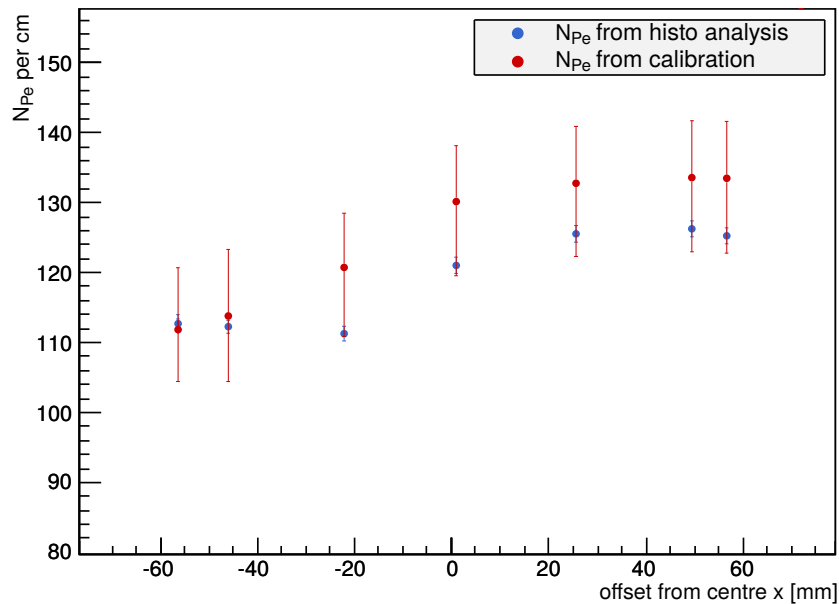
Figure 5.11: Typical example of a horizontal position scan result. The measurement was done during the beamtime in January 2016 (runs 196 to 275, except runs 213 to 236). Detector geometry II, Spectrosil 2000 quartz bar with optical outlet, Hamamatsu R11410 PMT, Alanod 4300UP wrap, no light guide. The large asymmetric errors stem from the large differences of N_{Pe} depending on the fit range and start parameters in the analysis of the QDC spectra. This dependence is particularly strong in this test series.
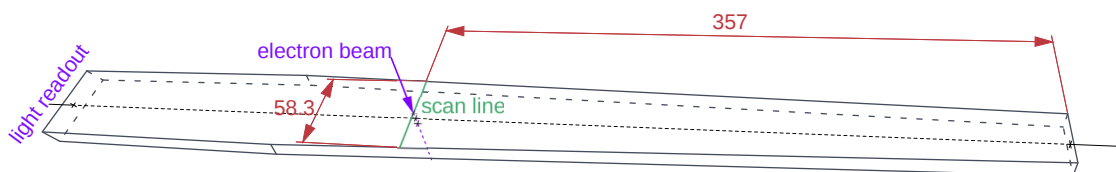
Figure 5.12: Vertical position scan. The position of electron incidence was varied along the indicated scan line.

The graph in figure 5.11 shows a typical result of a horizontal position scan. A 435 mm long detector prototype was scanned over an area of 140 mm around its horizontal center (marked in the plot as 0 mm). This is the range of the translation stage which was used to remotely move the detector relative to the beam.

5.4.2 Vertical Position Scans

As indicated in figure 5.12 the place of electron incidence onto the quartz bar was varied along a vertical line during vertical position scans.
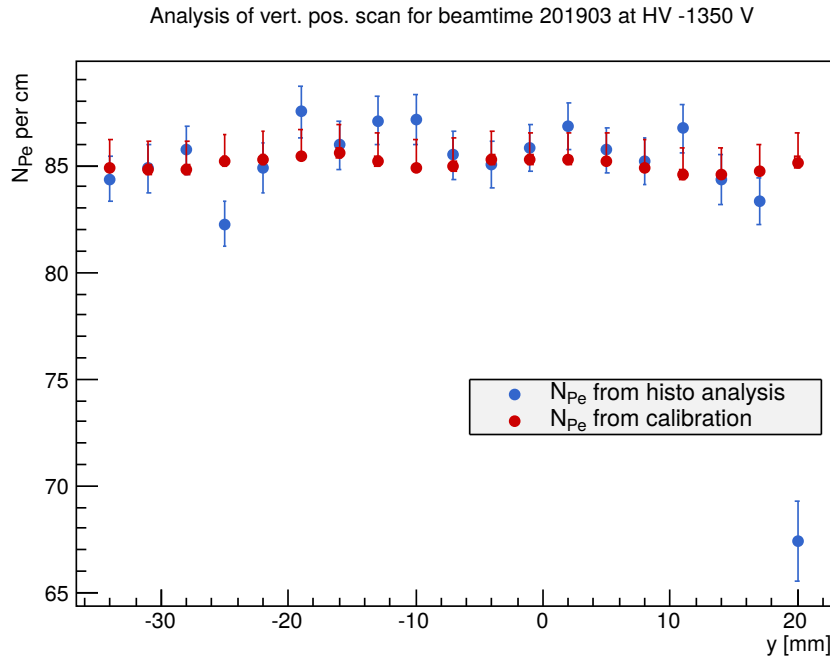
FIGURE 5.13: Detector response with varied vertical position of incidence of the MAMI electrons. Measurements done during beamtime 03/2019 with 650 mm long detector prototype. PMT: Hamamatsu R11410. Fused silica grade: Spectrosil 2000. Wrapping material: Alanod. Beam energy: 855 MeV

The graph in figure 5.13 shows an example for a vertical position scan. The signal exhibits no dependency of the vertical position of incidence of the beam on the detector module.

5.4.3   Angle Scans

Light containment and guidance towards the PMT was explained in 4.2.3.2 for primary electron incidences perpendicular onto the quartz surface. A strong signal dependence on this angle of incidence is expected. In order to examine this dependence the prototypes were therefore mounted on a rotation stage. The angle of electron incidence was varied by rotating the detector prototype. The angle of incidence α is defined as depicted in figure 5.14.

The plot shown in figure 5.15 is a typical example of an angle scan. The measurement was done during beamtime 11/2014 with a quartz bar of Geometry I (300 mm cuboid) with optical outlet. The x-axis is the relative angle between beam and quartz surface as defined in 5.14. The y-axis is the number of photoelectrons resulting from one electron incidence N_{Pe} normalised to the distance the primary electron travels inside the quartz. The maximum photoelectron yield can be noticed at approximately orthogonal incidence. The minimum is located around 45°. This can be explained using simple geometrical arguments: at normal
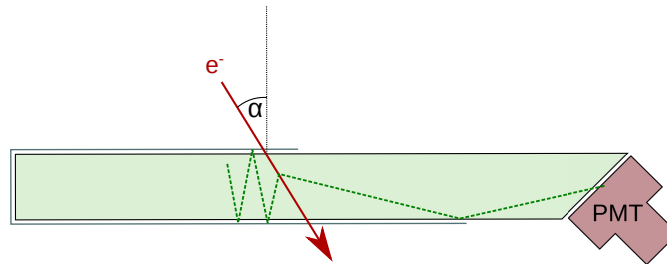
FIGURE 5.14: Definition of the angle of electron incidence α onto the quartz bar. During the angle scans at MAMI α was varied by rotating the detector by means of a remote rotation stage.
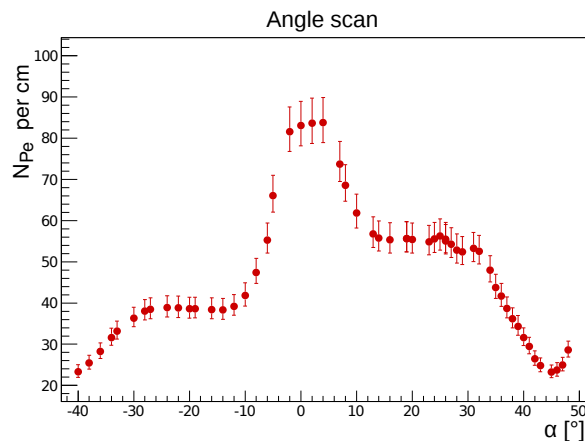
FIGURE 5.15: Typical dependence of the number of photoelectrons on the angle of incidence of the electron beam onto the quartz surface α. Data taken during beamtime 11/2014, runs 899 to 956, with a quartz bar of Geometry I (300 mm). The respective number of photoelectrons is determined using the QDC calibration.

incidence the light propagated on the Cherenkov cone is internally reflected on the plane parallel surfaces of the quartz bar. It reaches the optical outlet at 90° and can exit the bar at this face pointing towards the PMT. For 45° the Cherenkov light can in this model escape the bar at all faces but the optical outlet.

5.5   Comparative Material Studies

In seven beamtimes between 2013 and 2019 different detector prototypes were tested. The objective of the beamtimes was to determine the optimal geometry, set of materials, and assembly for a single detector element. Comparative measurements were done varying one of the detector parts while keeping the rest unchanged. In the following the results of several prototype tests, which lead to design choices for the P2 detector, will be presented.

5.5.1   Fused Silica Geometry

The preparatory considerations for the quartz bar geometry in section 4.2.3 have resulted into seven boundary conditions:

1. Ring shaped active detector area: $R \in [450\,\text{mm}, 900\,\text{mm}]$

2. 20 cm light guide to realise placement of PMTs behind photon shield

3. Wedge shaped quartz bars to avoid overlap of elements and minimise gaps

4. The number of elements has to be divisible by eight.

5. The sensitive area of a 3 inch PMT should cover the outpointing side of the quartz bar.

6. The thickness of the quartz bars should allow a high enough signal but small probability of particle showers. 10 mm is considered suitable.

7. The quartz geometry should allow manufacturing and handling without being prone to damage.

The simulations described in 4.2.2, which determined the inner and outer radius of the detector ring and therefore the length of the detector elements had not been finished when detector prototype testing at the MAMI beam started. Between 2013 and 2019 a range of different quartz geometries was tested. For the first beamtimes 300 mm long bars as sketched in figure 5.16 were ordered. These bars were then polished (comparison of different polishes in 5.5.3) and equipped with an optical outlet (signal yield comparison of quartz bars with and without optical outlet in 5.5.1.2) to make use of the internal reflections to guide the light towards the PMT. The 300 mm long bars were tested in three different thicknesses (5.5.1.1).

As it became clear that the signal electron loss due to large gaps between the detector elements is not acceptable, a new wedged geometry as shown in 5.17 was designed. This second version is 435 mm long because the particle rate distribution from a GEANT4 simulation (explained in 4.2.2) with new solenoid and shielding arrangement demanded the coverage of a ring with radius $R \in [450\,\text{mm}, 885\,\text{mm}]$.

The latest results of the particle rate distribution simulation are shown in figure 4.11 and suggest a ring shaped sensitive detector area with radius $R \in [450\,\text{mm}, 900\,\text{mm}]$ and the necessity of a 200 mm light guide. As a consequence the geometry depicted in figure 5.18 was tested to its response to electrons in MAMI beamtime 03/2019.
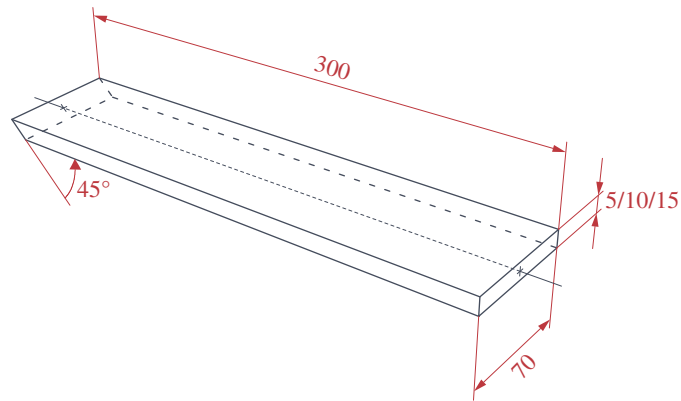
FIGURE 5.16: GEOMETRY I: 300 mm long and 70 mm wide cuboid quartz bar. This geometry was tested in three thicknesses (results shown in section 5.5.1.1) and with and without optical outlet (5.5.1.2).
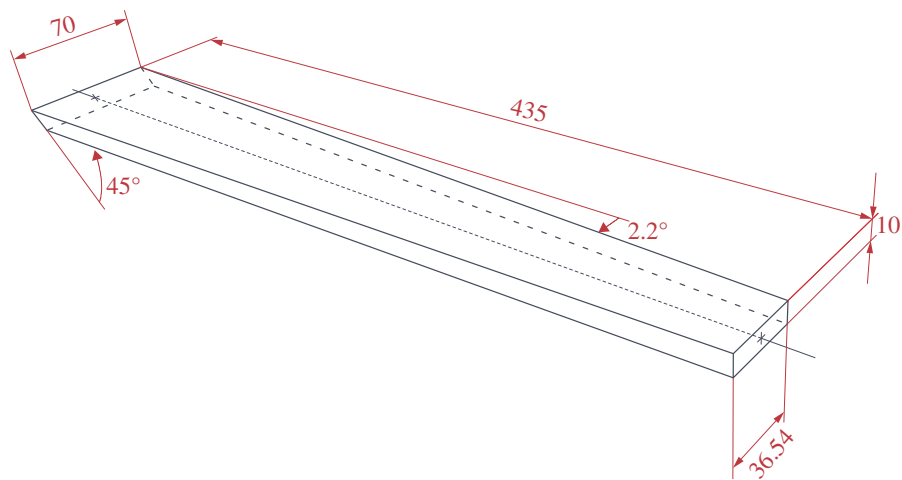

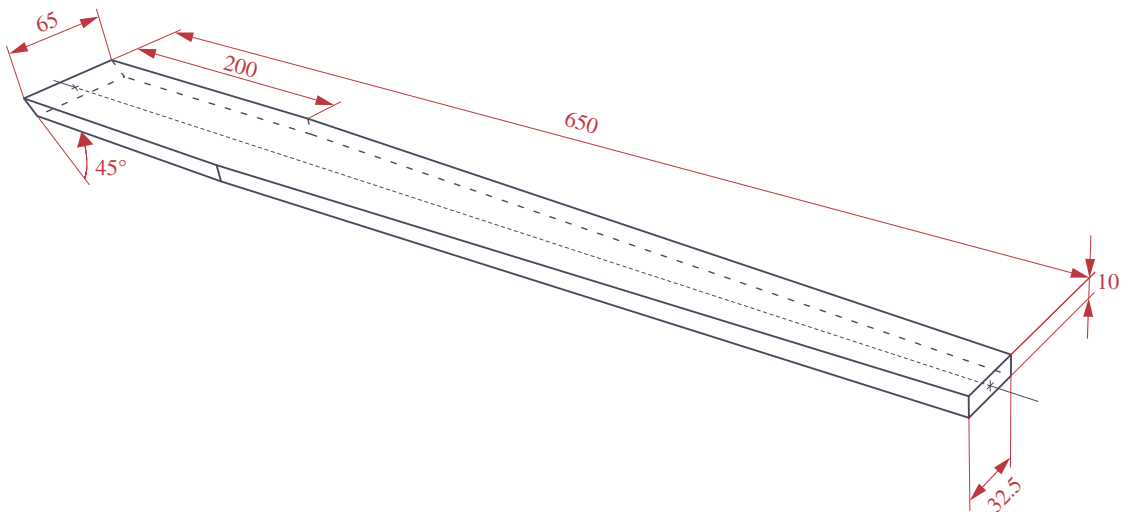FIGURE 5.17: GEOMETRY II: 435 mm long tapered quartz bar.

FIGURE 5.18: GEOMETRY III: 650 mm long tapered quartz bar with 200 mm long straight part serving as light guide.
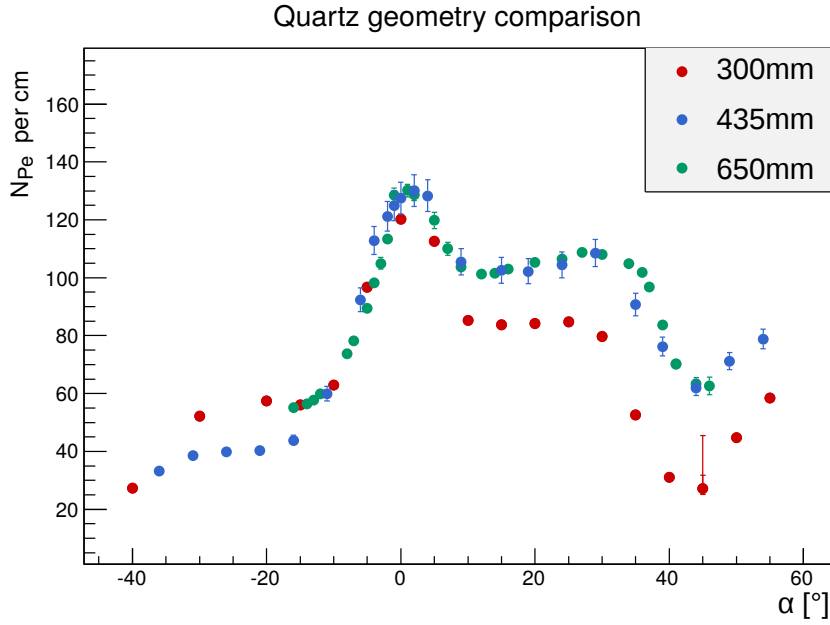
FIGURE 5.19: Signal yield comparison for the three quartz geometry genera-
tions by means of angle scans. Number of photoelectrons per cm of traversed
quartz per electron event is plotted against angle of incidence of the electron
onto the quartz surface. Quartz thickness: 10 mm, Schauglaspolitur, 45° cut,
Alanod 4300UP wrap. PMT: Hamamatsu R11410 serial number ZK6862. Ge-
ometry I (300 mm): beamtime 01/2014 runs 792 to 829, Geometry II (435 mm):
beamtime 01/2016 runs 212 to 236, Geometry III (650 mm): beamtime 03/2019
runs 12587 to 12617

A comparison of the photoelectron yield of detector assemblies with the three
quartz geometry generations is shown in figure 5.19. The three measurements were
done during different beamtimes but with the same setup aside from the detector
geometry. The plot contains data points for a range of different incidence angles.
The point of electron incidence was the horizontal and vertical center of the active
detector area. For quartz Geometry III the electrons hit the bar at the vertical and
horizontal center of its wedged part, since the 200 mm long straight part serves
merely as light guide. The signals of the two wedged quartzes (Geometry II and
III) do not differ significantly. Due to the exceptional UV transmittance, not much
signal loss occurs in the light guide part of the quartz bar with Geometry III. The
tapered detectors perform better in an angle range $\alpha \in [10°, 50°]$. When internally
reflected from the tapered faces the light from the Cherenkov cone gets directed
towards the PMT more quickly and effectively, needing fewer internal reflections.

The final design of the P2 detector includes 650 mm quartz bars consisting of a
tapered active detector part and a straight light guide of 200 mm in length as
shown in figure 5.18. Neither the tapering of the quartz bars nor the length of
650 mm mandated by the latest rate distribution simulations are of disadvantage
for the signal yield of the detectors.
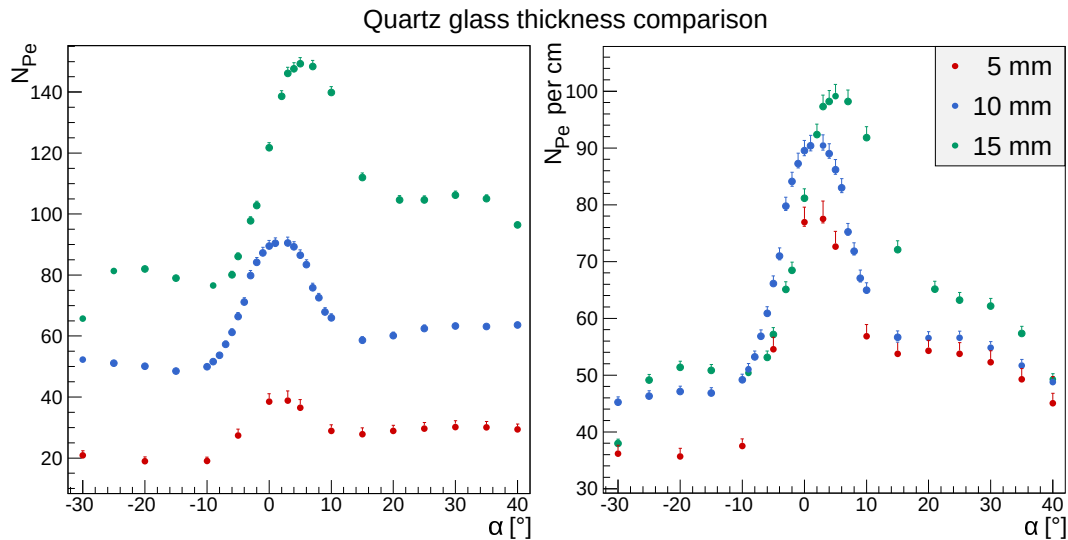
FIGURE 5.20: Total number of photoelectrons (left) and number of photoelectrons per cm of traversed quartz (right) per electron event for three quartz thicknesses. Data was taken during beamtime in 05/2015 with Spectrosil 2000 bars, Schauglaspolitur, 45° cut, Alanod 4300UP wrap, and ET9305QKMB photomultiplier serial number 518.

5.5.1.1 Thickness

It can be read from figure 4.5 that a relativistic electron passing through 10 mm of fused silica generates an average number of 810 photons in the wavelength range $\lambda \in [200\,\mathrm{nm}, 800\,\mathrm{nm}]$. After first material and geometry considerations we deduced that a sufficiently large fraction of these primary Cherenkov photons could be guided to the PMT cathode and lead to the emission of the required number of 50 photoelectrons to meet the criterion stated in equation 5.9. This assumption was validated during a MAMI beamtime in 05/2015. The signal of 10 mm thick quartzes was compared to that of 5 mm and 15 mm thick ones. All three bars were 300 mm long, 70 mm wide (Geometry I, 5.16) and had a 45° cut as optical outlet. Figure 5.20 shows the number of photoelectrons as function of the incidence angle α for all three bars.

With the 15 mm thick quartz the maximum number of 149 photoelectrons was measured at an impact angle α of 5°. The 10 mm and 5 mm thick bars deliver a maximum of 90 and 39 photoelectrons respectively at an angle of 3°. The right hand side of figure 5.20 shows these numbers normalised to the distance the primary electron travels in the fused silica. The intensity of Cherenkov light produced per electron event scales linearly with the distance travelled in the material. The electron passing the quartz can lead to secondary particles, which enhance the signal. These effects are more likely the more matter is traversed. Additionally the light loss in thicker quartz is smaller as less surface reflections take place before
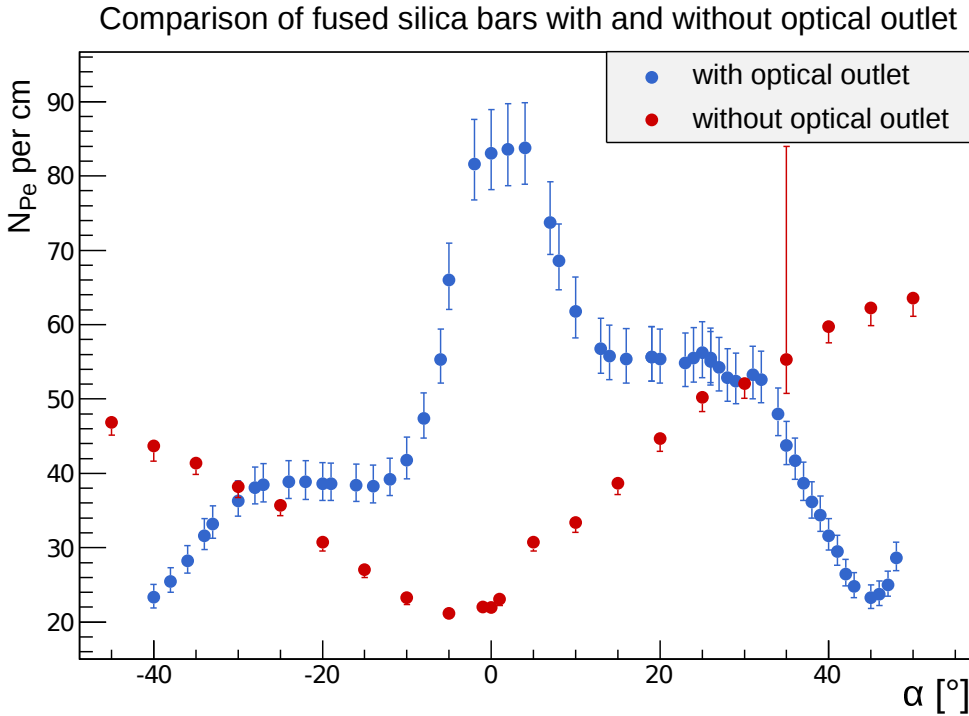
FIGURE 5.21: Comparison of angle scans with and without optical outlet applied to the quartz bar. Data taken during beamtime 11/2014. With optical outlet: runs 899 to 956. Without optical outlet: runs 1070 to 1091. Underlying QDC calibration: runs 840 to 898 and 1027 to 1109

the light reaches the PMT. It is thus expected that the signal yield per cm is larger for thicker quartz bars.

As a result of this measurement series we can state that 10 mm thick fused silica bars proved to deliver enough Cherenkov light to the photosensors. Thicker bars will lead to additional showers, and thinner ones are too fragile and therefore prone to damage during the polishing process. Furthermore we were not able to reach the critical number of 50 photoelectrons with a 5 mm quartz glass bar. Subsequent detector models were therefore built with 10 mm thick bars.

5.5.1.2   Optical Outlet

As both the Cherenkov angle for relativistic electrons and the critical angle of total internal reflection for UV light in fused silica are close to $45°$ the effect of internal reflections of the Cherenkov light occurs at all six surfaces of a nearly cuboid quartz bar. To allow the light to exit the bar at the side where the light sensor is attached, an optical outlet has to be applied.

Figure 5.21 contains measurement results of angle scans with 300 mm long quartz bars with and without $45°$ cut applied as optical outlet. The plot demonstrates

the necessity of the optical outlet, as the signal for electrons hitting the detector approximately perpendicularly is more than 70% smaller than the one measured with a quartz bar equipped with an optical outlet. In order to reach the critical amount of 50 photoelectrons the detector elements would have to be tilted by $\approx$ 45° so that they form a cone with apex towards the target. The individual bars would also have to be elongated by a factor of $\sqrt{2}$ in order to cover the same ring shaped detector area.

5.5.2 Fused Silica Material Grade

Two fused silica materials —Spectrosil 2000 and Suprasil 2A, both by Heraeus Conamic— were tested. The signal yield as a function of the impact angle and position respectively are compared in figures 5.23 and 5.22. The material comparison measurements were done during the first two detector test beamtimes and therefore with the first geometry generation (figure 5.16). All experimental conditions aside from the quartz material were kept equal in both measurement series. They were done during the same beamtime with the same data acquisition arrangement, PMT (ET 9305QKMB serial number 518 operated at $-1000\,\mathrm{V}$), PMT voltage divider, and quartz wrap. No light guide was in use. Merely the quartz bar was exchanged. Both quartz bars had the same geometry and underwent the same polishing process. Both an angle scan as well as position scan were performed to eventually observe effects of differences in the surface smoothness and differences in the transmittance of the two quartz grades on the signal.

No significant light yield difference was observed between the two materials. The slight discrepancies do not exceed statistical fluctuations and systematic errors caused by surface imperfections, impurities, and minor damaging of the synthetic quartz bars. Ultimately, Spectrosil was chosen over Suprasil due to the higher radiation hardness (subject of chapter 6) and lower cost.

5.5.3 Fused Silica Polishing

The amorphous quartz bars are cut from a large ingot and as their surface is rough they are initially opaque. In order to obtain the effect of internal reflections, which helps guide the Cherenkov light to the PMT, the fused silica bars have to be polished. Because quartz is brittle, chipping of the edges may easily occur, if no chamfer is applied prior to polishing.

In order to assess the required polishing quality, two different providers were entrusted with the task to polish sample bars. One batch of quartz bars was sent to
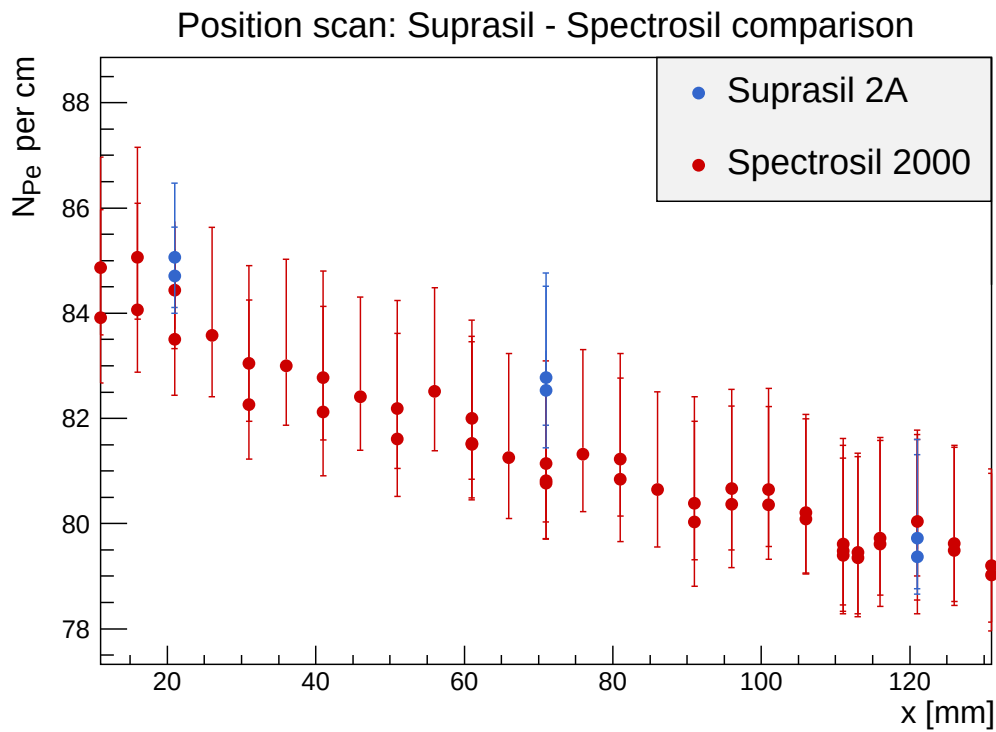
FIGURE 5.22: Position scans with 300 mm long Spectrosil 2000 and Suprasil 2A bars from beamtime 01/2014. Spectrosil 2000: runs 650 to 708. Suprasil 2A: runs 594 to 611. Run time: 180 s each.
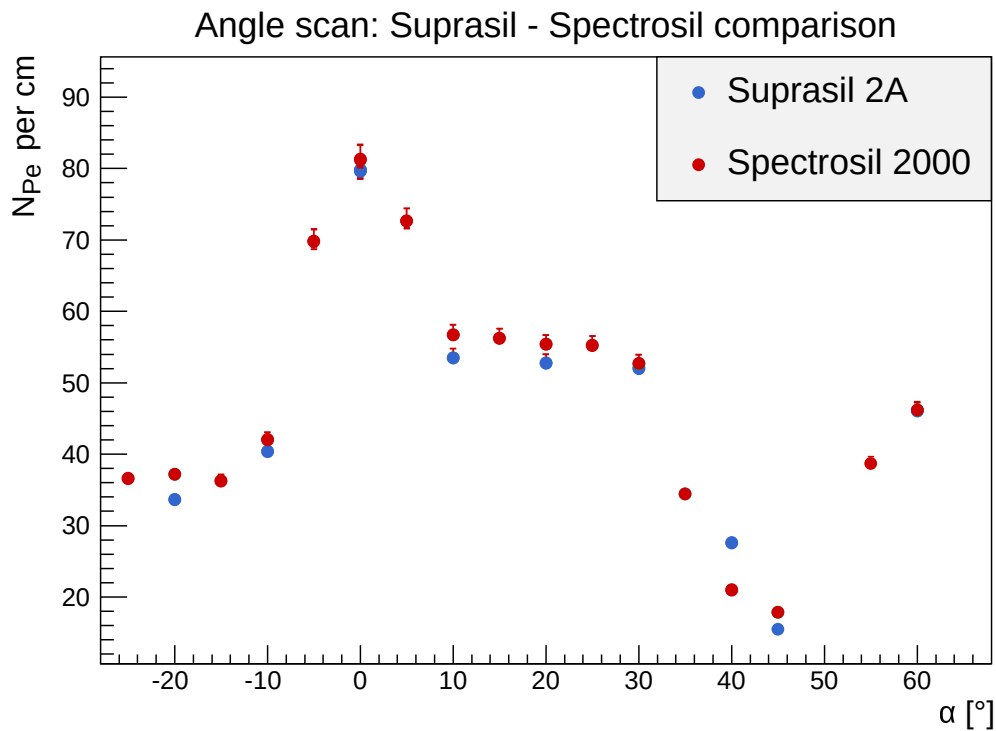
FIGURE 5.23: Angle scans with 300 mm long Spectrosil 2000 and Suprasil 2A bars from beamtime 01/2014. Spectrosil 2000: runs 709 to 752. Suprasil 2A: runs 633 to 648. Run time: 180 s each.
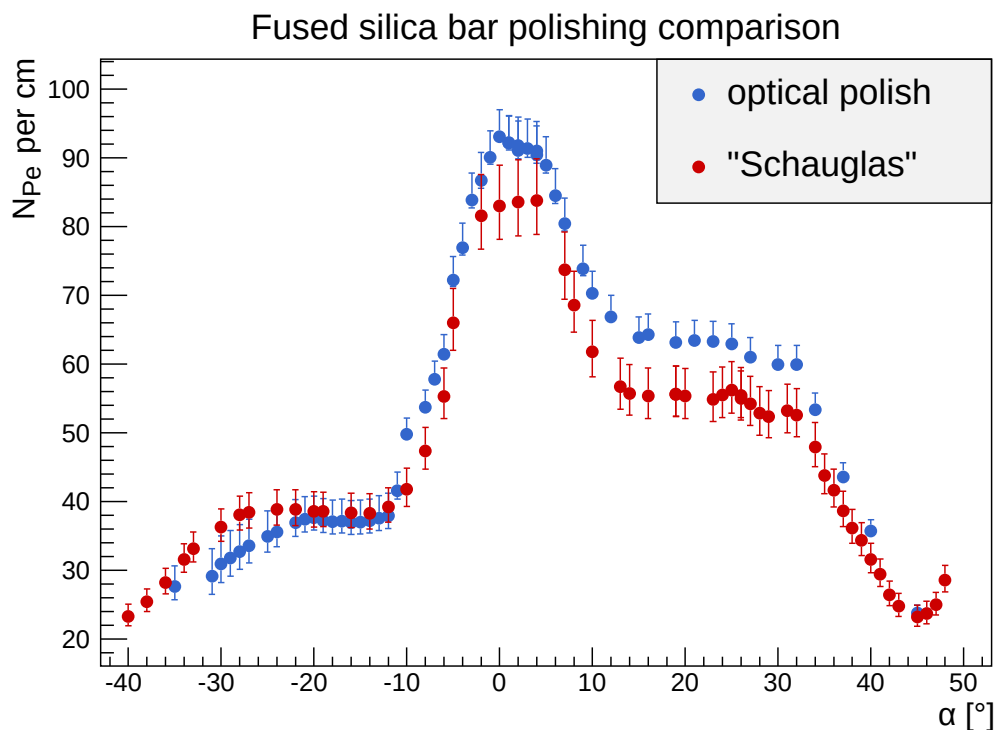
FIGURE 5.24: Comparison of angle scans with quartz bars with optical polishing and "Schauglas" polishing. Data taken during beamtime 11/2014. Optical polishing: runs 899 to 956. "Schauglas" polishing: runs 840 to 898. QDC calibration from runs 840 to 956.

Hellma[3], a company that processes silica for optical applications. In figure 5.24 the signal yields of such a bar and a sample of equal geometry polished by Heraeus are compared. The polishing done by Hellma is called "optical polish". The surface quality is specified as "$5/10 \times 1.6$" allowing 10 surface defects of class 0.16 corresponding to either scratches of up to $40\,\mu\text{m}$ or circular defects up to $180\,\mu\text{m}$. "Schauglas" (sight glas) polishing performed by Heraeus means that the surface is mechanically polished to a degree that the bar becomes transparent and no defects are visible to the bare eye.

Of the two tested samples the optically polished bar performs better by $\approx 10\%$ in the angle range $\alpha \in [-10°, 40°]$. In avoidance of the risk of further shipping and handling of the delicate material by another company successive quartz bars were ordered and delivered already polished by Heraeus.

5.5.4 Wrapping Material

During the preparatory material studies covered in 4.2.4 three potential wrapping materials for the P2 main detector Cherenkov medium were chosen for the

---

[3]Hellma GmbH & Co. KG, Klosterrunsstraße 5, 79379 Müllheim, Deutschland
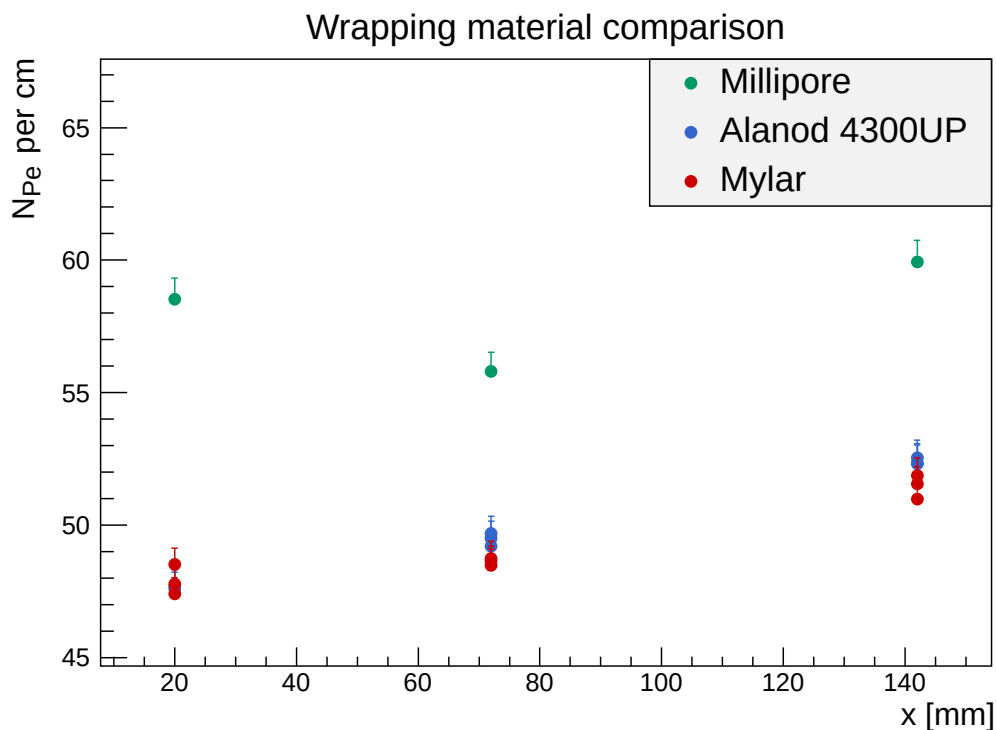
FIGURE 5.25: Comparison of Millipore Immobilon-P, Mylar foil, and Alanod 4300UP as wrapping materials on a flame polished quartz bar of dimensions 300 mm by 70 mm by 10 mm without optical outlet. The comparison measurements for wrapping materials was done during the beamtime in 10/2013. Alanod: runs 344 to 362. Millipore: runs 372 to 375. Mylar: runs 363 to 371.

prototype tests at MAMI. Alanod 4300UP is a 0.4 mm thick highly reflective aluminium sheet. Mylar is a thin foil of aluminised biaxially oriented polyethylene terephthalate. Millipore Immobilon-P is a thermoplastic fluoropolymer membrane used in bio-chemistry as substrate for fixing of amino acids and protein samples. The performance of these three materials has been tested during the beamtime in October 2013 using the very first detector prototype geometry and assembly. The quartz bar in use was a cuboid of 300 mm by 70 mm by 10 mm without optical outlet and flame polished[4]. The angle of incidence of the electron beam onto the quartz bar was 45°. Measurements were performed with three different positions of impact of the MAMI electron beam onto the fused silica bar. The number of photoelectrons from the PMT cathode reached when using Millipore Immobilon-P, Alanod 4300UP and Mylar respectively is plotted in figure 5.25.

---

[4]The material is exposed to heat, melting a thin layer, until the surface becomes smooth and glassy. The polishing was done by a local glass blower. It is not practicable for a larger number of quartz bars and was therefore not considered for the final P2 detector.
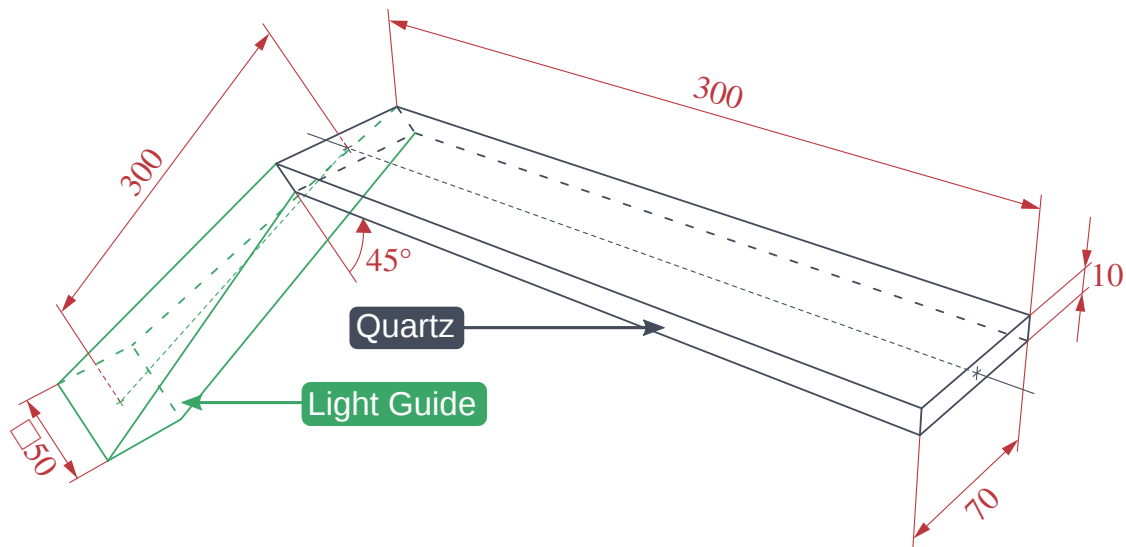
FIGURE 5.26: Detector prototype geometry with light guide to direct the light to the PMT. This design was tested during beamtime 01/2014 with different reflective surfaces on the inside of the light guide.

While the prototypes using Mylar and Alanod 4300UP perform equally well, an approximate 15% increase in signal can be recorded when using Millipore Immobilon-P. However the aluminium sheets have multiple advantages: Millipore Immobilon-P loses large parts of its reflectivity when exposed to humidity or greasy substances [45]. The radiation hardness of aluminium and its resistance to other environmental influences potentially occurring in the experimental hall during the run time of P2 is known to be very good. Alanod 4300UP sheets are self supportive and stiff, while Mylar foil is very thin and delicate. It waves and wrinkles easily, which is undesirable for a specular reflector. Therefore Alanod 4300UP was chosen as wrapping material for the P2 detector bars.

5.5.5 Light Guide

Light sensors and other delicate electronic parts of the experiment will have to be placed in a lower-radiation area further away from the beamline than the active detection area. A thick lead shield will cover the PMTs protecting them from radiation damage. That means that a device will be needed to efficiently guide the Cherenkov light from the quartz bar to the PMT, which will be placed 200 mm away from the outer edge of the detection ring. In the early stage of designing the experiment air light guides were considered for that purpose. An air light guide is a volume of air surrounded by highly reflective material to contain light in this volume. The light guide's geometry is ideally chosen to direct light from its origin to the place of detection with as few reflections as possible.
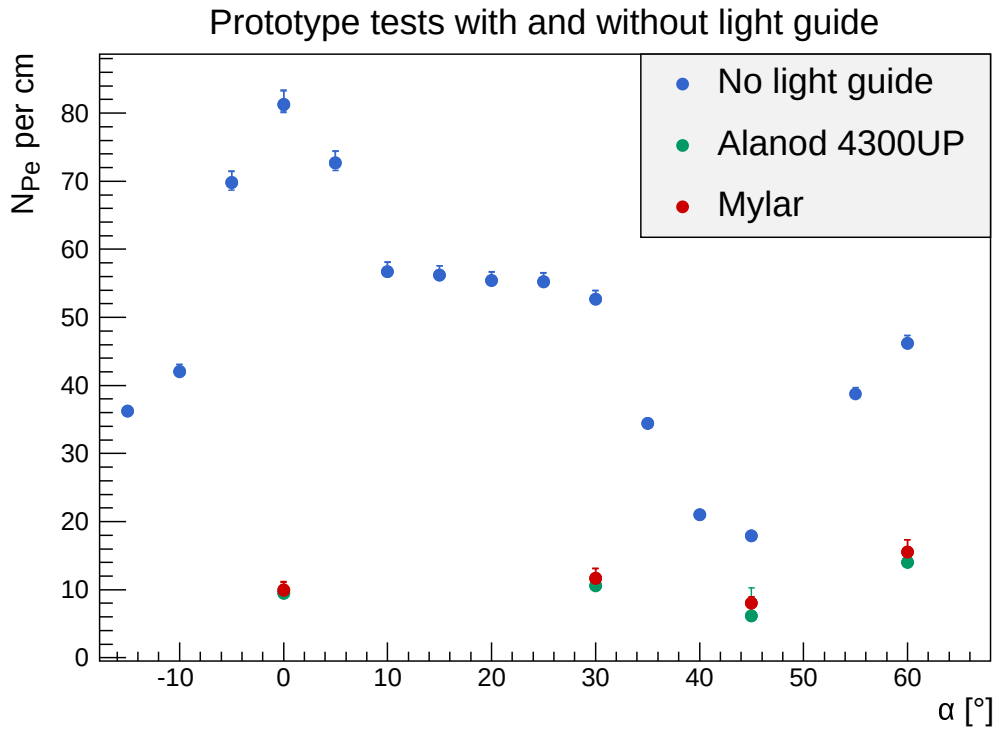
FIGURE 5.27: Test of air light guides made of Mylar foil and Alanod 4300UP. Measurement results are compared to a measurement with the same quartz bar with optical outlet wrapped in Alanod 4300UP, and the same PMT (ET9305QKMB serial number 518). For a numerical comparison see table 5.1. Data was taken during beamtime 01/2014 at MAMI. No light guide: runs 633 to 648. Alanod: 570 to 577. Mylar: 578 to 585.

The air light guide design depicted in figure 5.26 was tested on a 300 mm long (Geometry I) Spectrosil quartz glass bar with optical outlet wrapped in Alanod 4300UP. A comparison of measurements with and without light guide is shown in figure 5.27. The signal loss due to light guide usage is more than 80% as compared to the signal yield of a detector without light guide, when the quartz surface is perpendicular to the electron beam. This holds for both Alanod 4300UP and Mylar on the inside of the air light guide. Table 5.1 lists the signal yield of the detector prototype without light guide, with an air light guide made of Alanod 4300UP and with an air light guide made of Mylar foil along with relative signal loss because of the light guide interposition.

As a number of photoelectrons of at least $N_{Pe} = 50$ is needed, the signal loss in an air light guide like the ones tested is unacceptable. Therefore another approach was considered, which makes use of the effect of internal reflections in the quartz and the extremely good light transmittance of quartz. The idea is to elongate the quartz bars by 200 mm and add lead shielding around this inactive area of the detector, which will effectively serve as light guide, and around the PMTs at their ends. These considerations lead to quartz Geometry III (figure 5.18). Figure 5.28

	without light guide	Alanod		Mylar	
	N_{Pe}	N_{Pe}	loss [%]	N_{Pe}	loss[%]
0°	81.23	9.47	88.34	9.95	87.75
30°	52.65	10.61	79.79	11.73	77.72
45°	17.90	6.14	65.70	8.01	55.25
60°	46.20	14.02	69.65	15.56	66.32

TABLE 5.1: Signal yield in terms of photoelectrons from the PMT cathode of the measurements plotted in figure 5.27. The relative signal loss due to light guide interposition is listed for different incidence angles of the electron beam onto the quartz surface.
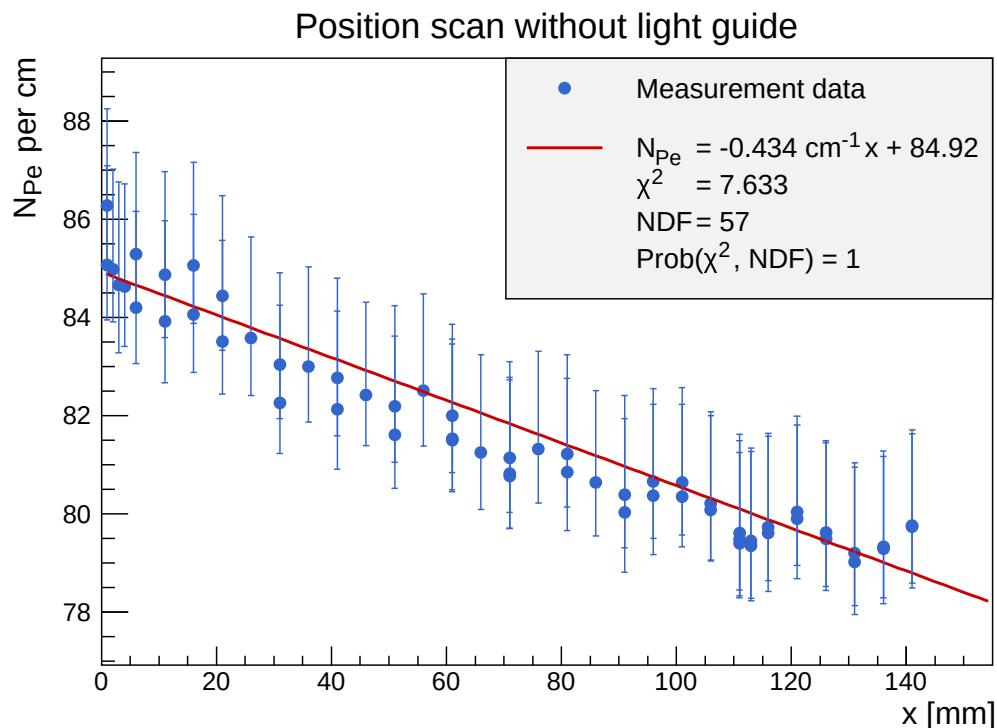
FIGURE 5.28: Horizontal position scan performed during beamtime 01/2014 (runs 650 to 708) with cuboid quartz bar: Detector Geometry I, 10 mm thick, 45° cut as optical outlet, Spectrosil 2000, "Schauglas" polish (with protection chamfers), PMT: ET 9305QKMB serial 518.

contains measurements done to determine the ability of quartz to efficiently guide the Cherenkov light with very little signal sacrifice. It was implemented by varying the distance of beam incidence of the MAMI beam on the quartz surface — and therefore the origin of Cherenkov light — from the photomultiplier.

The signal loss per 10 mm was as little as 0.434 photoelectrons. We concluded that the signal loss due to an additional 200 mm of fused silica would not lead

to critically low detector signals. Extensive tests of the new 650 mm long quartz Geometry III were done during beamtime 03/2019. The results of these tests are discussed in 5.5.1 and have confirmed that the 200 mm quartz light guide does not lead to a drastic signal loss.

5.5.6   Photomultiplier Tubes

Due to radiation hardness requirements and the high rates expected in the P2 Experiment the considerations for a light detector were limited to PMTs at a very early stage during the planing phase of P2. Semiconductor sensors like avalanche photodiodes were not tested for this specific experiment, because suitability investigations for other uses show a failure due to critical noise increase after radiation doses more than two orders of magnitude below those expected in the P2 Experiment [46].

We studied the properties of three different types of PMTs by two manufacturers:

- Hamamatsu R11410 ASSY [47]

- Electron Tubes ET9305 QKMB

- Electron Tubes ET9305 QKFL

All photomultipliers are specified for UV usage by the manufacturers due to very good quantum efficiency down to wavelengths of less than 200 nm as shown in figure 5.29. The tubes with serial numbers 509, 518 and 520 all belong to the same series called ET 9305QKMB, a model of 3 inch quartz window multiplier tubes with bialkali cathodes specified for high sensitivity in the deep UV. Model ET 9305QKA, of which the specimen with number 533 was tested, has a photocathode with yet enhanced quantum efficiency. A Hamamatsu R11410 photomultiplier was also tested in a prototype at the MAMI electron beam.

The graph of figure 5.29 shows measurement data taken during a test beam in March 2015. All measurements were taken with the same piece of fused silica, a 300 mm long, 70 mm wide and 10 mm thick Spectrosil 2000 bar with 45° cut where the PMT was attached. The bar was polished by the manufacturer Heraeus and wrapped in Alanod 4300UP. For each PMT a measurement series was performed varying the angle of impact of the MAMI electron beam onto the quartz surface.

The quantum efficiencies of the PMTs tested at MAMI are shown in figure 4.18. For all Electron Tubes photomultipliers a tabulated measurement of the quantum efficiency ranging from 200 nm to 700 nm in steps of 10 nm for each individual tube is included by standard. Hamamatsu on the other hand delivers copies of their
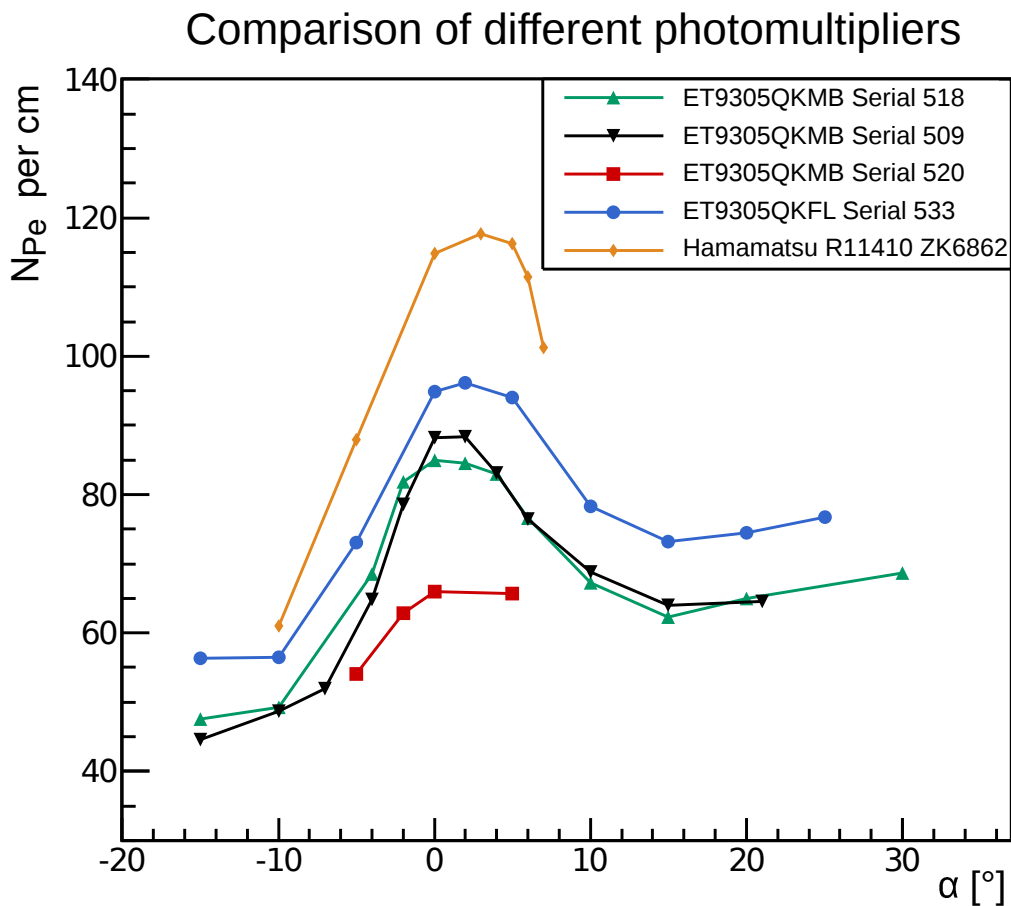
FIGURE 5.29: Detector signal yield in terms of photocathode electrons for different photomultipliers as a function of the angle of electron incidence onto the detector surface α. Data from beamtime 03/2015.

model R11410 with specific spectral response information for the spectrum from 165 nm to 200 nm only. The data for higher wavelength is taken from the data sheet [47]. These specifications have been published by the XENON collaboration [48] and represent average sensitivities which are subject to fluctuations in production.

The average value of the spectral quantum efficiency in the wavelength region between 200 nm and 300 nm as well as the number of cathode photons per electron event at 0° for each one of the tubes examined during the beamtime in March 2015 are listed in table 5.2. In order to put these values into relation, the quantum efficiency and cathode yield of the photomultiplier with serial 533 by Electron Tubes were defined as 100%. For all PMTs manufactured by Electron Tubes, the cathode yield is a linear function of the provided average quantum efficiency. The Hamamatsu R11410 showed a much better performance in our test than expected from the datasheet.

	ET 533	ET 509	ET 518	ET 520	Hamamatsu
QE[200nm,300nm]	33.75	30.36	29.37	22.09	31.55
	100.00%	89.96%	87.02%	67.85%	93.48%
$N_{\mathrm{Pe}}(0°)$	94.84	84.01	82.54	65.64	114.86
	100.00%	88.57%	87.02%	69.24%	121.10%

TABLE 5.2: Quantum efficiencies of the tested PMTs as an average of the spectral quantum efficiency between 200 nm and 300 nm and the cathode photoelectron yield to an incident electron of energy 180 MeV perpendicular to the detector surface. The quantum efficiency and number of photoelectrons for the Electron Tubes 9305QKA Serial 533 are defined as 100% and the values for the other photomultipliers are set into relation to them.

The XENON experiment [49], for which the Hamamatsu R11410 was designed, operates the PMTs in very low temperature environments like liquid Xenon ($-110\,°C$) and liquid Argon ($-186\,°C$). In addition the photomultipliers are made from low radioactivity materials to reduce background in the experiment. These features are irrelevant for the P2 Experiment, but increase the price of the device dramatically. Hamamatsu has ceased serial production of the R11410 and cannot offer any PMT with the same photocathode and diameter. The ET 9305QKMB offers a high enough signal yield and aside from having been tested extensively in the beamtimes described herein, designs of custom photomultiplier voltage dividers for the P2 Experiment with adjustable gain for different measurement modes have been made and tested by Thomas Jennewein during his Master thesis [37].

5.6 Detector Tests at the A2 Photon Tagger Facility

The P2 detector will be shielded against background particles firstly by the solenoid magnet, which binds Møller electrons and electrons from inelastic scattering close to the beam line and focuses signal electrons onto the detector plane, and secondly by lead shields which block the direct view of the detector onto the target. Uncharged particles from processes in the target can thus mostly be prevented from hitting the detector and causing background signals. However shielding efficiency is limited and secondary background particles can be produced by bremsstrahlung and pair production in the shield and other material involved in the experiment. Photons represent the most dominant background in the P2 Experiment by rate onto the detector. Therefore it is of paramount interest to determine the detector's efficiency to photons of the energy occurring during the runtime of the experiment.

As scintillation effects in fused silica are negligible, photons do not directly provoke a light signal in the detector. However they can interact in the quartz and other parts of the detector leading to secondary charged particles with can cause a background signal. Therefore the prototype's sensitivity to photons of various energies has been measured at the A2 facility at MAMI.

This section is going to explain the implementation of these tests and the data analysis. In chapter 7 a GEANT4 simulation of the detector signal is described. The simulation results concerning the photon sensitivity will already be addressed in this section when comparing them to the A2 measurement results.

5.6.1 The A2 Tagger Facility

Measurements of the Cherenkov detector prototype's response to photons were performed at the A2 facility [50], where tagged photons are generated via bremsstrahlung from MAMI beam electrons. Bremsstrahlung photons are produced, when high energy electrons interact with the electromagnetic field of atomic nuclei in a so-called bremsstrahlung target. In this process, a small amount of momentum p_{N} is transferred to the target material. Because of the vast mass difference between electron and nucleus, the energy transfer is negligible. If the target nucleus is initially at rest, momentum and energy conservation requires that for an incident electron with initial state $(E_0, \vec{p}_0)$, which produces a photon of momentum 4-vector $(E_\gamma, \vec{p}_\gamma)$ the final energies and momenta respectively sum up to the initial energy and momentum of the electron:

$$E_0 = E_e + E_\gamma \tag{5.22}$$

and

$$\vec{p_0} = \vec{p_e} + \vec{p_\gamma} + \vec{p_N} \tag{5.23}$$

The A2 Tagged Photon Spectrometer measures the final momentum of the electron after the bremsstrahlung process of MAMI beam electrons in a thin metal foil, which is usually used in the facility as bremsstrahlung target (radiator), by making use of the relation

$$r = \frac{p_e}{eB} \tag{5.24}$$

between the curvature radius r of the electron's path in the magnetic field B and the momentum p_e.

Figure 5.30 shows a floor plan of the A2 hall with the tagger on the left. After having produced a bremsstrahlung photon the electron with reduced energy E_e
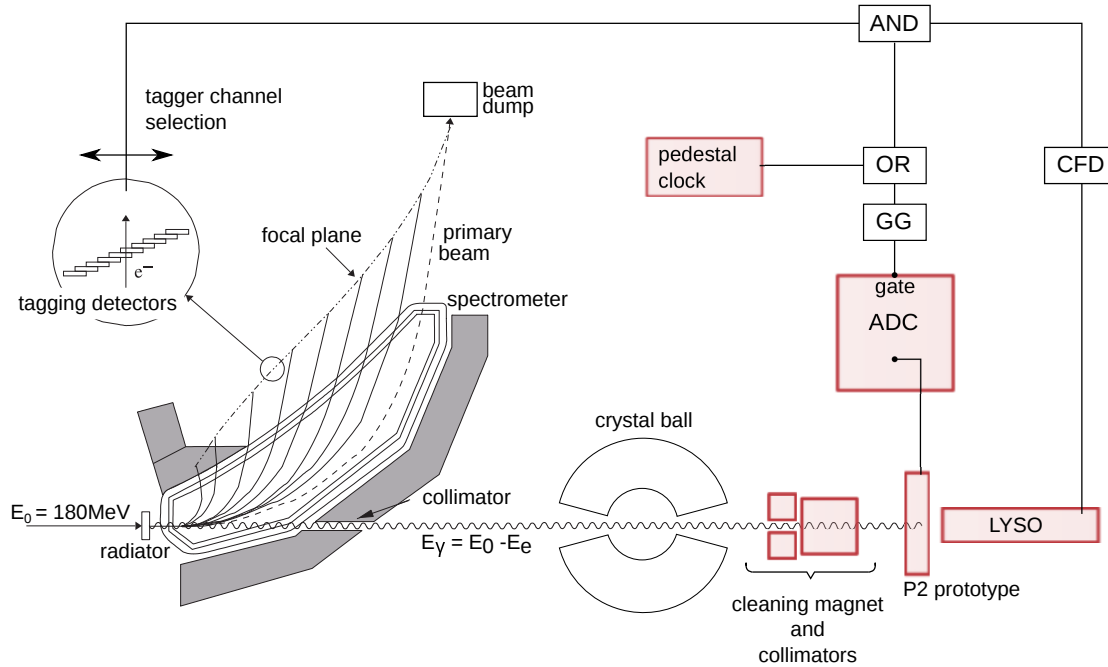
FIGURE 5.30: Schematic overview of the experiment setup used to determine the detector response to photons at the A2 photon tagger facility. GG: Gate generator, CFD: Constant fraction discriminator.

passes the magnetic field of a spectrometer. The place in which it hits the focal plane and causes a signal in the tagging scintillator detectors depends via 5.24 on its energy so that the energy of the bremsstrahlung photon can be determined using equation 5.22 by the tagger channel in which the electron was detected. Electrons which have passed the radiator without energy loss are deflected into a beam dump.

5.6.2 Implementation of the Measurement of the Detector Response to Photons

Included in the A2 floor plan 5.30 are in red the hardware components installed specifically for the P2 prototype tests as well as a scheme of the cabling and data acquisition configuration. A quartz Cherenkov detector element of Geometry II (435 mm wedged) was placed in the photon beam behind the A2 Crystal Ball detector, which was not in use during these measurements. A 0.4 T magnet was placed 60 cm upstream from it in order to deflect potential charged particles which could have been produced by conversion and ionizing effects of the photons in the vacuum window, collimators and other material close to the photon beam and keep them from causing signals in the P2 detector element. The light read out was performed with a Hamamatsu R11410 PMT, at a high voltage of 1400 V. The gate condition for the CAEN QDC to record signals from this detector was
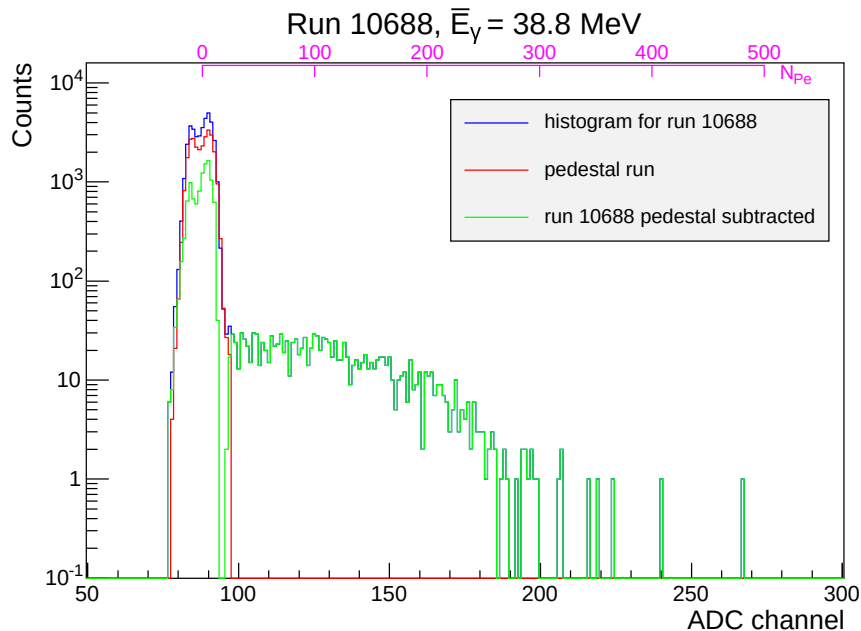
FIGURE 5.31: Example QDC histogram from a measurement run at the A2 photon facility. 5 tagger channels corresponding to a mean photon energy of 38.8 MeV served as trigger for the QDC gate. Run time: 600 s.

provided by a coincidence of selected tagger channels and an 20 cm long cuboid LYSO scintillation detector array placed directly behind the quartz and read out by a single ET9305QKMB phototube. The characteristics of the LYSO detector are described in [51], and its photon detection efficiency is for the purpose of the P2 test measurements presumed to be 100%. In addition a pedestal gate is generated in order to determine the electronic noise. A tagger channel selector allows to choose one or several tagging detectors for the trigger coincidence. Table B.1 in the appendix lists the photon energies which for a primary electron beam energy of 180 MeV correspond to the tagger channels used during the P2 prototype test.

5.6.3 Data Analysis

The histogram in 5.31 shows an example measurement taken with 5 tagger channels selected. The mean photon energy for this run is 38.8 MeV. A measurement of the electronic noise, during which only the pedestal clock served as trigger condition, was subtracted from the histogram and the result is plotted in green. The fact that the majority of entries is still within the electronic noise region of QDC channels, clarifies that most particle incidences which cause signals in the LYSO detector and therefore result into the opening of the QDC gate, do not cause a measurable signal in the quartz detector. With the assumption that the LYSO scintillator detects 100% of all photons, the detection efficiency of the P2 prototype to photons of the

selected energy can be expressed as the ratio of particle events in a histogram H, which are above the electronic noise level t

$$n_{\text{Sig}} = \sum_{i=t}^{4095} h_i \qquad (5.25)$$

where h_i is the i-th bin of H, to the total number of entries

$$n_{\text{tot}} = \sum_{i=0}^{4095} h_i \qquad (5.26)$$

corrected by the number of random gates n_{RC} generated during the measurement:

$$\eta_\gamma = \frac{n_{\text{Sig}}}{n_{\text{tot}} - n_{\text{RC}}} \qquad (5.27)$$

The highest channel in our 12-bit QDC is 4095.

These measurements were performed for mean energies ranging from $11.0\,\text{MeV}$ to $84.2\,\text{MeV}$ with an energy resolution of $\approx \pm\,1.1\,\text{MeV}$.

The raw histograms were analysed by scaling the x-axis by means of the QDC channel calibration described in chapter 5.3 which was performed with the same detector and QDC configuration during the electron beamtime in 2015. The histograms were rebinned, the pedestal was subtracted, and the detection efficiency was calculated in analogy to 5.27 using the sums over the electronic noise region $[0, t]$ and the whole histogram $[0, 4095]$. The mean signal in terms of numbers of photocathode electrons per signal-causing photon event is the arithmetic mean of the histogram entries above the pedestal threshold.

5.6.4   Discussion

The values obtained for the relative efficiency of the P2 detector prototype to photons are plotted as a function of the incident photon energy in figure 5.33(a). Figure 5.33(b) shows the mean signal strength of these events. The efficiency is subject to high fluctuations, and if the measurement were to be repeated, it might be advisable to collect better statistics. However, apart from 4 outliers out of 24 data points, the results coincide with the simulated data within 10%. The simulated mean number of photocathode electrons per signal exceeding the electronic noise is systematically higher than the measured value, and the discrepancy is more significant the lower the photon energy. An overestimation of the measured mean
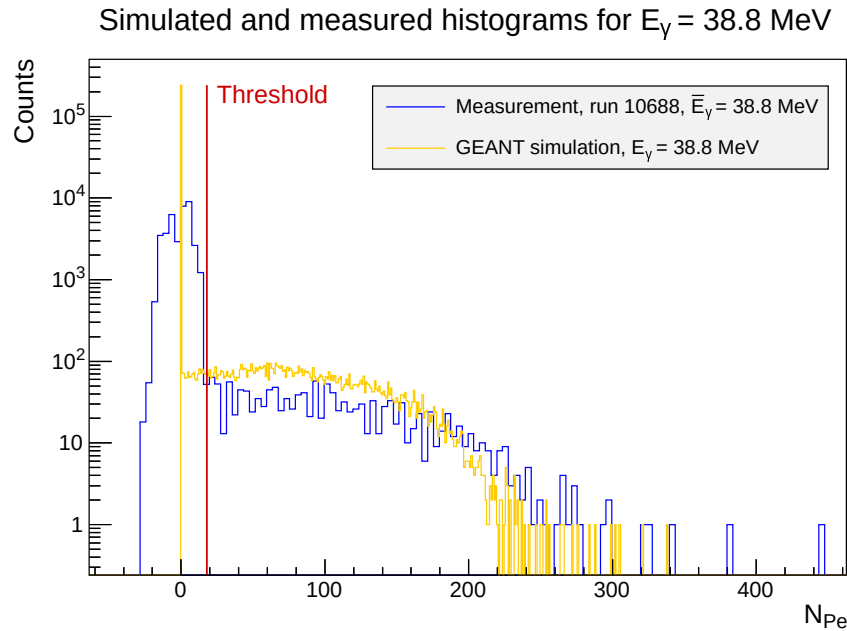
FIGURE 5.32: Example of a QDC spectrum with indicated threshold separating pedestal from signal superimposed with simulation data for the same photon energy as the mean tagged photon energy in the experiment.

signal during the analysis might be explained by low signals disappearing in the electronic noise pedestal and thus not contributing to the mean value. High electronic noise —possibly due to ground loops— was an issue during the experiment, which is manifested in the double pedestal peak in the histograms.

In conclusion, it can be said that in terms of signals caused in the P2 detector prototype, photonic background is suppressed by a factor of 25 compared to signals due to electrons, even for photon energies of 60 MeV or higher.
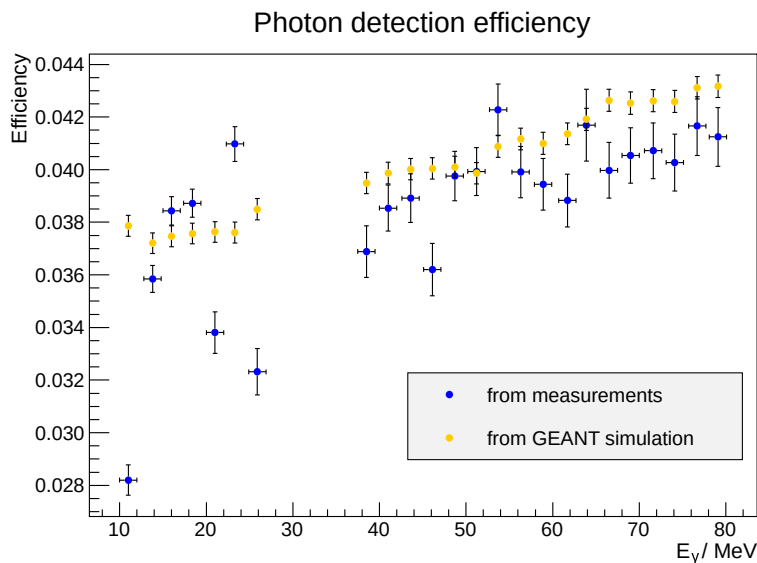
(a) Measured photon detection efficiency of the 435 mm wedged P2 detector prototype compared to GEANT4 simulation results
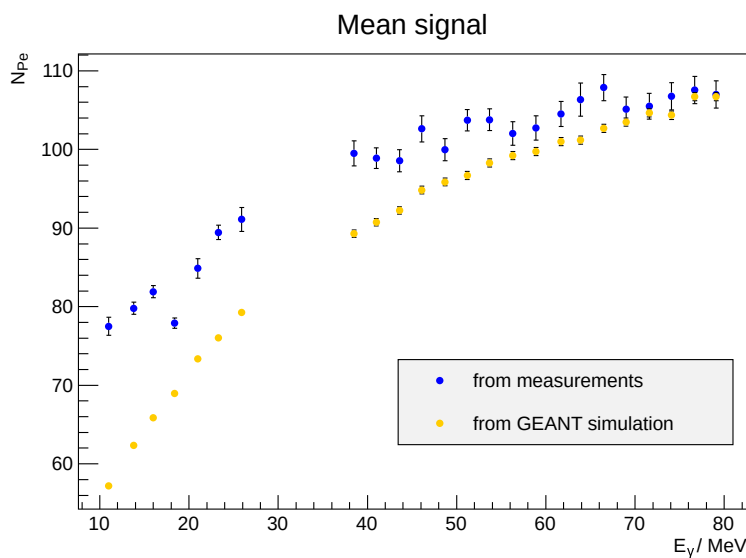
(b) Mean number of photoelectrons emitted from the PMT cathode per photon incidence, which caused a measurable signal in the quartz detector

FIGURE 5.33: Photon detection efficiency and mean signal plotted against the mean photon energy

5.7 Conclusion of the Detector Tests

The MAMI beam tests showed that it is possible to build a functional fused silica Cherenkov detector for the P2 Experiment. Several materials and geometries were tested, and their signal yield to electron impacts was compared. The prototype tests at the MAMI electron beam have shown that the requirement discussed in section 5.1 can be achieved.

For its good performance and practicability, I propose a detector of Geometry III. It combines a 450 mm long tapered part to cover the detector ring with minimal gaps between the bars and a straight section serving as light guide. As casing material, a radiation hard aluminium reflector like Alanod 4300UP is recommendable because of its exceptional reflectivity in the UV region. The 9305QKMB photomultipliers by Electron Tubes proved to have sufficient quantum efficiency to convert the Cherenkov light into a large enough electric signal. A prototype with these hardware components has been tested during the beamtime in 03/2019. Its specifications are implemented into the GEANT4 detector response simulation described in chapter 7. The resulting detector response database represents this detector prototype's photoelectron output.

Chapter 6

Radiation Hardness of Fused Silica

The hardness of all materials and devices used in the detector to radiation from electrons, photons and hadrons is paramount for a persistently satisfactory signal yield.

According to [52] one can use fused silica as a Cherenkov radiator for a detector of high radiation resistance. Fused silica is an amorphous rather than crystalline material and subject to a variety of changes under the influence of high radiation doses. The defects caused in the material are harder to describe and to quantify than in a crystalline structure. As fused silica is frequently utilized for lenses in high power laser applications, they have been studied extensively for laser induced radiation damage, but not very much for ionising radiation like high energy electrons.

For the application as a Cherenkov medium in the P2 Experiment, potential degradation of optical properties is most critical. The PANDA Cherenkov group have studied the decrease of optical transmittance of different types of fused silica after their exposure to ionising radiation. Absorption bands (color centres) were formed due to irradiation of the material rendering it opaque to certain wavelengths. However, these findings cannot be directly transferred to our case, as the fused silica pieces were irradiated with photons stemming from a Co-60 source [53] and —in another study— with 150 MeV protons at KVI's cyclotron in Groningen in the Netherlands [54]. In the P2 Experiment the quartz bars are going to be exposed to a variety of particles, primarily electrons, photons, and neutrons. The signal electrons themselves are a source of high radiation dose, which cannot be avoided. The mechanisms of optical degradation due to radiation induced color centres is still not very well understood and could differ drastically depending on the type of radiation [55]. This led to the decision to study the hardness of the potential Cherenkov medium to radiation of a similar energy as the signal electrons in the

P2 Experiment and a total dose comparable to the cumulative lifetime dose of the experiment.

6.1 Radiation Hardness Tests of Fused Silica at MAMI

At nominal operating conditions of the P2 Experiment, the area of $150\,\mathrm{cm}$ around the center of the quartz bar is going to be exposed to an average electron rate of $1.45 \times 10^7\,\mathrm{s^{-1}\,cm^{-2}}$. During the proposed runtime of the experiment this rate results to a number of electrons

$$n_e^{\mathrm{P2}} \approx 5.2 \times 10^{14}\,\mathrm{cm^{-2}} \tag{6.1}$$

traversing the quartz per square centimetre. Approximately 75% of these electrons are primary electrons from an elastic scattering process in the target. The energy distribution of these electrons at the location of the detector is shown in figure 6.1. The kinetic energies are mostly in the range of $120\,\mathrm{MeV}$ to $140\,\mathrm{MeV}$.

The aim of the radiation hardness tests is to inspect whether irradiation with electrons of a comparable energy and number as in the P2 Experiment is going to destroy the quartz bars or alter their optical properties to an alarming degree. Two samples —one of Heraeus Spectrosil 2000, one of Suprasil 3A— of $1\,\mathrm{cm}$ thick and $7\,\mathrm{cm}$ by $10\,\mathrm{cm}$ wide fused silica were irradiated with the MAMI electron beam

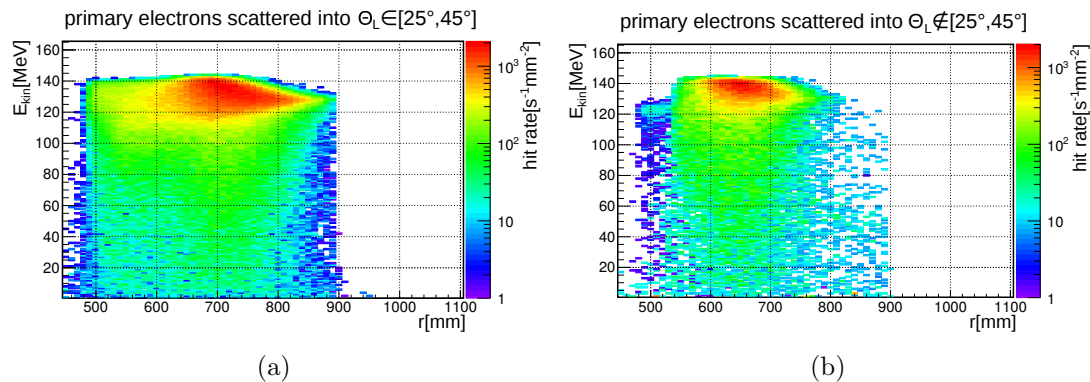(a)   (b)

FIGURE 6.1: Energy distribution of the elastically scattered electrons hitting the detector plane. The graphics show that the vast majority of the electrons have energies in the range of $E_{\mathrm{kin}} \in [130\,\mathrm{MeV}, 145\,\mathrm{MeV}]$. Picture courtesy of D. Becker.
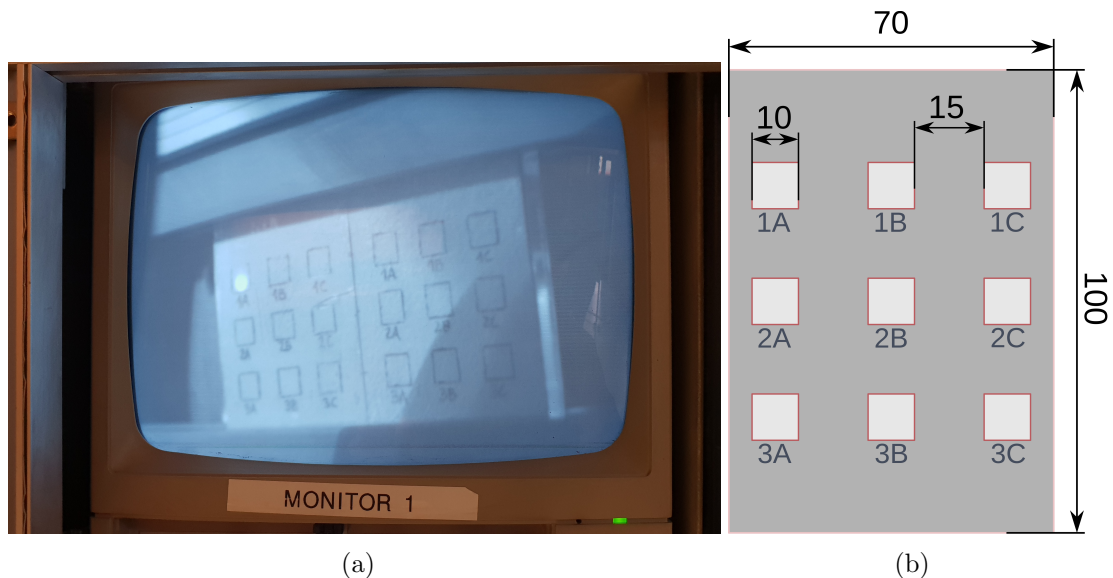
FIGURE 6.2: Left: Photo of the monitor in the MAMI control room showing the camera picture of the quartz samples in the beam with the beam spot on the screen. Right: Quartz sample dimensions and locations of the areas that were irradiated.

at $180\,\mathrm{MeV}$ at the X1 beam dump. The electron beam was periodically rastered over square areas of $1\,\mathrm{cm}$ by $1\,\mathrm{cm}$. On each sample 4 such squares were irradiated. A $0.4\,\mathrm{mm}$ thin $BaSO_4$-coated Aluminium sheet, on which 9 squares were indicated, was positioned in front of each quartz sample and a camera was pointed onto the screen. The camera picture was visible on a monitor in the MAMI control room, so that the electron beam spot could be seen and —using the Wedler[1]— directed onto the desired squares. The location of the squares on the quartz pieces as well as a photograph of the monitor in the MAMI control room are shown in figure 6.2.

Table 6.1 shows a list of the squares on both samples along with the beam current and the irradiation time. The number of electrons resulting from the beam current and time via

$$n_e = \frac{I \cdot t}{e} \tag{6.2}$$

where e is the elementary charge ($e \approx 1.6022 \times 10^{-19}\,\mathrm{C}$) is listed in the fourth column. The factor by which this number of electrons compares to the electrons which are going to hit the detector material during the run time of the experiment of $10\,000\,\mathrm{h}$ is found in the rightmost column.

The transmission spectra of the fused silica material at all 9 squares of the samples were measured before and after the irradiation with the spectrophotometer and measurement method described in 4.2.1.1. For each square, 6 measurement runs were taken, each with a different orientation of the sample inside the sample

---

[1]At MAMI small dipole magnets for the correction of the beam position are called "Wedler".

	square	I [nA]	t [s]	n_e	n_e/n_e^{P2}
	2B	100	415	$2.6 \cdot 10^{14}$	0.5
Suprasil 3A	3C	20	4150	$5.2 \cdot 10^{14}$	1
	3A	100	4150	$2.6 \cdot 10^{15}$	5
	1A	100	8300	$5.2 \cdot 10^{15}$	10

	square	I [nA]	t [s]	n_e	n_e/n_e^{P2}
	1A	20	2075	$2.6 \cdot 10^{14}$	0.5
Spectrosil 2000	3A	20	4150	$5.2 \cdot 10^{14}$	1
	3C	100	4150	$2.6 \cdot 10^{15}$	5
	1C	100	8300	$5.2 \cdot 10^{15}$	10

TABLE 6.1: Irradiated squares on the fused silica samples of Suprasil 2A and Spectrosil 2000 respectively. For each square the beam current and irradiation time is given. n_e is the resulting number of electrons hitting the sample during the irradiation. The right most column is approximately the ratio of this number of electrons to the number of electrons hitting one cm^2 during the planned 10 000 h of data taking in the P2 Experiment.

compartment. The transmittance data as shown in figure 6.3 is the arithmetic mean of these 6 measurements and the error is obtained from the deviation.

Figure 6.3 contains plots of the spectral transmittance of the quartz samples measured at the irradiated areas. As the transmittance for Spectrosil 2000 and Suprasil 2A before irradiation do not differ significantly, only one of the transmission spectra of the material before the irradiation is shown in black, and the Fresnel curve is added to clarify that this part of the light loss is due to surface reflection. The relative transmittance losses caused by the radiation is the difference of the transmittance measurements before $(T_b(\lambda))$ and after $(T_a(\lambda))$ the irradiation put in relation to the original transmittance:

$$\Delta T(\lambda) = \frac{T_b(\lambda) - T_a(\lambda)}{T_b(\lambda)} \tag{6.3}$$

These transmittance losses are plotted in figure 6.4. The spectra show three radiation induced absorption lines at $\lambda \approx 210\,\mathrm{nm}$, $\lambda \approx 270\,\mathrm{nm}$, and $\lambda \approx 630\,\mathrm{nm}$. With regard to all three of these color centres, the color transmittance loss is more severe in Suprasil than it is in Spectrosil. The color centers at $\lambda \approx 210\,\mathrm{nm}$ and $\lambda \approx 270\,\mathrm{nm}$ are much more pronounced than the one at $\lambda \approx 630\,\mathrm{nm}$. Light loss in the UV region is most detrimental for a Cherenkov detector. Therefore a more
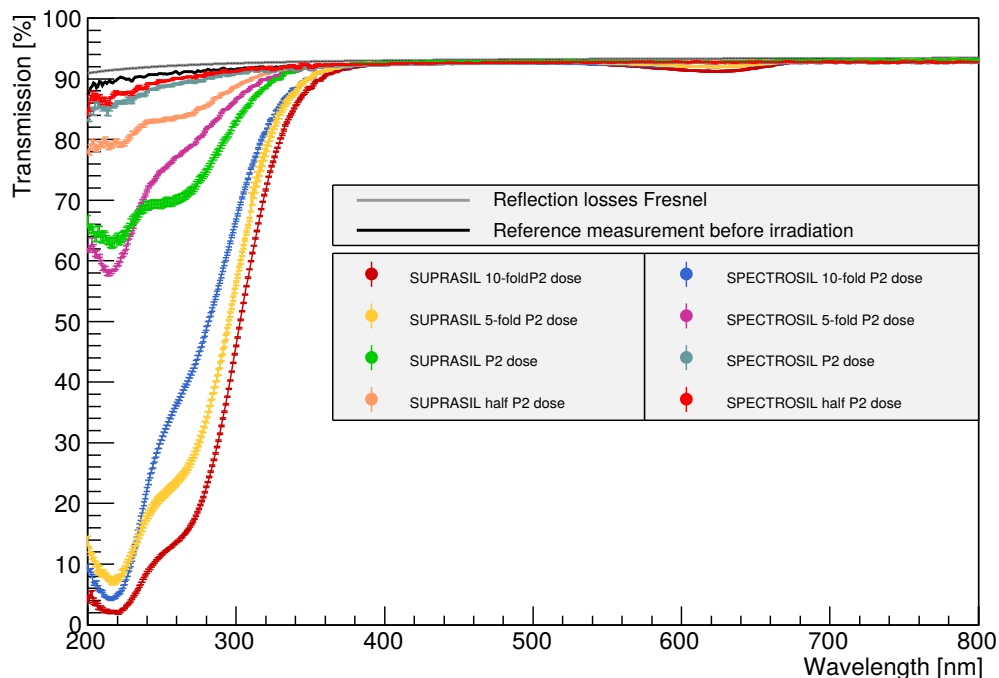
FIGURE 6.3: Raw transmittance data measured with the spectrophotometer before (black curve) and after the irradiation with 180 MeV electrons. The coloured data points are the transmittance of the fused silica samples irradiated with different doses, which are put in relation with the expected number of electrons hitting the amorphous quartz detector during 10 000 h of data taking time.

detailed view of the same data in the ultraviolet wavelength region is shown in figure 6.5.

The degradation of the transparency especially in the UV region is evident, and it is expected that the fused silica bars in the P2 Experiment will suffer from optical transmittance degradation during the run time of the experiment. We can also see that Suprasil 3A is more sensitive to electron irradiation than Spectrosil 2000. The two curves labelled "no dose" refer to cross-check transmission measurements performed after the irradiation of the samples but at a spot 15 mm away from any spot directly hit by the MAMI beam. While Spectrosil shows no significant degradation, the Suprasil sample lost up to 10% of its transmittance in the deep UV region, probably due to secondary particles produced in the beam dump.

6.1.1 Expected Signal Loss due to Radiation Damage

Using the measured transmission spectra of Spectrosil 2000 after the irradiation, Monte-Carlo simulations of the expected signal yield of Spectrosil detectors were
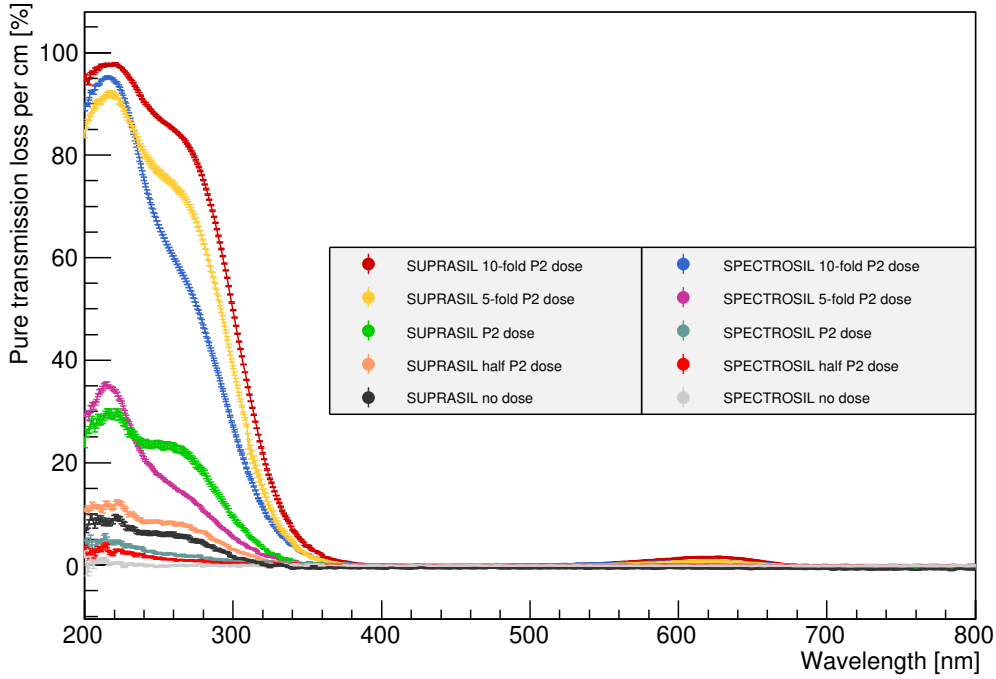
FIGURE 6.4: Transmission losses of the samples at the irradiated squares with respect to the transmittance measurement before the irradiation at the X1 beam dump. The measurements labelled "no dose" are taken after the irradiation of the samples but at places, which have not directly been hit by the beam. The radiation doses have been put into relation to the approximated P2 doses.

made. The data was generated employing the methods described in chapter 7 supplying the GEANT4 simulation with transmittance data measured before and after the irradiation of the sample. Figure 6.6 shows a comparison of the Cherenkov photons arriving at the PMT cathode of the Cherenkov detector for a Spectrosil bar with the original transmittance data and the degraded transmittance due to irradiation with $5.2 \cdot 10^{14}$ 180 MeV electrons.

The employed GEANT4 simulation was equipped with the detector Geometry III, light sensor data of the Hamamatsu R11410 PMT, and reflectivity of Alanod 4300UP for the detector bar wrapping material. With the original spectral transparency (listed in Appendix A) the signal yield to electrons hitting the center of the sensitive detector area perpendicularly in terms of photoelectrons emitted from the PMT cathode is

$$N_{\mathrm{Pe}}^{\mathrm{before}} = 136 \tag{6.4}$$

This number decreases to

$$N_{\mathrm{Pe}}^{\mathrm{after}} = 39 \tag{6.5}$$
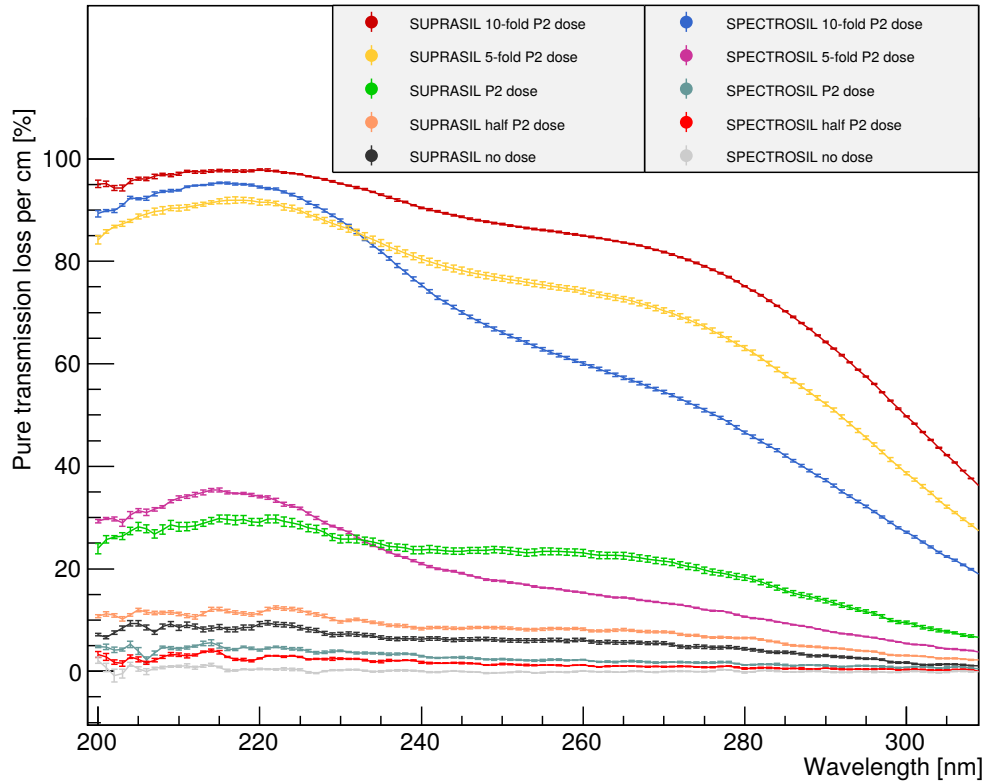
FIGURE 6.5: Detailed focus on the UV region of data shown in figure 6.4

for the altered transmittance spectrum for Spectrosil after "one P2 dose". The simulation predicts a drastic signal yield decrease with time. The number of photons emitted from the PMT cathode per electron incidence will fall short of the determined critical number of $N_{\text{Pe}} = 50$ within approximately one P2 lifetime.

6.1.2 Radiation Dose

A radiation dose can be calculated using the mass stopping power of the material exerted on the traversing particle by

$$D = \frac{1}{\rho} \frac{dE}{dx} n_e \cdot \frac{1}{A} \tag{6.6}$$

where A is the irradiated area. The mass stopping power $S(E) = \frac{1}{\rho} \frac{dE}{dx}$ of electrons in fused silica is plotted in 6.7. The figure shows total stopping power as well as the pure collision stopping power data accessible at the ESTAR database of the National Institute of Standards and Technology [56]. Additionally the graphic contains the collision stopping power calculated according to ICRU report 90 [57], which corresponds to the NIST data. Concerning the radiative stopping power

Monte-Carlo simulation of the Cherenkov photon spectrum at the location of the PMT cathode

FIGURE 6.6: Spectrum of the Cherenkov photons at the place of the photo-cathode. Data is generated by means of the GEANT4 simulation described in chapter 7. Fo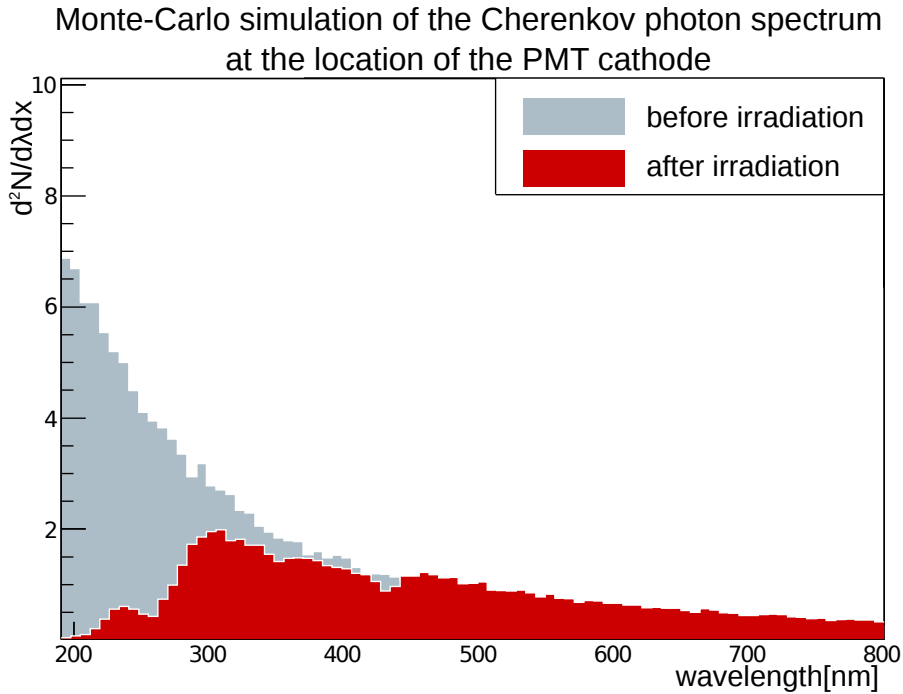r the grey histogram the transmittance data of fused silica before radiation damage is used, for the red histogram the transmittance of Spectrosil 2000 after the irradiation with one lifetime dose equivalent of electrons ($5.2 \cdot 10^{14}$ 180 MeV) is used.

exerted onto the electrons, the publications by Berger and Selzer [58] and the textbook by Krane [59] do not contain all higher order correction used by NIST and we were not able to completely reproduce the NIST values using only these models.

For the calculation of the radiation dose imposed onto the fused silica during the P2 Experiment the stopping power $S(E) = 6.7 \, \mathrm{MeV \, cm^3/g}$ according to NIST for 140 MeV electrons was used. The mass density of fused silica is $\rho = 2.203 \, \mathrm{g \, /cm^3}$. With these values the radiation dose deposited by $5.2 \cdot 10^{14}$ electrons is

$$D_{\mathrm{P2}} \approx 55 \, \mathrm{Mrad} \qquad (6.7)$$

At the location of the sample irradiation end point at MAMI the beam energy cannot be adjusted to energies lower than the RTM2 extraction energy without extensive changes to the accelerator operation. The irradiation therefore took place with 180 MeV electrons. As the total stopping power according to NIST for electrons of 180 MeV is higher than the one for 140 MeV electrons by a factor of 1.2, the radiation dose called "P2 dose" is exceeded by approximately the same factor. The elastically scattered electrons at the place of the P2 main detector
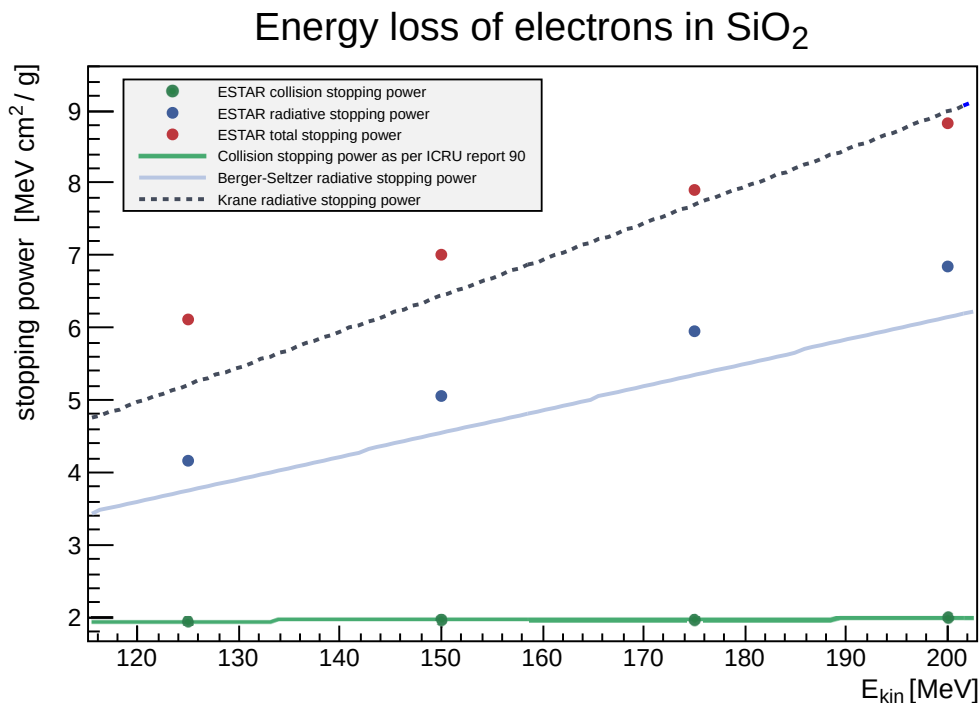
FIGURE 6.7: Stopping power of fused silica for electrons

are distributed about their energy expectation value of 140 MeV. This is not the case for the secondary and background electrons, which have been included into the total rate. These electrons are of significantly lower energies and make up 25% of the electrons hitting the detector plane but deposit a smaller dose per electron. What I call "P2 dose" is therefore overestimated by up to a factor of 1.5 compared to the real dose during the 10 000 h run time. Considering that the detector will also be hit by electrons during test and commissioning runs and an increase of the gross measurement time due to dead times, it makes sense to consider this potential overestimation as "safety factor". In this context it should be mentioned that during the P2 Experiment the fused silica will be exposed not only to electrons but also to background consisting of photons and neutrons. Radiation damage stemming from these particles has not been investigated herein.

6.1.3 Attempts to Reverse the Radiation Damage

The measurements suggest that the quartz transmittance will decrease significantly during the data taking time of the P2 Experiment. As predicted by GEANT4 simulations this will lead to deterioration of the signal yield, and it is of paramount interest to reverse this effect without having to disassemble the detector or even completely renew the Cherenkov bars. Optical and thermal bleaching are two methods which have proven to be effective in reversing radiation damage in
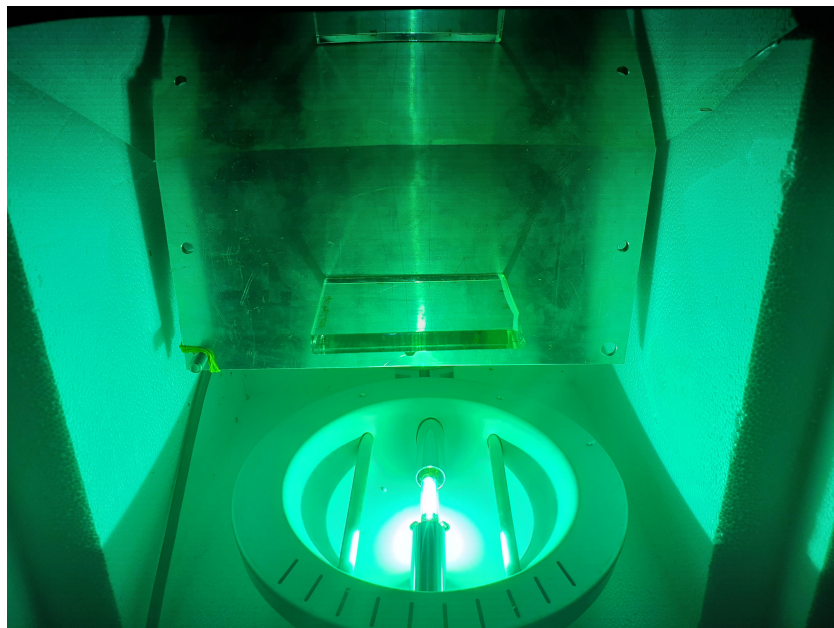
FIGURE 6.8: Fused silica sample in a sun lamp from the 1960's as an attempt
to reverse the radiation induced transmittance decrease.

the form of absorption bands in fused silica and crystalline quartz [60]. Thermal
bleaching means heating the fused silica material. In the publication [60] color
centres caused by gamma irradiation of a cobalt-60 source have shown to partly
heal when the sample was "baked" for several hours at temperatures of approx-
imately 350 °C. Optical bleaching refers to exposing the sample to wavelengths
corresponding to the absorption lines.

After unsuccessfully trying to heal the radiation damaged quartz bars in the July
sun for 10 days (50° northern hemisphere, cloudless sky), an attempt was made
with a sun lamp from the 1960's (no further specifications known). The photograph
in figure 6.8 shows the Spectrosil 2000 sample in the sun lamp, where it was
illuminated for 26 h. The spectra in figures 6.9, 6.10, and 6.11 show the quartz
transmittance measured in the spectrophotometer before and after this optical
bleaching attempt. For reference the transmittance of the 1 cm fused silica sample
before electron irradiation at MAMI is plotted in the same graph.

Figure 6.9 shows that the formation of absorption bands due to irradiation with
one nominal "P2 dose" was reversed by the illumination with UV light. Regarding
the sample, which had been irradiated with approximately 5 P2 doses ($2.6 \cdot 10^{15}$
electrons with 180 MeV) the transmittance at $\lambda = 218$ nm, which had been re-
duced to 57%, was improved by UV light healing to 80%. The irradiation of
approximately 10 P2 doses had turned the quartz almost completely opaque (10%
remaining transmittance) at $\lambda = 210$ nm. Optical healing for 26 h was able to
partly reverse this effect and restore the quartz' transparency to 30%.

FIGURE 6.9: Transmission spectra of the 1 cm Spectrosil 2000 sample at the location 3A, where it was irradiated with $5.2 \cdot 10^{14}$ electrons with $180\,\text{MeV}$ energy before and after optical bleaching for $26\,\text{h}$ in the sun lamp shown in figure 6.8. The spectrum before radiation damage is shown in black.
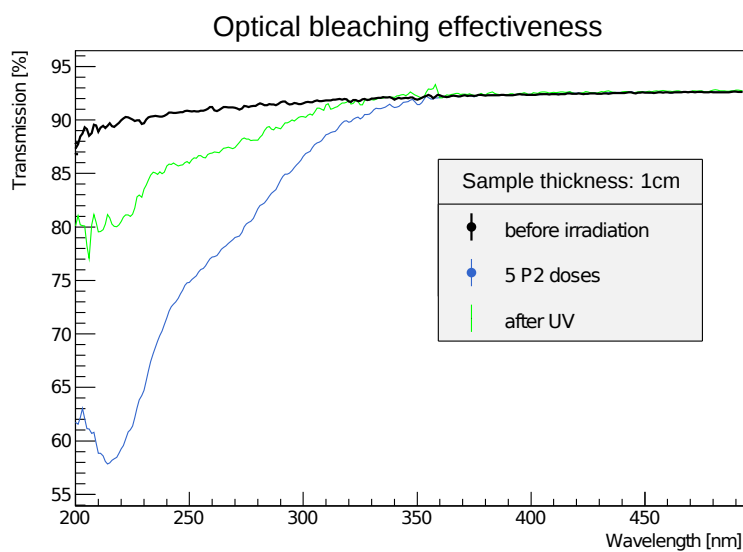
FIGURE 6.10: Transmission spectra of the 1 cm Spectrosil 2000 sample at the location 3C, where it was irradiated with $2.6 \cdot 10^{15}$ electrons with $180\,\text{MeV}$ energy before and after optical bleaching for $26\,\text{h}$ in the sun lamp shown in figure 6.8. The spectrum before radiation damage is shown in black.
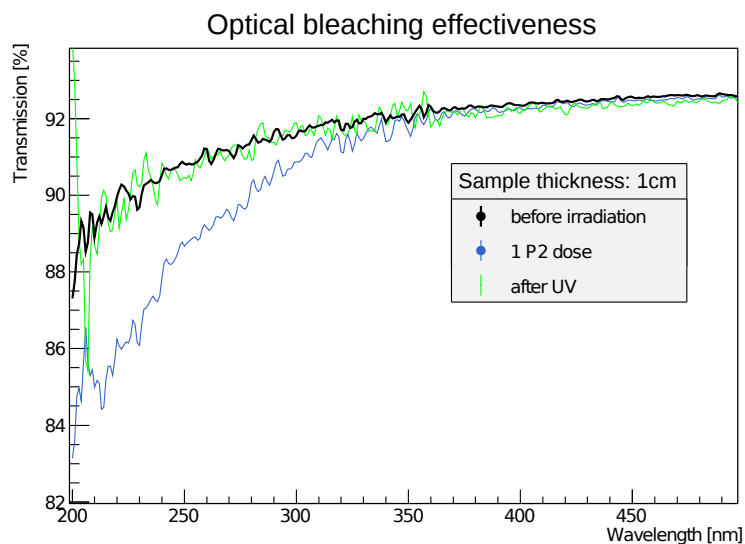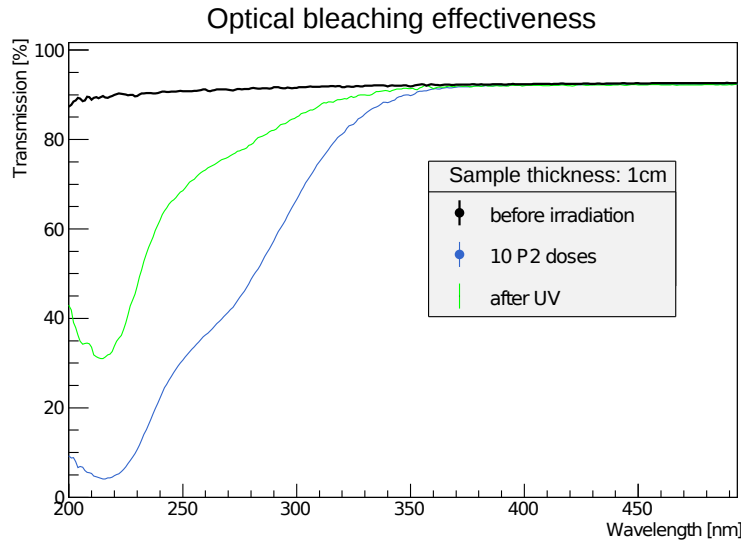
FIGURE 6.11: Transmission spectra of the 1 cm Spectrosil 2000 sample at the location 1C, where it was irradiated with $5.2 \cdot 10^{15}$ electrons with 180 MeV energy before and after optical bleaching for 26 h in the sun lamp shown in figure 6.8. The spectrum before radiation damage is shown in black.

6.1.4 Conclusion of Radiation Hardness Tests and Simulations

Radiation damage of the fused silica induced by incident electrons onto the detector bars are going to decrease the transmittance of the quartz to a degree that will drastically reduce the signal output. It is highly advised to further examine methods of reversing the radiation damage, and to construct the experiment in a way which makes it possible to access and exchange the quartz bars. The A4 Experiment at Mainz observed radiation induced absorption bands in their lead fluoride Cherenkov crystals during the runtime of the experiment. The transmittance losses were observed to be reversible by exposition of the crystals to blue light [61]. Regular bleaching periods were scheduled. By placing the blue light lamps directly into the detector to irradiate the crystals at the facility the necessity of dismantling the detector was avoided. The photograph in 6.12 shows the experimental setup during this procedure. As the absorption bands in the P2 fused silica bars are at lower wavelengths than the ones in the A4 lead fluoride bars, a similar solution using UV lamps could be of advantage.

FIGURE 6.12: A4 lead fluoride detector during illumination with blue light for the purpose of optical bleaching. Dedicated periods for this restoration of the crystal tranmittance were scheduled during the runtime of the experiment.

Chapter 7

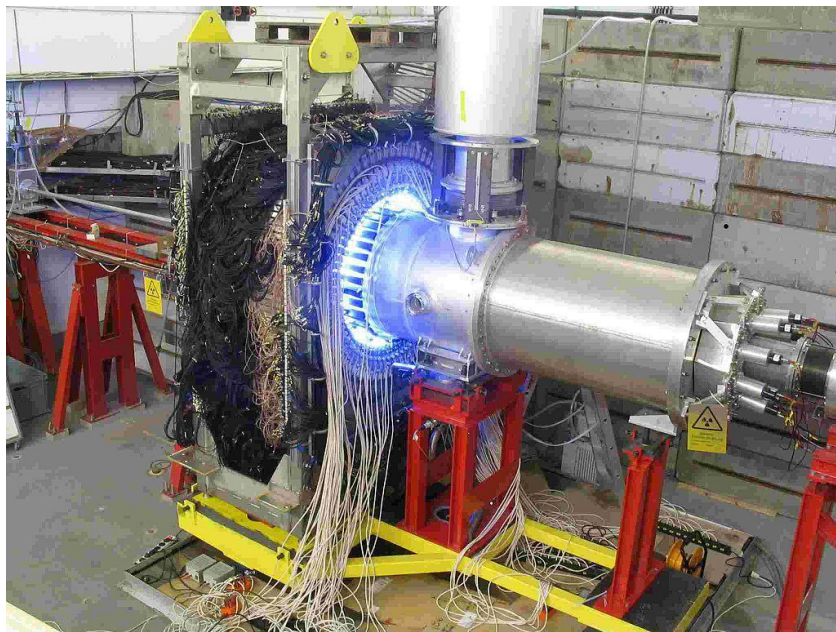# P2 Detector Response Simulation with GEANT4

During the beamtimes at MAMI described in chapter 5 the detector element prototype was tested for its response to ultrarelativistic electrons and photons of energies between $10\,\mathrm{MeV}$ and $90\,\mathrm{MeV}$. However, the quartz Cherenkov detector is going to be exposed to a much wider variety of signal and background particles (cf. particle hit rates on the detector shown in figure 8.2). In order to quantify the detector response to all types of particles of all energies and impact angles expected in the experiment a GEANT4 Monte-Carlo simulation was established, in which we can define the properties of the primary particle hitting the detector in terms of particle type, energy, and momentum, and obtain the detector output expressed in terms of the number of photoelectrons from the light sensor's cathode.

This chapter first gives an overview of the GEANT4 simulation and the data analysis method. The sections 7.1.1 to 7.1.4 go into detail regarding the method of providing primary particle characteristics, material and geometry data as well as information about the physical processes to consider to the program. Pragmatic concessions made by neglecting and simplifying small physical influences onto the result of the simulation are covered in section 7.2. A comparison of simulation results to theoretically expected behaviour as well as measurement data from the MAMI beamtimes is made and systematic errors are discussed in section 7.4.

By means of the detector response simulation a database containing the signal yield to the incidence of all relevant particles in the P2 Experiment was established. This database is the subject of section 7.5.
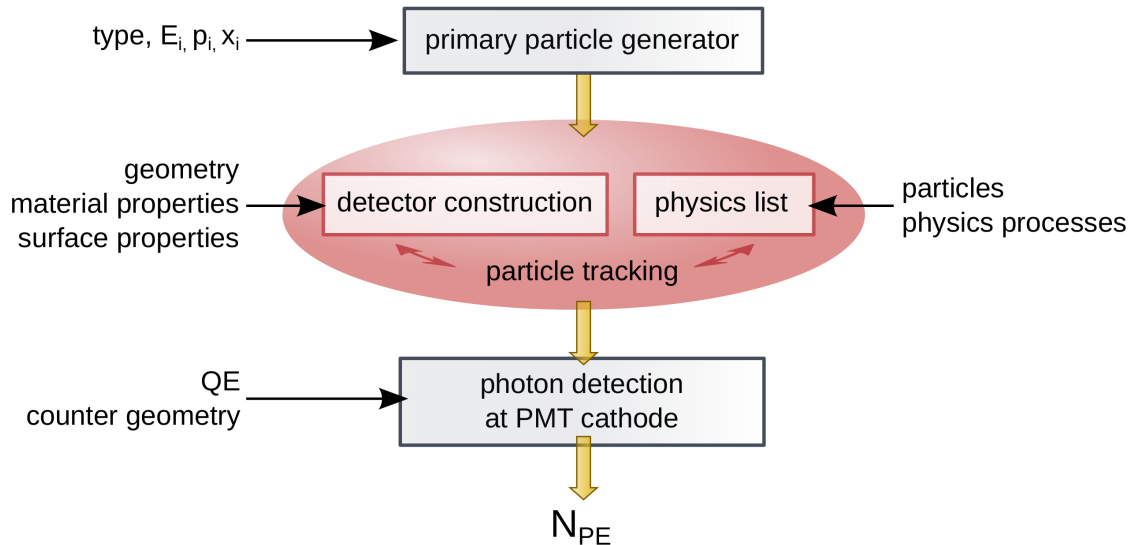
FIGURE 7.1: Overview of the GEANT4 P2 detector response simulation stucture

7.1   Details of the Simulation

The schematic in figure 7.1 shows the basic structure of the P2 detector response simulation. The setup geometry, material properties, and physics effects were implied in as much conformity with the experimental setup of the P2 detector prototype test[1] as feasible within the frame of this work. The P2 detector is going to consist of 72 modules arranged in a ring. As the P2 experimental setup will be symmetric with respect to rotations about the z-axis, simulating the response of one detector element is sufficient.

A so-called "event" in the simulation is tantamount to the generation of one primary particle. The key properties of that particle (particle type, kinetic energy, and momentum) are chosen by the user depending on the purpose of the simulation run. In order to enable the software to perform a realistic particle tracking, the geometry and material properties of all components of the setup have to be implied. This includes chemical and physical as well as optical properties and the nature and quality of material boundaries (surfaces). Aside from this, a list of particles to be tracked is provided to the simulation, along with the physical processes these particles can undergo. At the location of the PMT, a counter volume records passing optical photons and their wavelengths. The program then —using input from data files containing the spectral quantum efficiency as well as spatial cathode sensitivity of the photomultiplier— determines the number of photoelectrons from the PMT cathode.

---

[1]see chapter 5

7.1.1 Definition of the Primary Particle Hitting the Detector

The most important aspect when examining the performance of the P2 detector is the response to particles originating from signal and background events. In the setup presented herein the background is dominated by photons. Therefore the GEANT4 simulation was run for various energies and momenta of these primary particles in order to create a comprehensive database containing the PMT signal output for the most important particles hitting the detector during the P2 Experiment.

The GEANT4 package provides a database[2] which contains data like particle name, mass, charge, lifetime and spin of more than 100 particle types. This information is then passed to the GEANT4 class, in which the user defines the primary particle[3]. Initial kinetic energy E_i, initial momentum p_i and initial location x_i are assigned to the particle by the user.

The detector response to positrons was not simulated. In order to save computing time it is instead assumed equal to the response to electrons of the same energy, initial location and momentum.

7.1.2 Physics Processes and Particle Tracking

It is mandatory for the user to provide a physics list, which contains all particles one wishes to be tracked. Desired physics processes can be assigned to these particles. All particles and processes active in the the P2 detector simulation are represented in table 7.1.

Aside from electromagnetic, hadronic, and decay processes GEANT4 contains the ability to simulate optical photon processes. In this context it allows to specify optical properties for materials and surfaces as well as optical processes one wishes to investigate. GEANT4 provides wave optics in such a way that photons belonging to the GEANT4 class "G4OpticalPhoton" are subject to reflection and refraction. For such particles, the simulation also keeps track of their polarization. In this regard the G4OpticalPhoton and the G4Gamma are treated in substantially different ways and there is no smooth transition between them.

Within GEANT4 optical photons can be produced via the Cherenkov effect, via scintillation, and via transition radiation. In fused silica, the Cherenkov effect is the only relevant photon creation process. The created optical photons can then undergo the following optical processes:

---

[2]G4ParticleTable

[3]G4ParticleDefinition class

		transportation	pair production	compton scattering	photoeffect	multiple scattering	ionisation	bremsstrahlung	Cherenkov	absorption	boundary process
bosons	gamma particle	✓	✓	✓	✓						
	optical photon	✓								✓	✓
leptons	electron	✓				✓	✓	✓	✓		
	positron	✓				✓	✓	✓	✓		
	muon / antimuon	✓	✓			✓	✓	✓	✓		
				electro-magnetic					optical		

TABLE 7.1: List of particles active in the P2 detector response simulation along with the interactions they participate in

- Absorption

- Reflection and Refraction

- Rayleigh and Mie Scattering (neglected in this simulation)

Secondary particles may be created via

- Compton Scattering

- The Photoelectric Effect

- Gamma Conversion

7.1.3 Detector Geometry

GEANT4 offers classes for the definition of basic geometric shapes such as spheres, cuboids and extruded solids, but in order to implement more complex detector geometries and to quickly switch between different designs, a method to directly import 3-dimensional models from Computer Aided Design (CAD) software into the simulation is desirable. This is realised in the P2 detector simulation via an interface called CADMesh [62].

As a first step, a physical volume is defined, which contains all other components of the simulation. This volume represents the MESA hall, but as it is too complex and unnecessary to implement all parts of the accelerator and the P2 Experiment,
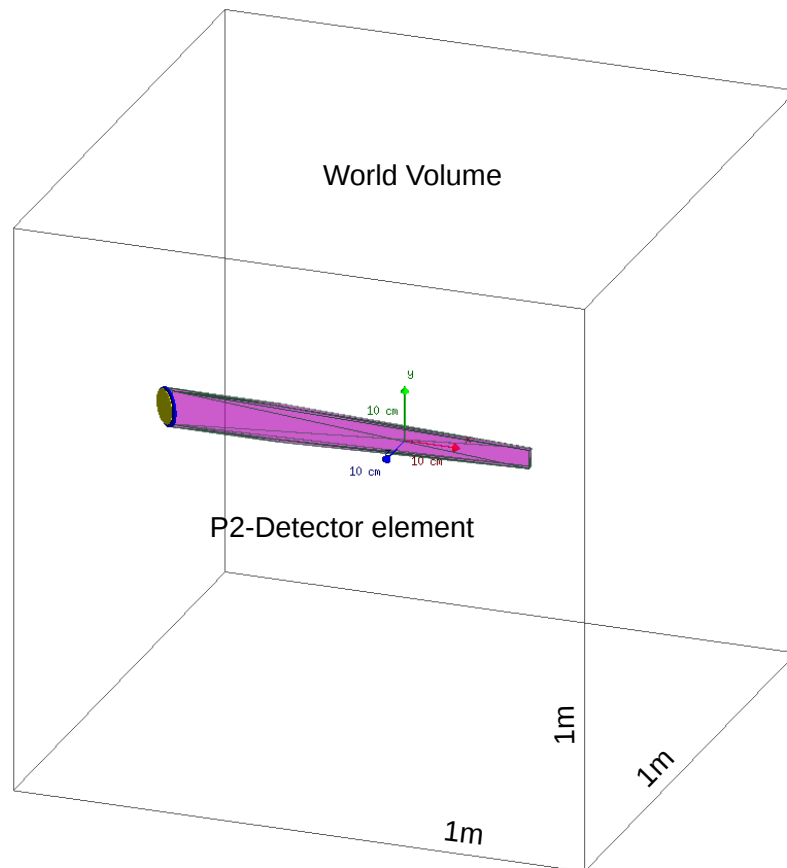
FIGURE 7.2: Visualization of the P2 detector prototype placed inside the simulation's "World Volume". See figure 7.3 for detailed view of the detector element.

a generic "World Volume" consisting of an air-filled cuboid of side length $1\,\mathrm{m}$ is used. As depicted in figure 7.2 the origin of a right-handed Cartesian coordinate system is placed in the center of this cube and its axes are parallel to the cube's edges. The z-axis is coextensive with the MESA beam in the experiment.

The P2 detector element is placed inside the World Volume in such a way that the spatial center (half way between the end face and the end of the wedged part) of its active detector part is congruent with the origin of the coordinate frame. The largest faces of the fused silica bar are orthogonal to the z-axis (beam direction) and the $45°$ cut is turned beam upstream, as visualized in figure 7.3. The detector parts are created by means of a commonly used CAD program called CATIA[4], and then exported via a tessellation algorithm as .stl-files[5]. This file format describes and approximates surfaces in terms of oriented triangles. The goodness can be determined by choosing the maximum distance between the model's surface and

---

[4]Dassault Systèmes, Vélizy-Villacoublay, France
[5]stereolithography-files

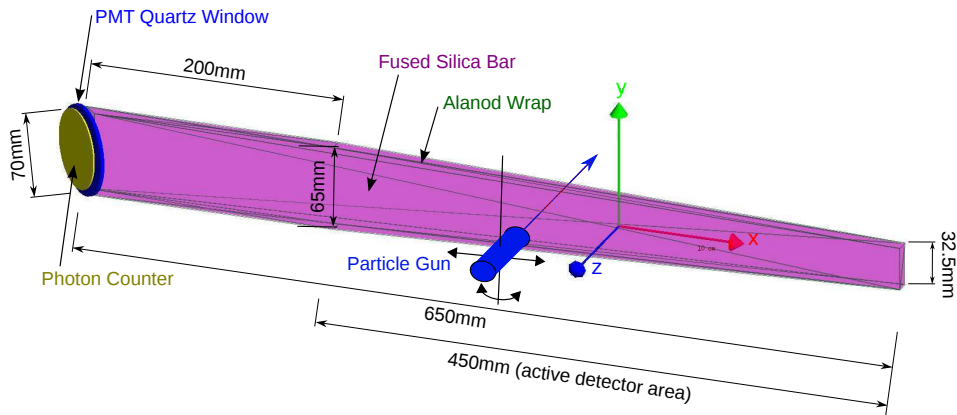FIGURE 7.3: Visualization of the P2 detector prototype. The wedged part is the active detector area, while the straight part closer to the PMT is going to be shielded by lead in the final experiment.

the approximated tessellated surface d_{max}. As the P2 detector module has no relevant curved surfaces, a value of $d_{max} = 0.1$ mm provides a good enough precision while not leading to extensive computational power. The .stl-files of each detector component can then be imported into the GEANT4 simulation.

Figure 7.3 shows a more detailed view of the detector element's geometry as implemented in the GEANT4 simulation. Neither the fused silica bar nor the wrapping material have any curved surfaces and can thus be precisely described by the tessellated surfaces. The reflective aluminium wrapping is visualized by a wireframe showing the boundaries of the triangular surfaces generated during the tessellation only, and the light tight vinyl wrap is not shown at all for sake of clarity. The PMT is not modelled in the simulation. Instead a photon counting flat cylindrical volume of 70 mm in diameter is placed behind another disc, which represents the PMT's fused silica window. All particles passing through this volume are counted and recorded along with properties of interest, which —depending on the investigation— are:

- Particle type

- Impact coordinates

- Momentum

- Energy / wavelength

All detector parts are static. When simulating the detector response to particle incidences at different positions on the quartz bar and at different angles, the primary particle source is moved and rotated.
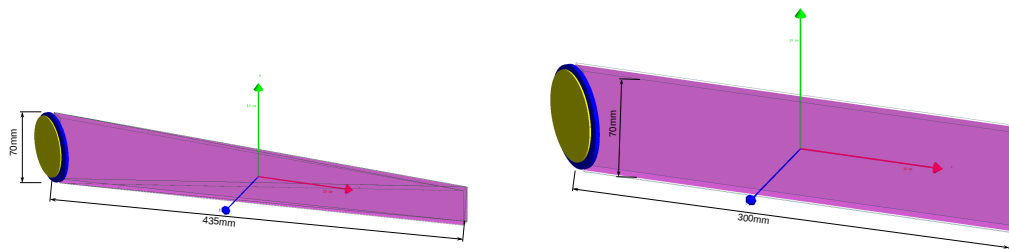
(a) 435 mm long quartz bar wedged over the full length with 45 ° cut (Geometry II).

(b) 300 mm cuboid quartz bar with 45 ° cut (Geometry I).

FIGURE 7.4: Detector geometries tested in the prototype tests at MAMI and in the GEANT4 simulations. All quartz bars are 10 mm thick. Depicted are: quartz bar with reflective wrapping (purple), PMT quartz window (blue) and detection volume of the simulation (yellow).

As the simulations and prototype tests were performed during the planning phase of the solenoid magnet and the solid angle to be covered by the quartz bars was still undergoing optimization procedures, three different detector geometries were examined both by simulation and experiment. The geometry and dimensions of the finally proposed prototype can be taken from figure 7.3, the two others are depicted in figure 7.4.

7.1.4 Material Properties

All particle creation and interaction processes listed in table 7.1 depend on material properties, which have to be implemented in the simulation. Like in nature a GEANT4 material consists of either an atomic or nuclear compound or a mixture thereof. The user first has to define the chemical isotopes which are contained in the material along with their atomic number and atomic mass. These isotopes are grouped into chemical elements. Chemical compounds are described by their chemical formula. If the material is a mixture, the code has to contain the percentage of all components.

Once a material is created in such a way, the user can assign macroscopic properties to it. These can be

- Mass density (mandatory)

- State of matter

- Temperature

- Pressure

Volume	Material		Z	A[g/mole]		ρ[g/cm^3]
World	Air	N$_2$	7	14.01	78%	1.29E-3
		O$_2$	8	16.00	22%	
Detector bar and PMT window	Fused silica	Si	14	28.09	SiO$_2$	2.20
		O	8	16.00		
Reflective wrap	Aluminium	Al	13	26.98	Al	2.70
Light tight wrap	Polyvinylchloride	C	6	12.01	C$_2$H$_3$Cl	1.39
		H	1	1.01		
		Cl	17	35.45		

TABLE 7.2: Materials of all detector components as defined in the GEANT4 detector response simulation. The components are implemented as geometric shapes (GEANT4 volumes) and material. Each material is defined by the chemical constituents along with their atomic charge number and atomic mass. The last column contains the mass density ρ of the material.

and optical properties like

- Index of refraction (mandatory for Cherenkov photon production)

- Optical photon absorption length

- Reflectivity

Table 7.2 lists all parts that are represented as volumes in the simulation along with the materials they consist of, information on what chemical elements and molecules they are composed of, and the materials' densities. All material temperatures and pressures are 293.15 K and 100 kPa. Thus the state of matter is gaseous for air and solid for all other materials.

7.1.4.1 Refractive Index

The emission spectrum of the Cherenkov process in GEANT4 is limited to the energy range, in which the refractive index of the Cherenkov medium is defined.

The refractive index is implemented in the detector definition by an array of values for a wavelength spectrum of 180 nm to 800 nm in steps of 20 nm. This spectral range was chosen, because the PMT's sensitivity drops to zero at 800 nm, and UV-light below 180 nm is not transmitted.

The spectral refractive index implemented into the simulation is tabulated in Appendix A.

7.1.4.2 Optical Absorption

In order to simulate bulk absorption processes, GEANT4 requires spectral absorption length data. The spectral absorption length $L_0(\lambda)$ of a material is defined as the distance travelled in the material, after which the initial spectral light intensity $I_0(\lambda)$ has dropped to $1/e$. The light intensity after $1\,\mathrm{cm}$ is then

$$I(\lambda) = I_0(\lambda)e^{-1\,\mathrm{cm}/L_0(\lambda)} \tag{7.1}$$

The optical transmittance per $1\,\mathrm{cm}$

$$T(\lambda) = \frac{I(\lambda)}{I_0(\lambda)} = e^{-\frac{1\,\mathrm{cm}}{L_0(\lambda)}} \tag{7.2}$$

is provided by the fused silica manufacturer and measured in section 4.2.1.1. The values used in the simulation are the ones provided for Spectrosil 2000 by Heraeus rounded to the fourth post decimal. These values are plotted in figure 7.5 and listed in Appendix A. They are passed to the GEANT4 detector response simulation and converted into values for the absorption length via

$$L_0 = -\frac{1\,\mathrm{cm}}{\ln T(\lambda)} \tag{7.3}$$

7.1.4.3 Surface Properties

Processes at boundaries between two materials include refraction and reflection. Since GEANT4 treats optical photons as particles, an optical boundary process can either be refraction or reflection. The simulation code must contain information on the type of transition between the two materials. In the case of fused silica and air we use the "dielectric-dielectric" process. Depending on the angle of incidence onto the surface and the refractive indices defined for both materials a photon of specific wavelength can then undergo total internal reflection, Fresnel reflection or Fresnel refraction.

Aside from perfectly plane surfaces, where the normal to the surface assumed by the boundary processes is perpendicular to the boundary at all positions, one can define a roughness of the surface, if the user chooses the GLISUR model and defines a value for the surface finish $p \in [0, 1]$ corresponding to a degree of polish. Figure 7.6 is a scheme of the principle. For each point of particle incidence $\vec{x}$ a random point $\vec{p}_r$ within the sphere of radius $(1-p)$ around $\vec{x}$ is generated, and the vector $\vec{p}_r - \vec{x}$ from the point of light incidence to this random point is added to the
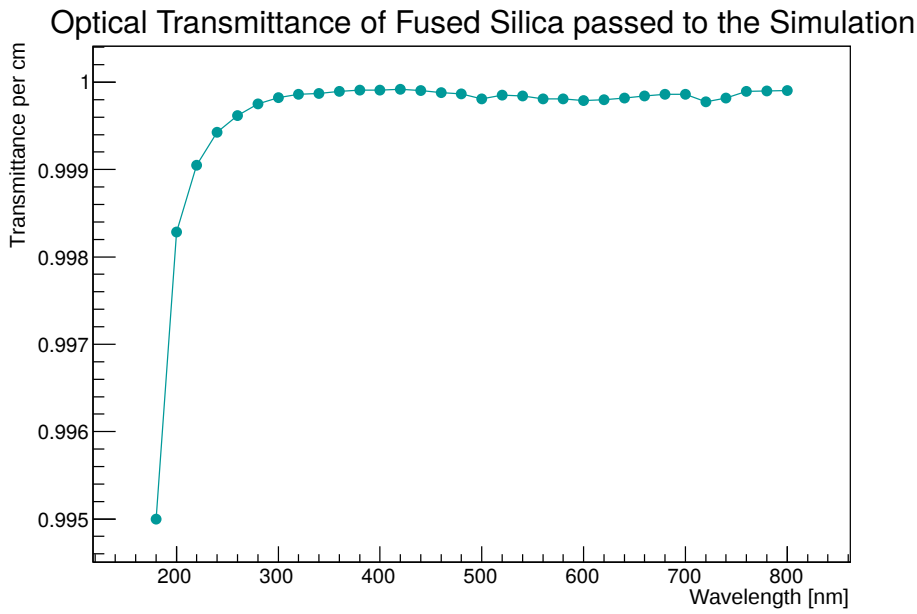
FIGURE 7.5: Spectral optical transmittance values as implemented in the
GEANT4 simulation

optical surface macro normal $\vec{n}_0$ defined by the detector geometry. The resulting
micro normal is

$$\vec{n}_e = \vec{n}_0 + \vec{p}_r \tag{7.4}$$

For optical processes at the surface the micro surface corresponding to $\vec{n}_e$ is used.
A value of $p = 1$ means perfectly polished and a value of $p = 0$ accordingly means
maximum roughness.

The quartz bars which are going to be implemented in the P2 Cherenkov detector
as well as the ones used for the prototypes are polished by their manufacturer
Heraeus Conamic in Hanau, Germany. The plane parallel sides as well as the planes
following the wedge are mechanically polished. Solely the optical outlet as well
as the opposite side are flame polished for technical reasons. Both methods lead
to a degree of polish described by Heraeus Conamic as "Schauglaspolitur" ("sight
glass polish"). This specification indicates the absence of visible inhomogeneities
and defects. It allows clear sight through the vitreous bars. As it is not possible to
translate this qualitative description into numerical surface parameters suitable for
Monte-Carlo simulations, the surface finish parameter in the GEANT4 GLISUR
model was varied and the results were compared to measurement results from
prototype tests. This was performed for all three detector geometries examined
in the MAMI beam tests. The angles of impact of the primary particle onto the
quartz surface were varied and the obtained simulation results were compared to
the angle scans with the respective detector prototype geometry. In this process
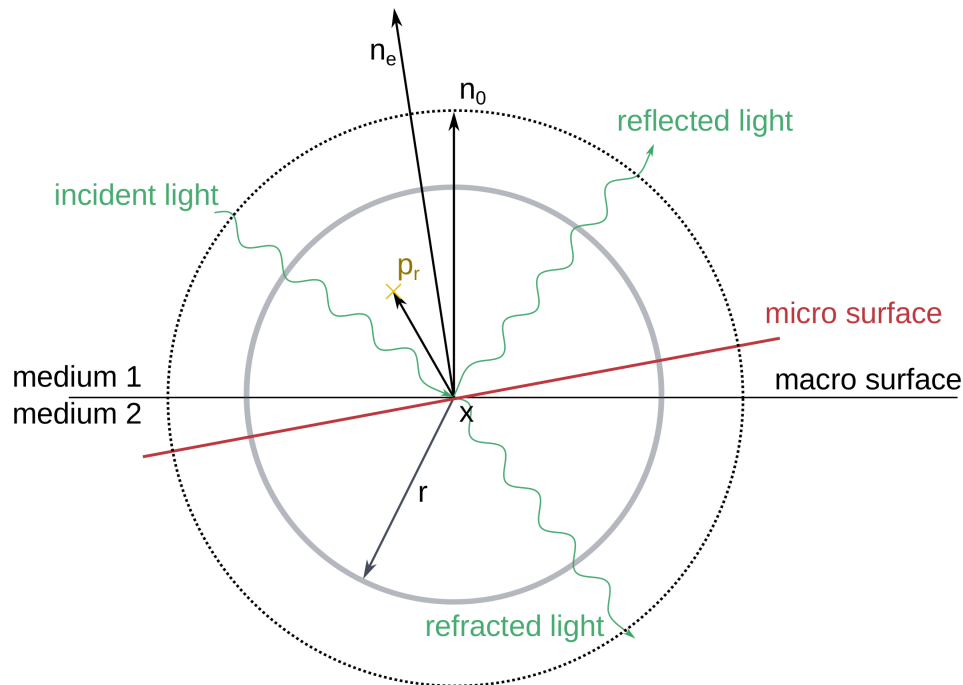
FIGURE 7.6: Graphical description of the GEANT4 GLISUR model. The choice of polish parameter p defines the radius $r = 1 - p$ of a sphere around the place of particle incidence. A point $\vec{p}_r$ within this is then randomly generated. The normal to the micro surface is then the sum of the normal to the macro surface and the position vector $\overrightarrow{xp_r}$.

the surface finish parameter was the only arbitrarily chosen parameter in the simulation.

Figures 7.7, 7.8, and 7.9 show the simulated detector response in terms of cathode photons as colored curves for detector geometry I, II, and III respectively.

All three angle scan measurement series show the characteristic "church steeple" shape, which the simulation is able to reproduce: The plots have a distinct maximum around an impact angle of $0°$, where the internal reflection of the Cherenkov light and the optical outlet are most effective. These maxima are more pronounced the better the surface polish. Minima are located around $\pm 45°$.

In order to determine the polishing parameter to be used in the simulation, simulation series for all three detector geometries were performed varying the polishing parameter p between 0.985 and 1 in steps of 0.005. An additional simulation was done with $p = 0.993$, as it showed that the best agreement between simulation and measurement is found with a polishing parameter between $p = 0.990$ and $p = 0.995$. No finer variation of the polishing parameter was performed, because all simulated curves exhibit a significant deviation from the measurement data, which cannot be compensated for by using a different polishing parameter. These deviations are likely to be caused by surface irregularities like protection chamfers,

(a) Measurement and simulations with various polishing parameters

(b) Difference between measurement and simulations
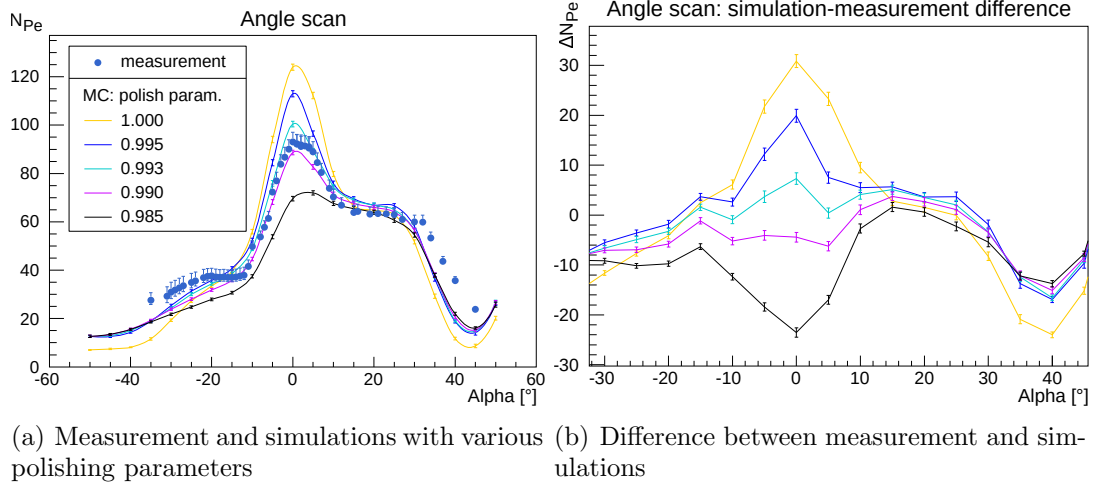
FIGURE 7.7: Measurement series with varying angle of electron impact from MAMI beamtime in 11/2014 (runs 899 to 956) compared to simulation data with corresponding configuration and varying polishing parameter. Quartz geometry I: 300 mm cuboid; PMT: ET9305QKMB Serial 518; Wrapping: Alanod 4300UP. Electron energy: 855 MeV

(a) Measurement and simulations with various polishing parameters

(b) Difference between measurement and simulations
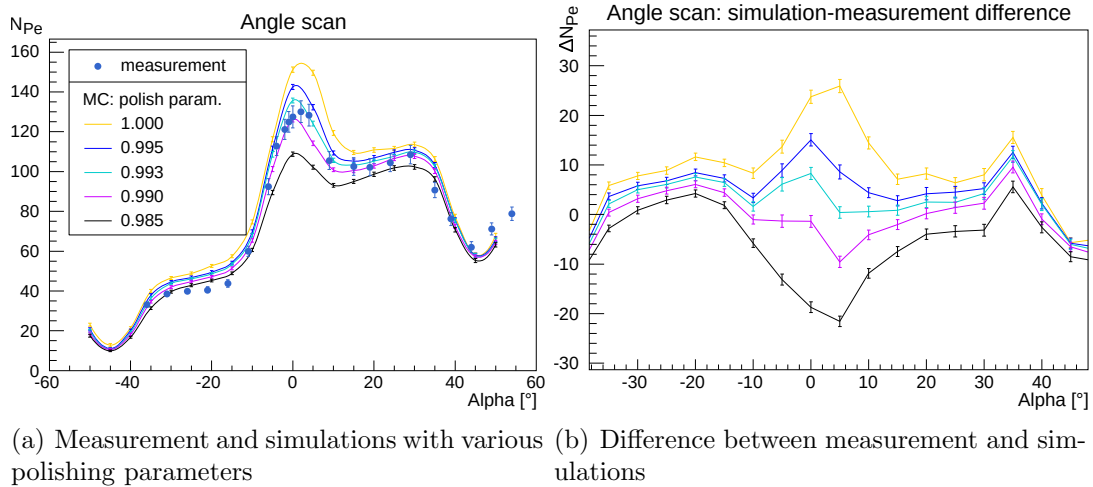
FIGURE 7.8: Quartz geometry II: 435 mm tapered; PMT: Hamamatsu R11410; Wrapping: Alanod 4300UP. Electron energy: 855 MeV

which — especially in the shorter bars produced earlier — have not been removed completely in the polishing process, scratches, contaminants, and chipping.

A quantitative comparison of the measured values of the angle scans for all three geometries can be given by the root mean square goodness of fit method:

$$\eta = \sqrt{\frac{\sum_{i=1}^{N} \left(n_i^{sim} - n_i^{exp}\right)^2}{N}} \tag{7.5}$$
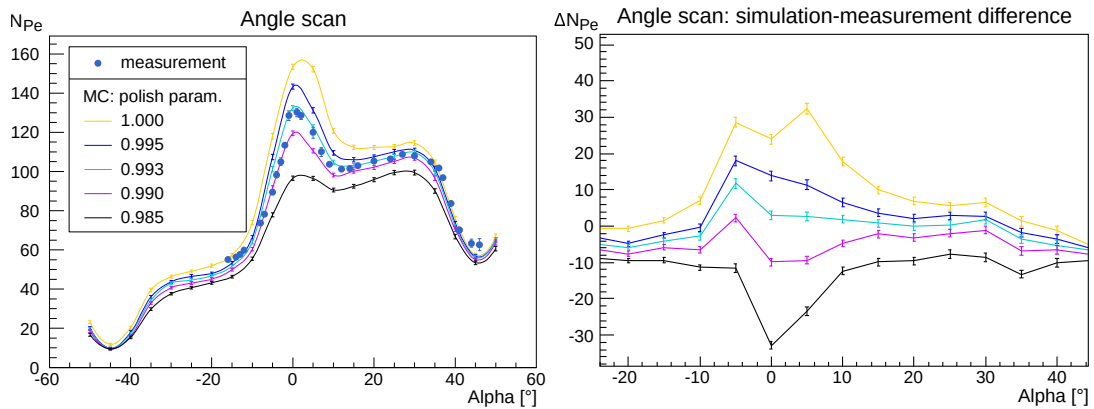
(a) Measurement and simulations with various polishing parameters

(b) Difference between measurement and simulations

FIGURE 7.9: Measurement series done during beamtime 03/2019. Quartz geometry III: 650 mm tapered with quartz light guide; PMT: Hamamatsu R11410; Wrapping: Alanod 4300UP. Electron energy: 855 MeV

geom. \ pol.	1 η	0.995 η	0.993 η	0.990 η	0.985 η
I	15.07	9.11	6.75	6.71	11.45
II	12.74	7.43	5.47	4.67	9.34
III	15.35	7.76	4.58	5.93	14.73

TABLE 7.3: Determination of the final polish parameter to use in the simulation. The angle scans shown in figures 7.7, 7.8, and 7.9 were compared to the corresponding simulations with 5 different polishing parameters ranging from 0.985 to 1.00.

where n_i^{sim} and n_i^{exp} are the simulated and measured numbers of photoelectrons respectively and N is the number of measurements done at different angles α. These values are listed for polishing parameters between 1 (perfectly smooth surface) and 0.985 and the three quartz geometries in table 7.3. For each measurement series the best fit with the simulation in terms of η is highlighted in orange. The resulting goodness of the quartz surface differs from bar to bar. Due to the limited number of samples, it is however impossible to decide whether this is a random effect or if indeed longer bars can be made with better surface quality. The measurement data with the shorter bars however show a better accordance with simulation data using a smaller polishing parameter. For the generation of the detector response database the polishing parameter $p = 0.993$ was chosen, as it showed the best agreement with the angle scan for quartz geometry III (650 mm), which is going to be used in the P2 Experiment.

7.2   Simplifications

7.2.1   Neglected Physical Processes

Fused silica is not considered a scintillating material. The study of scintillation in synthetic and natural quartz by J. Amaré from 2014 [40] confirms this general conception concluding that small amounts of scintillation can be observed for crystalline quartz but not for synthetic, fused quartz.

The situation is less straightforward for another relevant process: bulk scattering. In [63] the results of bulk scattering investigations in Heraeus fused silica are published. Bulk scattering coefficients α_{scat} between $6 \times 10^{-4}\,\mathrm{cm}^{-1}$ and $1.7 \times 10^{-3}\,\mathrm{cm}^{-1}$ depending on the OH concentration in the material were measured for $193\,\mathrm{nm}$ and a Rayleigh-like wavelength dependence of

$$\alpha_{\mathrm{scat}} \propto \frac{n^8}{\lambda^4} \tag{7.6}$$

was confirmed. Using these values the light attenuation due to scattering in the material

$$TS_{\mathrm{Vol}} = 1 - e^{-\alpha_{\mathrm{scat}} \cdot d} \tag{7.7}$$

is between 0.05 and 0.12 for $200\,\mathrm{nm}$ and a roughly estimated $100\,\mathrm{cm}$ average distance d in the quartz bar. [6] This value is substantially smaller for larger wavelengths.

Bulk scattering processes are part of the transmission losses measured in section 4.2.1.1 and are therefore taken into account by using the transmission spectrum of fused silica in the simulation. The measured transmission losses do not differentiate between light absorption and scattering. However, in the case of scattering, the light is not actually lost but merely continues propagating inside the fused silica bar but in different directions. Parts of the scattered light may still reach the photocathode. Unfortunately this effect cannot be included in the simulation by simply turning on Rayleigh scattering [7]. Using the transmission data, which contain light losses by scattering, and additionally incorporating light scattering into the simulation would be partial double counting of the attenuation effects. Since it is impossible to remove the scattering part from the measured attenuation lengths and as the scattered light will in general have to travel longer distances and suffer more attenuation, even if it were to reach the photocathode, it was decided to ignore the scattered light in the simulation.

The overestimation of the detector response in terms of numbers of photoelectrons N_{Pe} resulting from not treating light attenuation due to bulk scattering processes

---

[6]depending on the hydroxyl content in the fused silica bar
[7]Rayleigh scattering is identified as the primary mechanism of bulk scattering in [63]

separately from absorption processes can be assumed substantially smaller than the worst case 12%, which (from [63]) is the overall percentage of 200 nm photons to undergo any scattering while travelling through 100 cm of fused silica with the maximum OH content.

7.2.2 Geometric Simplifications

The exact shape of the fused silica bars is subject to manufacturing fluctuations. As an example table 7.4 shows the measured thickness of a quartz bar of geometry III along its length. A reduction of the nominal thickness can occur during the polishing process. This can be attributed to the fact that the fused silica bar of this geometry is longer than the polishing disc is wide, the bar has to be moved several times and the reduction of thickness is most severe in the middle of the bar. As the polishing process will be different when a larger batch of detector bars is processed, we do not expect this effect in the final detector bars, and this fluctuation of quartz thickness was neglected in the simulations. This is probably one source of the observed discrepancies between detector prototype tests and simulation data.

x [mm]	0	50	100	150	200	250	300	350	400	450	500	550	600	650
d [mm]	10	9.9	9.9	9.8	9.85	9.6	9.6	9.6	9.65	9.6	9.7	9.7	9.8	9.9

TABLE 7.4: Thickness d of the quartz bar used during the beamtimes measured along its length x. "0" is the narrow end of the quartz bar and "650" the end where the PMT is attached. The thickness is subject to manufacturing fluctuations, while it is defined 10 mm thick at every position in the simulation.

The longitudinal position was determined using a millimetre rule while the thickness was measured using a calliper. The uncertainty is estimated to be $\Delta x=0.5$ mm and $\Delta d=0.1$ mm respectively and is attributed mostly to the reading of the value by eye.

7.2.3 Simplification of the Photocathode

The quantum efficiency of a photomultiplier is generally not uniform over the whole photocathode but depends on the position of impact of the photon. Figure 7.10 shows this dependence for the Hamamatsu R11410 as specified by the manufacturer. Measurements published in [64] confirm this data. This spatial dependence of the cathode sensitivity was integrated into the simulation and used for the Hamamatsu PMT. However such data is not available for the Electron Tubes PMT. Therefore —as indicated by the red line in figure 7.10— a uniform
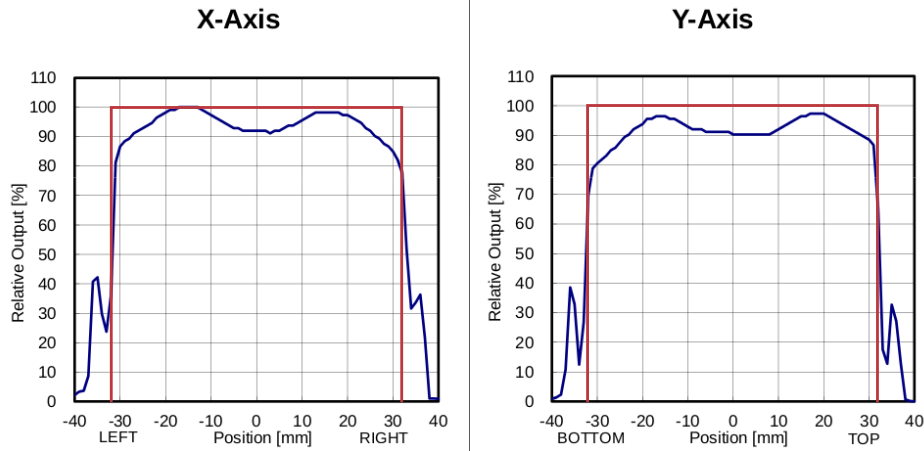
FIGURE 7.10: Blue line: Spatial sensitivity of photocathode in the Hamamtsu R11410 PMT, Red line: assumed uniform sensitivity of the Electron Tubes photomultipliers.

sensitivity of the whole quantum efficiency over a radius of 32 mm was assumed for these photomultipliers. For Cherenkov photon impacts at larger radii, a sensitivity of 0 was specified in the simulation.

7.3 Analysis of the Simulation Data

7.3.1 Detector Response to Electrons

The output of each simulated event is an integer value representing the number of photoelectrons emitted from the PMT cathode. The histograms in figure 7.11 show the distribution of this value for 100000 simulated events, in which 155 MeV electrons hit the 650 mm long fused silica bar in the center of its active area[8] perpendicularly ($\alpha = 0, \beta = 0$) to the detector's front surface. The difference between the two distributions is the following: For the blue histogram, all physics effects listed in section 7.1.2 were active and all resulting particles from these processes were fully considered, whereas for the red histogram, which resembles a Gaussian distribution, all secondary particles stemming from ionization, pair production, and Compton scattering were instantly removed from the simulation.

The production of secondary particles and the loss of energy inside the detector volume results in a tail towards higher signal values as qualitatively described in chapter 5.3. The analysis method of the measurement data from the MAMI beamtimes includes fitting the histograms with a Landau-Gauss convolution in order to separate the widening of the distribution caused by these effects from

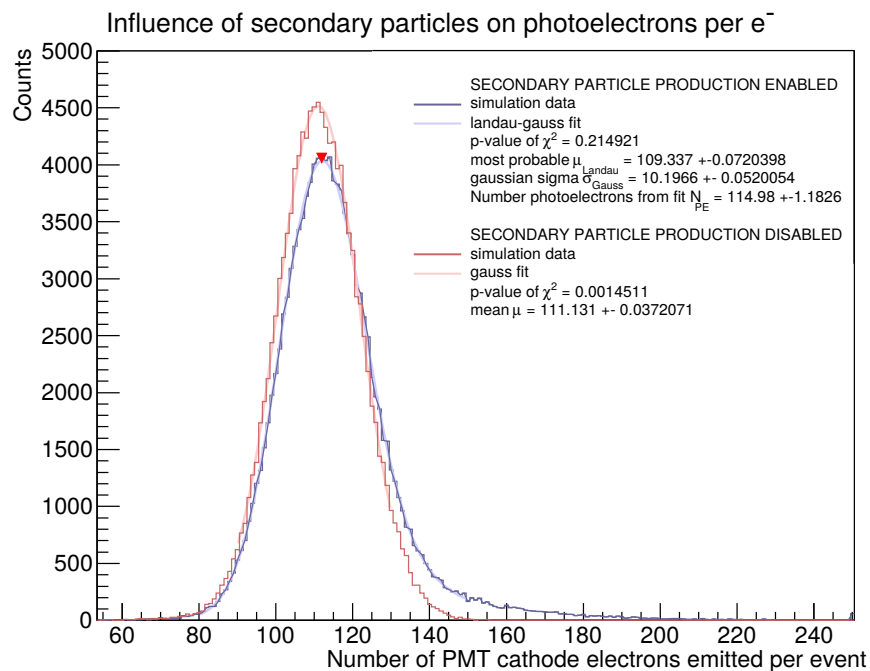---

[8]For exact definition see 7.1.3

FIGURE 7.11: Influence of secondary particles on the distribution of emitted photoelectrons from the PMT cathode.

the statistical variation of the signal. This is necessary because the measurement output is a signal in terms of a QDC channel, and the number of photoelectrons emitted from the PMT cathode needs to be reconstructed without exact knowledge of signal amplification and QDC calibration. The simulation on the other hand directly delivers the number of photoelectrons for each simulated event.

The expected number of photoelectrons N_{Pe} emitted from the cathode as a result of Cherenkov radiation generated in the quartz by a primary electron can be determined by either

- the arithmetic mean of the simulation without secondary particles or

- employing the same method as for the measurement data: Fitting a Landau-Gauss convolution and calculating N_{Pe} from the Gaussian width.

A comparison of the values obtained by both methods is shown for a few example simulation runs in table 7.5.

The fact that the arithmetic mean $N_{\mathrm{Pe}}^{\mathrm{M}}$ of the simulated N_{Pe} distribution delivers —within a 3.1% error— the same value as the number of photoelectrons $N_{\mathrm{Pe}}^{\mathrm{LG}}$ determined by the Landau-Gauss fitting procedure is a strong validation of the analysis method employed for MAMI beamtime data.

$\alpha[°]$	$N_{\mathrm{Pe}}^{\mathrm{M}}$	$N_{\mathrm{Pe}}^{\mathrm{LG}}$	$\sigma_{\mathrm{tot}} = \sqrt{\sigma_{\mathrm{M}}^2 + \sigma_{\mathrm{LG}}^2}$	$\Delta[\sigma_{\mathrm{tot}}]$
-10	56.77 ± 0.05	58.42 ± 0.64	0.641	2.6
-5	84.94 ± 0.05	82.40 ± 0.81	0.812	3.1
0	111.13 ± 0.07	109.34 ± 1.33	1.332	1.3
5	102.34 ± 0.07	101.86 ± 1.15	1.152	0.4
10	93.42 ± 0.06	94.88 ± 1.05	1.052	1.4

TABLE 7.5: Mean number of photoelectrons $N_{\mathrm{Pe}}^{\mathrm{M}}$ from simulation without secondary particle production compared to the number of photoelectrons $N_{\mathrm{Pe}}^{\mathrm{LG}}$ obtained from the simulation with enabled secondary particle production by means of Gaussian and Landau-Gauss fits respectively. The simulation runs were performed with 155 MeV electrons hitting the 650 mm fused silica bar. The error in N_{Pe}^{M} is the fit error of the Gaussian fit to the spectrum without secondaries. The error in $N_{\mathrm{Pe}}^{\mathrm{M}}$ is the fit error of the Landau-Gauss fit to the spectrum with secondaries.

As secondary particle tracking within the simulation is very time intensive, the method of determining the arithmetic mean from simulations without secondaries is employed for the simulation data.

7.3.2 Detector Response to High Energy Photons

For photons to cause a signal in the Cherenkov detector a physical process leading to the production of relativistic charged particles has to take place. This may happen via the Compton effect or via pair production in the detector.

Figures 7.12 and 7.13 show typical examples of histograms of the simulated detector response to photons. They are of a different phenotype than the ones showing the response to electrons. While the histograms for electrons show a clearly defined peak, the ones for photons exhibit a plateau-like structure with a smeared out edge. Moreover the simulation with electrons mirrors a 100% detection efficiency whereas most photons pass the detector without causing a signal. Hence these events are accumulated in the 0-bin.

For low energies the predominant process leading to relativistic charged particles in the Cherenkov radiator is the Compton effect. For higher photon energies gamma conversion becomes more and more relevant. The threshold energy at which both processes lead to the same average number of photoelectrons from the PMT cathode is around 11 MeV. At high photon energies —the graph for 120 MeV is a suitable example— gamma conversion can lead to a twice as high detector signal as Compton scattering. This is due to the fact that gamma conversion yields two charged particles.
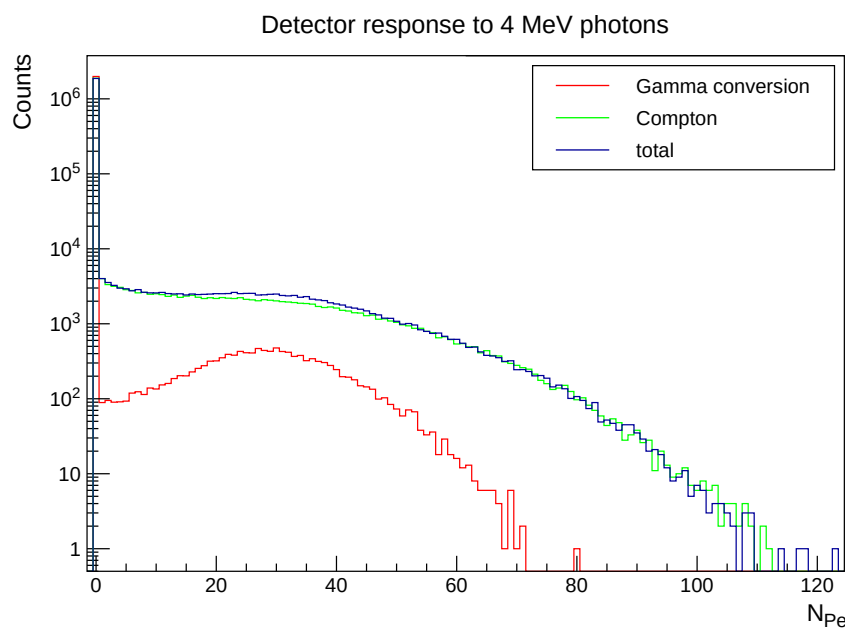
Detector response to 4 MeV photons

FIGURE 7.12: Detector response distribution for 4 MeV photons hitting the detector element perpendicularly at the horizontal and vertical center of the active detector area. For 4 MeV photons Compton scattering is the predominant process to lead to a signal in the Cherenkov detector.
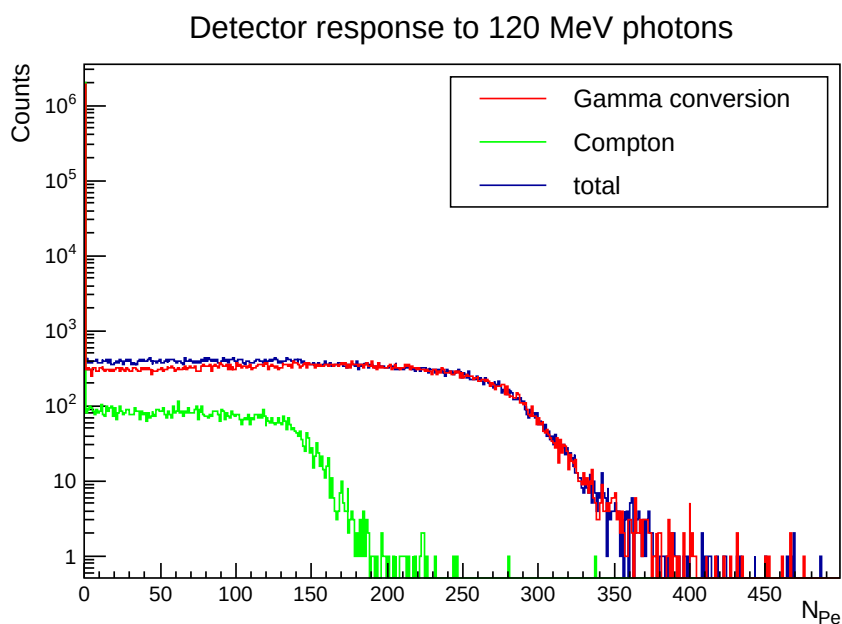
Detector response to 120 MeV photons

FIGURE 7.13: Detector response distribution for 120 MeV photons hitting the detector element perpendicularly at the horizontal and vertical center of the active detector area. For 120 MeV photons Gamma conversion is the predominant process to lead to a signal in the Cherenkov detector.

7.4   Validation of GEANT4 Simulation Data

As described in the preceding sections the GEANT4 simulation allows to implement a detector geometry and material characteristics and determine the detector response to impacting particles. In this section I will compare the results from this simulation with theory and with measurement data taken during the MAMI beamtimes described in chapter 5.

Figure 7.14 contains the simulated distribution of Cherenkov photons $n_{\text{Ch}}^{\text{Sim}}$ produced by a 155 MeV electron while traversing 10 mm of fused silica. The expectation value of $n_{\text{Pe}}^{\text{Sim}} = 1093$ agrees with the value $n_{\text{Pe}}^{\text{FT}} = 1094$ calculated with the Frank-Tamm formula 4.2 for wavelengths $\lambda \in [180\,\text{nm}, 800\,\text{nm}]$. The comparison demonstrating the congruence of the Cherenkov spectrum in the simulation and the calculated spectrum has been shown in figure 4.4.

The simulation is therefore able to reproduce the number of Cherenkov photons expected in theory by means of Monte-Carlo methods.
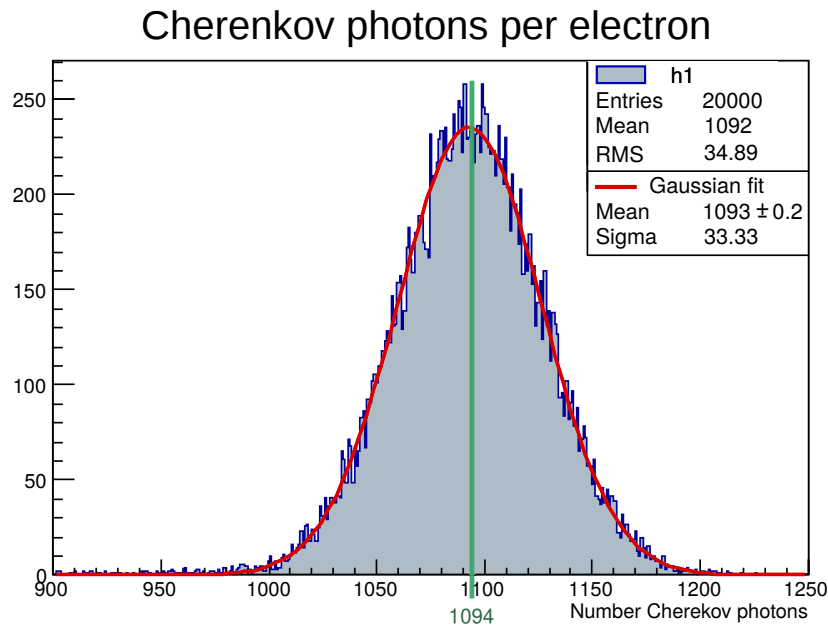

FIGURE 7.14: Distribution of the number of Cherenkov photons generated by a 155 MeV electron traversing 1 cm of fused silica in the GEANT4 simulation. Indicated in green is the expected number of Cherenkov photons in 1 cm of fused silica calculated with the Frank-Tamm formula 4.2.
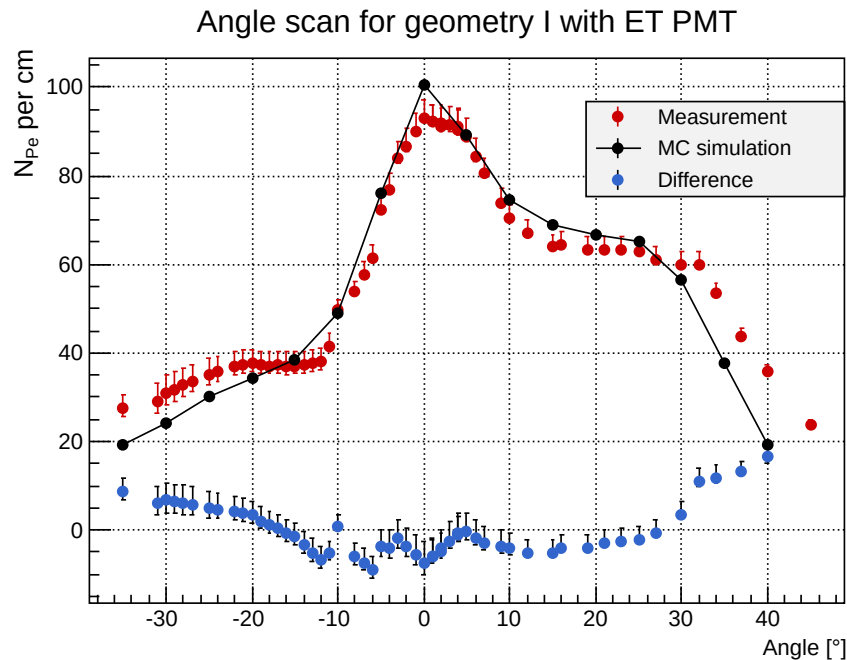
FIGURE 7.15: Measurement of the prototype detector response as a function of the electron impact angle taken at MAMI electron beam compared to simulation data. Detector Geometry I with optical outlet, Suprasil grade 2A, no light guide, ET 9305QKMB, wrap: Alanod 4300UP. Polishing parameter in the simulation: 0.993. The blue dots represent the absolute difference between measurement and simulation.

7.4.1 Agreement of Signal Yield from Simulation and from Measurement at the MAMI Electron Beam

Comparisons between simulated photoelectron yield to relativistic electrons hitting the detector and measurement data from MAMI was performed for all three prototype geometries. Angle scans were done, meaning that the angle between the electron beam and the quartz surface normal was varied by rotating the detector bar. In the simulation the primary particle's initial position and momentum were varied accordingly. Additionally horizontal position scans varying the position of impact onto the quartz as described in 5.4.1 were employed for comparison between simulation result and experimental data.

7.4.1.1 Angle Scans

Figures 7.15, 7.16, and 7.17 show the results from the angle scans performed at MAMI for the three detector geometries in direct comparison to the respective simulation results. The simulations were able to reproduce the typical angle dependence of the photoelectron yield with the maximum at perpendicular incidence
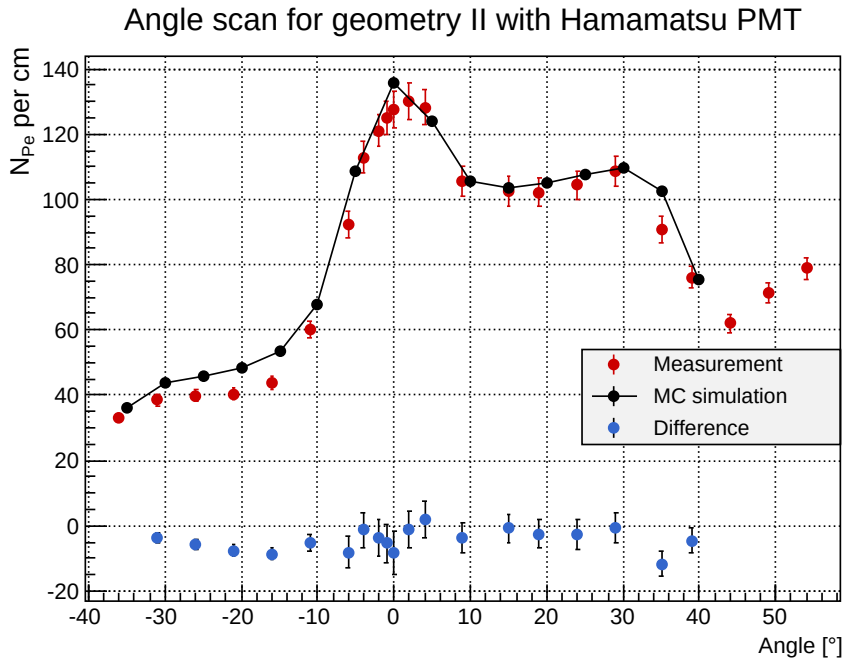
FIGURE 7.16: Measurement of the prototype detector response as a function of the electron impact angle taken at MAMI electron beam compared to simulation data. Detector Geometry II with optical outlet, Spectrosil 2000, Hamamatsu R11410, wrap: Alanod 4300UP. Polishing parameter in the simulation: 0.993. The blue dots indicate the absolute difference between measurement and simulation.

of the primary electron and minima at $+$ and $-45°$ both in shape and in absolute numbers.

The deviation between simulation and measurement is the largest for the 300 mm prototype. This might be attributed to the fact that the 300 mm long quartz bars have noticeable protection chamfers, which are necessary to avoid chipping of the edges during the polishing procedure. When the later versions of the quartz geometry were ordered, the manufacturing process was more elaborate and customised to the demands of P2, and the longer and wedged quartz bars were cut and polished in a way that the protection chamfers vanished when the quartz bars were polished.

For detector element geometries II and III the relative difference between measurement and simulation is well below 5%. For geometry III solely one simulation point at 5° lies off the measured points by more than 5%. It can be concluded that there is a good agreement between measurement and simulation data.
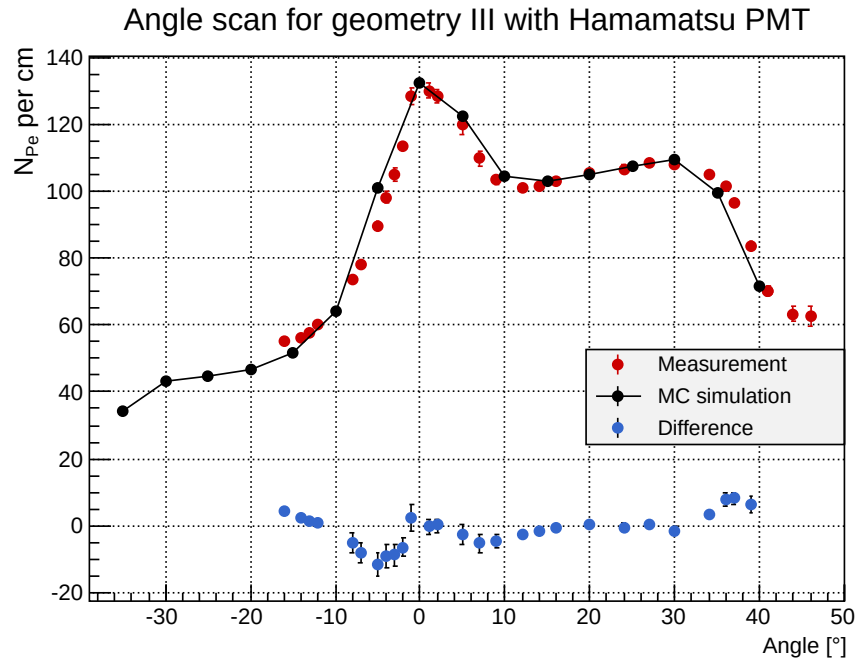
FIGURE 7.17: Measurement of the prototype detector response as a function of the electron impact angle taken at MAMI electron beam compared to simulation data. Detector Geometry III with optical outlet, Spectrosil 2000, 200 mm quartz light guide, PMT: Hamamatsu R11410 ZK6862, wrap: Alanod 4300UP. Polishing parameter in the simulation: 0.993. The blue dots are the absolute difference between measurement and simulation.

7.4.1.2 Impact Position Dependence of the Signal

The final detector prototype (geometry III) underwent position scans in order to also test the position dependence of the photoelectron yield. Figure 7.18 shows the result of this measurement compared to the simulation data for the same detector geometry and hardware.

As the translation stage has a travel of only 140 mm the detector module had to be repositioned manually 3 times to perform a scan over the range of 460 mm. The large set of data points closer to the PMT (-375 mm to -80 mm) was taken at the beginning of the beamtime. Afterwards vertical position scans were done. The dataset on the right was measured after these vertical position scans. Scanning the area around the middle of the active detector area has accidentally been left out. The measurements in which the beam hit the center of the active area (0 mm) stem from an angle scan series performed with the same detector immediately after the position scans.

The measurement series shows little resemblance to the simulation results. Additionally the data points taken during the angle scan lie 15-20% above the interpolation between the adjacent data points. It could be suspected that during

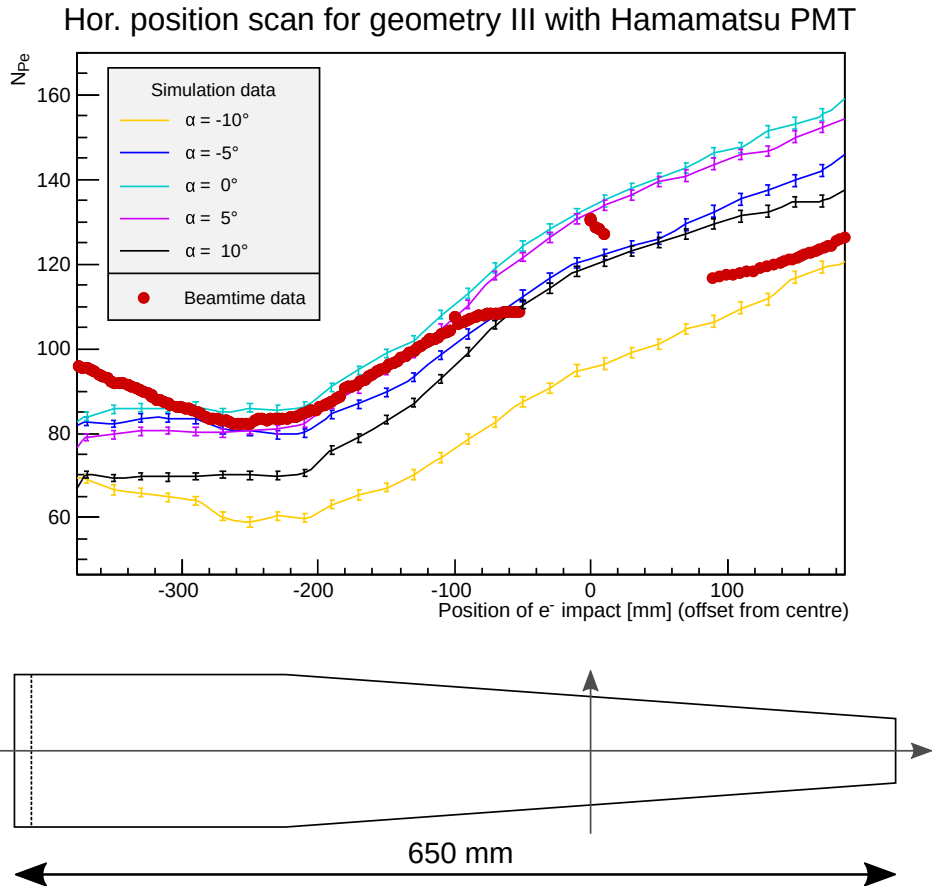## Hor. position scan for geometry III with Hamamatsu PMT

FIGURE 7.18: Comparison of horizontal position scan performed at the MAMI beam and simulation data for simulation parameters in accordance with the experimental setup: Detector Geometry III, Spectrosil 2000 quartz bar, Hamamatsu R11410 ZK6862 photomultiplier, Alanod 4300UP wrap, polishing parameter in simulation: 0.993. Data taken during beamtime 03/2019, runs 12396 to 12586

manual repositioning of the detector the relative angle between beam and detector surface was changed. The angle scans demonstrate that the angular dependence of the signal is strong enough for a variation of only 3° to cause such a drop of the signal. An improper alignment of the detector could thus be an explanation of the divergence between simulation results and experimental data. However, the large difference of the gradient of N_{Pe} in the light guide region cannot be explained. Presumably imperfections in the quartz material and geometry which the simulation does not take into account lead to this behaviour. These might be the fluctuations in the thickness of the quartz, small remnants of the protection chamfers, inaccurate adjustment of the quartz bar at the PMT window, and scratches and impurities of the fused silica surface.

Figure 7.19 shows a horizontal position scan done during an earlier beamtime in 2016 with a detector prototype of geometry II. The data points are in better congruence with the simulation than in the position scan of the 650 mm long
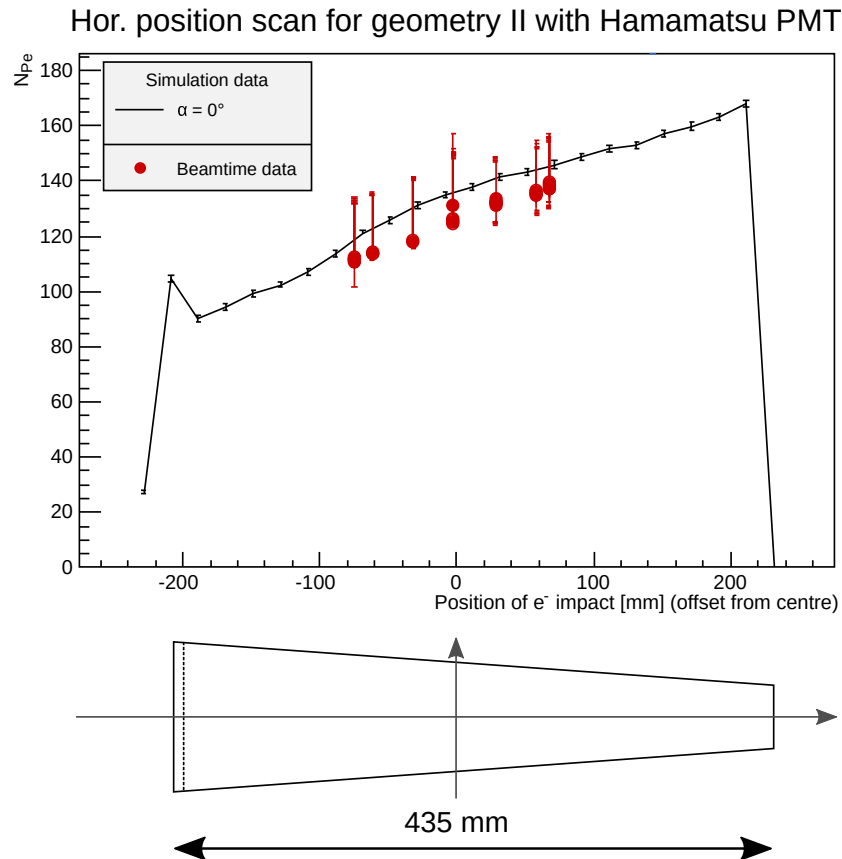
FIGURE 7.19: Comparison of horizontal position scan performed at the MAMI beam and simulation data for simulation parameters in accordance with the experimental setup: Detector Geometry II, Spectrosil 2000 quartz bar, Hamamatsu R11410 ZK6862 photomultiplier, Alanod 4300UP wrap, polishing parameter in simulation: 0.993. Electron energy: 855 MeV. Data taken during beamtime 01/2016, runs: 196 to 275 (angle scan runs 213 to 236 excluded)

quartz. However it should be noted that only a fraction of the 435 mm long detector has been scanned. The signal increase on the left of the simulation data curve at position -210 mm stems from Cherenkov light generated in the quartz PMT window.

As discussed in section 5.5.5, where the ability of fused silica to serve as light guide was examined, there is a slight decrease of the signal intensity in the cuboid quartz bar with larger distance of the location of beam incidence from the PMT. The simulation qualitatively reconstructs this behaviour, however the slope is even less pronounced than in the measurement data.

In the wedged quartz bars the signal dependence on the point of incidence is reversed. An attempt to explain this behaviour involves the wedged faces contributing to more effectively directing the Cherenkov light towards the PMT.

It must be concluded that it has not been proven that the simulation reproduces the impact position dependence of the signal, and that a horizontal position scan of the final prototype should be repeated as soon as given the opportunity. Special attention should be paid to the correct alignment of the detector in the beam, maximal precision in the geometry of the detector bar, and firm attachment of the quartz bar to the PMT window. On the other hand, matching the simulation to the geometry of a specific sample bar is pointless as it is unlikely that all bars that ultimately will be used in the P2 detector match exactly this geometry, and the simulation is to fit as well as possible to an average population of produced quartz bars which is best achieved by designing it to match the demand dimensions. An evenly thick quartz bar without protection chamfers might lead to better congruence between measurement and simulation.

The detector response to photons determined by experiment has already been compared to the simulation results in section 5.6.1. The simulation is able to reproduce the measured photon detection efficiency. Regarding the mean signal of photons measurement and simulation show a significant discrepancy, which is probably due to difficulties in the measurement data analysis. In particular, it was not possible distinguish low signals from the pedestal.

7.5 Detector Response Database

The GEANT4 simulation introduced in the previous sections allows to establish a parametrisation of the detector response to the various particles potentially impinging on the detector. For this purpose a database was established for a wide range of particle states defined by

- the particle type

- the particle's kinetic energy E_{kin} when hitting the detector plane

- the particle's angles of incidence α and β onto the quartz bar as defined in figure 7.20

- the particle's location of impact x onto the quartz bar

The detector module implemented in the simulation was exposed to single electrons and photons of energies ranging between $1\,\mathrm{MeV}$ and $150\,\mathrm{MeV}$. As there is a strong signal dependence on the angle of incidence onto the detector a wide range of momentum directions was included into the database. The angle definition is explained in figure 7.20. Both the angles α and β were varied by defining the position of the primary particle gun and the particle's momentum direction in the
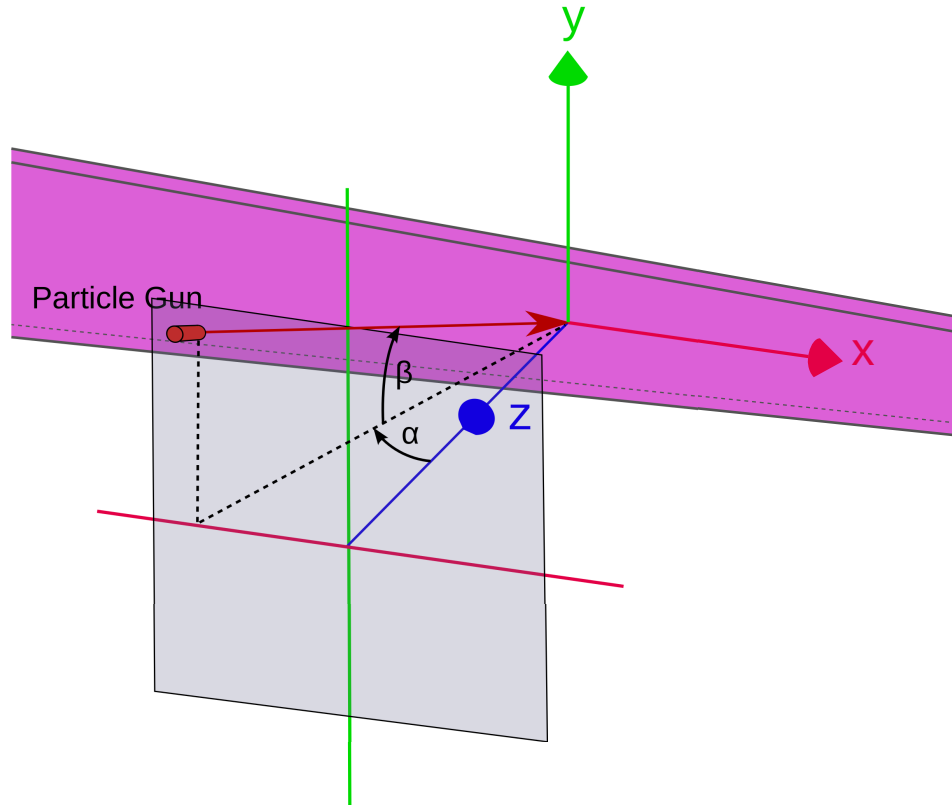
FIGURE 7.20: Definition of the incidence angles. α is the angle between the surface normal and the particle momentum's projection on the $x - z$-plane. β is the angle between the quartz surface normal and the particle momentum's projection onto the $y - z$-plane.

GEANT4 simulation. In order to do so an auxiliary plane, which was parallel to the detector surface and placed at a distance $P_z = 100\,\text{mm}$ in front of the detector was chosen, and the particle gun was positioned on this plane at x and y coordinates P_x and P_y. At the same time the momentum direction of the initial particle was defined to be:

$$
\begin{aligned}
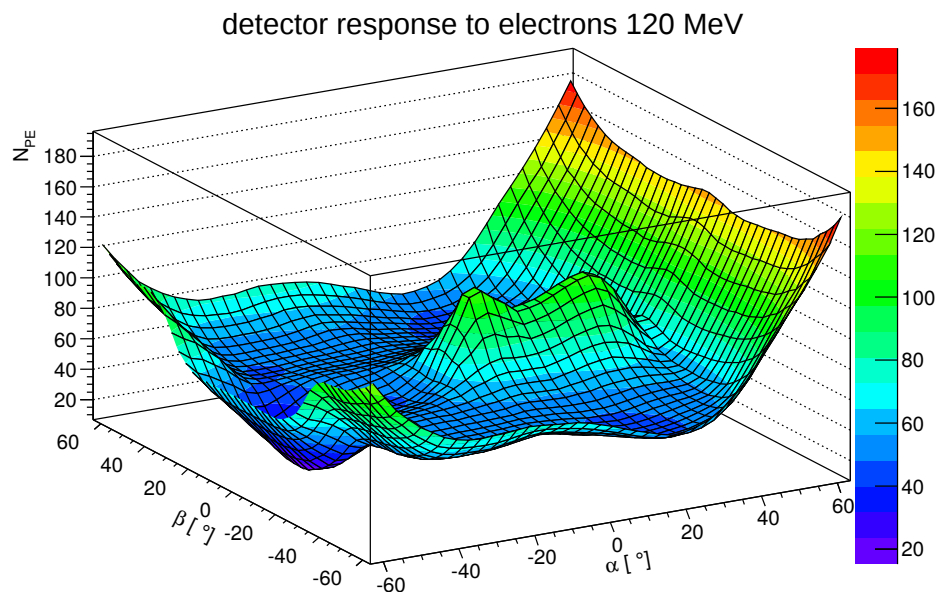p_x &= -P_x \\
p_y &= -P_y \\
p_z &= -P_z
\end{aligned}
\tag{7.8}
$$

FIGURE 7.21: The particle gun and momentum are defined within the detector response simulation in terms of the shown parameters P_x, P_y, and P_z.

The position of impact along the x-axis was varied by adding the offset x^i from the centre of the quartz to the position of the particle gun:

$$
\begin{aligned}
x^{\mathrm{PG}} &= P_x + x^i \\
y^{\mathrm{PG}} &= P_y \\
z^{\mathrm{PG}} &= P_z
\end{aligned}
\tag{7.9}
$$

The angles α and β are then

$$
\begin{aligned}
\alpha &= \arctan\left(\frac{P_x}{P_z}\right) \\
\beta &= \arctan\left(\frac{P_y}{\sqrt{P_x^2 + P_z^2}}\right)
\end{aligned}
\tag{7.10}
$$

For clarification, figure 7.21 shows how the position of the particle gun is defined in terms of P_x, P_y, and P_z.

For each particle state configuration 1000 events were simulated and formed into a histogram. The detector response was characterised by the resulting expectation

FIGURE 7.22: Excerpt from the detector response database. The plot shows the mean photoelectron output to electrons of energy $E_{kin} = 120\,\text{MeV}$ hitting the detector at the center of its active area under various impact angles. The database contains data of the same kind for electrons and photons of a variety of energies and impact positions.

value and the root mean square of the distribution. A small fraction of the database is for exemplary purposes illustrated in figures 7.22 and 7.23. These plots show the expectation value and the root mean square of the detector response to electrons of energy $120\,\text{MeV}$ hitting the detector at the vertical and horizontal center of the sensitive area, where the response is expressed in terms of photoelectrons.

As shown in figure 7.24 the dependence of the detector signal on the primary electron's energy is largest for small energies. The detector database therefore includes a fine scan of energies from $1\,\text{MeV}$ to $10\,\text{MeV}$. In order to save computing time the steps are chosen larger for energies above that.

In correspondence to figure 7.22 figure 7.25 shows the mean number of photoelectrons resulting from 2000 simulated $120\,\text{MeV}$ photon events. Figure 7.26 shows the respective root mean squared. The roughness of the plot surface is due to the fact that most photons pass though the detector without causing a signal, which results in lower statistics.

The following list contains the values of the parameters of the primary particle as included in the detector response database:
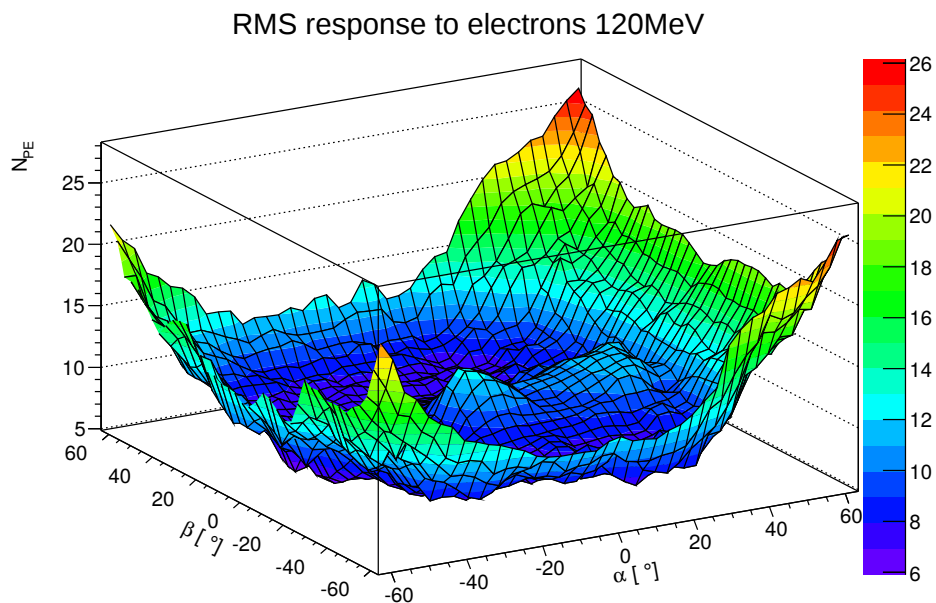
- Particle type

RMS response to electrons 120MeV

FIGURE 7.23: Root mean squared of the N_{Pe} distribution of the simulation runs, whose expectation values are plotted in figure 7.22.

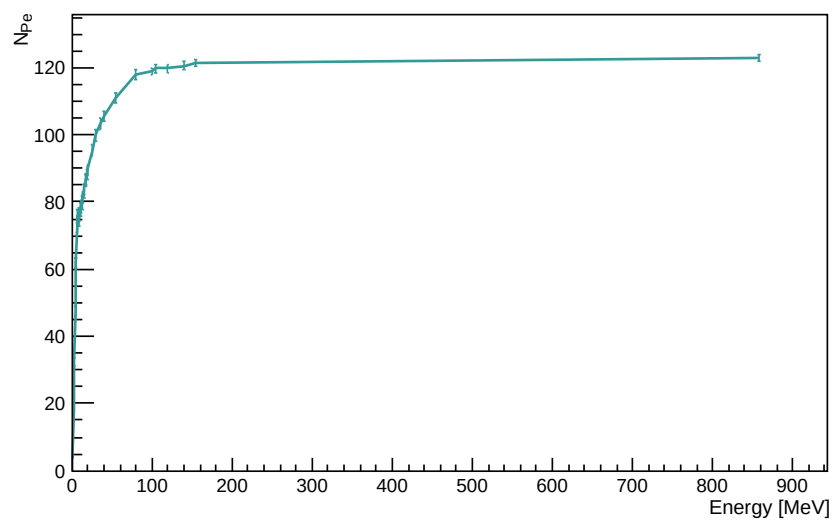Signal depending on the incident electron's energy

FIGURE 7.24: Dependence of the detector output on the primary electron's energy. Simulation run with detector geometry III, ET 9305QKMB serial 518 photomultiplier, Alanod 4300 UP wrap, 155 MeV primary electron energy.
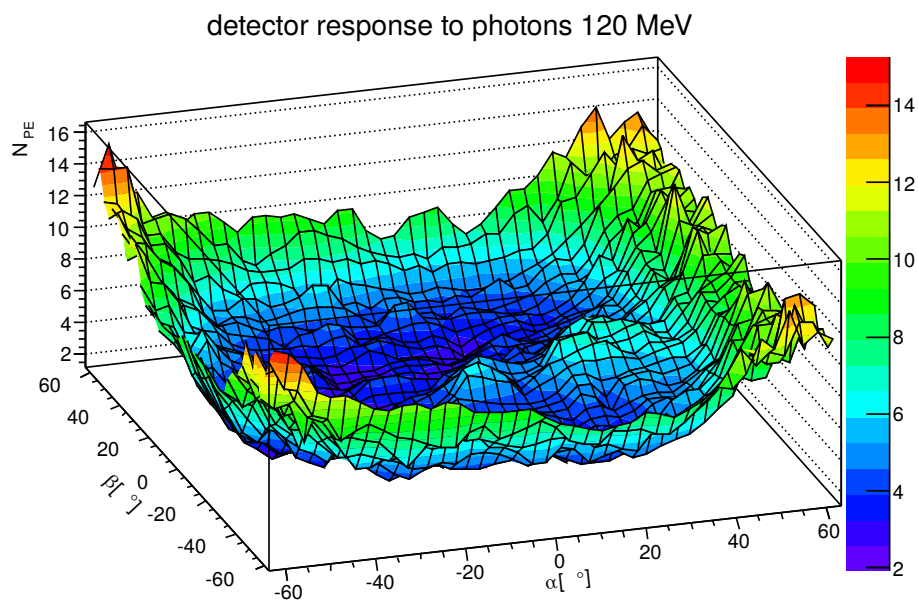
detector response to photons 120 MeV

FIGURE 7.25: Exerpt from the detector response database. The plot shows the mean photoelectron output to photons of energy $E_{kin} = 120\,\mathrm{MeV}$ hitting the detector at the center of its active area under various impact angles. The database contains data of the same kind for electrons and photons of a variety of energies and impact positions.
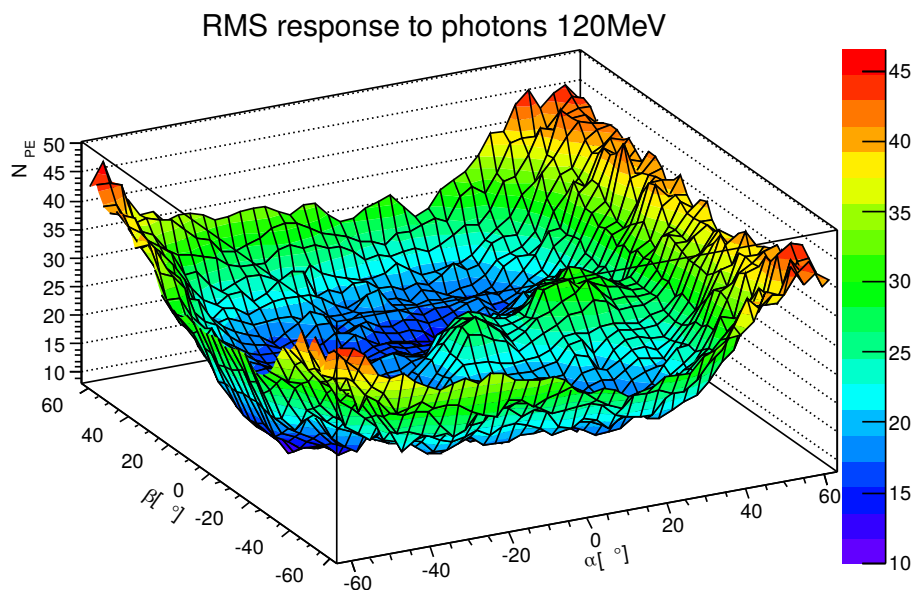
RMS response to photons 120MeV

FIGURE 7.26: Root mean squared of the N_{Pe} distribution of the simulation runs, whose expectation values are plotted in figure 7.25.

- – electron

- – photon

- • Kinetic energy

  - – $1\,\mathrm{MeV}$ to $10\,\mathrm{MeV}$ in steps of $1\,\mathrm{MeV}$

  - – $10\,\mathrm{MeV}$ to $20\,\mathrm{MeV}$ in steps of $2\,\mathrm{MeV}$

  - – $20\,\mathrm{MeV}$ to $50\,\mathrm{MeV}$ in steps of $5\,\mathrm{MeV}$

  - – $50\,\mathrm{MeV}$ to $150\,\mathrm{MeV}$ in steps of $20\,\mathrm{MeV}$

- • P_x from $-150\,\mathrm{mm}$ to $150\,\mathrm{mm}$ in steps of $10\,\mathrm{mm}$

- • P_y from $-150\,\mathrm{mm}$ to $150\,\mathrm{mm}$ in steps of $10\,\mathrm{mm}$

- • Position of particle impact x^i along the length of the quartz from $-230\,\mathrm{mm}$ to $230\,\mathrm{mm}$ in steps of $20\,\mathrm{mm}$

The complete set of detector response simulations used for the calculations described in chapter 8 is shown in the plots in appendix F. The impact position dependence was preliminarily not included therein.

Chapter 8

Expected Results for the P2 Experiment

The scattering kinematics and separation of signal electrons from undesired background in the solenoid magnetic field were the main subjects of Dominik Beckers doctoral thesis [25]. With the help of his simulation, a solution for the separation of background particles was designed in the form of a solenoid magnetic field, in which charged particles are deflected according to their momentum p.

The objective of a full simulation of the P2 Experiment is the conception of an optimal configuration of the hardware components on one hand and gaining a quantitative understanding of the detector signal in terms of the underlying physics processes on the other hand. This signal is caused by different particles hitting the Cherenkov detector and manifests as a PMT anode current. The knowledge of the nature and origin of the signal contributing particles allows to predict the uncertainty of the A_{PV} measurement and is a key factor for the extraction of $\sin^2(\Theta_W)$ from the raw data. However, simulating the whole chain of processes and particles in the P2 Experiment including

- scattering processes in the target,

- particle propagation in the magnetic field,

- secondary particle production and tracking,

- the Cherenkov effect in the main detector,

- optical photon propagation, and

- the photoelectric effect in the PMTs

is impractical. For a reasonably accurate simulation about 10^7 detected elastically scattered electron events must be analysed. If these were to be generated from primary beam electrons using the full chain mentioned above, this would require $\simeq 1.5 \cdot 10^{10}$ primary beam events and take several years to simulate [25, Chapter 7.2]. Therefore the simulation was split into three separate parts: interaction of the primary electrons in the target, propagation of particles in the magnetic field, and interaction of particles with the detector. These were performed independently, and the results of each step were later combined in an efficient way into a full simulation of the apparatus. For the beam-target interaction a special event generator was developed to generate the detectable events more efficiently [25, Chapter 7.2.1]. The detector response to incident particles was parametrised and provided to the main simulation in form of a database; this procedure is described in chapter 7.

This chapter is going to give a brief overview of the P2 main simulation as performed by Dominik Becker and present its results. Afterwards the impact of the newest detector response simulation with the final Cherenkov detector design on the resulting asymmetry $A_{\mathrm{PV}}^{\mathrm{exp}}$, the weak mixing angle $\sin^2(\Theta_W)$ and their uncertainties $\Delta A_{\mathrm{PV}}^{\mathrm{exp}}$ and $\Delta \sin^2(\Theta_W)$ is presented and discussed.

8.1   Simulation of Particle Flux onto the Detector

This section is going to give an overview of the simulation for the calculation of physical processes in the P2 Experiment as developed by Dominik Becker. The simulation was developed as a GEANT4 application, which included all standard hadronic processes provided by the GEANT4 package and a specially designed event generator for elastic electron-proton scattering. The program was supplied with the P2 experimental apparatus as depicted in figure 8.1 with the materials for the components listed in table 8.1. In order to reduce the computing requirements, sampling of primary beam-target interactions and tracking of the emerging particles through the spectrometer were treated separately. Details on the exact implementation of this simulation can be found in [25].

The detector response was not part of the main simulation. Instead a virtual sensitive volume was implemented at the place of the detector and the state of each particle entering this volume was queried and recorded. This included:

- the particle type
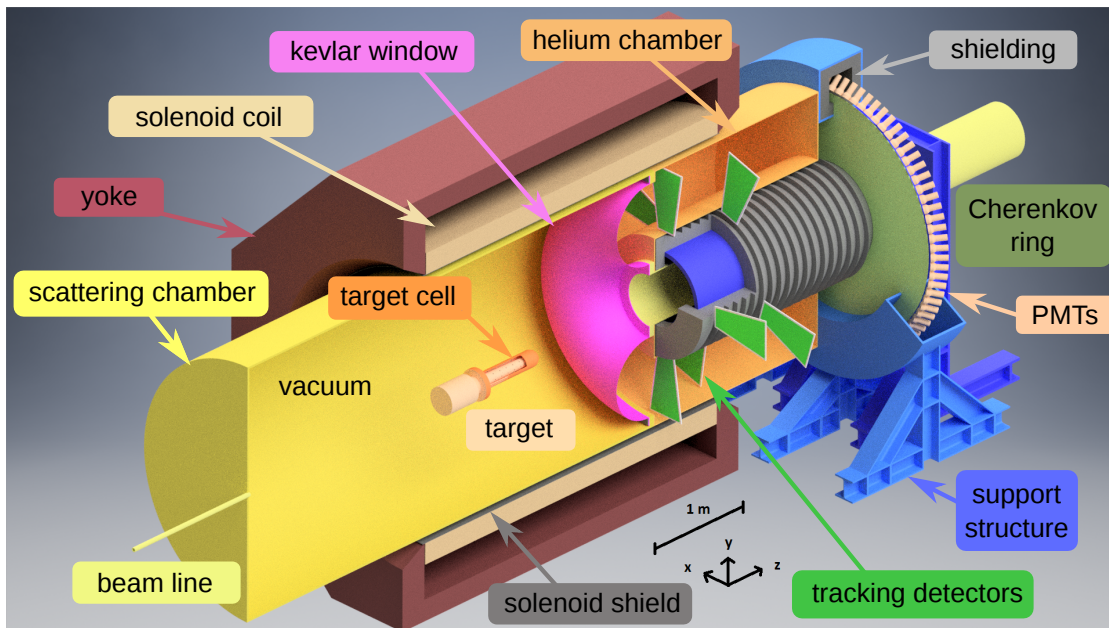
- the particle's kinetic energy E_{kin}

FIGURE 8.1: Experimental setup as implemented into the P2 main simulation. Materials defined in GEANT4 are listed in table 8.1.

Component	Material	Component	Material
target	lH2	helium chamber	Al
target cell	Al	helium gas	He
solenoid shield	Pb	kevlar window	kevlar
solenoid coil	Cu	support structure	stainless steel
yoke	Fe	PMTs	glass
shielding	Pb	Cherenkov ring	fused silica
beam line	Al	tracking detectors	Si
scattering chamber	Al		

TABLE 8.1: Materials of the components used in the P2 main simulation as depicted in 8.1.

- the particle's momentum when hitting the detector

Early design considerations for the P2 detector intended short cuboid detector bars. These detectors do not exhibit a strong dependence of the signal yield on the particle's position of impact onto the detector. Therefore impact position dependence is neglected in the simulation. Instead, a uniform detector response equal to that for particles hitting the center of the active area was assumed across the whole detector. However, as the detector response database includes variation of the impact position, a refinement of the procedure described herein could be achieved by considering the signal dependence on the position of impact.
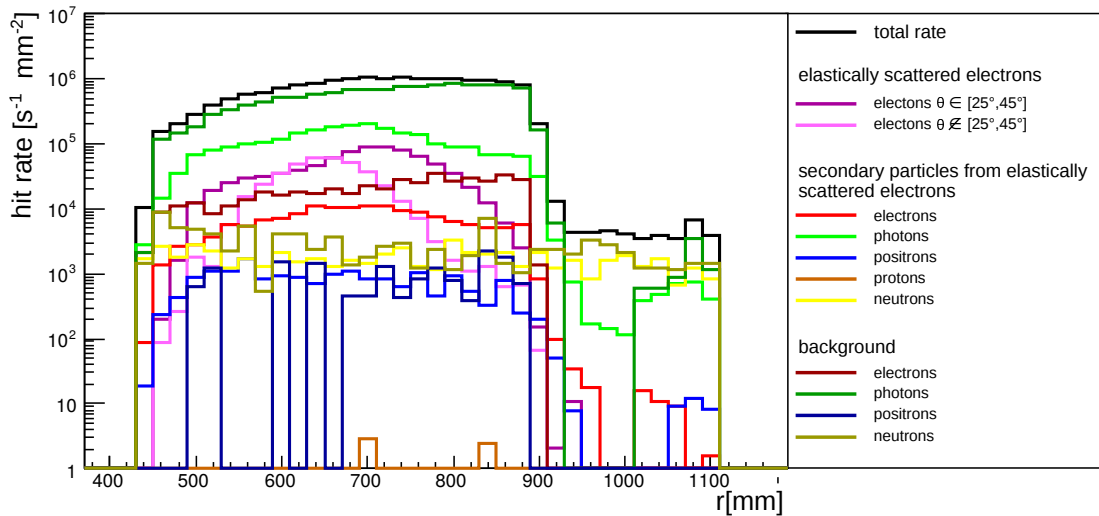
FIGURE 8.2: Particle hit rates onto the detector plane plotted against the radial position of particle impact r from the beam line. Included in the simulation but not occurring at the position of the detector plane are primary and background protons.

In case the detected particle originated from an elastic electron-proton scattering process in the target, the initial and final state of the involved electron were additionally queried. This is necessary to deduce the scattering angle Θ_L and the squared momentum transfer Q^2 of the scattering process and thus quantify the contribution of the particle to the experimental asymmetry.

Hit rates onto the Cherenkov detector ring are listed in table 8.2, and figure 8.2 shows the radial distribution of these particles on the detector plane. It is presented in the same way as introduced in section 4.2.2.

In order to predict the detector signal, this intermediate result now has to be combined with the detector response parametrisation.

8.2   Resulting Photoelectron Current

Figure 8.3 shows the angular distribution of electrons from elastic electron-proton scattering in the target reaching the detector plane. The data includes all electrons, which have been scattered from target protons into scattering angles $\Theta_L \in [25°, 45°]$. The electron incidence angles are distributed around $0°$, their expectation values being $\langle \alpha \rangle = 2.32°$ and $\langle \beta \rangle = -0.66°$. As demonstrated in chapter 7 the detector response simulation shows a maximum in the number of photoelectrons at normal incidence of the electron onto the quartz bar. This behaviour is intuitive and was also observed in the prototype tests at the MAMI electron beam. To
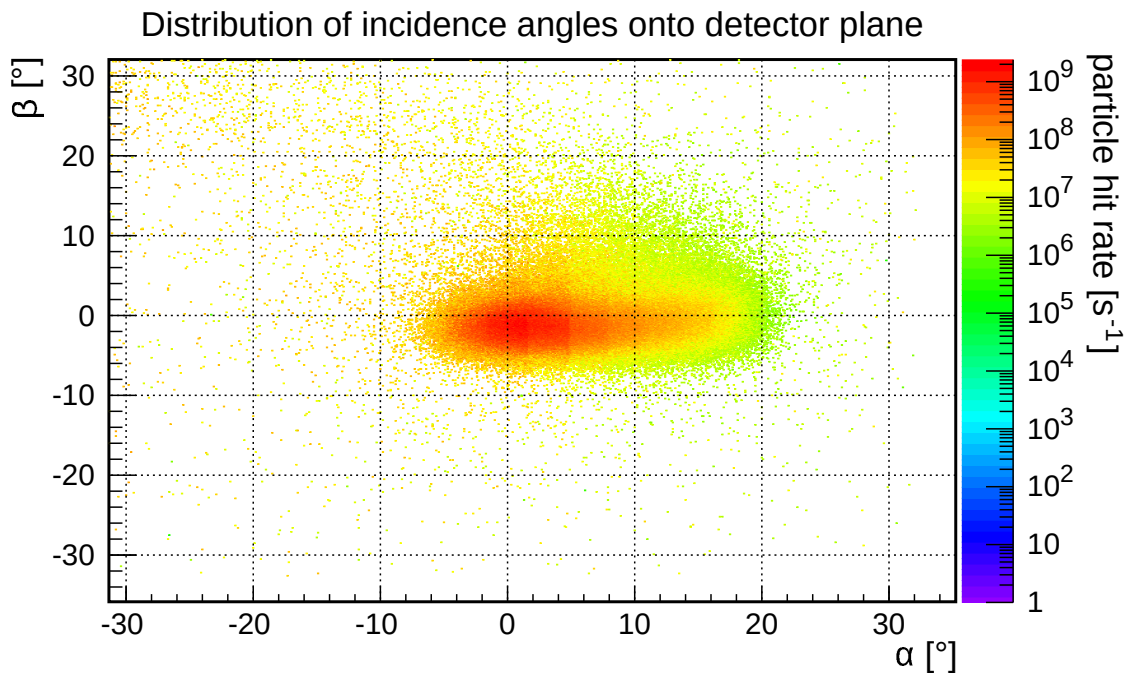
FIGURE 8.3: Distribution of incidence angles of elastically scattered electrons (scattering angle $\Theta_L \in [25°, 45°]$) onto the virtual detector plane. Picture courtesy of Dominik Becker.

maximise the signal response the detector elements can be aligned approximately perpendicular to the expectation value of the incidence angle and therefore as a disc in the xy-plane around the beam axis (z). If critical helicity correlated changes in the beam lead to large false asymmetries due to a change of incidence angle, it might be of disadvantage to chose this local maximum in the orientation of the quartz bars. Instead one could tilt the bars by 20° so that most signal electrons hit the detector element at an angle where the signal yield has a plateau with respect to the incidence angle α. However covering the same ring area with tilted detector modules would imply that they have to be longer by a factor of the cosine of the tilting angle, and manufacturing the polished fused silica bars is already challenging for 650 mm. Fortunately beam monitoring and stabilisation at MESA are expected to perform well enough for the helicity correlated beam parameter changes to be small enough to not cause a problem. In the following a disc shaped alignment is therefore assumed.

The detector response database established with the GEANT4 detector response simulation presented in this thesis allows to convert the raw hit rates onto the detector shown in figure 8.2 into photoelectron distributions. This has been performed in [25] using the response parametrisation for detector Geometry I, and was repeated in the course of this thesis with a newly established parametrisation for Geometry III. It should be noted that protons are assumed to cause no signal, as their Cherenkov threshold in fused silica is above the electron beam energy.
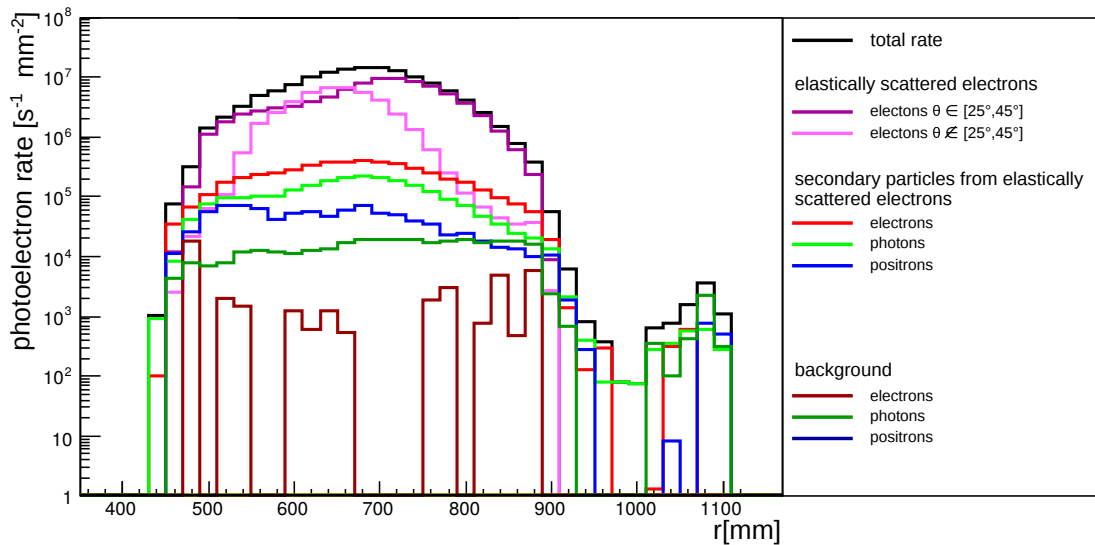
FIGURE 8.4: PMT cathode photoelectron rate plotted against the distance r of the impact position of the signal evoking particle from the beam line. The underlying data has been generated by combining the hit rates onto the detector plane shown in figure 8.2 with the detector response database. Included but not occurring or not causing a detector signal are neutrons and primary, secondary, and background protons.

Positrons have not been included in the database. They are assumed to cause the same signal as electrons of equal energy and momentum.

For each particle hitting the virtual detector plane its type, energy and momentum are recorded and the expected detector signal in terms of the mean number of photoelectrons from the PMT cathode as well as its standard deviation is queried from the detector response database. Figure 8.4 shows in black the total rate of photoelectrons as a function of the radial position of impact of the signal causing particle. This total photoelectron rate is broken down by particle types and originating physics processes of the particles evoking the detector signal.

As intended when designing the experimental configuration, the main contribution to the detector signal in figure 8.4 are electrons which have been elastically scattered from protons in the target. The large photonic background seen in figure 8.2 is suppressed by two orders of magnitude with respect to the elastically scattered electrons. The active detector area will reach from $r = 450\,\mathrm{mm}$ to $r = 900\,\mathrm{mm}$. The distance between the active detector area and the PMTs ($r = 900\,\mathrm{mm}$ to $r = 1100\,\mathrm{mm}$) is bridged by the light guide part of the fused silica bar. As this part is shielded there is a noticeable decline of signal at $r = 900\,\mathrm{mm}$.

In [25] the method of determining the expected uncertainty in the weak mixing angle from the detector signal is thoroughly derived. The method and algorithms developed there will be applied to the newly-derived results presented here in order

to assess the impact of the geometry design choice on the measurement accuracy. They are based on a net data taking time of $T = 10^4\,\mathrm{h}$, where dead times as well as insensitive detector areas caused by minimal unavoidable gaps between the quartz bars are not considered.

Table 8.2 lists the particle hit rates Φ onto the Cherenkov ring detector, the resulting photoelectron current I_{Pe}, and the contained parity-violating asymmetry $\langle A_{\mathrm{PV}}^{\mathrm{ep}} \rangle_{\mathrm{exp}}$. In order to calculate the latter, each particle originating from an elastic electron-proton scattering process as well as secondary particles resulting from interaction of these particles have to be tagged with kinematic information regarding the target scattering process. The expected value of the parity-violating asymmetry $\langle A_{\mathrm{PV}}^{\mathrm{ep}} \rangle_{\mathrm{exp}}$ of the elastic electron-proton scattering process within the P2 Experiment is expressed as [25]:

$$
\langle A_{\mathrm{PV}}^{\mathrm{ep}} \rangle_{\mathrm{exp}} \equiv \frac{\displaystyle\int_{m_e c^2}^{155\,\mathrm{MeV}} dE_i \int_{0°}^{180°} d\Theta_L \left(N_{\mathrm{Pe}}(E_i, \Theta_L) \cdot A_{\mathrm{ep}}(E_i, \Theta_L)^{\mathrm{PV}} \right)}{N_{\mathrm{Pe}}^{\mathrm{bg}} + \displaystyle\int_{m_e c^2}^{155\,\mathrm{MeV}} dE_i \int_{0°}^{180°} d\Theta_L \left(N_{\mathrm{Pe}}(E_i, \Theta_L) \right)} \tag{8.1}
$$

where $A_{\mathrm{ep}}^{\mathrm{PV}}$ is the parity-violating asymmetry of the elastic electron-proton scattering process. N_{Pe} is the number of photoelectrons released from the PMT cathodes as a result of elastic electron-proton scattering with initial energy E_i and scattering angle Θ_L during half of the data taking time $T/2 = 5 \times 10^3\,\mathrm{h}$. $N_{\mathrm{Pe}}^{\mathrm{bg}}$ is the total number of photoelectrons, released over half the data taking time as a result of background processes. The numeric evaluation of 8.1 within the analysis of the P2 main simulation under consideration of the Cherenkov detector response database results into an asymmetry of

$$
\langle A_{\mathrm{PV}}^{\mathrm{ep}} \rangle_{\mathrm{exp}} = -35.00\,\mathrm{ppb} \tag{8.2}
$$

This value as well as contributions by the respective particles is displayed in table 8.2.

The value for the asymmetry $\langle A_{\mathrm{PV}}^{\mathrm{ep}} \rangle_{\mathrm{exp}}$ determined using the old detector response database for detector Geometry I was published in [25] as $\langle A_{\mathrm{PV}}^{\mathrm{ep}} \rangle_{\mathrm{exp}}^{\mathrm{geom\ I}} = -32.57\,\mathrm{ppb}$. Thus, the new value is increased by 7.5%. This could be achieved due to the higher signal yield of the new detector design to the desired electrons.

	Particle type	Φ [s^{-1}]	$I_{\mathbf{Pe}}$ [μA]	Contribution to $\langle A_{\mathbf{PV}}^{\mathrm{ep}} \rangle_{\mathbf{exp}}$ [ppb]
elastic $e-p$	primary electrons $\Theta_L \in [25°, 45°]$	$7.10 \cdot 10^{10}$	1.18	-26.14
	primary electrons $\Theta_L \notin [25°, 45°]$	$3.21 \cdot 10^{10}$	0.55	-6.70
	secondary electrons	$1.33 \cdot 10^{10}$	0.07	-1.28
	secondary photons	$2.12 \cdot 10^{11}$	0.03	-0.64
	secondary positrons	$1.47 \cdot 10^{9}$	0.01	-0.25
	secondary protons	$5.11 \cdot 10^{5}$	0	0
background	electrons	$4.05 \cdot 10^{10}$	$5.4 \cdot 10^{-4}$	0
	photons	$1.14 \cdot 10^{12}$	$4.6 \cdot 10^{-3}$	0
	positrons	$1.40 \cdot 10^{9}$	0	0
	secondary neutrons	$5.41 \cdot 10^{9}$	0	0
	neutrons	$8.31 \cdot 10^{9}$	0	0
	TOTAL	$\mathbf{1.53 \cdot 10^{12}}$	**1.85**	**-35.00**

TABLE 8.2: Hit rates of different particles on the Cherenkov detector medium. Particles stemming from elastic electron-proton scattering are here all events, where elastic electron-proton scattering is the first physical process. Secondary particles are all particles stemming from interactions of elastically scattered electrons and contribute to the parity-violating asymmetry. Particles created in other processes are listed as background.

8.3 Expected Uncertainty in the Measurement of the Weak Mixing Angle

In order to make a prediction of the achievable precision in the P2 Experiment, error propagation calculations are necessary. I herein follow the method developed in [25] under consideration of the photoelectron current distribution given in section 8.2 for the detector response database for the newest detector prototype.

It is assumed that

$$\langle A_{\mathrm{raw}} \rangle_{\mathrm{exp}} = P \cdot \left[(1-f) \cdot \left(\langle A_{\mathrm{PV}}^{\mathrm{ep}} \rangle_{\mathrm{exp}} + \langle A^{\mathrm{H2}} \rangle \right) + f \cdot \langle A_{\mathrm{PV}}^{\mathrm{eAl}} \rangle \right] + A_{\mathrm{false}} \qquad (8.3)$$

contains all relevant contributions to the measured raw asymmetry including the parity-violating elastic electron-proton scattering, contributions $\langle A^{\mathrm{H2}} \rangle$ resulting from target polarisation in the magnetic field and $\langle A_{\mathrm{PV}}^{\mathrm{eAl}} \rangle$ from scattering processes from the aluminium target cell windows respectively. A_{false} sums up all helicity correlated beam and target fluctuations. In equation 8.3 $\langle A_{\mathrm{PV}}^{\mathrm{ep}} \rangle_{\mathrm{exp}}$ refers to the expectation value of the parity-violating asymmetry in the elastic electron-proton

variable	value	uncertainty
P	85%	0.425%
f	0.010	0.0005
$\langle A_{\mathrm{PV}}^{\mathrm{eAl}} \rangle$	400 ppb	6 ppb
$\langle A^{\mathrm{H2}}(T = 15\,\mathrm{K}) \rangle$	0.086 ppb	0.01 ppb
A_{false}	0 ppb	0.1 ppb
$\mathrm{Re}(\square_{\gamma Z})$	0.00106	0.00019
$N_{\mathrm{bg}}^{\mathrm{target}}$	2.04×10^{19}	4.52×10^{9}
$\bar{N}_{\mathrm{Pe}}^{\mathrm{bg}}$	2.96×10^{-2}	6.58×10^{-12}

TABLE 8.3: Input variables used in the Monte-Carlo determination of the error in the asymmetry measured in the P2 Experiment.

scattering given in equation 8.1. P is the beam polarisation which is assumed to be 85 %. f is the ratio of scattering processes from target protons and from aluminium nuclei. Uncertainty contributions by γZ box graph interactions are contained in $A_{\mathrm{PV}}^{\mathrm{ep}}$ and are listed in table 8.3.

The uncertainty determination is based on a data taking time of 10^4 h with a beam energy of $155\,\mathrm{MeV}$ and beam current of $150\,\mathrm{\mu A}$ corresponding to 2.4×10^7 simulated beam electrons. It is calculated by means of a Monte-Carlo method, in which the input variables listed in table 8.3 are varied according to their uncertainties.

The resulting asymmetry and its error are

$$\langle A_{\mathrm{raw}} \rangle_{\mathrm{exp}} = -26.07 \quad \mathrm{ppb} \tag{8.4}$$

and

$$\Delta \langle A_{\mathrm{raw}} \rangle_{\mathrm{exp}} = 0.60 \quad \mathrm{ppb} \tag{8.5}$$

giving a relative uncertainty of

$$\frac{\Delta \langle A_{\mathrm{raw}} \rangle_{\mathrm{exp}}}{\langle A_{\mathrm{raw}} \rangle_{\mathrm{exp}}} = 2.30\% \tag{8.6}$$

The corresponding squared sine of the weak mixing angle at $\mu = m_Z c$ is

$$\sin^2(\Theta_W)(\mu = m_Z c) = 2.31 \times 10^{-1} \tag{8.7}$$

$$\Delta \sin^2(\Theta_W)(\mu = m_Z c) = 3.47 \times 10^{-4} \tag{8.8}$$

giving a relative uncertainty of

$$\frac{\Delta \sin^2(\Theta_W)(\mu = m_Z c)}{\sin^2(\Theta_W)(\mu = m_Z c)} = 0.15\% \tag{8.9}$$

The values generated with the detector response for detector Geometry I as published in [25] were

$$\left(\frac{\Delta \langle A^{\mathrm{raw}} \rangle_{\mathrm{exp}}}{\langle A^{\mathrm{raw}} \rangle_{\mathrm{exp}}} \right)_{\mathrm{geom\ I}} = 2.32\% \tag{8.10}$$

and

$$\left(\frac{\Delta \sin^2(\Theta_W)(\mu = m_Z c)}{\sin^2(\Theta_W)(\mu = m_Z c)} \right)_{\mathrm{geom\ I}} = 0.16\% \tag{8.11}$$

The achievable uncertainty of the measurement of the weak mixing angle is thus slightly better with the new wedged detector element geometry than it would be using cuboid detector bars. This difference is not significant enough to justify the immense extra cost of the wedged bars. The reason to chose the detector geometry III is merely the optimal coverage of the desired laboratory angle, which can only be achieved by using wedged detector elements[1].

---

[1] See section 4.2.3.1

Chapter 9

Summary and Conclusion

Within this doctoral thesis, a concept for a detector for the parity-violating measurement of the proton's weak charge has been developed. After material and geometry considerations and preparatory studies of the characteristics of potential hardware components, several prototype detector elements have been built. These have been tested at the MAMI electron beam and the A2 real photon facility in Mainz. A range of the different models has proven to fulfil the signal yield requirements. A series of comparative measurements done during nine beamtimes at the MAMI accelerator allowed us to decide in favour of a specific detector geometry and set of components and materials.

In order to provide a good detection efficiency and signal yield to electrons while suppressing the signal of photonic background, the P2 collaboration is going to use a Cherenkov detector. The ring-shaped detector area will be divided into 72 individual independent modules, each consisting of a fused silica bar acting as Cherenkov medium and a photomultiplier as Cherenkov light sensor. To efficiently cover the ring-shaped detector area, these modules will be tapered over a length of 450 mm. In total, the detector bars are going to be 650 mm long. The outermost 200 mm is going to serve as light guides to direct the Cherenkov light to the PMTs, which will be placed behind a shielding to protect them from radiation.

Regarding the fused silica grade, we propose Spectrosil 2000 by Heraeus Conamic. The comparison between Spectrosil and Suprasil has shown no significant differences, neither in material investigations nor in prototype tests at MAMI. Transmittance, as well as Cherenkov light yield, are the same in both material grades. However, Spectrosil 2000 is superior to the Suprasil in terms of radiation hardness. Of a variety of PMTs tested during the beamtimes, the model 9305QKMB by Electron Tubes is suitable both by its specifications and performance during the measurements at MAMI.

A detector prototype of this material and geometry has been tested at the MAMI electron beam. It has shown to provide a signal yield well in excess of the demanded critical number of PMT photoelectrons.

The signal output of the Cherenkov detector elements under the impact of relativistic electrons and high energy photons has been studied both experimentally at the MAMI beam as well as in GEANT4 simulations. The detector response from simulations is in good agreement with the measurements. A detector response database for all relevant particle types, energies and impact angles and positions onto the detector was established. By means of this database, the particle flux hitting the detector was converted into signal contribution data. Using the kinematic data of the scattering process these particles underwent, their signal yield allows conclusions regarding the particles' contribution to the measured asymmetry. On this basis, it can be concluded that the P2 experimental setup along with the fused silica Cherenkov detector ring is suitable for the measurement of the weak mixing angle with an accuracy of 0.15%.

Appendix A

Optical Properties of Hardware Used in the GEANT4 Detector Simulation

λ[nm]	$n(\lambda)$	$T(\lambda)$	$R(\lambda)$(Alanod)	$QE(\lambda)$(Hama)	$QE(\lambda)$(ET)
800	1.45332	0.9999	0.7	0	0
780	1.45367	0.9999	0.75	0	0
760	1.45404	0.9999	0.76	0	0
740	1.45444	0.9998	0.78	0	0
720	1.45485	0.9998	0.75	0	0
700	1.45529	0.9999	0.78	0	0
680	1.45576	0.9999	0.80	0.0121	0
660	1.45627	0.9998	0.80	0.0211	0
640	1.45681	0.9998	0.80	0.0329	0.0014
620	1.45740	0.9998	0.80	0.0468	0.0053
600	1.45804	0.9998	0.79	0.0628	0.0143
580	1.45873	0.9998	0.80	0.0833	0.028
560	1.4595	0.9998	0.81	0.1115	0.0453
540	1.46034	0.9998	0.81	0.1461	0.069
520	1.46128	0.9998	0.81	0.1848	0.1209
500	1.46232	0.9998	0.82	0.2118	0.1600

480	1.46350	0.9999	0.82	0.2330	0.1863
460	1.46483	0.9999	0.82	0.2621	0.2146
440	1.46634	0.9999	0.82	0.2904	0.2458
420	1.46809	0.9999	0.84	0.3187	0.2673
400	1.47012	0.9999	0.85	0.3266	0.2887
380	1.47248	0.9999	0.85	0.3396	0.2982
360	1.47529	0.9999	0.86	0.3349	0.3212
340	1.47865	0.9999	0.88	0.3435	0.3180
320	1.48274	0.9999	0.90	0.3452	0.3154
300	1.48779	0.9998	0.91	0.3392	0.3021
280	1.49416	0.9997	0.88	0.3215	0.2914
260	1.50239	0.9996	0.87	0.3026	0.2794
240	1.51333	0.9994	0.73	0.2937	0.269
220	1.52845	0.999	0.55	0.282	0.2914
200	1.55051	0.9983	0.41	0.2839	0.3379
180	1.58529	0.9883	0	0.3450	0

TABLE A.1: Spectral data as used in the GEANT4 Detector response simulation. λ is the wavelength, $n(\lambda)$ the spectral refractive index and $T(\lambda)$ the light transmittance of fused silica, $R(\lambda)$(Alanod) is the reflectivity of the reflective wrapping material Alanod 4300UP, $QE(\lambda)$(Hama) and $QE(\lambda)$(ET) are the quantum efficiencies of the Hamamatsu R11410 and the Electron Tubes ET 9305QKMB Serial No. 509 respectively. The quantum efficiencies are taken from the same sources as in 5.29.

Appendix B

A2 Tagger Channel Calibration

tagger channel	photon energy [MeV]	energy width [MeV]
211	80.694	0.567
212	80.191	0.571
213	79.68	0.558
214	79.184	0.546
215	78.68	0.549
216	78.176	0.552
217	77.672	0.555
218	77.167	0.558
219	76.662	0.561
220	76.157	0.564
221	75.651	0.567
222	75.146	0.569
223	74.639	0.572
224	74.133	0.575
225	73.619	0.563
226	73.12	0.55
227	72.613	0.553
228	72.105	0.556
229	71.598	0.558

230	71.09	0.561
231	70.582	0.564
232	70.074	0.567
233	69.566	0.57
234	69.058	0.572
235	68.549	0.575
236	68.04	0.578
237	67.524	0.567
238	67.022	0.556
239	66.513	0.559
240	66.003	0.561
241	65.494	0.564
242	64.984	0.567
243	64.475	0.569
244	63.965	0.572
245	63.455	0.575
246	62.945	0.578
247	62.435	0.58
248	61.925	0.583
249	61.407	0.571
250	60.904	0.56
251	60.394	0.562
252	59.883	0.565
253	59.373	0.567
254	58.862	0.57
255	58.352	0.573
256	57.841	0.576
257	57.331	0.578
258	56.82	0.581

259	56.309	0.583
260	55.799	0.586
261	55.281	0.574
262	54.778	0.562
263	54.267	0.564
264	53.757	0.567
265	53.247	0.569
266	52.736	0.572
267	52.226	0.574
268	51.716	0.577
269	51.205	0.58
270	50.695	0.582
271	50.185	0.584
272	49.675	0.587
273	49.159	0.577
274	48.655	0.567
275	48.146	0.569
276	47.636	0.571
277	47.126	0.574
278	46.617	0.576
279	46.108	0.579
280	45.599	0.581
281	45.09	0.584
282	44.581	0.586
283	44.072	0.589
284	43.563	0.591
285	43.047	0.578
286	42.547	0.565
287	42.038	0.567

288	41.53	0.57
289	41.023	0.572
290	40.515	0.574
291	40.008	0.576
292	39.5	0.579
293	38.993	0.581
294	38.486	0.584
295	37.98	0.586
296	37.473	0.588
297	36.96	0.577
298	36.461	0.566
299	35.955	0.569
300	35.449	0.571
301	34.944	0.573
302	34.439	0.575
303	33.934	0.577
304	33.429	0.58
305	32.925	0.582
306	32.421	0.584
307	31.917	0.586
308	31.413	0.589
309	30.903	0.577
310	30.407	0.566
311	29.904	0.568
312	29.401	0.57
313	28.899	0.572
314	28.397	0.575
315	27.895	0.577
316	27.394	0.579

317	26.893	0.581
318	26.392	0.583
319	25.892	0.585
320	25.391	0.587
321	24.891	0.589
322	24.385	0.578
323	23.893	0.566
324	23.394	0.568
325	22.895	0.57
326	22.397	0.572
327	21.899	0.574
328	21.401	0.576
329	20.904	0.578
330	20.407	0.58
331	19.911	0.582
332	19.415	0.584
333	18.919	0.586
334	18.423	0.588
335	17.921	0.576
336	17.433	0.564
337	16.939	0.566
338	16.445	0.568
339	15.951	0.57
340	15.458	0.572
341	14.965	0.574
342	14.472	0.575
343	13.98	0.577
344	13.489	0.58
345	12.997	0.581

346	12.506	0.583
347	12.016	0.585
348	11.518	0.573
349	11.036	0.56
350	10.546	0.562
351	10.057	0.564
352	9.569	0.566

TABLE B.1: A2 photon tagger calibration for 180 MeV primary electrons.

Appendix C

Cherenkov Threshold for Electrons in Fused Silica

The Cherenkov angle depends on the charged particle's velocity and on the refractive index of the medium:

$$\cos \Theta_C = \frac{1}{n(\lambda)\beta} \tag{C.1}$$

Solving

$$E = \frac{m_0 c^2}{\sqrt{1 - \beta^2}} \tag{C.2}$$

for β and inserting into equation C.1 gives

$$\Theta_C = \arccos \left(\frac{1}{n(1 - \frac{m_0^2 c^4}{E^2})} \right) \tag{C.3}$$

The velocity in the Cherenkov medium has to be larger than the phase velocity of light:

$$v_S \geq \frac{c}{n} \tag{C.4}$$

where

$$\beta = \frac{v}{c} \tag{C.5}$$

It follows for the threshold that

$$\beta_S = \frac{1}{n} \tag{C.6}$$

The necessary energy of the particle

$$E = \gamma m c^2 = \frac{1}{\sqrt{1 - \beta^2}} \cdot m c^2 \tag{C.7}$$

is then

$$E_S = m c^2 \cdot \frac{1}{\sqrt{1 - \frac{1}{n^2}}} \tag{C.8}$$

Inserting the electron mass $0.511 \, \mathrm{MeV/c^2}$ and the refractive index for fused silica ($n \approx 1.45$) delivers an energy threshold of $0.71 \, \mathrm{MeV}$.

Appendix D

QDC Channel Calibration Data
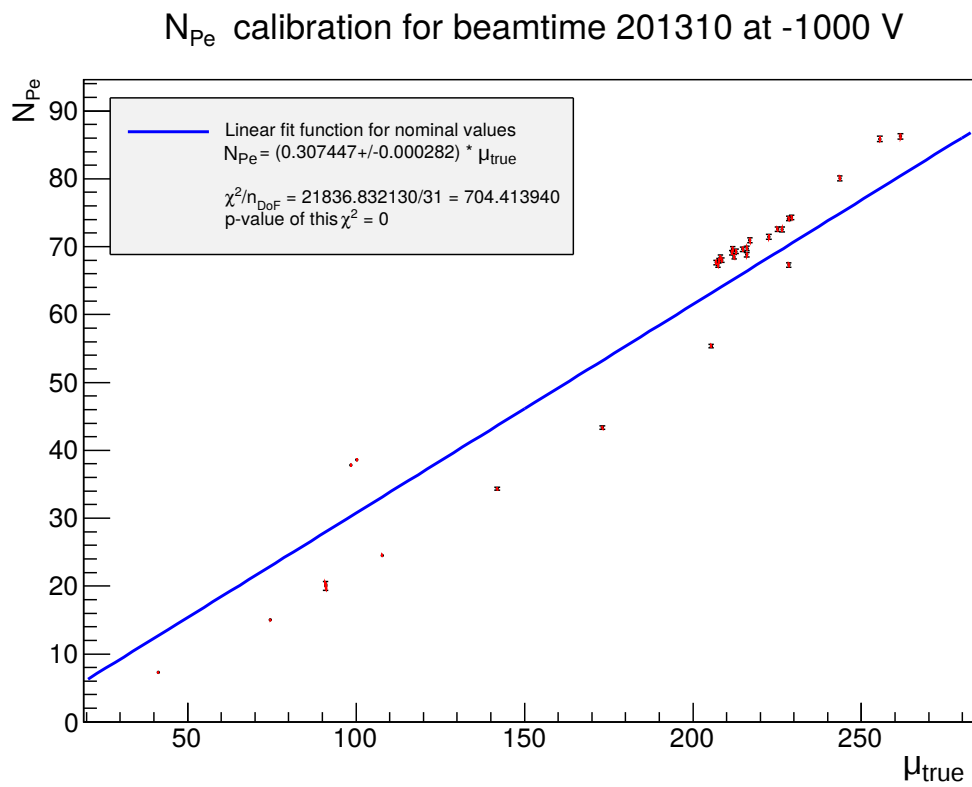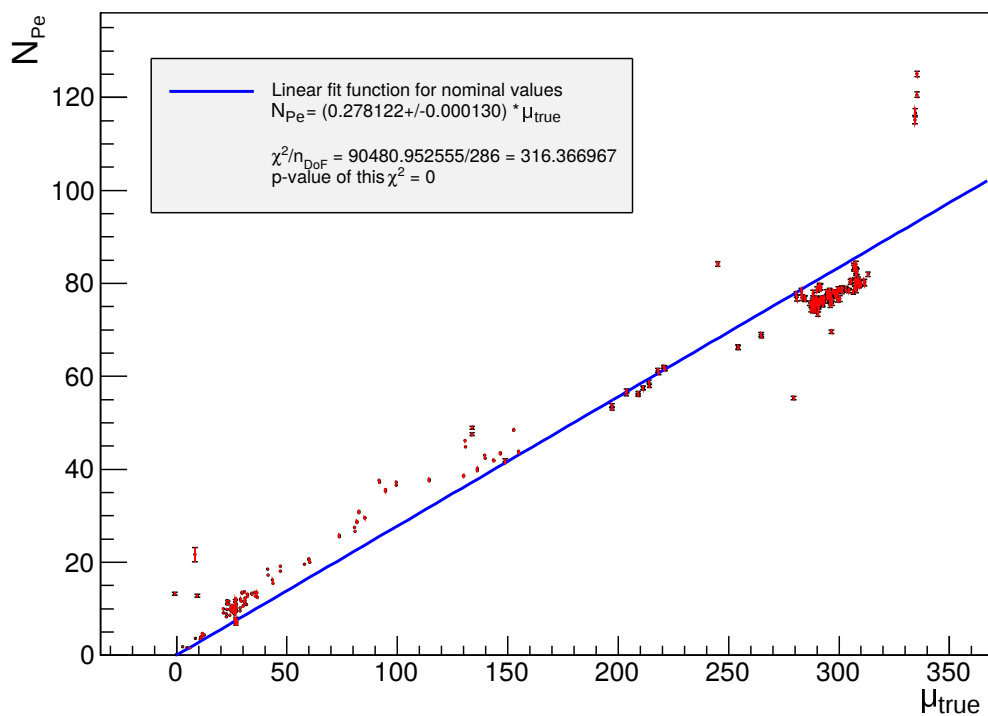
N_{Pe} calibration for beamtime 201310 at -1000 V

Linear fit function for nominal values
$N_{Pe} = (0.307447+/-0.000282) * \mu_{true}$

$\chi^2/n_{DoF} = 21836.832130/31 = 704.413940$
p-value of this χ^2 = 0

FIGURE D.1

FIGURE D.2

FIGURE D.3

N_{Pe} calibration for beamtime 201411 at -1200 V

Linear fit function for nominal values
$N_{Pe} = (0.060933 +/- 0.000033) * \mu_{true}$

$\chi^2/n_{DoF} = 55478.125968/172 = 322.547244$
p-value of this $\chi^2 = 0$

FIGURE D.4

N_{Pe} calibration for beamtime 201411 at -1000 V

Linear fit function for nominal values
$N_{Pe} = (0.271722 +/- 0.000147) * \mu_{true}$

$\chi^2/n_{DoF} = 13719.782143/67 = 204.772868$
p-value of this $\chi^2 = 0$
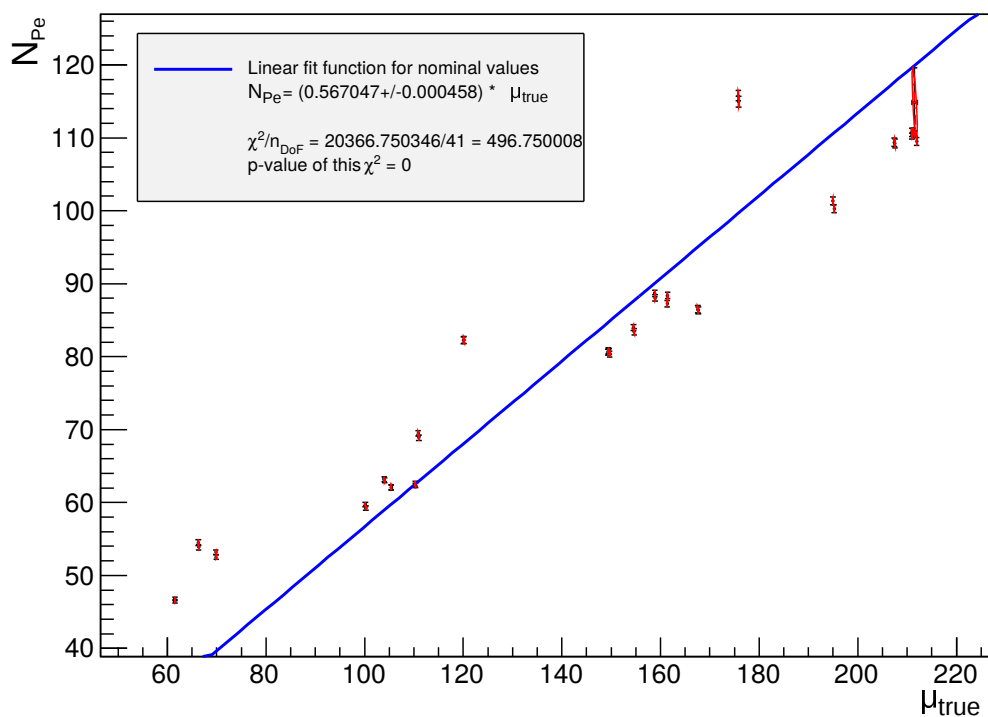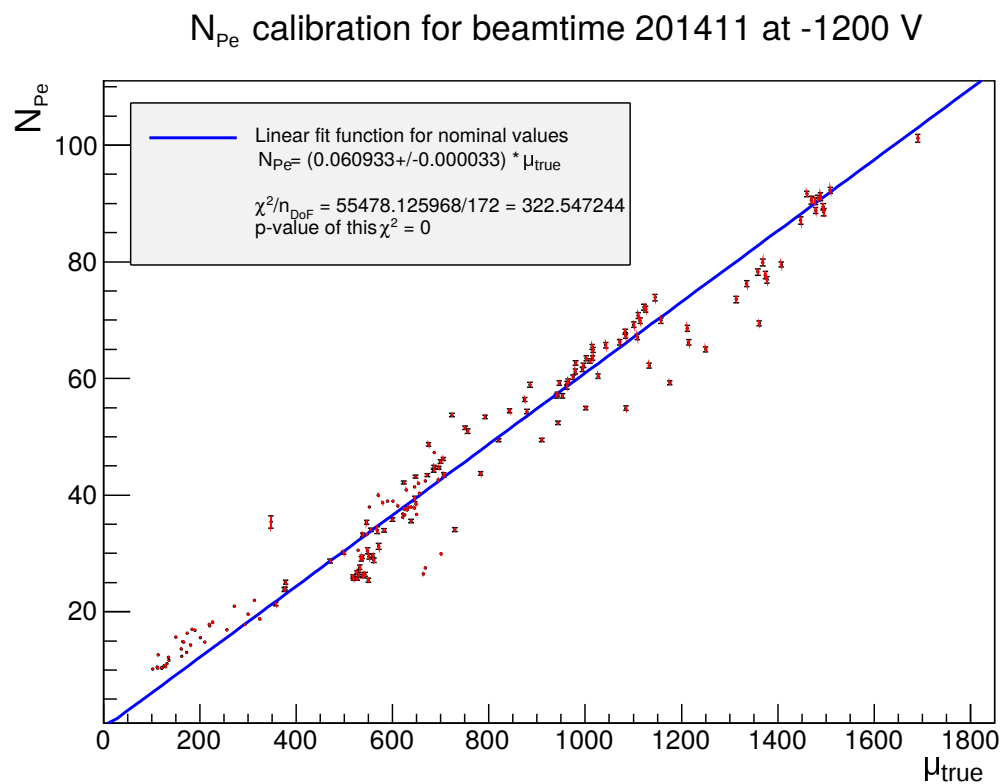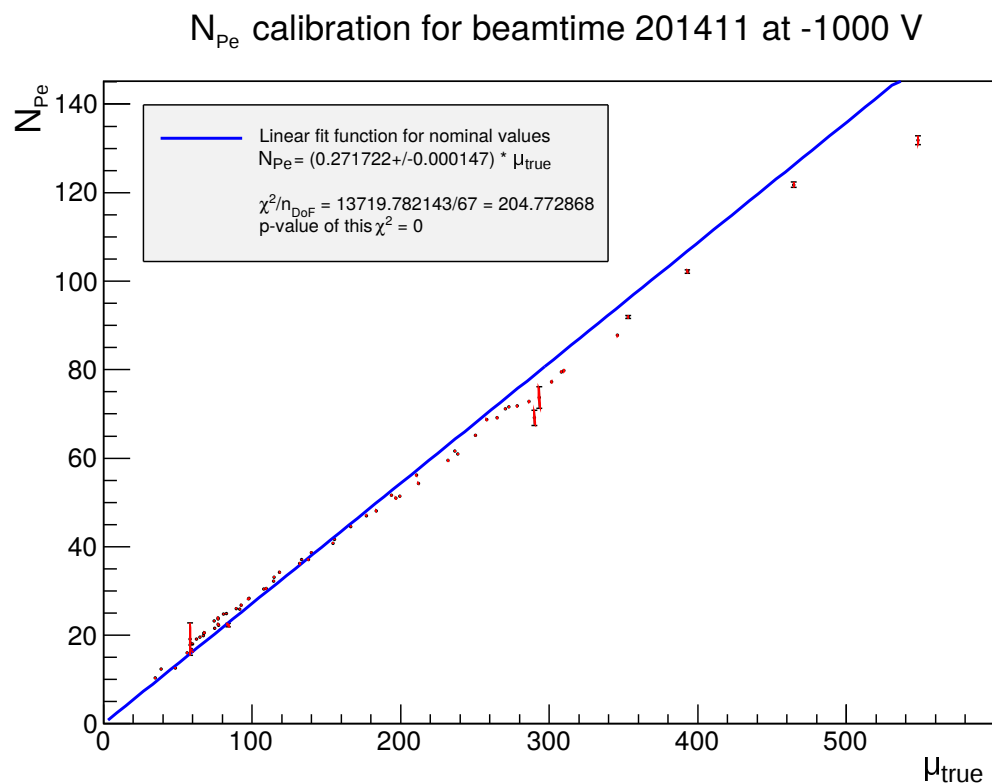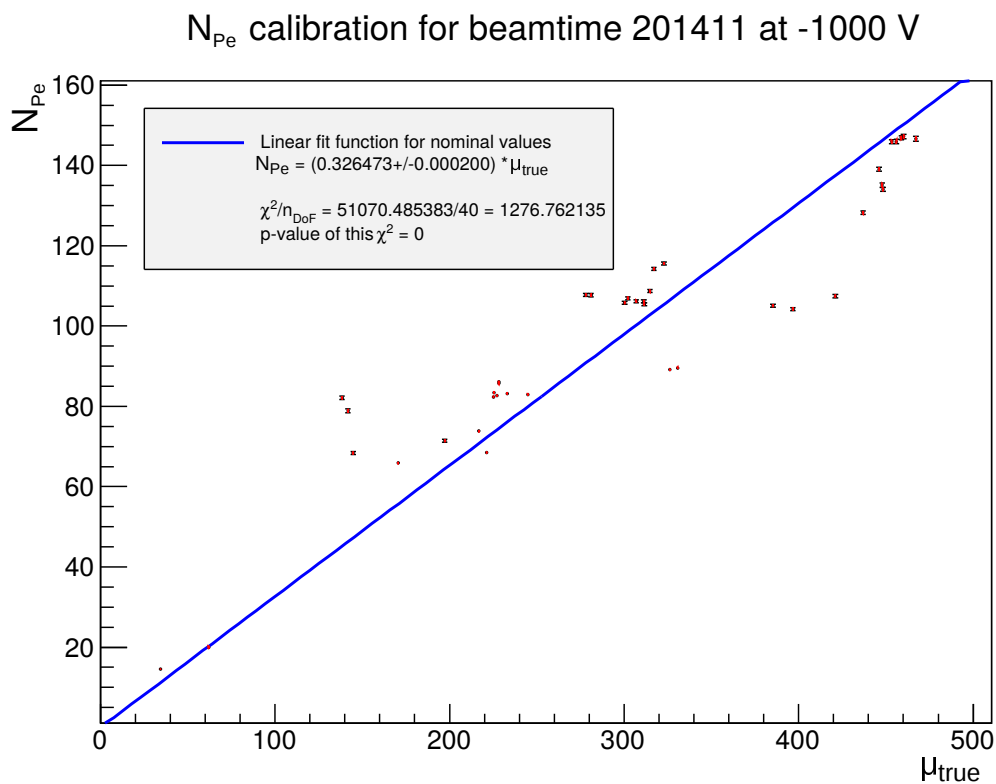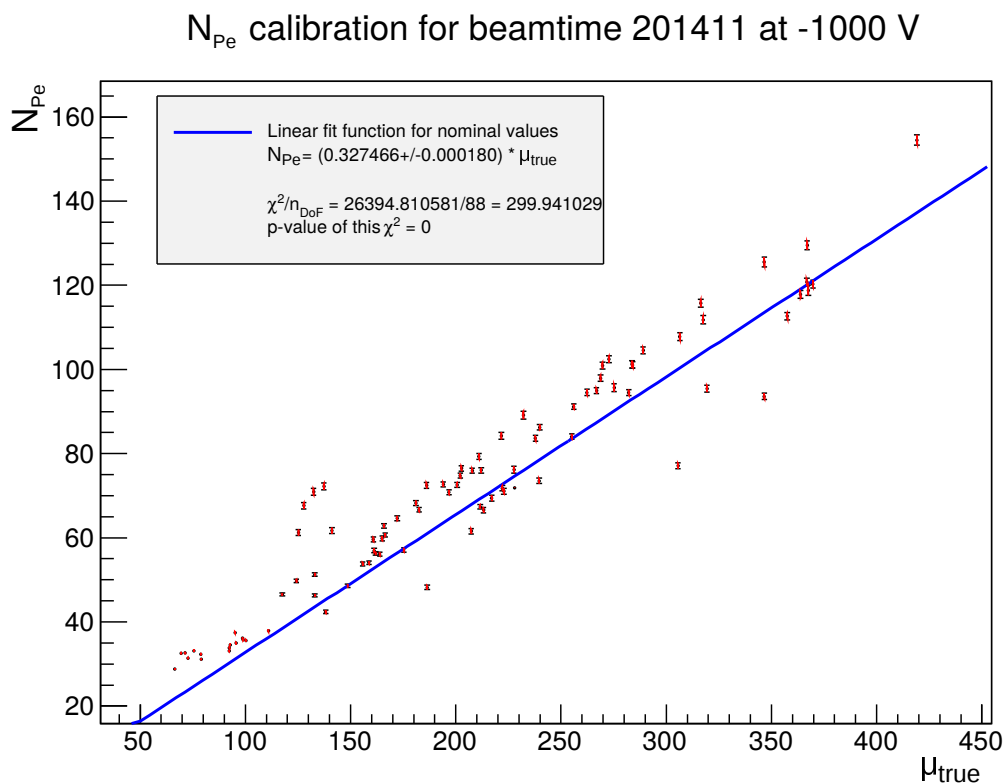
FIGURE D.5

N$_{Pe}$ calibration for beamtime 201411 at -1000 V
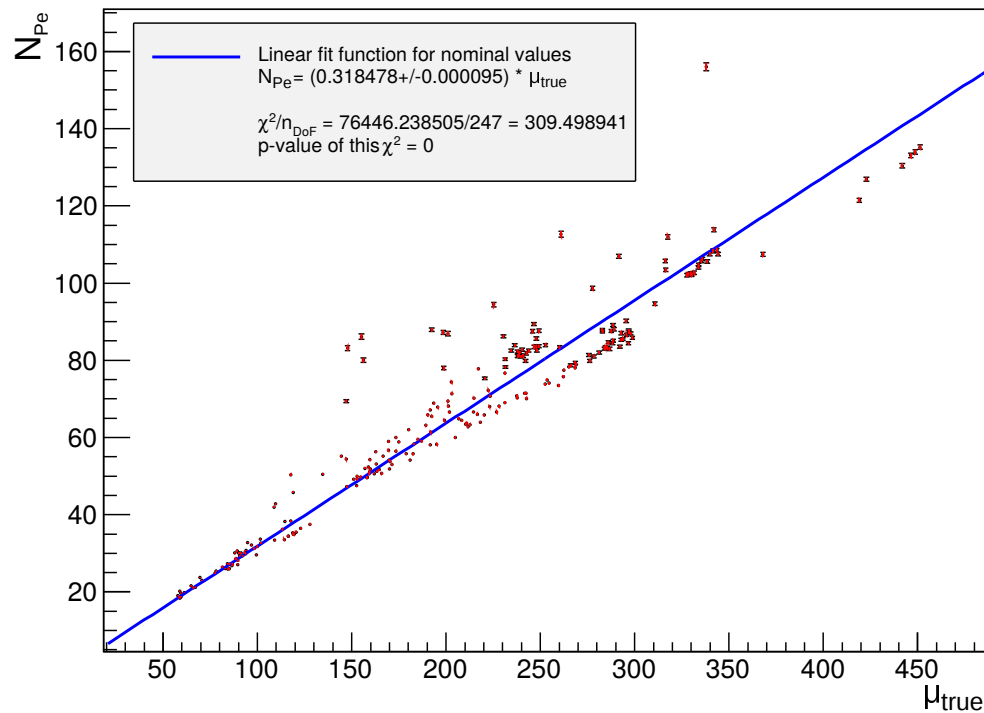
FIGURE D.6

N$_{Pe}$ calibration for beamtime 201411 at -1000 V
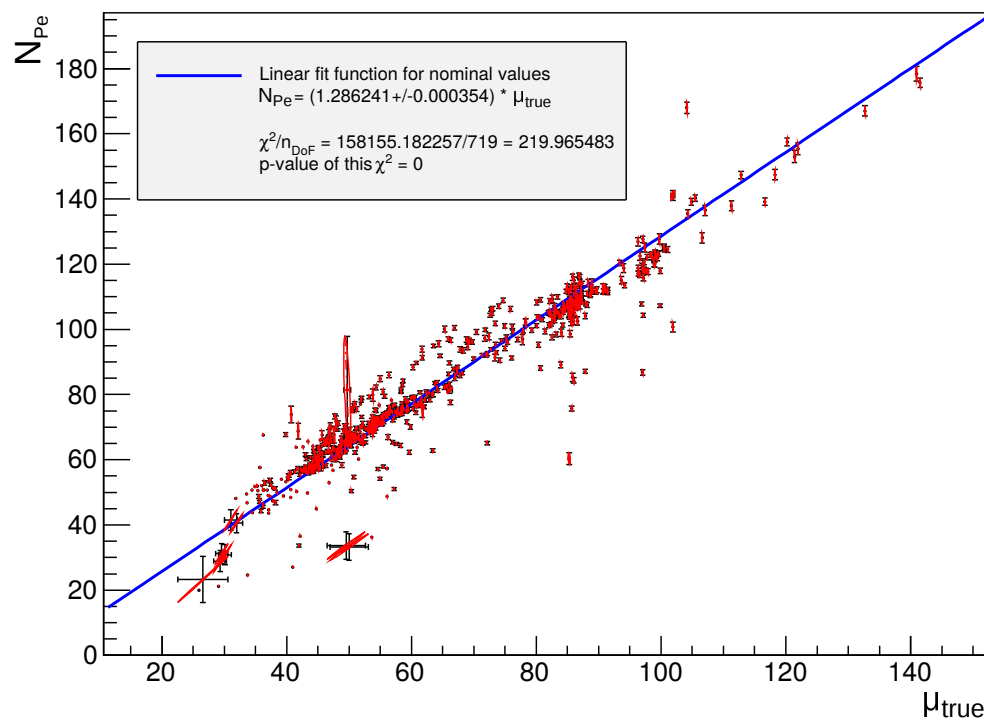
FIGURE D.7

FIGURE D.8

FIGURE D.9

N_{Pe} calibration for beamtime 201903 at -1200 V

Linear fit function for nominal values
$N_{Pe}= (0.087185+/-0.000122) * \mu_{true}$

$\chi^2/n_{DoF} = 2972.488418/61 = 48.729318$
p-value of this χ^2 = 0
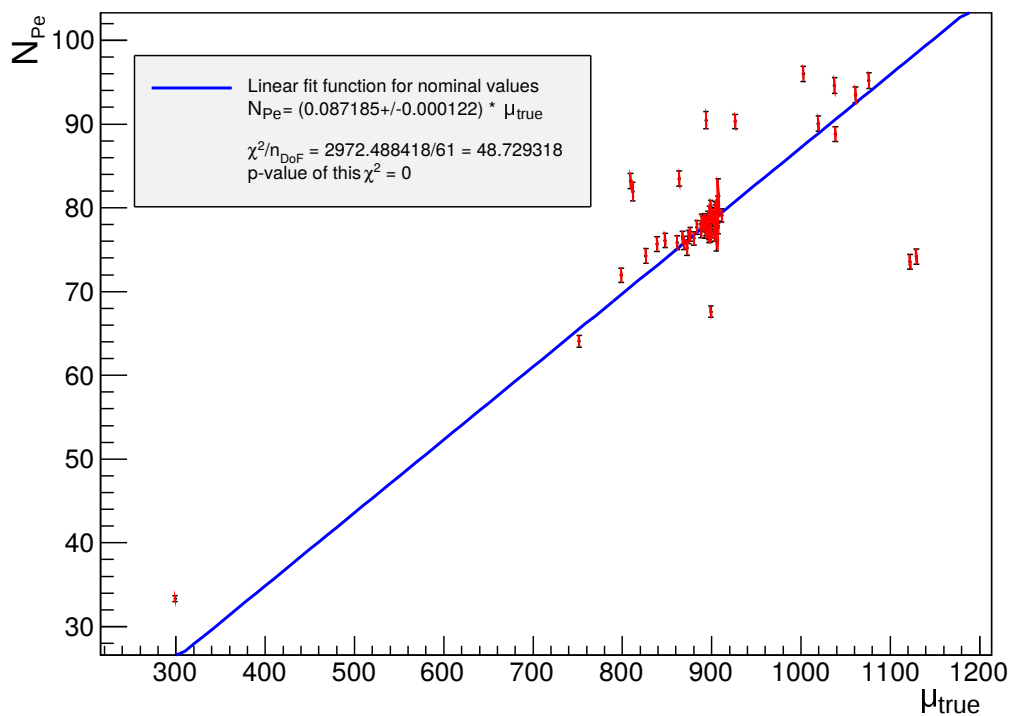
FIGURE D.10

N_{Pe} calibration for beamtime 201903 at -1350 V

Linear fit function for nominal values
$N_{Pe}= (1.499724+/-0.001204) * \mu_{true}$

$\chi^2/n_{DoF} = 1179.527315/211 = 5.590177$
p-value of this χ^2 = 2.92674e-134
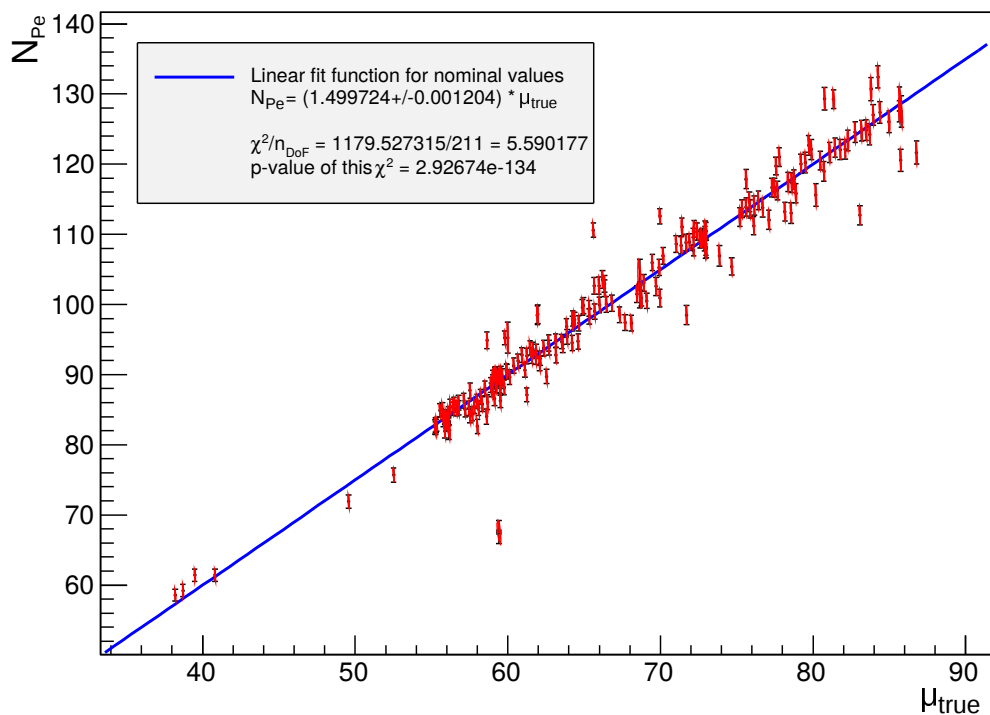
FIGURE D.11

Appendix E

High Voltage Scans

HV Scan for ET 9305QKMB, serial 518

FIGURE E.1

HV Scan for Hamamatsu R11410, serial ZK6862
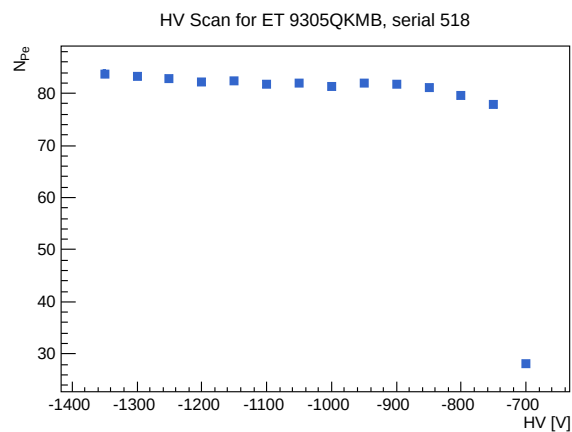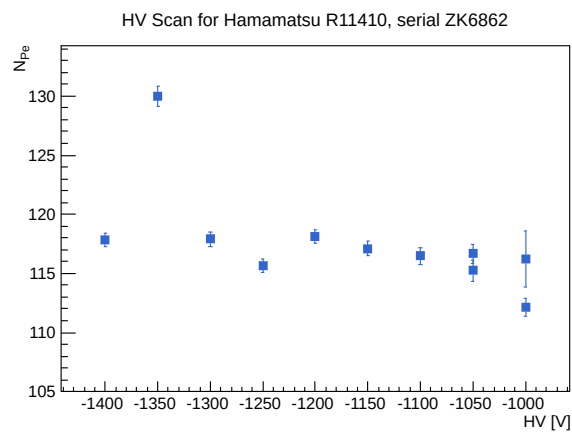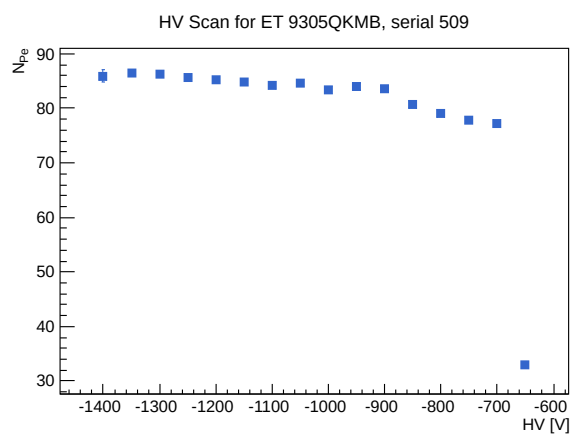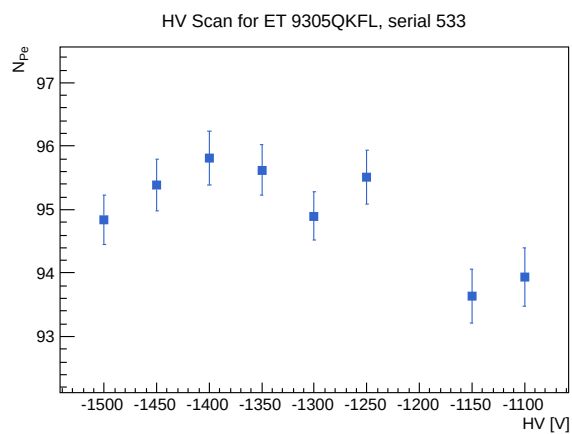
FIGURE E.2

FIGURE E.3

FIGURE E.4
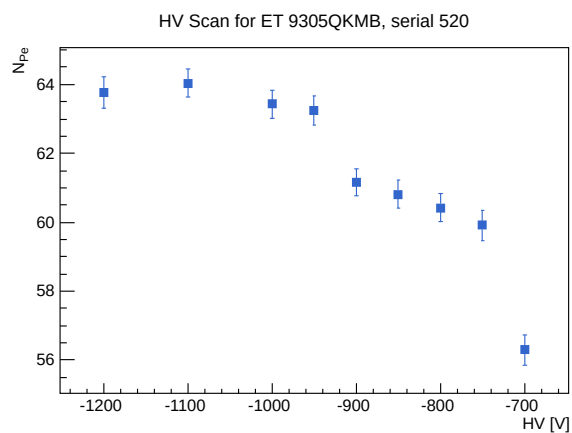
FIGURE E.5

Appendix F

Detector Response Database

F.1 Detector Response to Electrons
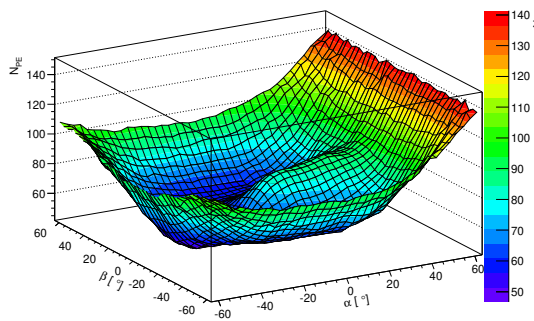

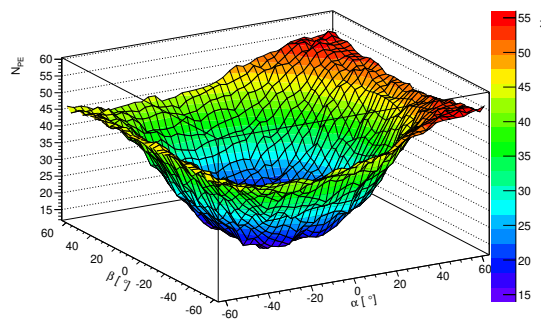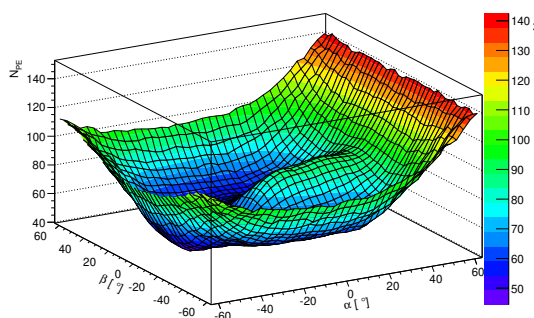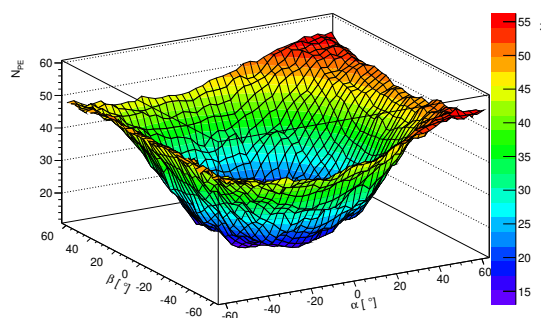detector response to electrons 0.5 - 1.5 MeV

RMS response to electrons 0.5 - 1.5 MeV

detector response to electrons 1.5 - 2.5 MeV

RMS response to electrons 1.5 - 2.5 MeV
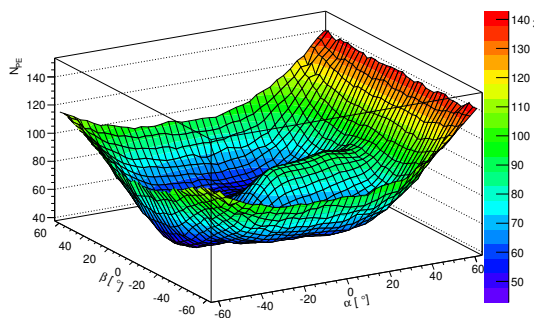
detector response to electrons 2.5 - 3.5 MeV

RMS response to electrons 2.5 - 3.5 MeV

detector response to electrons 3.5 - 4.5 MeV

RMS response to electrons 3.5 - 4.5 MeV

detector response to electrons 4.5 - 5.5 MeV

RMS response to electrons 4.5 - 5.5 MeV
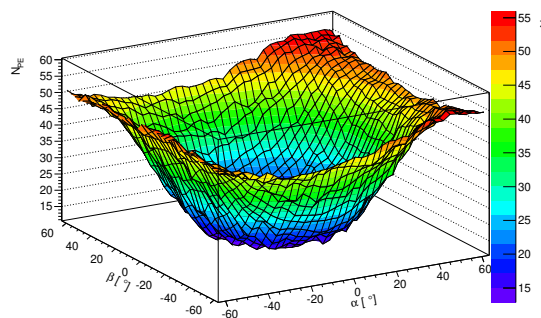
detector response to electrons 5.5 - 6.5 MeV
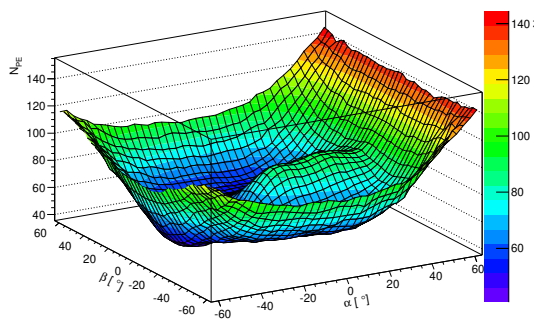
RMS response to electrons 5.5 - 6.5 MeV

detector response to electrons 6.5 - 7.5 MeV

RMS response to electrons 6.5 - 7.5 MeV

detector response to electrons 7.5 - 8.5 MeV
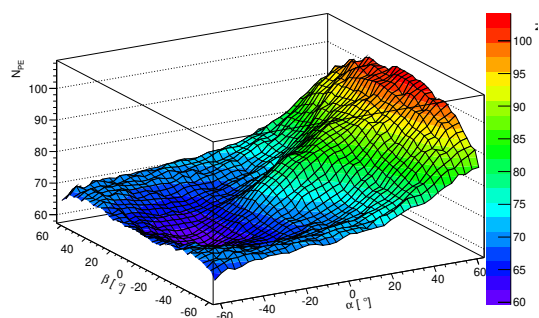
RMS response to electrons 7.5 - 8.5 MeV
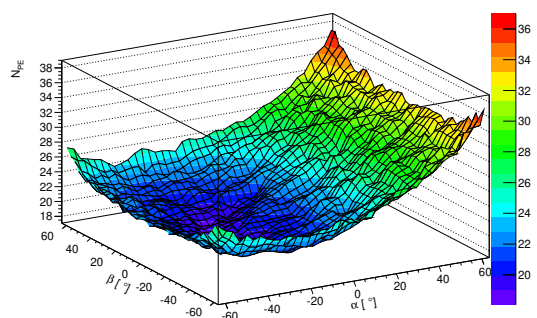
detector response to electrons 8.5 - 9.5 MeV
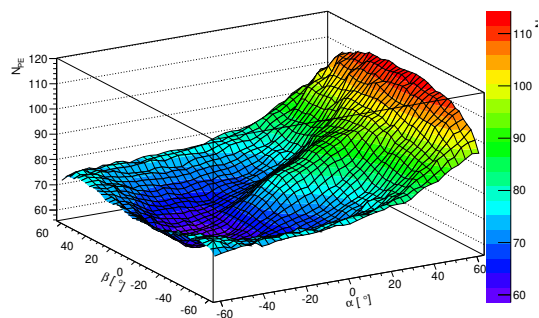
RMS response to electrons 8.5 - 9.5 MeV
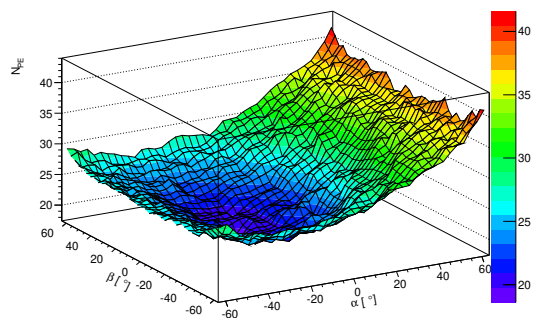
detector response to electrons 9.5 - 10.5 MeV

RMS response to electrons 9.5 - 10.5 MeV

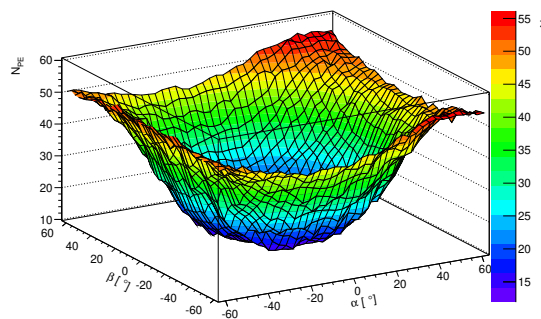detector response to electrons 10.5 - 11.5 MeV

RMS response to electrons 10.5 - 11.5 MeV

detector response to electrons 11.5 - 12.5 MeV

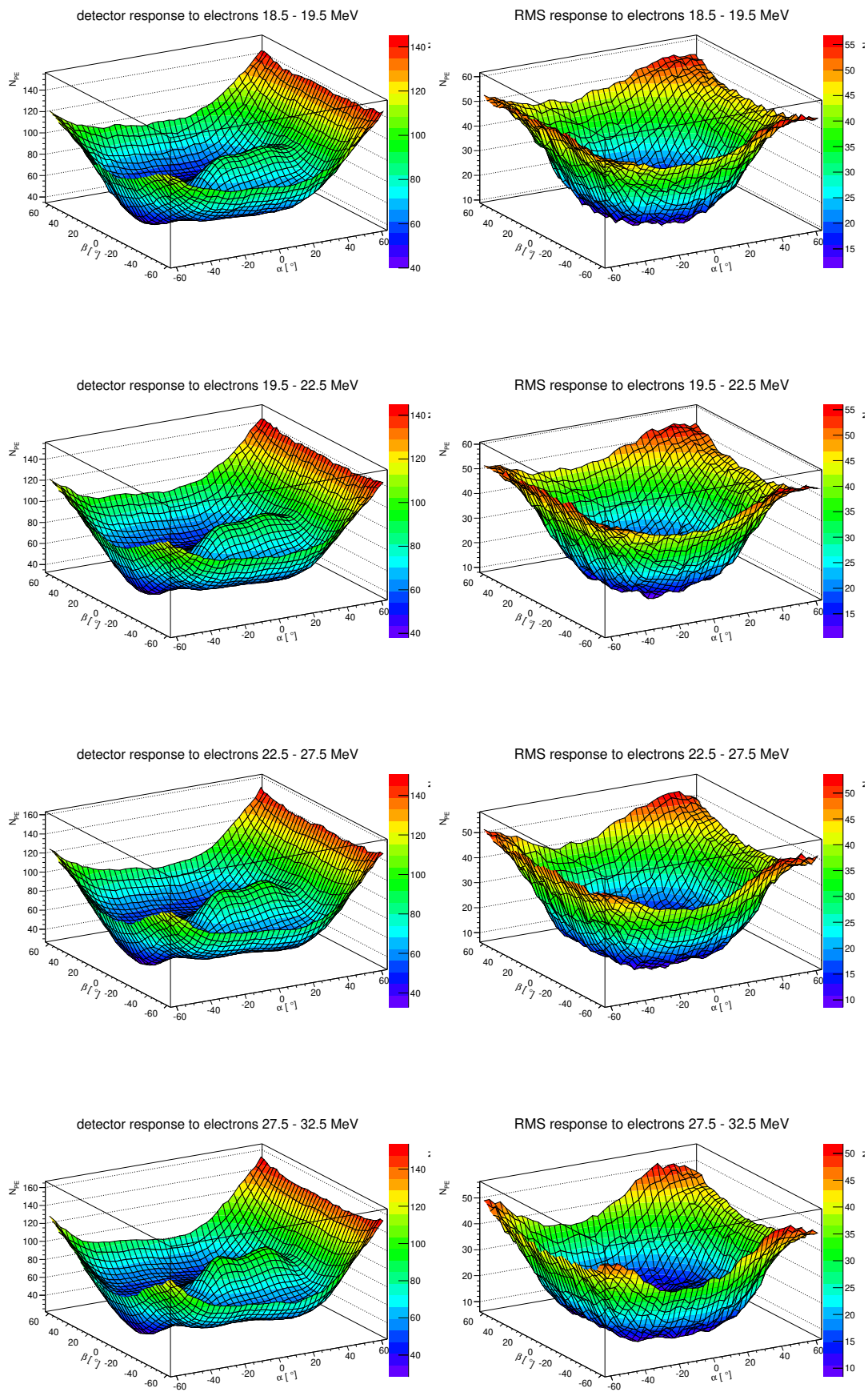RMS response to electrons 11.5 - 12.5 MeV

detector response to electrons 12.5 - 13.5 MeV

RMS response to electrons 12.5 - 13.5 MeV

detector response to electrons 13.5 - 14.5 MeV
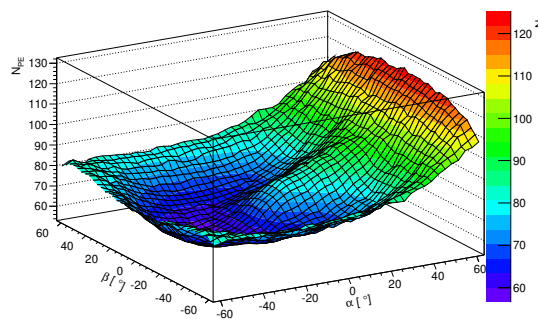
RMS response to electrons 13.5 - 14.5 MeV
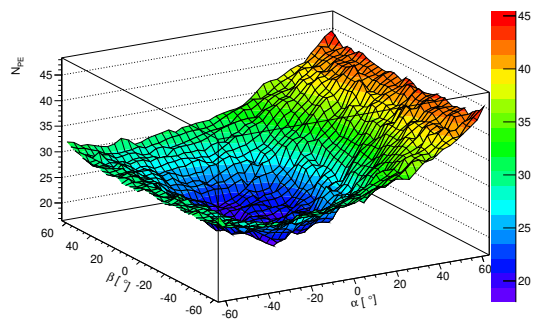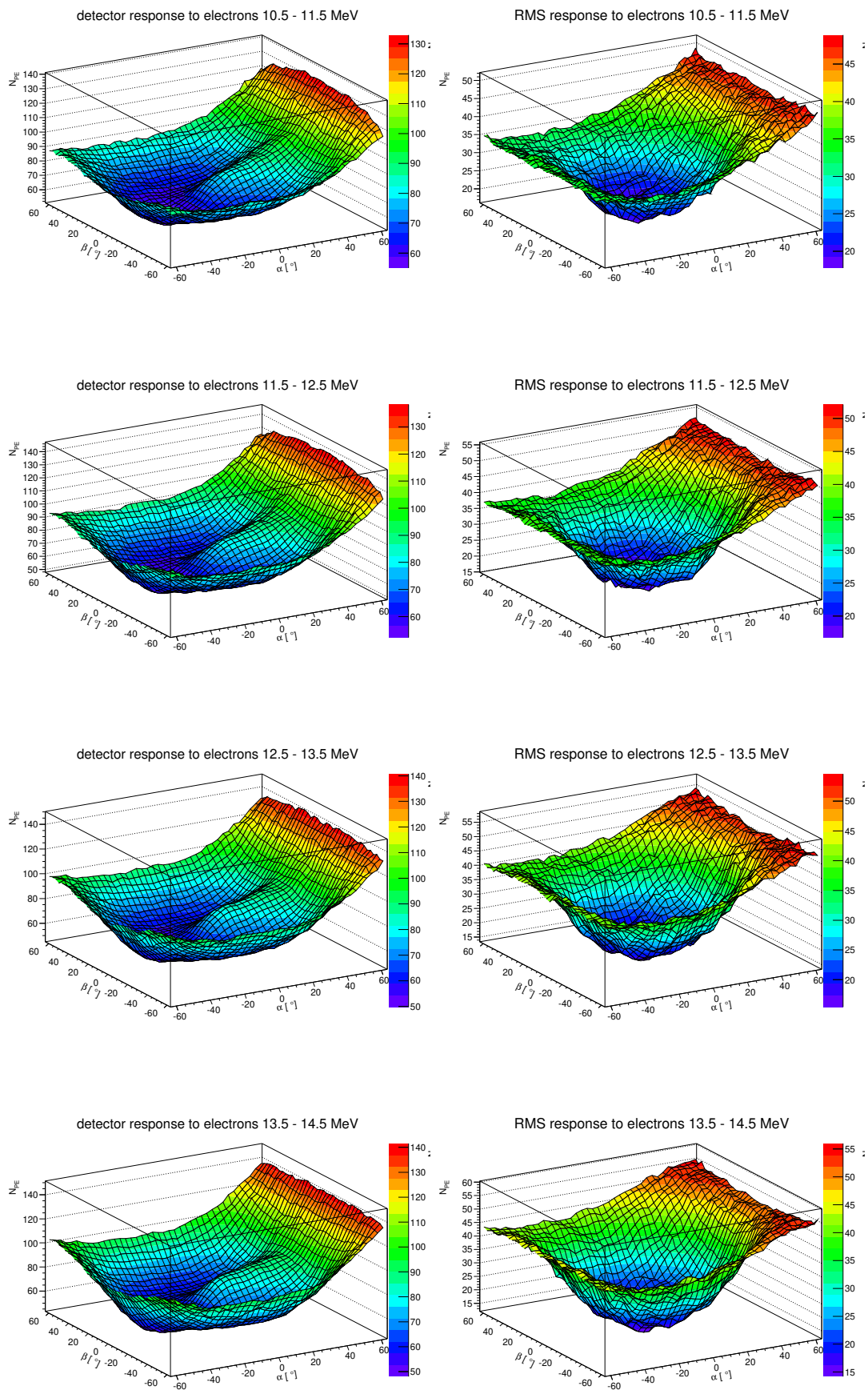
detector response to electrons 14.5 - 15.5 MeV

RMS response to electrons 14.5 - 15.5 MeV

detector response to electrons 15.5 - 16.5 MeV

RMS response to electrons 15.5 - 16.5 MeV

detector response to electrons 16.5 - 17.5 MeV
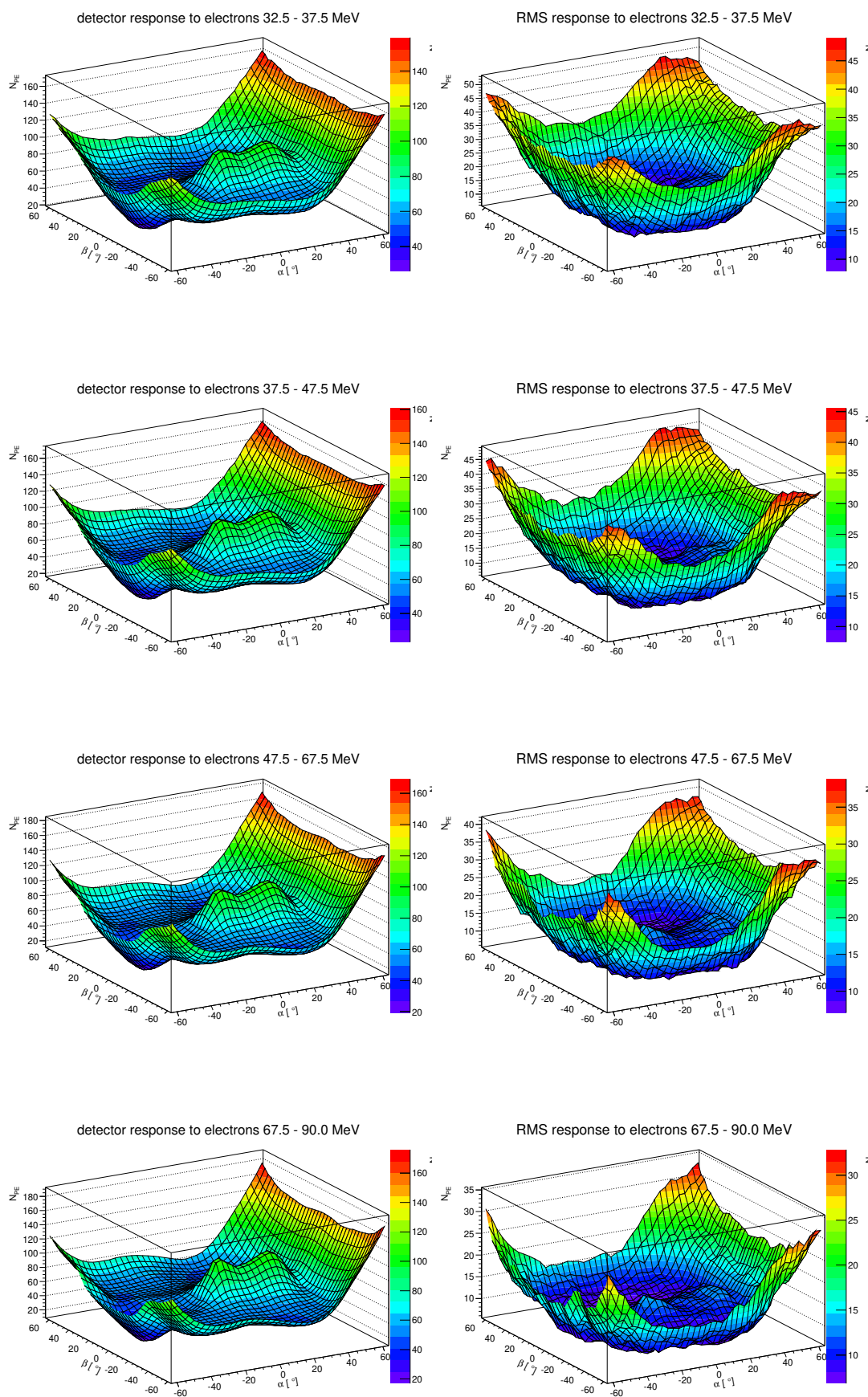
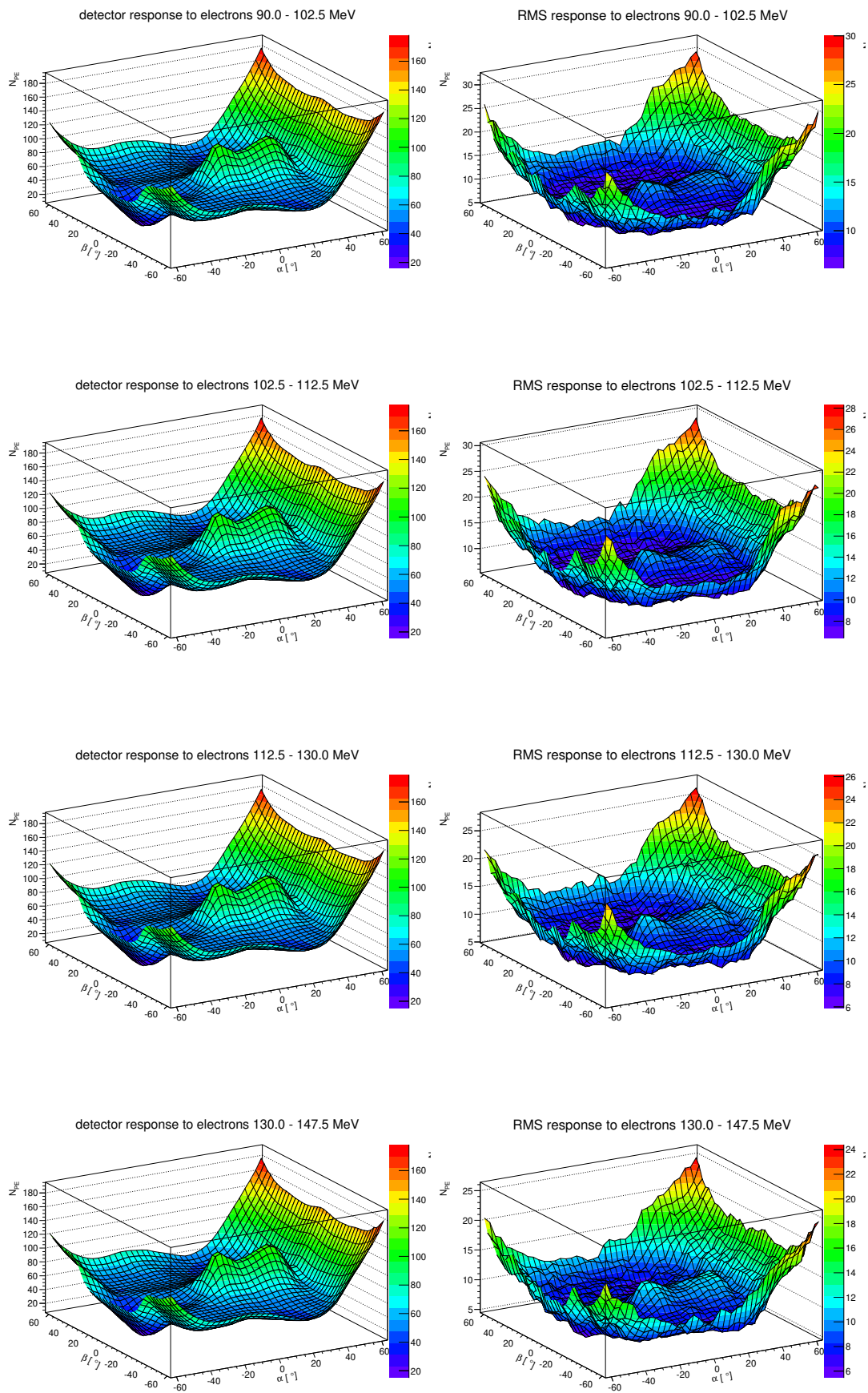RMS response to electrons 16.5 - 17.5 MeV
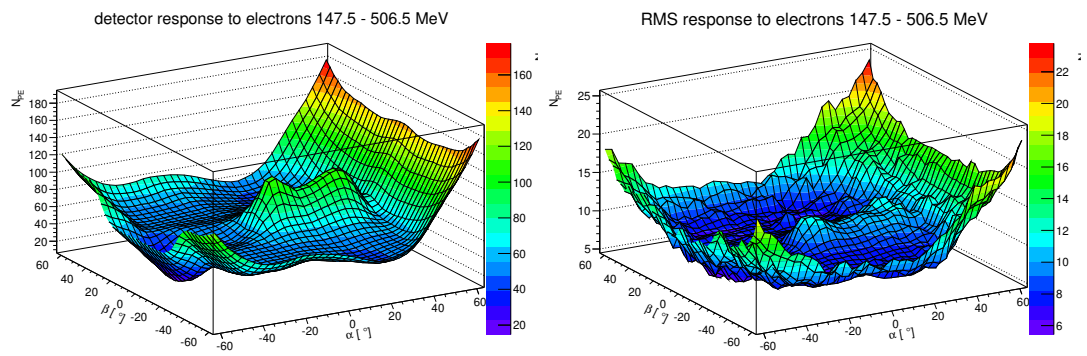
detector response to electrons 17.5 - 18.5 MeV

RMS response to electrons 17.5 - 18.5 MeV

detector response to electrons 18.5 - 19.5 MeV
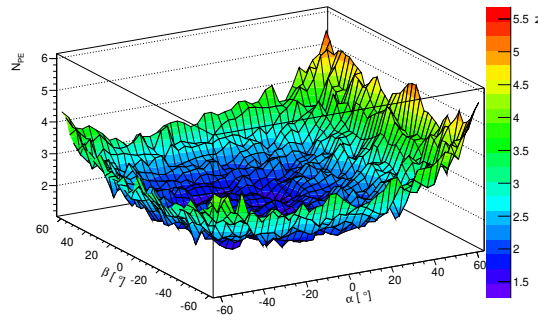
RMS response to electrons 18.5 - 19.5 MeV

detector response to electrons 19.5 - 22.5 MeV

RMS response to electrons 19.5 - 22.5 MeV

detector response to electrons 22.5 - 27.5 MeV

RMS response to electrons 22.5 - 27.5 MeV
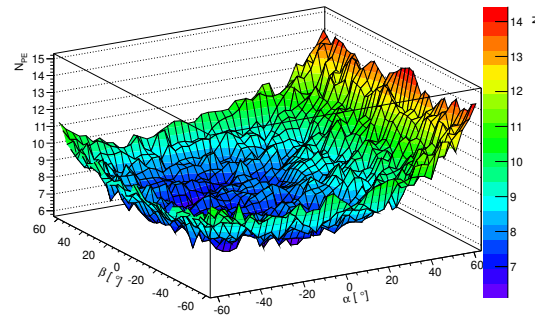
detector response to electrons 27.5 - 32.5 MeV

RMS response to electrons 27.5 - 32.5 MeV

detector response to electrons 32.5 - 37.5 MeV

RMS response to electrons 32.5 - 37.5 MeV

detector response to electrons 37.5 - 47.5 MeV

RMS response to electrons 37.5 - 47.5 MeV

detector response to electrons 47.5 - 67.5 MeV

RMS response to electrons 47.5 - 67.5 MeV

detector response to electrons 67.5 - 90.0 MeV

RMS response to electrons 67.5 - 90.0 MeV

detector response to electrons 90.0 - 102.5 MeV

RMS response to electrons 90.0 - 102.5 MeV

detector response to electrons 102.5 - 112.5 MeV

RMS response to electrons 102.5 - 112.5 MeV

detector response to electrons 112.5 - 130.0 MeV

RMS response to electrons 112.5 - 130.0 MeV

detector response to electrons 130.0 - 147.5 MeV

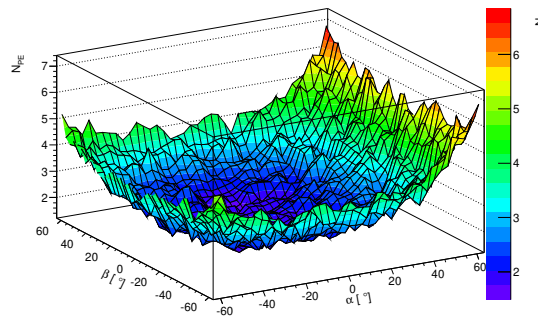RMS response to electrons 130.0 - 147.5 MeV

F.2 Detector Response to Photons

detector response to photons 0.5 - 1.5 MeV

RMS response to photons 0.5 - 1.5 MeV

detector response to photons 1.5 - 2.5 MeV

RMS response to photons 1.5 - 2.5 MeV

detector response to photons 2.5 - 3.5 MeV

RMS response to photons 2.5 - 3.5 MeV
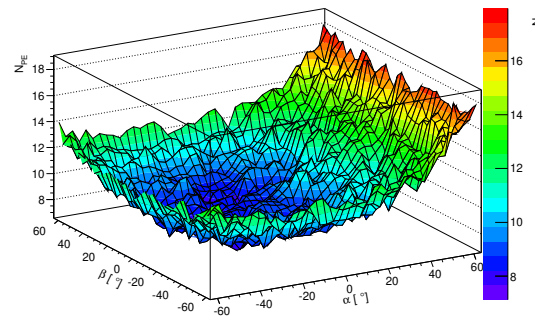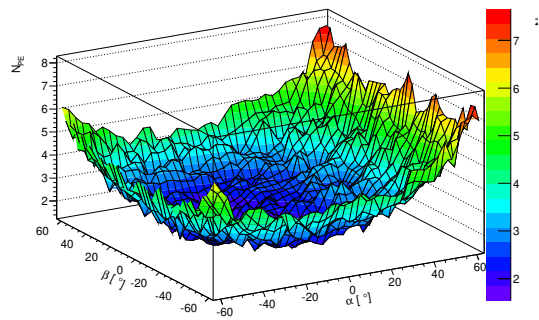
detector response to photons 3.5 - 4.5 MeV

RMS response to photons 3.5 - 4.5 MeV

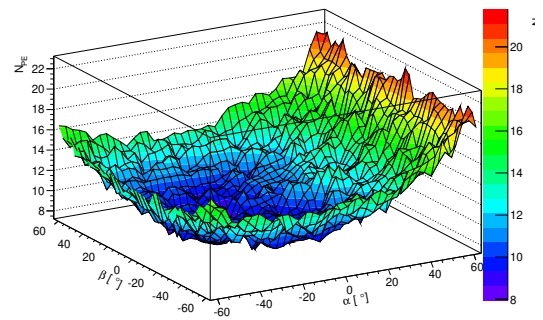detector response to photons 4.5 - 5.5 MeV
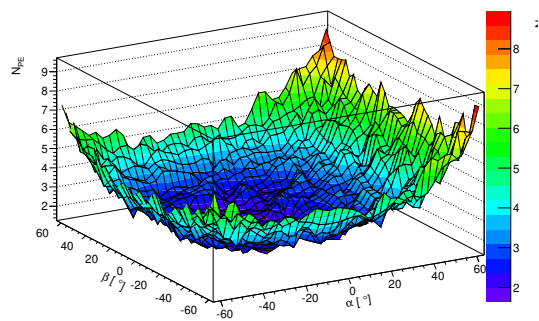
RMS response to photons 4.5 - 5.5 MeV

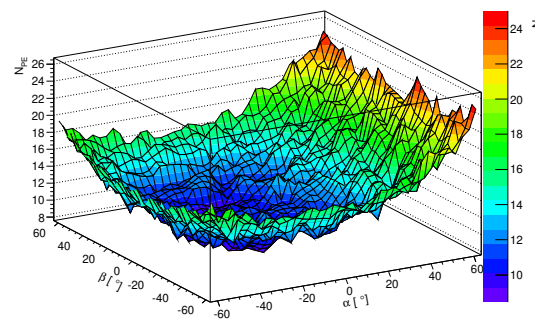detector response to photons 5.5 - 6.5 MeV
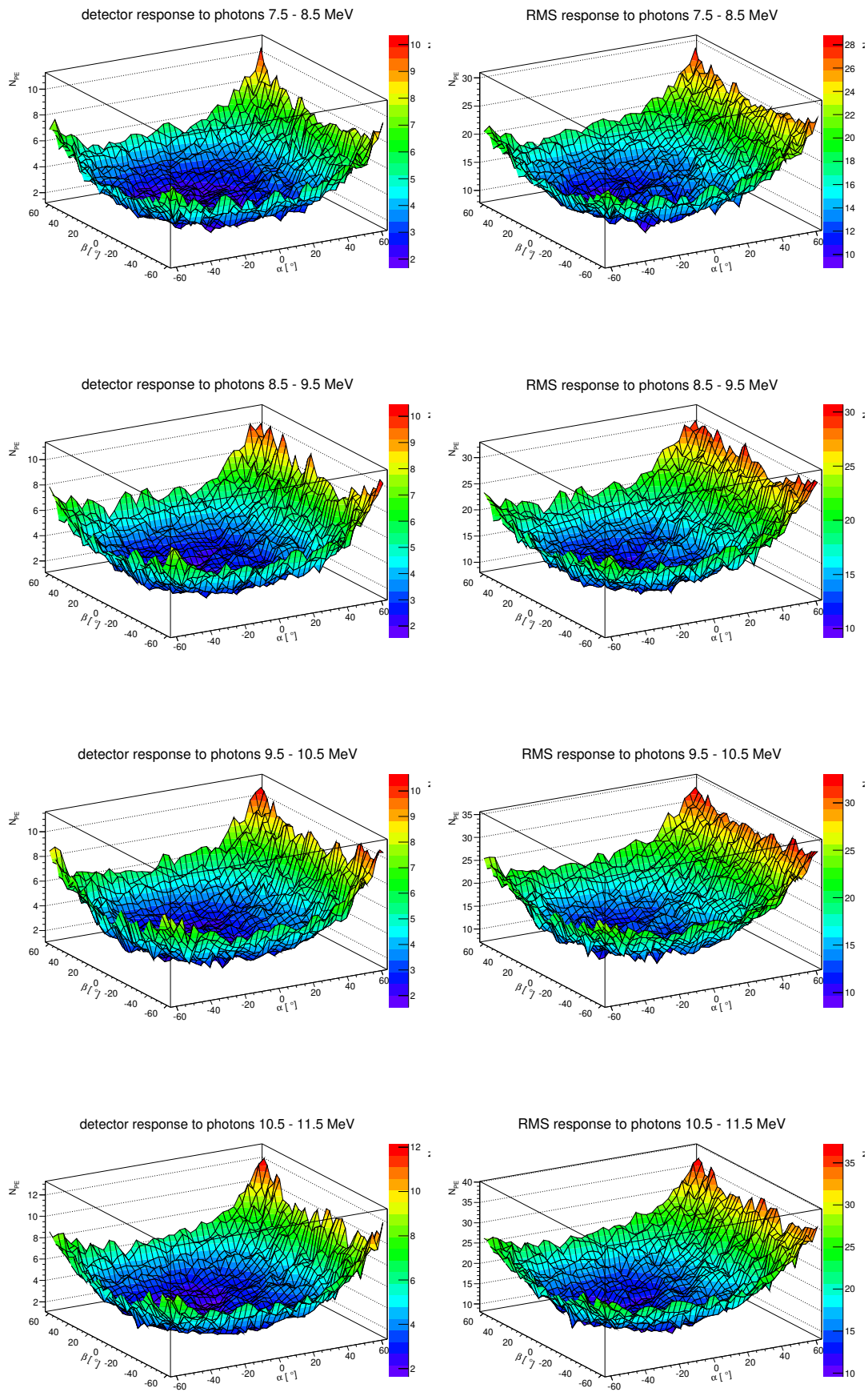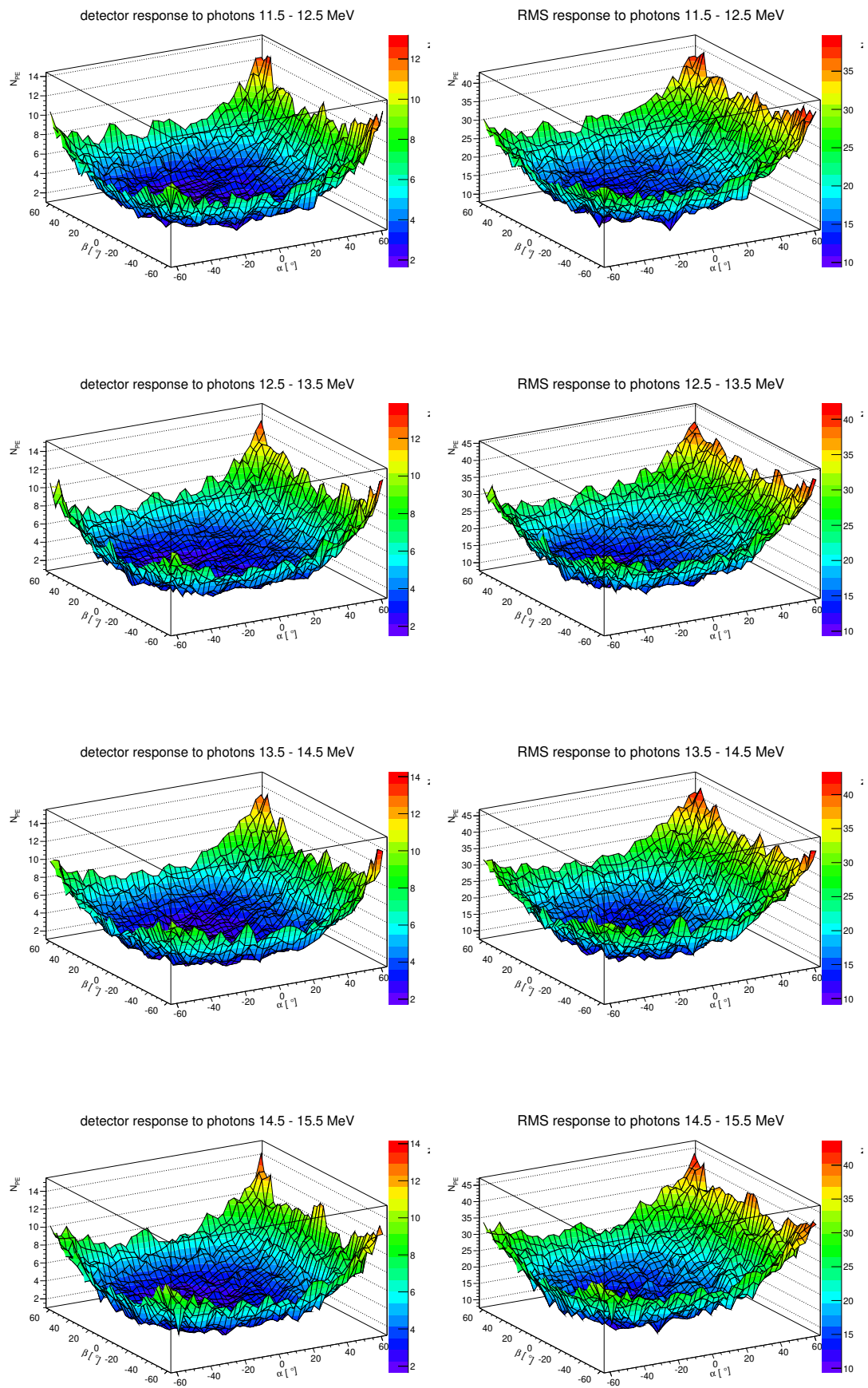
RMS response to photons 5.5 - 6.5 MeV

detector response to photons 6.5 - 7.5 MeV

RMS response to photons 6.5 - 7.5 MeV

detector response to photons 7.5 - 8.5 MeV

RMS response to photons 7.5 - 8.5 MeV

detector response to photons 8.5 - 9.5 MeV

RMS response to photons 8.5 - 9.5 MeV

detector response to photons 9.5 - 10.5 MeV

RMS response to photons 9.5 - 10.5 MeV

detector response to photons 10.5 - 11.5 MeV

RMS response to photons 10.5 - 11.5 MeV

detector response to photons 11.5 - 12.5 MeV

RMS response to photons 11.5 - 12.5 MeV

detector response to photons 12.5 - 13.5 MeV

RMS response to photons 12.5 - 13.5 MeV

detector response to photons 13.5 - 14.5 MeV

RMS response to photons 13.5 - 14.5 MeV

detector response to photons 14.5 - 15.5 MeV

RMS response to photons 14.5 - 15.5 MeV

detector response to photons 15.5 - 16.5 MeV

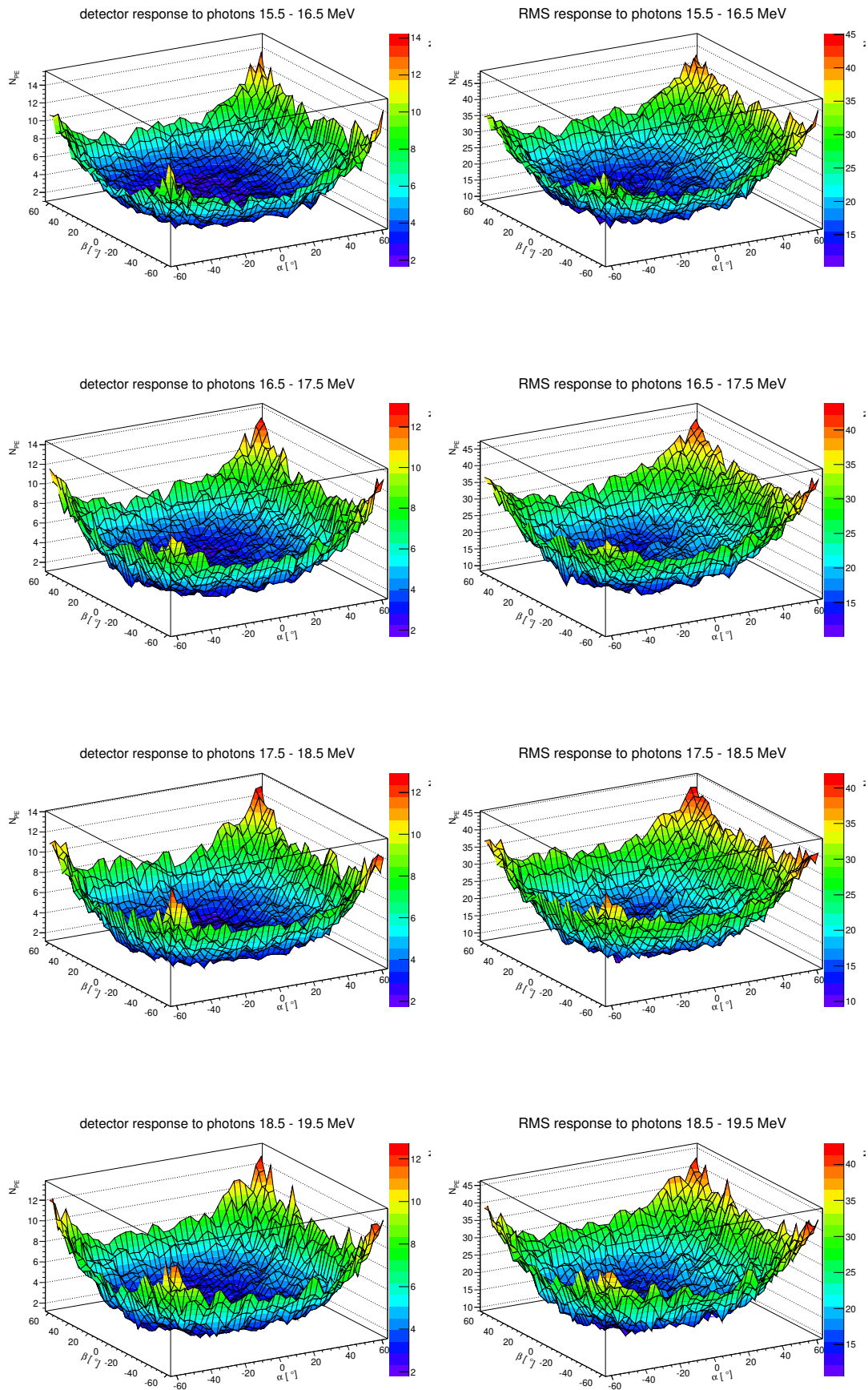RMS response to photons 15.5 - 16.5 MeV

detector response to photons 16.5 - 17.5 MeV

RMS response to photons 16.5 - 17.5 MeV

detector response to photons 17.5 - 18.5 MeV

RMS response to photons 17.5 - 18.5 MeV

detector response to photons 18.5 - 19.5 MeV
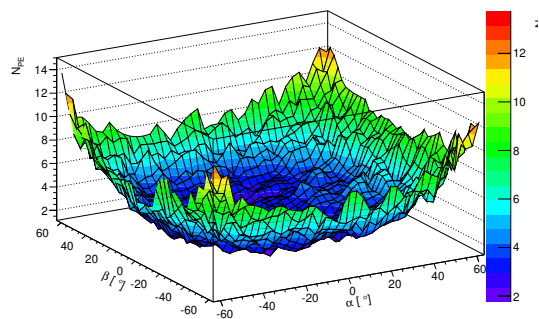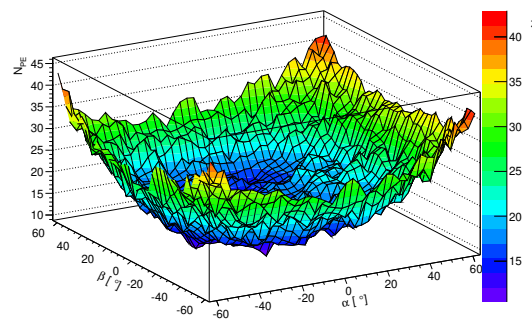
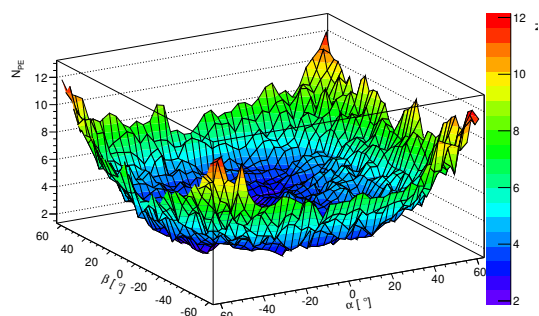RMS response to photons 18.5 - 19.5 MeV
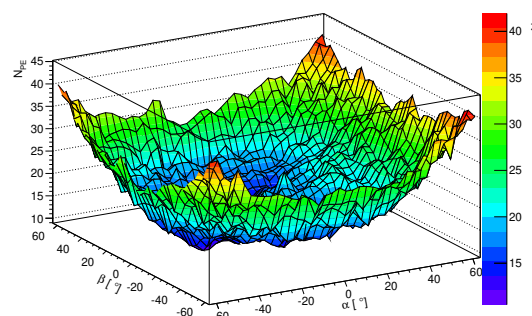
detector response to photons 19.5 - 22.5 MeV
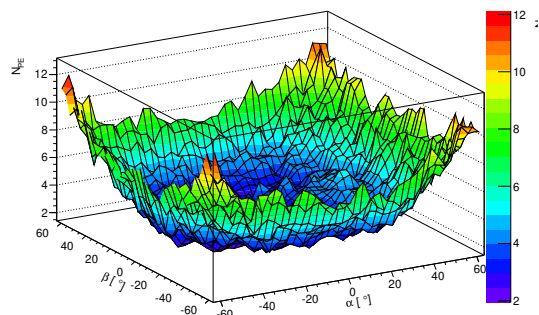
RMS response to photons 19.5 - 22.5 MeV

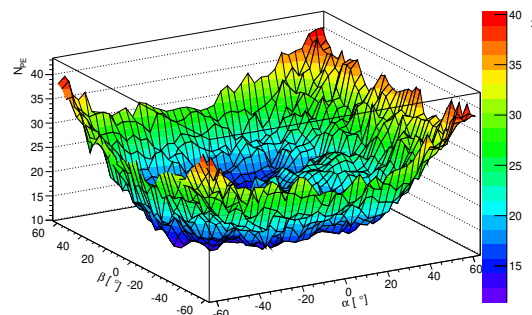detector response to photons 22.5 - 27.5 MeV

RMS response to photons 22.5 - 27.5 MeV

detector response to photons 27.5 - 32.5 MeV

RMS response to photons 27.5 - 32.5 MeV

detector response to photons 32.5 - 37.5 MeV

RMS response to photons 32.5 - 37.5 MeV

detector response to photons 37.5 - 47.5 MeV

RMS response to photons 37.5 - 47.5 MeV

detector response to photons 47.5 - 67.5 MeV

RMS response to photons 47.5 - 67.5 MeV
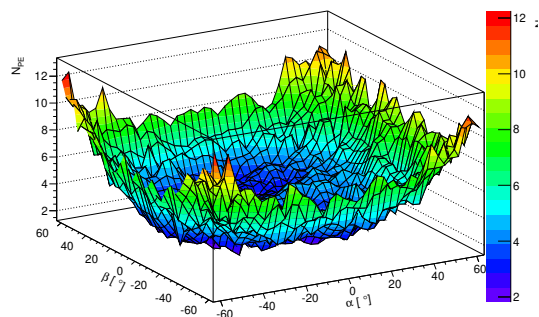
detector response to photons 67.5 - 90.0 MeV

RMS response to photons 67.5 - 90.0 MeV

detector response to photons 90.0 - 102.5 MeV

RMS response to photons 90.0 - 102.5 MeV

detector response to photons 102.5 - 112.5 MeV

RMS response to photons 102.5 - 112.5 MeV

detector response to photons 112.5 - 130.0 MeV

RMS response to photons 112.5 - 130.0 MeV

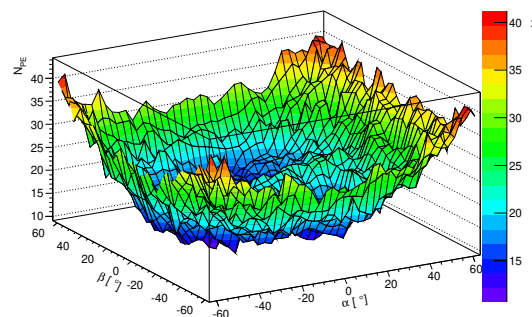detector response to photons 130.0 - 147.5 MeV

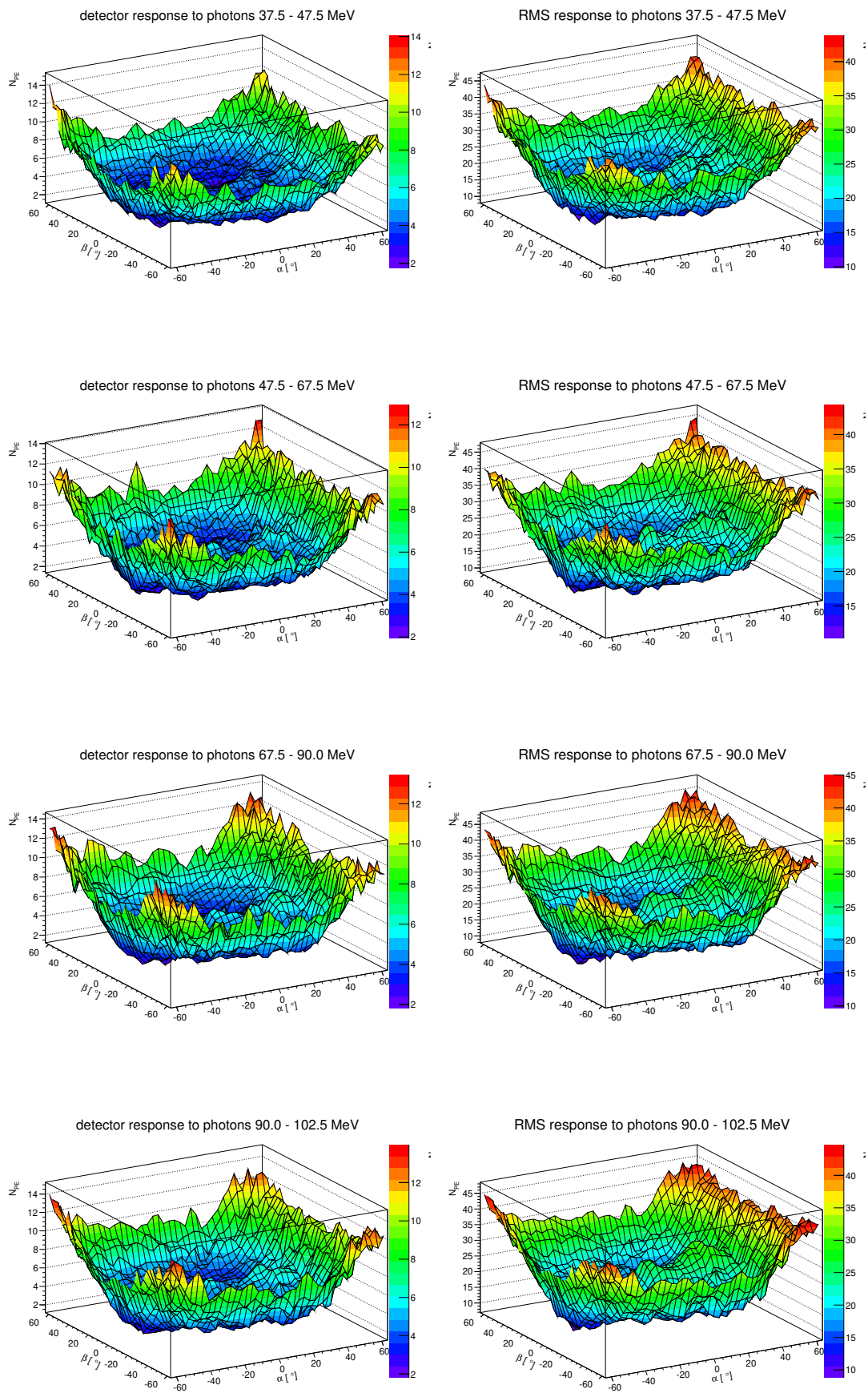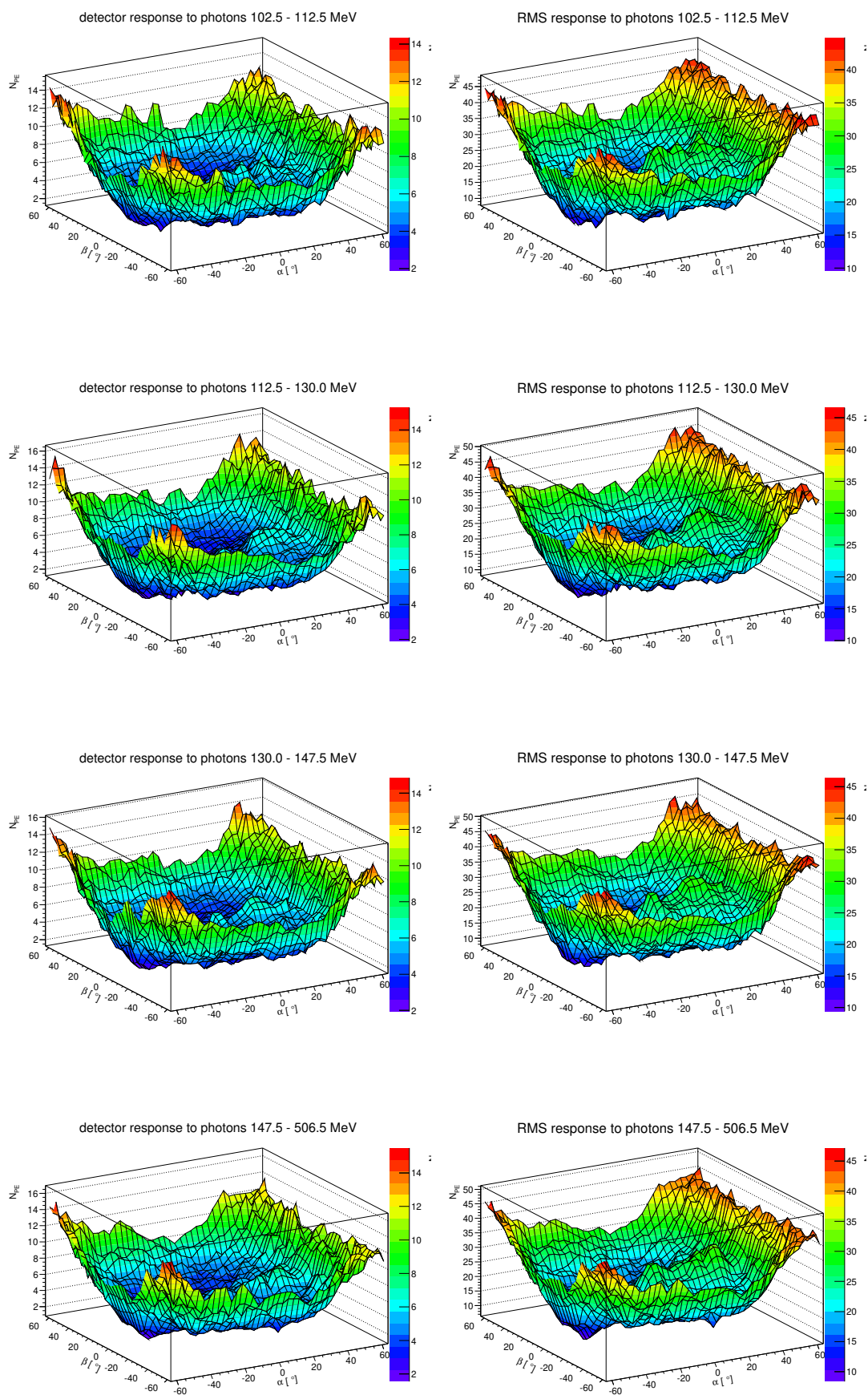RMS response to photons 130.0 - 147.5 MeV

detector response to photons 147.5 - 506.5 MeV

RMS response to photons 147.5 - 506.5 MeV

Bibliography

[1] F. Halzen and A. D. Martin. *Quarks and Leptons*. John Wiley & Sons, 1st edition, 1984. ISBN 0-471-88741-2.

[2] G. Kane. *Modern Elementary Particle Physics*. Cambridge University Press, 2nd edition, 2017. ISBN 978-1-107-16508-3.

[3] S. L. Glashow. Partial-symmetries of weak interactions. *Nuclear Physics*, 22: 579 – 588, 1961.

[4] S. Weinberg. A model of leptons. *Physical Review Letters*, 19:1264 – 1266, 1961.

[5] A. Salam. Weak and electromagnetic interactions. In N. Svartholm, editor, *Elementary Particle Theory. Relativistic Groups and Analyticity. Proceedings of the eighth Nobel Symposium, Lerum (Sweden), 1968*, pages 367 – 377. John Wiley & Sons, 1968.

[6] J. Beringer et al. Review of particle physics. *Physical Review D*, 86:010001, 2012.

[7] J. Erler and M. J. Ramsay-Musolf. Weak mixing angle at low energies. *Physical Review D*, 72:073003, 2005.

[8] D. Androić, D. S. Armstrong, et al. Precision measurement of the weak charge of the proton. *Nature*, 557:207 – 211, 2018.

[9] A. Denig. Review of dark photon searches. In A. Wrońska, A. Magiera, C. Guaraldo, and H. Ströher, editors, *Proceedings of the 14th International Workshop on Meson Production, Properties and Interactions (MESON) 2016, Cracow (Poland), 2016*, volume 130 of *EPJ Web of Conferences*, page 01005, 2016.

[10] K. S. Kumar et al. Low-energy measurements of the weak mixing angle. *Annual Reviews of Nuclear and Particle Science*, 63:237 – 267, 2013.

[11] K. Abe et al. High-precision measurement of the left-right Z boson cross-section asymmetry. *Physical Review Letters*, 84:5945 – 5949, 2000.

[12] J. Alcaraz et al. Precision electroweak measurements and constraints on the standard model. Technical Report CERN-PH-EP-2007-039, CERN, Geneva, December 2007.

[13] P. Spentzouris. Precision electroweak measurements from NuTeV. In A. Eskreys, J. Kwiecinski, and J. Szwed, editors, *Proceedings of the 10th International Workshop on Deep Inelastic Scattering (DIS), Cracow (Poland), 2002*, volume 33 of *Acta Physica Polonica B*, pages 3843 – 3847, 2002.

[14] P. G. Zeller et al. Precise determination of electroweak parameters in neutrino-nucleon scattering. *Physical Review Letters*, 88:091802, 2002. [Erratum: Physical Review Letters 90, 239902 (2003)].

[15] S. Davidson et al. Old and new physics interpretations of the NuTeV anomaly. *Journal of High Energy Physics*, 2002:037, 2002.

[16] C. E. Wieman. Parity nonconservation in atoms; past work and trapped atom future. *Hyperfine Interactions*, 83:27 – 34, 1993.

[17] S. C. Bennett and C. E. Wieman. Measurement of the $6S \rightarrow 7S$ transition polarizability in atomic cesium and an improved test of the standard model. *Physical Review Letters*, 82:2424 – 2487, 1999. [Erratum: Physical Review Letters 82, 4153 (1999); Physical Review Letters 83, 889 (1999)].

[18] F. E. Maas and K. D. Paschke. Strange nucleon form-factors. *Progress in Particle and Nuclear Physics*, 95:209 – 244, 2017.

[19] J. Erler, A. Kurylov, and M. J. Ramsey-Musolf. Weak charge of the proton and new physics. *Physical Review D*, 68:016006, 2003.

[20] G. M. Urciuoli. Parity violation in electron scattering. *La Rivista del Nuovo Cimento*, 38:1 – 72, 2015.

[21] P. A. Souder et al. Measurement of parity violation in the elastic scattering of polarized electrons from C-12. *Physical Review Letters*, 65:694 – 697, 1990.

[22] K. Gerz et al. Measurement of the weak charge of the carbon-12 nucleus within the P2 experiment in mainz. In R. Milner, R. Carlini, and F. Maas, editors, *Proceedings of the Workshop to explore Physics Opportunities with intense, polarized Electron Beams at 50 – 300 MeV, Cambridge, MA (USA), 2013*, volume 1563 of *AIP Conference Proceedings*, pages 86 – 89, 2013. ISBN 978-0-7354-1191-3.

[23] D. Androić et al. Parity-violating inelastic electron-proton scattering at low Q^2 above the resonance region. *Physical Review C*, 101:055503, 2020.

[24] D. Androić et al. First determination of the weak charge of the proton. *Physical Review Letters*, 111:141803, 2013.

[25] D. Becker. *Voruntersuchungen zur Messung der schwachen Ladung des Protons im Rahmen des P2-Experiments.* PhD thesis, Johannes Gutenberg-Universität, Mainz, November 2018.

[26] M. J. Musolf et al. Intermediate-energy semileptonic probes of the hadronic neutral current. *Physics Reports*, 239:1 – 178, 1994.

[27] P. Larin. Voruntersuchungen für ein neues Präzisionsexperiment zur Messung der schwachen Ladung des Protons. Master's thesis, Johannes Gutenberg-Universität Mainz, 2011.

[28] P. Souder and K. D. Paschke. Parity violation in electron scattering. *Frontiers of Physics*, 11:111301, 2016.

[29] M. Gorchtein, C. J. Horowitz, and M. J. Ramsey-Musolf. Model dependence of the γZ dispersion correction to the parity-violating asymmetry in elastic ep scattering. *Physical Review C*, 84:015502, 2011.

[30] V. Bechthold. *Untersuchung von Multi-Alkali-Verbindungen im Hinblick auf ihre Eignung zur Erzeugung hochbrillanter Elektronenpulse.* PhD thesis, Johannes Gutenberg-Universität, Mainz, November 2018.

[31] T. U. Stengler. *Entwicklung eines supraleitenden Beschleunigermoduls für den rezirkulierenden Betrieb am Mainz Energy-Recovering Superconducting Accelerator (MESA).* PhD thesis, Johannes Gutenberg-Universität, Mainz, February 2020.

[32] Y. Imai. *Messung und Optimierung der Lichtpolarisation des A4-Compton-Rückstreupolarimeters.* PhD thesis, Johannes Gutenberg-Universität, Mainz, November 2018.

[33] R. F. Kempf. *Stabilisation der Strahlparameter für das P2-Experiment an MESA.* PhD thesis, Johannes Gutenberg-Universität, Mainz, July 2020.

[34] D. Becker et al. The P2 Experiment. *European Physical Journal A*, 54:208, 2018.

[35] S. D. Covrig et al. The cryogenic target for the G^0 experiment at Jefferson Lab. *Nuclear Instruments and Methods in Physics Research A*, 551:218 – 235, 2005.

[36] K. Arndt et al. Technical design of the phase I Mu3e experiment. Technical report, PSI, Villigen, September 2020.

[37] T. Jennewein. Erste Erfahrungen mit der Messelektronik für das P2-Experiment an MESA. Master's thesis, Johannes Gutenberg-Universität, Mainz, September 2015.

[38] Ig. Tamm. Radiation emitted by uniformly moving electrons. *Journal of Physics USSR*, 1:439 – 454, 1939.

[39] I. H. Malitson. Interspecimen comparison of the refractive index of fused silica. *Journal of the Optical Society of America*, 55:1205 – 1209, 1965.

[40] J. Amaré et al. Study of scintillation in natural and synthetic quartz and methacrylate. *Optical Materials*, 36:1408 – 1417, 2014.

[41] J. Ritman. The FOPI detector at SIS/GSI. In E. Borchi, S. R. Majewski, J. Huston, A. L. Penzo, and P. G. Rancoita, editors, *Proceedings of the 4th International Conference on Advanced Technology and Particle Physics, Como (Italy), 1994*, volume 44 of *Nuclear Physics B – Proceedings Supplements*, pages 708 – 715, 1995.

[42] C. Lu et al. Detection of internally reflected Cherenkov light, results from the BELLE DIRC prototype. *Nuclear Instruments and Methods in Physics Research A*, 371:82 – 86, 1996.

[43] A. G. Wright. *The photomultiplier handbook*. Oxford University Press, 1st edition, 2017. ISBN 978-0-19-956509-2.

[44] R. Brun and F. Rademakers. ROOT – an object oriented data analysis framework. *Nuclear Instruments and Methods in Physics Research A*, 389:81 – 86, 1997.

[45] C. P. Achenbach. *Aufbau eines Bleifluorid-Kalorimeters zur Messung der Paritätsverletzung in der elastischen Elektronenstreuung*. PhD thesis, Johannes Gutenberg-Universität, Mainz, May 2001.

[46] V. Kushpil et al. Radiation hardness investigation of avalanche photodiodes for the Projectile Spectator Detector readout at the Compressed Baryonic Matter experiment. *Nuclear Instruments and Methods in Physics Research A*, 787:117 – 120, 2015.

[47] Photomultiplier tube R11410, 2011. Data Sheet.

[48] K. Lung et al. Characterization of the Hamamatsu R11410-10 3-in. photomultiplier tube for liquid xenon dark matter direct detection experiments. *Nuclear Instruments and Methods in Physics Research A*, 696:32 – 39, 2012.

[49] D. S. Akerib et al. An ultra-low background PMT for liquid xenon detectors. *Nuclear Instruments and Methods in Physics Research A*, 703:1 – 6, 2013.

[50] I. J. D. MacGregor. Research with real photons at the MAMI 1.6 GeV electron accelerator. In G. Giardina, S. Eidelman, G. Venanzoni, and G. Mandaglio, editors, *Proceedings of the International Symposium "Lepton and Hadron*

Physics at Meson-Factories", Messina (Italy), 2013, volume 72 of *EPJ Web of Conferences*, page 00014, 2014.

[51] J. Diefenbach. *Bestimmung der Analysierstärke des A4-Compton-Rückstre-upolarimeters zur Messung der longitudinalen Spinpolarisation des MAMI-Elektronenstrahls.* PhD thesis, Johannes Gutenberg-Universität, Mainz, July 2010.

[52] C. Grupen and B. Shwartz. *Particle Detectors*, volume 26 of *Cambridge Monographs on Particle Physics, Nuclear Physics and Cosmology.* Cambridge University Press, 2nd edition, 2008. ISBN 978-0-521-84006-4.

[53] M. Hoek. Tailoring the radiation hardness of fused silica. In G. Hallewell, R. Forty, W. Hofmann, E. Nappi, and B. Ratcliff, editors, *Proceedings of the Seventh International Workshop on Ring Imaging Cherenkov Detectors (RICH), Cassis (France), 2010*, volume 639 of *Nuclear Instruments and Methods in Physics Research A*, pages 227 – 230, 2011.

[54] M. Hoek et al. Radiation hardness study on fused silica. In A. Bressan, S. Dalla Torre, B. Gobbo, and F. Tessarotto, editors, *Proceedings of the Sixth International Workshop on Ring Imaging Cherenkov Detectors (RICH), Trieste (Italy), 2007*, volume 595 of *Nuclear Instruments and Methods in Physics Research A*, pages 190 – 193, 2008.

[55] M. Antonini et al. Comparison of heavy-ion, proton and electron irradiation effects in vitreous silica. *Radiation Effects*, 65:41 – 48, 1982.

[56] M. J. Berger et al. ESTAR, PSTAR and ASTAR: Computer programs for calculating stopping-power and range tables for electrons, protons and helium ions (version 1.2.3). [Online] Available: `https://physics.nist.gov/Star` [2019, June 27], 2005.

[57] S. M. Seltzer et al. Key data for ionizing-radiation dosimetry: Measurement standards and applications. Technical Report ICRU Report 90, The International Commission on Radiation Units and Measurements, Bethesda, MD, 2014.

[58] R. M. Sternheimer, M. J. Berger, and S. M. Seltzer. Density effect for the ionization loss of charged particles in various substances. *Atomic Data and Nuclear Data Tables*, 30:261 – 271, 1984.

[59] K. S. Krane. *Introductory Nuclear Physics.* John Wiley & Sons, 1st edition, 1987. ISBN 978-0-471-80553-3.

[60] C. M. Nelson and J. H. Crawford, Jr. Optical absorption in irradiated quartz and fused silica. *Journal of Physics and Chemistry of Solids*, 13:296 – 305, 1960.

[61] P. Achenbach et al. Radiation resistance and optical properties of lead fluoride Cherenkov crystals. *Nuclear Instruments and Methods in Physics Research A*, 416:357 – 363, 1998.

[62] C. M. Poole et al. A CAD interface for GEANT4. *Australasian Physical & Engineering Sciences in Medicine*, 35:329 – 334, 2012.

[63] S. Schröder et al. Bulk scattering properties of synthetic fused silica at 193 nm. *Optics Express*, 14:10537 – 10549, 2006.

[64] S. D'Amato. SandBox: A facility for XENON photosensors characterization and measurements of photocathode uniformity. Bachelor's thesis, Universität Zürich, August 2014.

Acknowledgements

The acknowledgements are omitted in this edition due to privacy regulations.

Curriculum Vitae

The CV is omitted in this edition due to privacy regulations.